

Universität
Rostock



Traditio et Innovatio

Analysis of Sub-Cycle Nanoplasma Dynamics via Low-Order Harmonic Generation

Dissertation zur Erlangung des akademischen Grades
Doctor rerum naturalium
der Mathematisch-Naturwissenschaftlichen Fakultät
der Universität Rostock

vorgelegt von
Benjamin Liewehr, geb. am 7. April 1991 in Itzehoe

https://doi.org/10.18453/rosdok_id00004400

Betreuer: Prof. Dr. T. Fennel, Universität Rostock

Gutachter: Prof. Dr. T. Fennel, Universität Rostock
Prof. Dr. M. Wollenhaupt, Universität Oldenburg

Einreichung am: 14.04.2023

Verteidigung am: 07.07.2023

Abstract

The nonlinear optical response of dielectrics under intense laser fields gives rise to various important effects ranging from four-wave mixing and solitary wave formation to self-focussing and self-phase modulation. These well-known processes take place at intensities low enough to avoid permanent material modification and optical breakdown and can usually be described accurately by the third-order Kerr response. At higher intensities, additional contributions to the nonlinear response such as dynamical Bloch oscillations and recollision effects emerge and have recently been studied in great detail in the context of high-order harmonic generation. As yet unresolved is the significance of strong-field ionization and plasma formation for the nonlinear optical response and the resulting optical signals although ionization-induced wave mixing and harmonic emission have been proposed more than 30 years ago. This thesis describes a systematic analysis that aims at closing this gap. To this end the role and signatures of ionization-induced nonlinearities in wide bandgap dielectrics are investigated theoretically via local plasma simulations and ionization-radiation models and compared to experiments to reveal their nature and their potential for imaging and controlling strong-field ionization down to the sub-cycle time scale. The central results of this thesis are (i) the identification of the dominance of ionization induced low order harmonic emission near the damage threshold through the so far overlooked injection current, (ii) the demonstration of the resulting opportunities for monitoring ultrafast plasma formation via non-perturbative wave mixing, and (iii) the analysis of the potential of sub-cycle plasma formation with shaped laser fields for the generation of optically controlled sub-wavelength structures and gratings in laser material modification.

Kurzzusammenfassung

Die nichtlineare Strahlungsantwort dielektrischer Festkörper auf starke Laserfelder führt zu verschiedenen wichtigen Effekten, die von Vier-Wellen-Mischung, Solitonenerzeugung bis hin zur Selbstfokussierung und Selbstphasenmodulation reichen. Diese wohlbekanntesten Prozesse laufen bereits bei Intensitäten ab, die niedrig genug sind, um eine dauerhafte Materialveränderung bzw. einen optischen Zusammenbruch zu vermeiden und lassen sich üblicherweise vollständig durch die Kerr-Antwort dritter Ordnung beschreiben. Bei höheren Intensitäten treten weitere Beiträge zur nicht-linearen Antwort auf, wie dynamische Blochoszillationen und Rekollisionseffekte, die bereits detailliert im Zusammenhang mit hoher Harmonischerzeugung untersucht wurden. Bisher ungeklärt ist dabei der Einfluss der Starkfeldionisation und der Plasmaerzeugung auf die nichtlineare optische Antwort und die daraus resultierenden optischen Signale, obwohl ionisationsinduzierte Wellenmischung und Harmonischerzeugung vor bereits 30 Jahren erstmals vorgeschlagen wurden. Diese Dissertation beschreibt eine systematische Analyse, um diese Lücke zu schließen. Hierzu werden Rolle und Signaturen von ionisationsinduzierten Nichtlinearitäten in Dielektrika mit großer Bandlücke theoretisch mittels lokaler Plasmasimulationen und Ionisationsratenmodellen untersucht und mit Experimenten verglichen, um ihr Potential für Abbildung und Kontrolle der Starkfeldionisation bis hinunter zur Subzyklenzeitskala aufzuklären. Die zentralen Ergebnisse dieser Arbeit sind (i) die Identifikation des dominanten Beitrags ionisationsinduzierter Harmonischer niedriger Ordnung nahe der Zerstörschwelle anhand des bisher unberücksichtigten Injektionsstroms, (ii) der Demonstration der sich daraus ergebenden Möglichkeiten zur Beobachtung ultraschneller Plasmaerzeugung durch nicht-perturbative Wellenmischung und (iii) die Identifizierung von Potenzialen zur Subzyklenplasmaerzeugung mittels maßgeschneiderter Laserfelder für die Erzeugung optisch kontrollierter Subwellenlängenstrukturen und Gitter für die Lasermaterialbearbeitung.

Contents

Abstract – Kurzzusammenfassung	iv
Publications and Conference Contributions	ix
List of figures	x
List of tables	xi
List of Symbols	xiii
1 Introduction	1
2 Identification of Tunneling-Induced Low-Order Harmonics	7
2.1 Experimental setup and beam parameters	8
2.2 Experimental results	10
2.3 Metrology for the effective nonlinear order	12
2.4 Ionization-induced nonlinearity	13
2.4.1 Ensemble derivatives	14
2.4.2 Nonlinear current and dipole acceleration	14
2.4.3 Physical picture of relevant nonlinear mechanisms	15
2.4.4 Role of the injection current for energy conservation	16
2.4.5 Numerical analysis of injection and Brunel harmonic contribu- tions	17
2.5 Conclusion	18
3 Local Strong-Field Medium Response	19
3.1 Nonlinear polarization	20
3.1.1 Single-color polarization and degeneracy weights	20
3.2 Emission of harmonics from nonlinear source terms	21
3.2.1 Solution of the nonlinear wave equation for a thin film	21
3.2.2 Spectral weights of harmonic far-field response	22
3.2.3 Role of transverse beam profile for spectral amplitudes	23
3.3 Two-color wave-mixing	25
3.3.1 Parallel polarization scenario	26
3.3.2 Degeneracy in self-phase and cross-phase modulation	27
3.3.3 Intensity ratio: Parallel versus perpendicular scenario	27
3.3.4 Polarization direction of wave-mixing harmonics	28
3.3.5 Circularly polarized harmonics in two color case	29
3.3.6 Intensity ratios between different polarization scenarios	30
3.4 Scaling analysis of injection and Brunel response	31
3.4.1 Power-law ansatz for ionization rate	32
3.4.2 Distinct nonlinear orders of Brunel and injection mechanism	33
3.4.3 Intensity ratios of Brunel and injection harmonics	34
3.4.4 Dominant contribution of the ionization response	36
3.5 Temporal signatures	37

3.6	Characteristic phases of local response mechanisms	39
3.6.1	Phase of harmonic currents	40
3.6.2	Phase of harmonic fields in thin film scenario	40
3.6.3	Effect of Gouy phase in Gaussian beam scenario	41
3.7	Conclusion	42
4	Collisional Effects in the Extreme Nonlinear Response	43
4.1	Phase shift of quiver motion and Brunel harmonics	43
4.1.1	Drude model – Scenario of constant elastic damping	44
4.2	Tunneling-induced vs. collisional Brunel harmonics	45
4.2.1	Phase of collisional Brunel harmonics in a simple man’s approach	45
4.3	Kinetic model for capturing collisional effects	46
4.3.1	Collision rates	46
4.3.2	Calculation of the velocity distribution	47
4.4	Effect of impact ionization on nonlinear response	48
5	Reconstruction of the Strong-Field-Driven Plasma Dynamics	51
5.1	Phase retrieval algorithm and convergence	52
5.2	Optimal conditions for reconstruction	55
5.2.1	Role of the polarization configuration	55
5.2.2	Role of competing nonlinear mechanisms	56
5.3	Reconstruction from experimental spectra	57
6	FDTD Ionization-Radiation Model	61
6.1	Electromagnetic field propagation via FDTD	61
6.2	Self-consistent polarization, ionization and plasma response	62
6.2.1	Ionization degree	64
6.2.2	Nonlinear currents	64
6.2.3	Temperature and drift-dependent elastic and inelastic collision rates	65
6.2.4	Valance band depletion	66
6.2.5	Temperature and drift update	66
6.2.6	Bound electron response: Dispersive nonlinear Lorentz model	70
6.2.7	Unidirectional source – Total-field scattered-field boundary	72
6.2.8	Absorbing boundary condition	72
6.3	Energy deposition via ionization	73
6.3.1	Impact of standing waves on the spatio-temporal plasma build-up	74
6.4	Effect of plasma formation on reflection, transmission, and absorption	79
6.4.1	Delay dependence	79
6.4.2	Intensity dependence	80
6.4.3	Focal averaging	81
6.5	Conclusion	82

7	Harmonics from Nonlinear Reflection	83
7.1	Amplitude and phase for nonlinear reflection	83
7.1.1	Benchmark of reflected injection and Brunel harmonics	85
7.1.2	Signatures of the nonlinear reflection mechanism	86
7.1.3	Longitudinal length-scale of reflection response	88
7.2	Linking reflected harmonics and local current	88
7.3	Real space perspective on tunneling injection in periodic potential	91
7.3.1	SiO ₂ model for quantum mechanical tunneling dynamics	91
7.3.2	Quantum mechanical strong-field ionization current	93
7.3.3	Decomposition and analysis of the field-induced current	96
8	Conclusions and Outlook	98
	Appendix	100
A	Identification of Tunneling-Induced Low-Order Harmonics	101
A.1	Difference quotient for ensemble derivative	101
B	Local Strong-Field Medium Response	102
B.1	Fields emitted from currents in a thin sheet	102
B.2	Amplitude and phase of the Hertzian dipole	103
B.3	Harmonic emission in Gaussian beam scenario	104
B.4	Calculation of circular pump polarization direction	106
B.5	Generalization of intensity ratios for $n > 1$ mixing signals	108
B.6	Temporal width and delay dependence of wave-mixing signals	109
C	Collisional Effects in the Extreme Nonlinear Response	112
C.1	Phase of quiver motion according to Drude model	112
C.2	Gabor transform	113
D	Harmonics from Nonlinear Reflection	114
D.1	Reflected harmonics	116
D.2	Degeneracy of Brunel emission	119
D.3	Computing the band structure in Fourier representation	120
D.4	Velocity-Verlet integration of electron and hole trajectories	122
	Bibliography	125
	Academic Curriculum Vitae	140
	List of Presentations	142
	Statement of Authorship	144
	Acknowledgement – Danksagung	145

Publications and Conference Contributions

Contributions related to this thesis:

- [JLK⁺20] P. Jürgens, B. Liewehr, B. Kruse, C. Peltz, D. Engel, A. Husakou, T. Witting, M. Ivanov, M. Vrakking, T. Fennel, and A. Mermillod-Blondin, *Origin of strong-field-induced low-order harmonic generation in amorphous quartz*, *Nature Physics* **16**, 1035–1039 (2020).
- [JLK⁺22a] P. Jürgens, B. Liewehr, B. Kruse, C. Peltz, T. Witting, A. Husakou, A. Rouzee, M. Ivanov, T. Fennel, M. J. Vrakking and A. Mermillod-Blondin, *Characterization of laser-induced ionization dynamics in solid dielectrics*, *ACS Photonics* **9**, 233–240 (2022).
- [JLK⁺22b] P. Jürgens, B. Liewehr, B. Kruse, C. Peltz, T. Witting, A. Husakou, A. Rouzéé, M. Ivanov, T. Fennel, M. J. J. Vrakking and A. Mermillod-Blondin, *Reconstruction of Strong-Field-Driven Carrier Generation Dynamics from Injection Harmonics in Solid Dielectrics*, *The International Conference on Ultrafast Phenomena*, Tu4A.14 (2022).
- [MBJL⁺19] A. Mermillod-Blondin, P. Jürgens, B. Liewehr, B. Kruse, C. Peltz, T. Witting, A. Husakou, M. Ivanov, T. Fennel and M. J. Vrakking, *Study of plasma formation in solid dielectrics with the help of low-order harmonic emission*, *SPIE LASE Proceedings* **10905**, 64–69 (2019).
- [KLPF20] B. Kruse, B. Liewehr, C. Peltz and T. Fennel, *Quantum coherent diffractive imaging*, *Journal of Physics: Photonics* **2**, 024007 (2020).

Further contributions:

- [LB19] B. Liewehr and M. Bachmann, *Smart polymeric recognition of a hexagonal monolayer*, *EPL (Europhysics Letters)* **127**, 68003 (2019).
- [QLK⁺19] K. Qi, B. Liewehr, T. Koci, B. Pattanasiri, M. J. Williams and M. Bachmann, *Influence of bonded interactions on structural phases of flexible polymers*, *The Journal of chemical physics* **150**, 054904 (2019).

List of figures

1.1	Experimental evidence of ionization induced harmonics	4
2.1	Mechanisms of harmonic emission in solids	7
2.2	Experimental setup for low-order harmonic wave mixing	9
2.3	Delay-dependent harmonic spectrum	10
2.4	Dependence of harmonic wave-mixing signal on crystal orientation . .	11
2.5	Measured effective order of nonlinearity	13
2.6	Physical picture of polarization, Brunel, and injection response	15
2.7	Bandgap-dependent lift-off of the effective order of nonlinearity	18
3.1	Degeneracy of low-order wave-mixing	21
3.2	Spectral weight coefficients of low-order harmonics	23
3.3	Harmonic emission from thin film	24
3.4	Polarization of the $n = 1$ wave-mixing harmonic in the experiment . .	28
3.5	Intensity ratios as function of nonlinear order	31
3.6	ADK tunneling rate and tunneling exponent vs. driving field	33
3.7	Intensity ratio, injection vs. Brunel response, in the local model	36
3.8	Pulse duration, and width on delay axis of harmonics	38
3.9	Phase of local, non-linear currents in pointer diagram	39
3.10	Phase relation of emitted harmonic fields	41
4.1	Phase of Brunel harmonics as function of collision rate	44
4.2	Elastic and inelastic collision rate as function of electron velocity	47
4.3	Gabor-transform analysis of dominant harmonic emission mechanisms	49
5.1	Reconstruction error as function of pump intensity	56
5.2	Retrieval of tunnel ionization traces from $n = 1$ injection signal	59
6.1	FDTD update equations for ionization radiation model	63
6.2	Drift and temperature-dependent collision rates	66
6.3	Energy balance for tunneling-induced plasma formation	74
6.4	Spatio-temporal structure of plasma formation	75
6.5	Hot and cold avalanching in time trace of inelastic collision rate	78
6.6	Transmission, reflection, and absorption vs. delay and intensity	80
6.7	Focal averaged loss of transmission in two-color scenario	82
7.1	Harmonic amplitude and phase from different emission geometries . .	84
7.2	Single color reflection benchmark	86
7.3	Phase of harmonic polarization and field at the front interface	88
7.4	Scaling of wave-mixing harmonics in reflection direction	89
7.5	Band structure and energy eigenstates of the SiO ₂ model system	92
7.6	Strong-field-induced, quantum mechanical current	94
7.7	Spatio-temporal structure and physical significance of intra- and inter-band contributions	96

List of tables

3.1	Box-arrow notation for degeneracy analysis	27
5.1	Ptychographic retrieval algorithm in pseudo-code	54
6.1	Mean energy per collision and ionization electron	68
6.2	Parameters of the Lorentz-oscillator model for SiO ₂ and gold	70
7.1	Mechanism-specific harmonic amplitude scaling	87
7.2	Mechanism-specific phases for different emission geometries	87

Navigation in the Document

References to sections, figures, equations, etc. are compiled as hyperlinks. After following a hyperlink, most PDF viewers allow to return to the previous position in the document by pressing either the keyboard shortcut [Alt] + [←] or [Alt] + [L].

List of Symbols

Natural constants used in SI units

c	–	speed of light in vacuum
e	–	absolute value of electron charge
m_e	–	electron mass
\hbar	–	reduced Planck constant
ε_0	–	vacuum permittivity
μ_0	–	vacuum permeability
k_B	–	Boltzmann constant

Symbols chapter 1 Introduction

γ	–	Keldysh parameter
ω	–	carrier wave angular frequency
E_g	–	band gap energy
n_{ior}	–	index of refraction
I_{med}	–	intensity of the laser field transmitted into the medium

Symbols chapter 2 Identification of Tunneling-Induced Low-Order Harmonics

λ	–	vacuum wave length
τ	–	pulse width, intensity full-width half-maximum
E_p	–	pulse energy
n, ℓ	–	Two-color harmonic wave mixing order, eq. (2.1)
ω_n^{mix}	–	angular frequency of wavemixing signal, eq. (2.1)
\mathbf{E}	–	electric field, eq. (2.2)
$\mathbf{P}_L, \mathbf{P}_{NL}$	–	linear and nonlinear medium polarization density, eq. (2.2)
t	–	time, eq. (2.3)
m	–	order of nonlinear response, eq. (2.2)
μ	–	substitution for nonlinear order $\mu = \frac{m-1}{2}$, eq. (2.2)
I_{\parallel}, I_{\perp}	–	intensity in parallel and perpendicular two-color field polarization configuration, eq. (2.4)
$\chi^{(3)}$	–	third order nonlinear susceptibility
q	–	carrier charge, eq. (2.5)
n_0	–	number density of molecules in nonlinear medium, eq. (2.5)
\mathbf{x}	–	charge displacement, eq. (2.5)
N	–	number of particles, eq. (2.6)
ρ	–	normalized ionization degree (conduction band occupations), eq. (2.5)
\mathbf{J}	–	current density, eq. (2.10)

u_{EM}	–	energy density of the electromagnetic field, eq. (2.13)
$\dot{\rho}_{tun}$	–	effective tunneling rate, including depletion of valance band, eq. (2.14)

Symbols chapter 3 Local Strong-Field Medium Response

$\chi^{(m)}$	–	m^{th} order nonlinear susceptibility, eq. (3.2)
h	–	harmonic order, eq. (3.5)
$D_h^{(m)}$	–	degeneracy factor of harmonic order h , generated by m^{th} order nonlinear mechanism, eq. (3.5)
d_z	–	medium thickness, along the z-axis (optical axis), eq. (3.6)
n_L	–	linear refractive index, eq. (3.6)
z_R	–	Rayleigh length, eq. (3.8)
w_0	–	beam waist radius, eq. (3.8)
β	–	spectral weight coefficient, eq. (3.7)
Γ	–	tunneling rate, eq. (3.29)
s	–	tunneling exponent, eq. (3.33)
$\tau_{out}^{(m)}$	–	intensity FWHM pulse duration of harmonics, eq. (3.59)
$\tau_{delay}^{(m)}$	–	width of wave mixing signal with respect to delay axis, eq. (3.59)
ϕ_n	–	temporal phase of n -th order mixing signal, eq. (3.60)
ϕ^{mech}	–	mechanism specific phase, eq. (3.60)
ϕ_n^{mix}	–	phase due to wave-mixing, eq. (3.60)
ϕ_n^{CE}	–	carrier envelope phase of wave-mixing harmonics, eq. (3.61)
ϕ^{Gouy}	–	Gouy phase, eq. (3.62)

Symbols chapter 4 Collisional Effects in the Extreme Nonlinear Response

γ	–	damping coefficient, eq. (4.1)
$\sigma_{el}, \sigma_{inel}$	–	elastic and inelastic cross section, eqs. (4.6), (4.7)
a_L, s_L	–	Lotz parameter, eq. (4.7)
γ_{el}, γ_e	–	elastic collision rate per conduction electron, eq. (4.5)
γ_{inel}, γ_i	–	inelastic collision rate per cond. el. with neutral molecules, eq. (4.5)
f	–	electron phase space distribution, eq. (4.8)
\mathbf{v}	–	velocity, eq. (4.8)
\mathbf{F}	–	force, eq. (4.8)

Symbols chapter 5 Reconstruction of the Strong-Field-Driven Plasma Dynamics

σ_{eff}	–	effective conductivity, eq. (5.2)
I_{pu}	–	slowly evolving intensity envelope, eq. (5.3)
$I_{\text{exp}}(\omega, \tau_j)$	–	experimental two-color delay spectrum, eq. (5.4)
\mathcal{F}	–	(fast) Fourier transform, eq. (5.4)

$S(t, \tau)$	–	time domain source function, eq. (5.6)
R_S	–	residuum of source function, eq. (5.7)
R_ρ	–	residuum of plasma density, eq. (5.17)

Symbols chapter 6 FDTD Ionization-Radiation Model

\mathbf{D}	–	displacement field, eq. (6.3)
\mathbf{H}	–	magnetic field strength, eq. (6.4)
\mathbf{P}	–	polarization (density), eq. (6.3)
\mathbf{M}	–	magnetization (density), eq. (6.4)
Δt	–	time step, eq. (6.5)
Δz	–	spatial grid spacing, eq. (6.5)
$\mathbf{v}_d, \langle \mathbf{v} \rangle$	–	average drift velocity, eq. (6.13)
a, b	–	parameters of roots in Crank-Nicolson update, eq. (6.9), (6.10)
T	–	temperature, eq. (6.15)
E_{kin}	–	kinetic energy, eq. (6.21)
E_{therm}	–	thermal energy, eq. (6.22)
ω_k, γ_k, f_k	–	resonance frequency, damping coefficient, oscillators strength of k^{th} oscillator in Lorentz model, eq. (6.39)
ω_R, γ_R	–	Raman resonance frequency, Raman damping coefficient for rovibrational response in nonlinear Lorentz model, eq. (6.43)
C	–	Courant number, eq. (6.53)
d_{Au}	–	thickness of reflective gold coating
$\langle t \rangle_\Gamma$	–	first temporal moment with respect to tunneling rate, eq. (6.54)
L	–	loss in transmission, eq. (6.55) eq. (6.55)

Symbols chapter 7 Harmonics from Nonlinear Reflection

$f_{\text{PNL}}^{\text{ref}}$	–	reflection coefficient relative to nonlinear polarization, eq. (7.1)
$a_{\text{Inj}}, a_{\text{Br}}$	–	spectral width, eq. (7.4)
ℓ	–	number of cascaded nonlinear interactions, table 7.1
$\Phi_{\text{mech,h}}^{\text{scen}}$	–	harmonic phase factor, tabel 7.2
n_{crit}	–	critical plasma density, sect. 7.2
ψ	–	single electron wave-function, eq. (7.6)
V_0	–	finite-periodic lattice potential, eq. (7.6)
V_{las}	–	laser potential, eq. (7.6)
$E_n(k)$	–	eigenenergies, band structure, Fig. 7.5
E_C	–	lowest energy of conduction band wrt. the vacuum level, Fig. 7.5
E_V	–	highest energy of valence band wrt. the vacuum level, Fig. 7.5
N	–	number of considered unit-cells, Fig. 7.5
a	–	size of unit-cell, Fig. 7.5
k	–	crystal momentum, eq. (7.7)
v_n	–	group velocity of the electron wave packet in the n^{th} energy band, eq. (7.7)

- J_{el} – particle flux of electrons Fig. 7.6
 $\phi_{n\kappa}$ – windowed wave functions, eq. (7.8)

Subscripts

- \square_{ex} – existing elements in derivative of ensemble average, eq. (2.6)
 \square_{new} – new elements in derivative of ensemble average, eq. (2.6)
 \square_{pu} – pump beam, eq. (2.1)
 \square_{pr} – probe beam, eq. (2.1)
 \square_h – contribution to the h^{th} harmonic, eq. (3.5)
 \square_n – two-color wave mixing order, eqs. (2.1), (3.16)
 \square_{inj} – injection, eq. (2.14)
 \square_{Br} – Brunel, eq. (3.32)
 \square_{self} – self phase modulation (SPM), table 3.1
 \square_{cross} – cross phase modulation (XPM), table 3.1
 \square_{eff} – effective, eq. (5.2)
 \square_{exp} – experimentally determined, eq. (5.4)
 \square_{corr} – correction, eq. (5.14)
 \square_{rec} – reconstructed, eq. (5.17)
 $\square_{sim}, \square_{0,sim}$ – simulated, simulated in single color reference scenario, eq. (5.17)
 \square_{sub} – sub cycle, eq. (5.19)
 \square_{ca} – cycle averaged, eq. (5.19)
 $\square_{free}, \square_f$ – free, corresponding to free or conduction band electrons, eq. (2.5)
 \square_d – drift, eq. (6.14)
 \square_{dof} – per degree of freedom, eq. (6.23)
 \square_{kin} – kinetic, eq. (6.21)
 \square_{pot} – potential
 \square_{EM} – electromagnetic
 \square_a – electron partition, table 6.1
 \square_k – k^{th} oscillator in Lorentz model eq. (6.39)
 \square_R – Raman, eq. (6.43)
 $\langle \square \rangle_{foc}$ – focal averaged quantity,

Superscripts

- $\square^{(m)}$ – m^{th} order nonlinear response, eq. (2.2)
 $\hat{\square}$ – time domain amplitude, eq. (2.3)
 $\check{\square}$ – initially unknown true solution of reconstructed variable, eq. (5.7)
 $\tilde{\square}$ – including depletion, eq. (6.17)
 $\square_{||}$ – parallel polarization direction of pump and probe beam, eq. (2.4), (3.16)
 \square_{\perp} – perpendicular polarization direction of pump and probe beam, eq. (2.4), (3.17)
 \square° – circular pump and linear probe polarization, eq. (3.24)

\square^{cf}	–	constant field of circular pump beam wrt. linear scenario, sec. 3.3.5
\square^{ci}	–	constant intensity of circular pump beam wrt. linear scenario, sec. 3.3.5
\square^{med}	–	Medium super scripts, med={ vac (vacuum), mat (material) }
\square^{com}	–	center of mass, eq. (6.21)
\square^{ref}	–	reflected, eq. (7.1)
\square^{+}	–	positive frequency contribution, eq. (3.3)
\square^{-}	–	negative frequency contribution, eq. (3.3)
\square^{*}	–	complex conjugate, eq. (B.8)
$\square^t, [\dots]^t$	–	time index for finite-difference time-domain (FDTD) discretization, eq. (6.13)

Numerical discretization indices

$\lfloor \frac{t}{z} \rfloor$	–	discrete integer time index t , and discrete half-integer spatial index z , for E -field, eq. (6.5)
-------------------------------	---	---

Mathematical constants and notation

\mathbf{e}_x	–	unit vector in x -direction
e	–	Euler's number
i	–	imaginary unit
π	–	Pi
$\square!$	–	factorial
LHS,	–	left and right-hand side of equation
RHS	–	
<i>c.c.</i>	–	complex conjugate of RHS

1. Introduction

With the increasing availability of sources for strong and extremely short laser pulses, intense laser-matter interaction has become a topic of outstanding interest from both the applied and the fundamental perspective. For example, the opportunity to resolve the temporal evolution of light absorption in dielectrics down to sub-cycle time scales via attosecond metrology provides unprecedented insights into the ultrafast reversible and non-reversible nonlinear polarization dynamics and energy transfer processes that govern the response of electrons to electric field waveforms during an optical period [1,2]. Controlling or even switching currents on such time scales may open routes to overcome clock-rate limitations of today's electronic devices by orders of magnitude [3,4].

Today laser pulses with precisely controlled field waveform have become key tools for analyzing the field-driven nonlinear polarization response, which has been demonstrated even for near single-cycle optical pulses [5]. In any case and besides the contribution of bound electron dynamics to the nonlinear polarization, persistent electronic excitation up to the generation of a dense electron-hole plasma becomes increasingly important at high intensities. The waveform dependence of the latter is of key interest for applications such as controlled material modification through tailored laser fields because of the different dependence of the elementary processes like ionization and collisional heating on the laser temporal and spectral characteristics [6]. The idea of using sub-cycle effects to control the generation of free carriers, e.g. via the sub-cycle modulation of strong-field ionization and its dependence on the phase of the waveform, may open novel avenues for laser machining schemes.

Besides specific aspects such as the dependence of strong-field ionization on the atomic ionization potential in gases or the band gap in solid media, the strong sensitivity of the ionization rate on the instantaneous laser field provides a basis for waveform-controlled plasma formation. However, the exposure of solids to strong fields is associated with a broad spectrum of response effects [7], reaching from substantial ionization in the TW/cm^2 intensity regime to defect formation [8,9] and changes in the refractive index [10], used for fs-laser fabrication of waveguides [11–13] or even plasma ablation, relevant for drilling [6,14] and cutting applications [15]. Over decades, experiments have been conducted to clarify the underlying physical processes, ranging from heat diffusion on microsecond time scale to carrier relaxation on picosecond time scales [16,17]. One precursor of material damage [18] that indicates substantial energy deposition almost directly on the time scales of excitation is the optical breakdown, i.e. the abrupt change of optical properties of previously transparent dielectrics due to instantaneous strong field ionization followed by an impact ionization avalanche [19–23]. Signatures for this metallization process and opportunities for the sub-cycle control of the conductivity have been recently investigated on SiO_2 nanoparticles [24]. Although underlying excitation mechanisms are

established [14, 25], their relative contribution as function of time and the full spatio-temporal resolution of the electronic response from the first ionization event towards the formation of an electron-hole plasma at critical density remains challenging.

In the focus of this work is the question how ionization-driven nonlinearities affect the polarization response and how the associated emission of low and high harmonics of the light field can be utilized to characterize the excitation dynamics on attosecond time scales. Conceptually, the nonlinear character of laser-induced ionization can be described using two different pictures [26, 27]. In the picture of multi-photon ionization (MPI), several photons are absorbed simultaneously to excite a bound electron, leading to a strongly nonlinear intensity dependence with a power law scaling that reflects directly the order of the process. The MPI picture naturally predicts above-threshold ionization with the associated comb in the photoelectron energy distribution that reflects the absorption of integer multiples of the photon energy [28]. However, because of its origin in the spectral domain, the MPI picture only captures envelope effects and cannot explain the sub-cycle dependence of the photoionization process and the energy transfer from the field across a single cycle of the field waveform. The tunnel ionization picture, on the other hand, can be understood in the time domain and assumes the periodic suppression of the potential barrier for ionization due to the field. The tunneling picture can predict the sub-cycle modulation of ionization and captures the spectral features of the emission due to interference of various quantum pathways. The sub-cycle evolution arises from the evolving tunnel probability and automatically creates a strong field dependence. In particular at long wavelengths, where tunneling dominates¹, attosecond bursts of ionizing electrons are expected at the crest of every half-cycle. In this picture the formation of ATI peaks is understood by the intercycle interference of subsequently emitted electron wave packets, corresponding to a double-slit in time, that leads to maxima in the energy spectrum [29, 30].

Irrespective of the picture, the nonlinearity of strong-field ionization provides a central basis to harness and control the ultra-fast electron dynamics on sub-cycle time scales and became fundamental to the research fields today known as attosecond science [31] and extremely nonlinear optics [32, 33]. One of the resulting central processes in strong-field science is high-harmonic generation (HHG), which is well-known from atoms and molecules since decades and can impressively be described by the conceptually straightforward 3-step model of ionization, acceleration and stimulated recombination of electron wave-packets. In particular, the maximum energy of recolliding electrons could quantitatively explain the energy cut-off in the spectra of high harmonics and its scaling with field intensity [34, 35]. For the analysis of high harmonic emission from solids, which was intensely studied only since

¹Tunneling dominates over multi-photon ionization for small Keldysh parameters [26],

$$\gamma \ll \frac{\omega}{e} \sqrt{\frac{m_e c n_{\text{ior}} \varepsilon_0 E_g}{I_{\text{med}}}} \quad (1.1)$$

about a decade [36–38], it was, therefore, logical to search for similarities with the gas phase picture, e.g. regarding the cut-off scaling [39, 40]. Interestingly, different cut-off scaling behaviours as function of intensity were identified in solids, suggesting that additional processes are significant compared to atomic targets. On the other hand, also indications for similarities with the recollision picture were found in the analysis of the phase dependence of harmonics from condensed matter systems under two-color fields [41, 42]. Obviously, the physics in condensed matter systems is more subtle. In addition to interband excitation [43], which is to some extent similar to the gas phase case, also intraband motion in anharmonic conduction bands [39, 40] known as dynamical Bloch oscillations [44, 45] plays a major role and is absent in atoms. Ultimately electron-electron and electron-ion scattering in the bulk as well as plasma effects [46] are more complex than in atoms and are expected to lead to further nonlinear contributions of the electron response.

Several studies support, that the HHG cut-off from solids can even exceed the atomic limit due to strong interband couplings [47]. The possibility to generate or even control the resulting broader spectrum is highly relevant for the technological development of new broadband light sources [48] with potential for tabletop attosecond laser pulse generation [38]. Furthermore, a higher reproducibility of HHG waveforms was reported in solids [49]. Finally, because of the more convenient technological implementation of optoelectronics and nanoswitching devices using condensed matter and nanostructured media, ultrafast science of solids is a field that currently receives rapidly increasing attention [50, 51]. Since the first experimental observation of harmonics from bulk solids [39] some of the fundamental concepts known from gas phase HHG could be generalized to crystalline [41, 52] and amorphous [53] solids. However, the physics of HHG in solid shows several unique characteristics that differ from atoms and require a specific physical description. Today, a wide range of computational methods to calculate high harmonic spectra from solids exists [54, 55] based on the numerical solution of the time-dependent Schrödinger equation [44, 56] (TDSE), semiconductor Bloch equation (SBE) [57, 58], and time-dependent density functional theory (TDDFT) [59–61].

Whereas a multitude of experimental and theoretical works has studied the physics of *high* harmonic generation in solids, the origin and physics of *low* harmonic emission has so far found comparably little attention. One key concept that is linked directly to strong field ionization dates back to Brunel, who predicted that the sub-cycle modulation of the electron emission, with two steps per cycle, leads to a strong temporal modulation of the free electron population that is accelerated by the field. As a result of this modulation, low-order harmonics are predicted [62, 63]. First experimental signatures that support the existence of such type of harmonic emission were reported in the gas phase [64]. Later, also the step-wise plasma density build-up that underlies Brunel's idea was confirmed directly in an attosecond tunneling experiment in gases based on time-of-flight detection of generated ions [65], and attosecond streaking experiments on surfaces [66]. However, these methods are not directly applicable to bulk targets in order to verify the presence of a step-wise sub-

cycle ionization as required for Brunel harmonics. Instead, an all-optical method was put forward [67] in order to resolve the sub-cycle ionization via ellipticity changes of the ionizing pulse as a result of the nonlinear absorption. However, so far no ultimate verification of the presence of a step-wise sub-cycle ionization in solids has been achieved.

A first study that reports experimental evidence for the presence of ionization-induced low-order harmonic emission in dielectrics was published by the Baltuška group [68]. With their setup, the authors could track the time-evolution of the harmonic signal by sum frequency generation from two beams [69]. Their analysis relies on the idea that ionization is driven by a strong infrared pump pulse while the nonlinear response is probed with a much weaker time-delayed probe pulse. The resulting delay-dependent wave-mixing signal, which was attributed to the ionization response, was clearly detected for a linearly polarized pump beam, see Fig. 1.1 a, but was absent for a circularly polarized pump beam b. The authors interpret these observations as a verification of harmonic emission due to step-wise ionization in the linear case and explain the absence of emission with circular polarization with the missing sub-cycle modulation of the instantaneous laser field. As a result of the latter, no ionization steps were expected. A similar behavior was found for various wide bandgap materials such as soda lime silicate, CaF_2 , and MgF_2 . These results directly motivated the question whether the harmonic emission signal can be utilized to reconstruct the ionization dynamics.

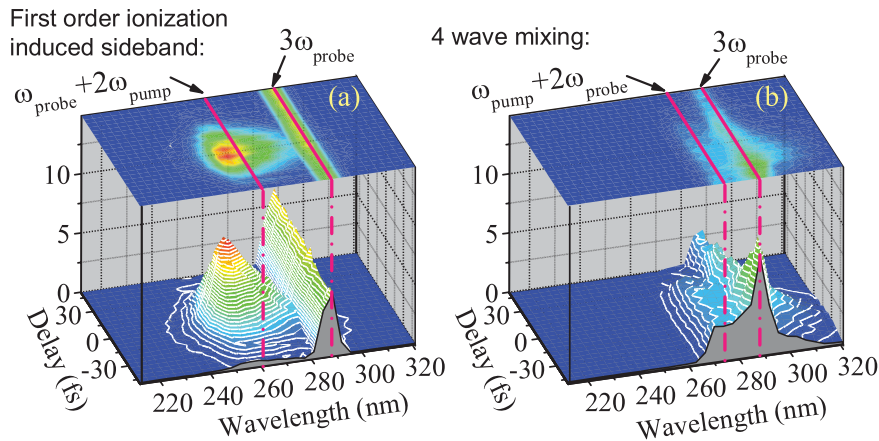


Figure 1.1.: Two color harmonic wave-mixing signals for linear (a) and circular (b) pump polarization, detected from a 0.5 mm thick fused silica plate. Figure adapted from [69].

The above-described signature, however, is only an indirect indication for harmonic emission due to step-wise sub-cycle ionization and needs careful analysis. For example, there may be other possible reasons for the vanishing signal in the circular polarization case such as the complete drop of the ionization yield when using a circularly polarized pulse that has the same pulse energy as the linearly polarized one. Due to the strong dependence of the ionization rate on the peak field strength this trivial field reduction would effectively stop ionization. If, as will be shown here,

the circularly polarized pulse is prepared with equal peak field strength, a careful analysis of the ionization-induced process would predict an increase of the harmonic yield, contradicting the logic of the original conclusion. In their paper, however, Mitrovanov et al. do not specify if they have kept the field strength or pulse energy constant in the comparison of the measurements with linear and circular pump pulse polarization. Without this knowledge a conclusive interpretation seems impossible, leaving the question for the physical picture unanswered.

The main goal of this work is to clarify the physical picture and to answer the question if and how the emitted radiation is related to ionization and if it can be used to characterize the ultrafast dynamics of ionization. It will be analyzed to which extent ionization steps can be verified, and how the effect of the emerging ionization avalanche modifies the ionization dynamics. The latter aspect is particularly important for the identification of optimal conditions for reliable reconstruction of the ionization dynamics using the emitted fields arising from wave mixing.

A key idea pursued in this thesis is the analysis of all stages of the ionization process regarding their impact on the harmonic emission. This explicitly includes the electron transfer from the bound to the excited (or free) state that one would associate with the tunneling process itself in strong field ionization in long wavelength fields. Interestingly, this step was neglected by Brunel but will be shown to even play the dominant role for specific conditions. In fact, the corresponding injection contribution to the polarization response was routinely considered in the context of ionization-induced absorption of gases [70] and solids [1, 71], but so far not considered as a possible source of harmonics.

For the analysis of relevant mechanisms of harmonic generation, the nonlinear contributions of injection, Brunel and Kerr effect are first compared by means of a local analytical model that accounts for the effect of the tunneling rate on the nonlinear medium polarization. Furthermore, secondary processes such as electron scattering from the bulk lattice, impact ionization as well as propagation effects are investigated, which require different numerical methods. The impact dynamics is calculated using a rate-based kinetic model that resolves the full velocity distribution of conduction electrons. For the following consideration of propagation effects, the self-consistent computation of electromagnetic fields with high spatial resolution becomes necessary. Background is that the degree of phase matching, that is related to the coherent superposition of fields emitted at different spatial points, affects the amplitude of harmonic signals. This spatial accumulation is particularly relevant to harmonics below the bandgap, which are much less absorbed by the medium than higher-order harmonics [72, 73]. Besides harmonics, the incident pulse is modified by propagation effects such as self-phase modulation or self-steepening [74]. Also the absorption-induced clipping of the driving pulse at a threshold intensity, known as the lawn-mower effect [67, 75] results in a substantial modification of the driving pulse. These effects can be in general accounted for by rate equations [23, 76] and coupled with nonlinear pulse propagation models [77]. Typical carrier-resolved models for nonlinear pulse propagation include the unidirectional pulse propagation

equation (UPPE) [78], the forward Maxwell equation (FME) [79], and first-order propagation equation (FOP) [70]. These approaches consider mainly the forward propagating pulse. In our scenario, close to the optical breakdown regime, however, the evolution of the local plasma density becomes very sensitive to slight changes in the driving field, consisting of forward but also of reflected field contributions. Due to the high nonlinearity of ionization, even a small increase in plasma reflectivity can have a large impact on the energy deposition in the remaining part of the pulse. In this work, we couple rate equations based on electron drift and temperature to the explicit calculation of the full electromagnetic field via the finite difference time domain (FDTD) method [80–82] and address where ionization takes place as function of time and which amount of pulse energy is deposited through various mechanisms. The outline of this work is structured into the following chapters.

In chapter 2 the relevance of ionization-driven generation of low-order harmonics is demonstrated on the basis of experimental findings where corresponding results were published in [JLK⁺20]. Subsequently, a detailed characterization of the nonlinear response is provided based on a local analysis that includes spectral amplitude ratios and the phase of harmonics emitted by different mechanisms in chapter 3. The effects of collisions and impact ionization on the phase and temporal structure of emitted fields are discussed in chapter 4. Here, the determination of impact-specific signatures is central to allow for the isolation of injection contributions. The latter are used in chapter 5 to reconstruct the sub-cycle modulated tunnel ionization rate by means of a ptychographic method, which was first tested on simulated data. The subsequent application to an experimentally measured harmonic is discussed, supplementing the main conclusions of our publication [JLK⁺22a]. Next, the self-consistent treatment of the nonlinear propagation via rate-coupled finite-difference-time-domain (FDTD) simulation is discussed in chapter 6. The main use case is the analysis of ionization dynamics in terms of transiently changing transmittance and reflectance, with particular emphasis on the observation of ionization hot spots at the backside of the medium. Due to the complex behavior observed in the transmission direction, the nonlinear reflection of harmonics is investigated in chapter 7, allowing for a much-simplified, direct connection between emitted fields and local nonlinearities at the medium interface. For this ideal scenario, we study the full quantum mechanical current using a numerical solution of the time-dependent Schrödinger equation and identify tunneling-induced LOHG in the observed quantum trajectories. Finally, the results of this thesis are merged and considered in their entirety, in chapter 8, to draw comprehensive conclusions concerning the research objectives outlined at the outset.

2. Identification of Tunneling-Induced Low-Order Harmonics

When a solid dielectric medium is irradiated by a sufficiently strong laser field, the linear response of the medium that determines the refractive index is accompanied by additional nonlinear contributions. With increasing intensity, several additional effects become relevant. First, bound electrons show a fully reversible, nonlinear Kerr-type response to the external field that results in a transient excited state population associated with the so-called virtual [83,84] conduction band population. At higher intensities, initially bound electrons are persistently excited to the conduction band and the electromagnetic response of the medium becomes more complex, as shown in Fig. 2.1. After ionization in the first step, this real electron population is accelerated in a nonparabolic conduction band leading to the emission of intraband harmonics [39,44,45] in step 2. Finally, in the third step, electrons emit excess energy upon recombination as interband harmonics [34,35]. In the following, we show that in addition to the intraband acceleration and to the interband recombination, both relevant for high harmonic orders, the sub-cycle dynamics of the electron excitation in step 1 leads to a particularly strong response at *low* harmonic orders. A corresponding

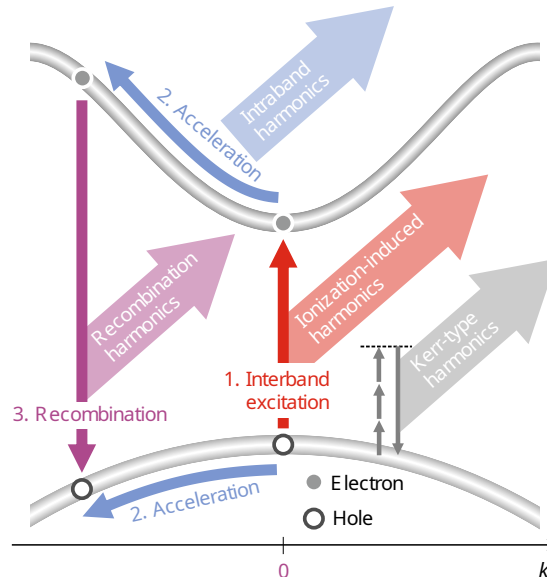


Figure 2.1.: Mechanisms of harmonic emission in solids. The three steps of interband excitation, acceleration of electrons and holes along the momentum axis, and recombination constitute each a distinct nonlinear response with characteristic harmonic emission denoted as ionization induced, intraband, and interband recombination harmonics. These highly nonlinear mechanisms compete with the low-order perturbative Kerr-type response. Figure adapted from [JLK⁺20].

concept was proposed by Brunel, who predicted even for a purely sinusoidal motion of continuum electrons in gas phase systems that the twice-per-cycle density modulation at the peak of the driving field leads to low-order harmonic emission [62]. He characterized the spectral fingerprint of this effect by a rapid fall-off with harmonic order that does not lead to a spectral plateau. Even though consistent signatures have been observed after the theoretical prediction also in experiments [64, 69, 85], the highly nonlinear current associated with ultra-short electron injection through the tunneling-barrier has not been considered so far. Therefore, the clarification of the relative contribution of injection current compared to Brunel-type and other nonlinearities, including the perturbative Kerr-type response, is of particular interest in the following sections.

The strategy of our research aims at providing evidence for a dominant injection current at intensities near the damage threshold. Besides a strong pump beam, we use an orders of magnitude weaker probe beam to gain time resolution via nonlinear wave-mixing. This allows us to simultaneously detect the temporal signature at multiple harmonic orders. Furthermore, we utilize the laser polarization degree of freedom as a second, even more powerful diagnostic tool to expose that the underlying mechanism for low-order harmonic emission is not the density modulation, but the charge displacement in the excitation step. As a target, we first study amorphous fused silica (SiO_2), an isotropic nonlinear medium that is commonly used in a wide variety of optical components. We exploit, that this wide bandgap material is transparent for multiple low-order harmonics of our mid-infrared driving laser field. The long wavelength ensures the tunneling picture to be prevalent over multiphoton ionization in the excitation step.

2.1. Experimental setup and beam parameters

An overview of the experiment is provided in Figure 2.2. The experiment was set up and conducted by P. Jürgens at the Max Born Institute Berlin in the collaborating group of Prof. Dr. M. J. J. Vrakking using the following parameters. The subsequent discussion is closely oriented on the corresponding publication [JLK⁺20] where figures are adapted from.

In this experiment low-order harmonics are generated in 500 μm thick amorphous SiO_2 (UV Grade fused silica, Corning 7980) by nonlinear wave mixing between a strong mid-infrared pump pulse ($\lambda_{\text{pu}} = 2100 \text{ nm}$, $\tau_{\text{pu}} = 140 \text{ fs}$ and $E_{p,\text{pu}} \leq 40 \mu\text{J}$) and a much weaker near-infrared (NIR) probe pulse ($\lambda_{\text{pr}} = 0.8 \mu\text{m}$, $\tau_{\text{pr}} = 45 \text{ fs}$ and max. $E_{p,\text{pr}} \leq 250 \text{ nJ}$). Further specifications of the Ti:Sapphire laser system and the optical parametric amplifier used for pulse generation as well as the spectrometers for visible and near-infrared range can be found in [JLK⁺20] and [86]. Note, however, the incommensurate wavelengths and pulse durations. These parameters were chosen to spectrally separate wave-mixing signals in the harmonic side bands. A significantly

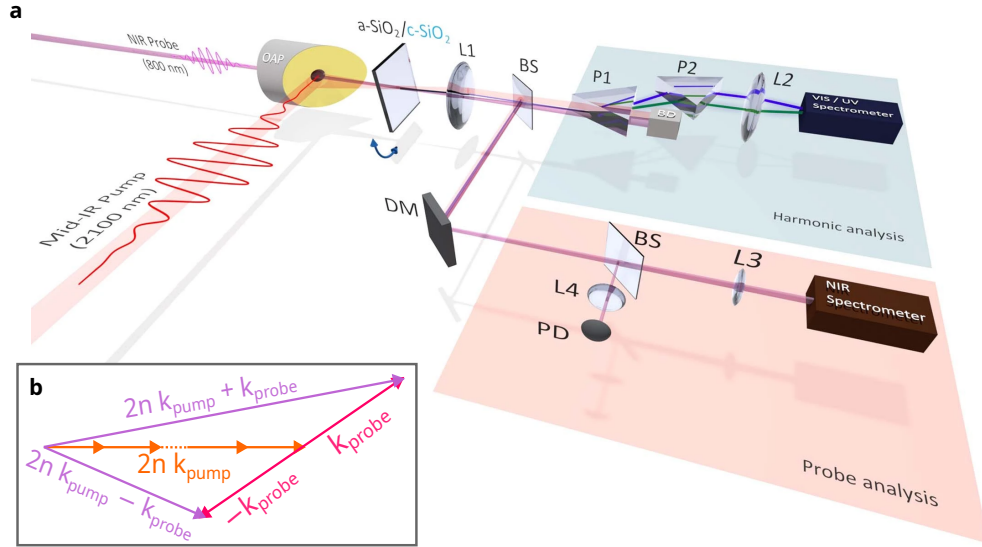


Figure 2.2.: **a** Two-color pump-probe setup: Linearly polarized pump and probe pulse, focused by off-axis parabolic (OAP) onto a-SiO₂ and c-SiO₂ samples. CaF₂ lenses (L1, L2) are used to collimate emitted harmonics, dispersed by CaF₂ prism (P1) and UV-grade fused silica prism (P2) onto an optical-to-ultra violet (VIS/UV) spectrometer. Beam splitters (BS) and dielectric mirrors (DM) are used for simultaneous analysis of the probe beam on a photodiode (PD) and near-infrared (NIR) spectrometer. Inset **b**, spatial separation of sum and difference frequency signals. Figure adapted from [JLK⁺20].

shorter probe pulse was used to improve the time resolution. Furthermore, close-to-collinear focusing allowed to spatially separate the delay-dependent wave-mixing from pump-only harmonics (see arrows panel **b**).

Focusing of the pump pulse was realized with a gold coated off-axis parabolic (OAP) reflector (see panel **a**) with a focal length of 50 mm to a spot with a radius of 33 μm (intensity dropped by $1/e^2$), corresponding to a Rayleigh length of $z_R = 1.6$ mm. The probe pulse was collimated over a focal length of 300 mm down to a waist radius of 75 μm , corresponding to a Rayleigh length of 22.4 mm. These parameters provide that the experiment was conducted under relatively weak focusing conditions. In the experiment, the target is positioned to optimize the detected signal.

Key parameter, that was varied besides the pump intensity, was the relative field polarization direction between the linearly polarized pulses. Also, the orientation of the two samples, i.e. the crystalline c-SiO₂ and the amorphous a-SiO₂, were varied with respect to the field polarization direction, as discussed in the following sections.

2.2. Experimental results

The main observation of this experiment are delay-dependent wave-mixing signals, located at the sum frequencies of multiple pump photons and a single probe photon,

$$\omega_n^{\text{mix}} = 2n \omega_{\text{pu}} + \omega_{\text{pr}}, \quad (2.1)$$

labeled by mixing order n . These wave-mixing harmonics are detected as function of delay and wavelength, see Fig. 2.3 a. The absence of even-number wave-mixing photons is attributed to the inversion symmetry of the sample. The lack of difference-frequencies and harmonics without probe photons is attributed to angular selection resulting from phase matching. Due to the finite angle $\alpha_{\text{pu-pr}} = 5^\circ$ between pump and probe beam, all wave-mixing harmonics are emitted in different directions. This is seen as follows.

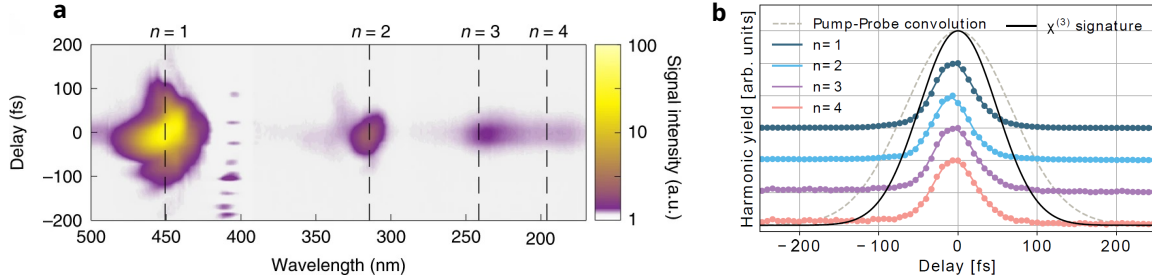


Figure 2.3.: **a** Delay-dependent harmonic spectrum showing the first four $n = 1..4$ wave mixing signals ω_n , at $12 \text{ TW}/\text{cm}^2$ pump intensity. **b** Vertical cuts of each signal along the delay axis (dashed lines in **a**) show a common delay width $\tau_{\text{delay}} = 63 \text{ fs}$. Colored curves are shifted for better visibility. Figure adapted from [JLK⁺20].

Under the weak focusing conditions discussed here, the emission direction of harmonics is given by the vector sum of pump and additional probe photon (Fig. 2.2 inset **b**). The sign of the wave vector agrees with the sign of the frequency contribution. The detected wave mixing frequencies indicate that $2n$ net positive pump photons need to be considered (orange arrows). All negative pump photons are compensated by remaining positive pump contributions. The much weaker probe beam (pink arrow), on the other hand, contributes only one photon, either with positive or negative frequency, that leads to emission directions on opposite sides of the optical axis defined by the pump pulse (violet arrows). Furthermore, it is found from the inset that the emission direction for $n = 1..4$ is much less affected for sum-frequency generation (violet arrow pointing upwards) as opposed to difference-frequency generation (arrow pointing downwards). In the present experiment only signals in the sum-frequency direction could be simultaneously collimated and analyzed on the detector stage. In the following, the delay and intensity dependence of these signals is used to identify the dominant generation mechanism.

To exclude an ordinary $\chi^{(3)}$ -Kerr-type wave-mixing mechanism, that would be consistent with the frequency of the strongest signal ($n = 1$), we inspect the temporal profiles, i.e. the vertical cuts (dashed lines in panel Fig. 2.3 a), in b (dark blue). It is found that the delay dependence is significantly shorter than what is expected for a $\chi^{(3)}$ response (solid black line in b). This is already one strong argument against the ordinary Kerr-type mechanism. Comparing also higher harmonic signals $n = 2, 3, 4$ on a normalized scale (blue, violet, and red), shows that all signals share the same delay dependence, indicating that all signals are generated by the same non-perturbative mechanism, of nonlinear order $m > 3$.

The recombination process can be excluded by examining the photon energy that corresponds to the wavelength of emitted harmonics. It is noticeable that the photon energy 2.75 eV of the strongest signal at 450 nm, is significantly smaller than the bandgap (7.7 eV). Therefore, electron-hole recombination is ruled out for the observed signal.

To examine the role of an intraband mechanism, on the other hand, the experiment was repeated in crystalline SiO₂, where the sample was rotated about the propagation axis of the pump beam, as indicated in Fig. 2.2 a by a blue arrow. Here a strong orientation dependence, that is expected for intraband harmonics, was observed at low intensities, see Fig. 2.4 a. However, close to the damage threshold, at 12 TW/cm² the signal is isotropic, c.f. panel b, which is consistent with an ionization-driven mechanism. The formation of an electron-hole plasma was confirmed by determining the maximal loss of transmission to about 6% of the probe beam through the focal volume, showing that the peak of the plasma build-up is well beyond 150 fs [87]. This indicates that the plasma is indeed plausible for harmonic generation. Finally, as the absorption coefficient due to real-population transfer remains significantly below unity, coherent wake emission, known from dense plasmas can be safely excluded, consistent with reports of undercritical plasma buildup in the below-threshold regime [8]. These indications hint at the plasma generation via strong field tunnel ionization being the source for the observed signal. To further substantiate this conclusion the nonlinear order of the observed process is examined next.

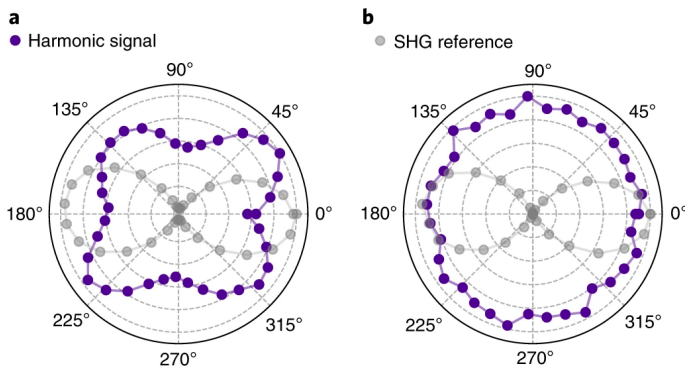


Figure 2.4.: Harmonic signal (blue) as function of crystal orientation, shows in a 4-fold symmetry at 4 TW/cm² and in b an isotropic response at 12 TW/cm². Simultaneously measured second harmonic generation (gray) is used as reference for the crystal orientation. Figure adapted from [JLK+20]

2.3. Metrology for the effective nonlinear order

To identify the generating mechanism, we present a new metrology for the effective nonlinear order based on the comparison of the wave mixing signal for two polarization configurations. Starting point is the assumption that the physical response can be approximated by a generic m^{th} order nonlinear, instantaneous, local polarization. For an isotropic medium the latter can be written as

$$\mathbf{P}_{\text{NL}} = \varepsilon_0 \chi^{(m)} |\mathbf{E} \cdot \mathbf{E}|^\mu \mathbf{E}, \quad \text{with} \quad \mu = \frac{m-1}{2}. \quad (2.2)$$

Here the nonlinear susceptibility is so far just a parameter. To determine the effective order of nonlinearity m we use the specific dependence of the signal yield on the relative polarization direction of the pump and probe fields,

$$\mathbf{E} = \frac{\hat{\mathbf{E}}_{\text{pu}}}{2} e^{i\omega_{\text{pu}} t} + \frac{\hat{\mathbf{E}}_{\text{pr}}}{2} e^{i\omega_{\text{pr}} t} + c.c. . \quad (2.3)$$

Inserting this total field into eq. (2.2) yields a sum of terms that reflect the resulting mixing signals. As an important additional prerequisite for a simple analysis, we utilize that the probe field has a significantly smaller amplitude $|\hat{\mathbf{E}}_{\text{pr}}| \ll |\hat{\mathbf{E}}_{\text{pu}}|$. In this case, we can neglect all terms containing the probe field beyond linear order, as they are so small. As a result, only mixing signals containing one probe field term remain (apart from the pump-only mixing terms that we are not interested in). Considering the resulting mixing signals, i.e. terms linear in probe field, it is easy to see that in the perpendicular scenario only terms proportional to $|\hat{\mathbf{E}}_{\text{pu}} \cdot \hat{\mathbf{E}}_{\text{pu}}|^\mu \hat{\mathbf{E}}_{\text{pr}}$ are non-vanishing. This effectively restricts the probe field to the last field factor of \mathbf{P}_{NL} , because all scalar products with perpendicular pump and probe photon are zero. This restriction is lifted for the parallel polarization configuration. In the parallel case, the probe field can enter in any of the m field factors, effectively increasing the polarization amplitude such that the corresponding intensity ratio between observed mixing signals, is directly related to the nonlinear order,

$$m = \sqrt{\frac{I_{\parallel}}{I_{\perp}}}. \quad (2.4)$$

It turns out that this quite brief consideration is key for the identification of the experimental signal. A more formal derivation is provided in chapter 3 to discuss also circular polarization configurations, examine scaling with harmonic order, and discuss how the delay dependence of the observed signals can be related to the nonlinear order m .

Here, the effective nonlinear order is measured, according to eq. (2.4), by repeating the experiment for both polarization scenarios in amorphous SiO_2 . A systematic scan of the effective nonlinear order as function of pump intensity is shown in Fig. 2.5. While violet data points show at low intensities a nonlinear order of $m = 3$, that can

be attributed to the $\chi^{(3)}$ response, a steep increase beyond values of 10 is seen close to the damage threshold. Error bars indicate statistical deviations, corresponding to maximum intensity fluctuations over 10 shots in each configuration, where the sample was constantly moved in the transverse direction to supply fresh media. Outliers beyond 15 TW/cm² are attributed to permanent damage of the target, verified by analysis with an optical microscope. The fact that the transition to high nonlinear orders $m > 10$ is seen close to the damage threshold is strong evidence for the ionization response for two reasons. First, damage of the material is a clear indicator that a high plasma density was formed within one laser shot. Second, for the present parameter set, about 13 pump photons are needed to overcome the bandgap, giving a rough estimation for the nonlinear order that is expected. This agrees quite well with the observation. To examine which mechanism is responsible for the ionization mechanism, a simple semi-classical ionization radiation model for the nonlinear source current is compared to the experimental observation, next.

2.4. Ionization-induced nonlinearity

For the source current \mathbf{J} we consider the non-relativistic strong-field limit and specify the dipole acceleration $\frac{\partial \mathbf{J}}{\partial t}$ by a commonly used [70], semi-classical electron transport model, that governs the effect of the step-wise increase of conduction band population, associated with Brunel emission [62], and tunneling-injection. Starting point to describe ionization-induced harmonics is the polarization due to free charges,

$$\mathbf{P}_{\text{free}}(t) = n_0 \rho q \langle \mathbf{x}(t, t_b) \rangle, \quad (2.5)$$

with molecular density n_0 , normalized ionization degree (conduction band occupation) ρ , electron charge $q = -e$, and the displacement \mathbf{x} where the dependence on birth time t_b is accounted for, by averaging over the ensemble of all electron trajectories. The first time derivative of this is the free current. Since differentiation of av-

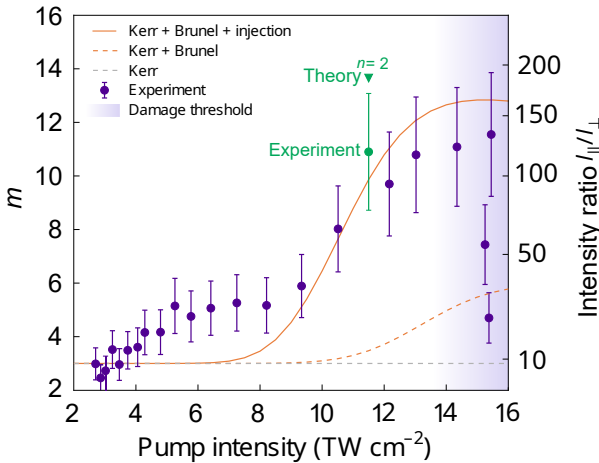


Figure 2.5.: Measured effective order of nonlinearity (left axis), extracted from intensity ratio parallel versus perpendicular (right axis) of the $n = 1$ wave mixing signal (violet). Prediction of ionization-radiation model including the Kerr type nonlinear refractive index, the Brunel and the injection mechanism shown by solid and dashed lines. Figure adapted from [JLK⁺20].

eraged quantities is an important step for the identification of physical mechanisms discussed in the following, it is briefly summarized.

2.4.1. Ensemble derivatives

For derivatives of mean values, the ordinary product rule accounts for the fact, that the number of N ensemble elements (conduction band electrons) can change,

$$\frac{d}{dt}(N\langle x \rangle) = N\left\langle \frac{\partial x}{\partial t} \right\rangle_{\text{ex.}} + \frac{\partial N}{\partial t} \langle x_0 \rangle_{\text{new}} \quad (2.6)$$

which follows directly from the difference quotient (Appendix A.1). In the first term on the right, the derivative of the displacement x of all elements that are already existing (ex.) is evaluated and then averaged. The second term corresponds to the average initial value x_0 of new elements, generated at the rate $\frac{\partial N}{\partial t}$. For higher derivatives, existing electrons do only contribute in terms where N is fixed,

$$\frac{d^2}{dt^2}(N\langle x \rangle) = N\left\langle \frac{\partial^2 x}{\partial t^2} \right\rangle_{\text{ex.}} + \frac{\partial N}{\partial t} \left\langle \frac{\partial x_0}{\partial t} \right\rangle_{\text{new}} + \frac{\partial N}{\partial t} \frac{\partial \langle x_0 \rangle_{\text{new}}}{\partial t} + \frac{\partial^2 N}{\partial t^2} \langle x_0 \rangle_{\text{new}}. \quad (2.7)$$

On the right, it is seen that derivatives of N are multiplied with initial conditions of new elements, indicated by a subscript zero. Here $\left\langle \frac{\partial x_0}{\partial t} \right\rangle_{\text{new}}$ denotes the average initial velocity. The change of the avg. initial location with time is denoted as $\frac{\partial \langle x_0 \rangle_{\text{new}}}{\partial t}$ in the third term.

2.4.2. Nonlinear current and dipole acceleration

In the scenario discussed in the eq. (2.5), it is assumed that all electrons at a fixed birth time, share the same initial conditions. Applying the ensemble derivative eq. (2.6) the current reads,

$$\mathbf{J}(t) = \frac{\partial \mathbf{P}_{\text{free}}}{\partial t} = qn_0 \left(\rho \langle \dot{\mathbf{x}}(t, t_b) \rangle + \dot{\rho} \mathbf{x}_0(t) \right) \quad (2.8)$$

where $\langle \dot{\mathbf{x}} \rangle$ is the average velocity of conducting charge, and \mathbf{x}_0 is the dipole length of charge that is separated at the time t . Further differentiation results in the dipole acceleration, that reads according to eq. (2.7)

$$\frac{\partial \mathbf{J}}{\partial t} = \frac{\partial^2 \mathbf{P}}{\partial t^2} = qn_0 \left[\rho \langle \ddot{\mathbf{x}} \rangle + \dot{\rho} \mathbf{v}_0 + \frac{\partial}{\partial t} (\dot{\rho} \mathbf{x}_0) \right], \quad (2.9)$$

where the last term takes explicitly the time dependence of the tunnel exit $\mathbf{x}_0 \equiv \mathbf{x}_0(t)$ into account. The initial velocity of carriers, born during $[t, t + dt]$, is denoted by \mathbf{v}_0 . The average acceleration of free charge $\langle \ddot{\mathbf{x}} \rangle$ is driven by the external field and colli-

sions,

$$\langle \ddot{\mathbf{x}} \rangle = \frac{q\mathbf{E}}{m_e} - \langle \dot{\mathbf{x}}(t, t_b) n_0 \sigma_{\text{trans}} \rangle \quad (2.10)$$

where σ_{trans} is the transport cross section, damping the ballistic current. To determine an upper limit for the acceleration-driven Brunel response, we now switch off the effect of damping which will be discussed separately in chapter 4. With this simplification, the dipole acceleration is found as,

$$\frac{\partial \mathbf{J}}{\partial t} = qn_0 \left[\frac{q}{m_e} \mathbf{E} \rho + \mathbf{v}_0 \dot{\rho} + \frac{\partial}{\partial t} (\mathbf{x}_0 \dot{\rho}_{\text{tun}}) \right]. \quad (2.11)$$

2.4.3. Physical picture of relevant nonlinear mechanisms

To provide a physical picture of nonlinear effects, relevant in our scenario, we depart from perturbative harmonic generation that stems from the polarization of bound states as seen in Fig. 2.6 panel **a** that is observed for all media. Here the negatively charged electron cloud in gray (orbital for gases, Wannier wavefunction in solids), is displaced with respect to the parent ion nonlinearly by a strong driving field. In solids, this quasi instantaneous Kerr polarization [74] is associated with virtual conduction band population [1, 84] that is tightly linked to the presence of the driving field.

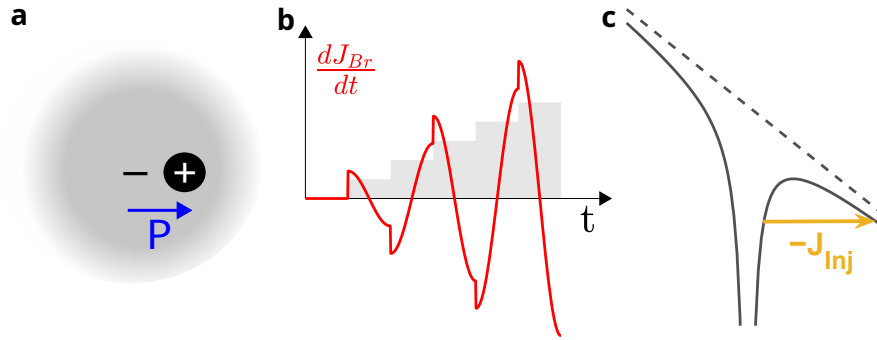


Figure 2.6.: Mechanisms of harmonic generation included in the semi-classical ionization radiation model: **a** Polarization (blue) of bound states, electron distribution (gray) shifted wrt. parent ion in; **b** dipole acceleration (red) sharply modulated by a step-wise increase of free carrier density (gray) leading to the emission of Brunel harmonics; **c** injection current (yellow) generated by charge displacement in quasi-static tunneling.

A corresponding picture for ionization-induced components is obtained from the interpretation eq. (2.11). The first term leads to harmonic generation through the charge acceleration of modulated conduction band population. This emission of so-called Brunel harmonics is understood as follows. Since the ionization rate is strongly

field dependent, ρ increases in a step-like manner every half-cycle of the laser field, shown as gray area in panel **b**. As a result, the dipole acceleration (red) shows an abrupt increase in magnitude at the crest of the field, leading to high-frequency contributions.

The next term in eq. (2.11), accounts for multiphoton excess energy that is transferred to the initial velocity v_0 . In the scenario considered here, this velocity is negligible due to the low photon energy. Note that the first two terms have already been considered in the seminal work by Brunel in the context of harmonic generation in gases [62] and were studied by means of particle-in-cell (PIC) simulations for laser-induced plasmas by Bauer et al. [63].

There is, however, a third term, which was not considered in the context of harmonic emission so far. It is due to the current created by charge displacement in field-driven tunneling. In panel **c** it is seen that the electron is moved a finite distance from the bound state to the tunneling exit, located at x_0 . While this picture applies directly to atoms, the injection dynamics in solids is in general more complicated [88]. Nevertheless, current contributions equal to this injection current, i.e. parallel to the driving field are necessary to realize energy transfer from the field to the electron.

2.4.4. Role of the injection current for energy conservation

The important role of the injection current for energy conservation can be understood by the following consideration. Assuming electrons to carry no kinetic energy after tunneling, the absorbed power density required to promote electrons at tunneling rate $\dot{\rho}_{\text{tun}}$ across the gap energy E_g , must be balanced by a decrease of energy density $\dot{u}_{\text{EM}} < 0$ of the electromagnetic field

$$\int d^3x [n_0 \dot{\rho}_{\text{tun}}(\mathbf{x}) E_g + \dot{u}_{\text{EM}}(\mathbf{x})] = 0 \quad (2.12)$$

where the volume integral contains the electron wave packet. According to Maxwell's equations, absorption must be realized by a current

$$-\dot{u}_{\text{EM}} = \mathbf{J}_{\text{inj}} \cdot \mathbf{E}. \quad (2.13)$$

This notion is commonly used in plasma simulations where the current is determined from intensity-dependent multi-photon ionization rate eq. [89]. Here, we consider the long wavelength limit where field-induced tunneling is relevant. The corresponding injection current \mathbf{J}_{inj} is understood as a charge transfer from the atom towards the classical tunneling exit,

$$\mathbf{J}_{\text{inj}} = n_0 \dot{\rho}_{\text{tun}} q \mathbf{x}_0. \quad (2.14)$$

According to Fig. 2.6 a direct relation between the charge displacement and the bandgap

$$\mathbf{x}_0 = \frac{E_g}{q} \frac{\mathbf{E}}{|E^2|}, \quad (2.15)$$

can be established for an instantaneous, field-driven excitation process. From this short, semi-classical analysis it becomes clear that the charge transport due to the decreasing wave function on the inner side and simultaneously increasing wavefunction on the outer side of the tunneling barrier is key to fulfill the energy balance in tunneling-induced electron excitation. Even though considered here for one atom, it is clear that energy balance must also be fulfilled in a solid, that can be pictured by the tilt of the real-space energy landscape in the focus region. Albeit the important role of the injection current for energy conservation and the fact that ultra-short bursts of the injection current are only emitted during a very short period at the crest of the field, it was previous to this study not reported as a mechanism for harmonic emission. In the following, the numerical evaluation of the full ionization current is used to show that the injection current leads eventually to the strongest contribution and is responsible for the swift increase in effective nonlinearity.

2.4.5. Numerical analysis of injection and Brunel harmonic contributions

The nonlinear current eq. (2.11) is solved numerically for the experimental pulse parameters, using the Asommov–Delone–Krainov (ADK) tunneling rate [90]. As in the experiment, the intensity ratio of the wave-mixing harmonic is examined. To identify the relevant contribution, different terms of the nonlinear current are switched on, see Fig. 2.5.

Good agreement with the experimental data was only found when the injection contribution was included (compare solid orange line with violet dots). Considering just the Kerr plus the Brunel contribution, by setting the injection contribution to zero in the simulation (orange dashed line), shows a significantly smaller increase in the effective nonlinearity, and the lift-off from the purely perturbative third-order Kerr response (dashed gray) shifts to higher intensities.

It was verified that this simulation result does not change qualitatively with the bandgap parameter. In Fig. 2.7 panel a, it is seen that increasing the gap energy just shifts the lift-off to higher intensities. For the same set of gap energies, it is found that the emitted relative radiative power of the injection contribution (solid lines in panel b), is stronger than the Brunel response by at least one order of magnitude (dashed lines, same color) for all inspected intensities. Further, the lift-off in nonlinearity corresponds to the intensity where injection and Kerr response (gray dashed) become equally strong, seen by the comparison of both panels.

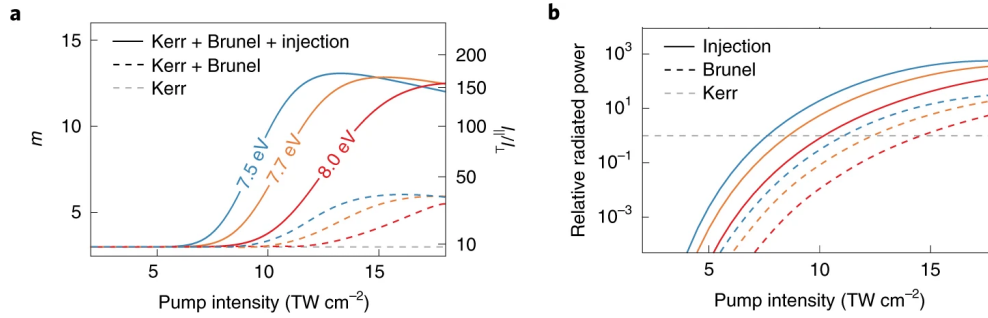


Figure 2.7.: Bandgap dependent lift-off of the effective nonlinearity **a**. Radiative power of Injection and Brunel harmonic, relative to Kerr harmonic **b**. Colors encode the bandgap parameter in both panels.

From the agreement between simulation and experiment it is found that the injection mechanism is the dominant contribution to low-order harmonics at high intensities. This result exemplifies that tunneling-induced ionization results in a highly nonlinear medium response. To understand the high value of nonlinear order beyond $m > 10$ and the relative strength between injection and Brunel mechanism we inspect the role of the tunnel ionization rate in the next chapter.

2.5. Conclusion

In conclusion, the presented metrology, based on repeated low-order harmonic wave-mixing measurements where only the polarization direction of the weak probe beam needs to be changed, turned out to be a very robust tool to determine the effective order of the nonlinear response. The robustness of this technique is due to the pump intensity that can be kept fixed for each data point such that active focal volume and the condition of the emerging plasma dynamics remains comparable. Here harmonic generation from a process of high nonlinearity was observed showing the strongest response at low harmonic orders. Whereas experimental results allowed to exclude anharmonic intraband driving and interband recombination, the emergence of the detected response close to the damage threshold was interpreted as an indicator of an ionization-driven process. By comparison with a simple numerical, ionization radiation model the detected lift-off signature of the effective nonlinearity was attributed to the tunneling injection current. This strong-field tunneling injection signal was found well below the threshold for permanent modification and therefore allows for the detection of plasma formation prior to severe material damage. The dominance of the injection contribution will be further examined by a formal scaling analysis of the local nonlinear response and in particular of ionization-induced nonlinearities in the following chapter. Furthermore, this will allow to connect the measured order of nonlinearity with the observed time dependence of harmonics.

3. Local Strong-Field Medium Response

In the previous chapter, the effective nonlinearity extracted from the polarization dependence of the two-color wave mixing was used to characterize the dominant mechanism that emits harmonics in our experimental scenario. In the following, we discuss the effective order of nonlinearity from a general point of view, allowing for a detailed analysis of the spectral response. A key concept is the degeneracy of wave-mixing contributions. It explains the relative strength of harmonics and motivates why the highly-nonlinear ionization-driven response generates particularly strong fields at low harmonic orders. To understand corresponding spectral weights at the detector, the coupling between the nonlinear current and the electric far field is addressed. Here, we focus on the simplest case of thin media, which allows us to predict distinct intensity scalings with harmonic frequency and driving field for Brunel and injection harmonics. Further, mechanism-specific properties such as time dependence and the relative phase with respect to the driving field are identified, providing means to separate signal contributions. Their discussion is motivated on the one hand by several recent reports where low-order harmonics have been attributed to the Brunel mechanism [85,91–93], also known for example from terahertz generation via zeroth order harmonic [94–96] and by the injection mechanism on the other hand, that has been observed in further recent works, e.g. in EUV high-order wave mixing [97] with potential applications for coherent XUV light sources [98]. Therefore, we present multiple complementary signatures that allow to disentangle the contributions of the nonlinear mechanisms to the harmonic response for a broad range of laser and material parameters.

Starting point of this chapter is the nonlinear wave equation of the transverse electric field,

$$\nabla \times (\nabla \times \mathbf{E}) + \frac{1}{c^2} \frac{\partial^2 \mathbf{E}}{\partial t^2} = -\frac{1}{\varepsilon_0 c^2} \left[\frac{\partial^2 \mathbf{P}_L}{\partial t^2} + \frac{\partial^2 \mathbf{P}_{NL}}{\partial t^2} \right] \quad (3.1)$$

that governs the response of a medium to an incident light field. The source terms on the right, consisting of the linear and nonlinear polarization \mathbf{P}_L and \mathbf{P}_{NL} , respectively, include possible current contributions of excited carriers via $\mathbf{J} = \frac{\partial \mathbf{P}}{\partial t}$. All polarization terms are dependent on the local driving field. For simplicity, the medium permeability is assumed to be given by $\mu_r \mu_0 = \frac{1}{\varepsilon_0 c^2}$ i.e. the vacuum speed of light c and the permittivity ε_0 . Now, we continue to use the general form for the nonlinear polarization, introduced in sect. 2.3, to develop a simple yet sufficient local model, that allows for a detailed interpretation of the experimentally observed signatures.

3.1. Nonlinear polarization

For the simplest case of isotropic media, an instantaneous nonlinear response can be expressed as a power series with respect to the electric field, in terms of the m^{th} order susceptibility $\chi^{(m)}$ and summation index $\mu = \frac{m-1}{2}$,

$$\mathbf{P}_{\text{NL}} = \varepsilon_0 \sum_{\mu} \chi^{(m)} |\mathbf{E} \cdot \mathbf{E}|^{\mu} \mathbf{E}. \quad (3.2)$$

Based on this ansatz we derive spectral weights for harmonic generation in the single and multi-color case.

3.1.1. Single-color polarization and degeneracy weights

Using a plane wave ansatz,

$$\mathbf{E} = \underbrace{\frac{\hat{\mathbf{E}}}{2} e^{i(\omega_0 t - k_0 z + \phi_0)}}_{\mathbf{E}^+} + \underbrace{\frac{\hat{\mathbf{E}}}{2} e^{-i(\omega_0 t - k_0 z + \phi_0)}}_{\mathbf{E}^-} \quad (3.3)$$

for the local field ($z = \phi_0 = 0$) and picking one term of the sum (3.2), with fixed order m yields

$$\mathbf{P}_{\text{NL}}^{(m)}(t) = \frac{\hat{\mathbf{P}}_{\text{NL}}^{(m)}}{2} \left(e^{i\omega_0 t} + e^{-i\omega_0 t} \right)^m \quad \text{with} \quad \hat{\mathbf{P}}_{\text{NL}}^{(m)} = 2\varepsilon_0 \mathbf{e}_x \chi^{(m)} \frac{\hat{E}^m}{2^m}. \quad (3.4)$$

The multiplication of bracketed field terms can be carried out explicitly and results in a spectral decomposition of the polarization

$$\mathbf{P}_{\text{NL}}^{(m)}(t) = \frac{\hat{\mathbf{P}}_{\text{NL}}^{(m)}}{2} \sum_{h=1,3,5\dots}^m D_h^{(m)} e^{ih\omega_0 t} + c.c. \quad , \quad D_h^{(m)} = \binom{m}{\frac{m+h}{2}} = \frac{m!}{\frac{m+h}{2}! \frac{m-h}{2}!}. \quad (3.5)$$

Here the nonlinear polarization amplitude¹ $\hat{\mathbf{P}}_{\text{NL}}^{(m)}$ shows the same dependence on the m^{th} power of the field amplitude, \hat{E}^m , for all harmonic orders h . The single color degeneracy factor $D_h^{(m)}$ governs the relative amplitude between different harmonics h and is here given by a binomial coefficient. Visualizing degeneracy coefficients by Pascal's triangle in Fig. 3.1, where positive frequency contributions at odd harmonic orders are shown in blue, it is seen that for the $m = 3$ polarization, the response at the fundamental, $h = 1$, is 3-fold degenerate and thus 3 times larger than the third harmonic. This is because there are three possible permutations to combine two positive with one negative photon, as indicated by the box-arrow notation (inset lower left). For the third harmonic $h = 3$ the degeneracy is reduced to one, as all photons

¹Time domain amplitudes are indicated by a hat over respective symbols throughout this thesis.

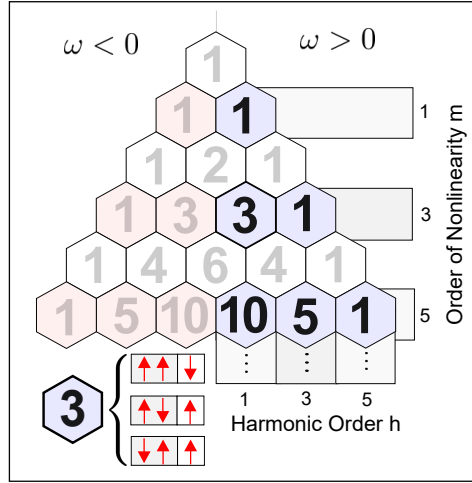


Figure 3.1.: Degeneracy of low-order wave mixing follows the structure of Pascal's triangle. The number of odd-order permutations leading to positive harmonic frequency are shown in blue. For the third harmonic response at the fundamental frequency ($m=3$, $h=1$) all three possible combinations of positive (red arrow up) and negative (red arrow down) photons are shown in the inset.

must contribute to the positive frequency. This trend of decreasing degeneracy is confirmed also for higher nonlinear orders, such as $m = 5$ (see lower blue tiles).

3.2. Emission of harmonics from nonlinear source terms

The previous section provided that the relative strength between different harmonic contributions of the polarization is understood by degeneracy ratios. To explain the relative strength between emitted harmonics, it is further necessary to link the local response to the detected far field, by solving the inhomogeneous wave equation, given in eq. (3.1). Goal of this section is to understand that in the simplest case where phase matching is negligible, emitted harmonics are proportional to the nonlinear current, i.e. the first derivative of the nonlinear polarization $\frac{\partial P_{\text{NL}}}{\partial t}$. This relationship is important firstly for the relative phase between local current and detected field and secondly for the characteristic spectral amplitude fall-off with frequency. The latter will be considered later when using the injection response for the reconstruction of the ionization dynamics.

3.2.1. Solution of the nonlinear wave equation for a thin film

For now, we consider the simplest scenario of a nonlinear medium with thickness $d_z \ll \lambda$ much less than the wavelength of the incoming plane wave. This reduces the problem to one dimension. Solving the wave equation with the spatial delta function

ansatz for the source terms shows that emitted fields are proportional to the negative current,

$$\mathbf{E}_h(z, t) = -\frac{dz}{2n_L} \sqrt{\frac{\mu_0}{\varepsilon_0}} \mathbf{J}_h(t_r) , \quad (3.6)$$

at the retarded time $t_r = t - \frac{|z|}{c}$, with linear refractive index n_L , as explicitly calculated in appendix B.1, also see e.g. [63]. Eq. (3.6) is particularly important, as it connects the amplitude and phase of each harmonic h of the field, to the corresponding harmonic contributions of the local current. This result is idealized [99], as the infinite size of the thin film removes any dependence on the propagation distance z such that the near and far field behavior become the same. We come back to this point when examining the effect of the focusing geometry, after discussing the implications for the observable spectral weights.

3.2.2. Spectral weights of harmonic far-field response

We determine the frequency dependence of the spectrum based on the two, previously discussed building blocks, namely the polarization response eq. (3.4) with degeneracy eq. (3.5) that we insert into the relation of the harmonic field (3.6). Using the proportionality of the detected intensity to the squared harmonic field, yields,

$$I_{\text{out}}^{(m)}(h\omega_0) \sim \chi^{(m)2} \underbrace{I_0^m \omega_0^2}_{\alpha^{(m)}(I_0, \omega_0)} \underbrace{\frac{1}{2^m} \binom{m}{\frac{m+h}{2}}^2}_{\beta^{(m)}(h)} h^2, \quad (3.7)$$

which shows two important properties. First, for a given nonlinear order m all emitted harmonics scale with the same intensity dependence I_0^m and grow quadratically with the driver frequency ω_0^2 , summarized in scaling factor $\alpha^{(m)}$. Second, the relative strength between different harmonic orders is given by the spectral weight β that comprises the degeneracy weights of the local response via binomial coefficients and the h^2 factor from the scaling with dipole velocity. The spectral weight is shown in Figure 3.2, as function of harmonic order. Even for high nonlinear orders m , low harmonics dominate the output signal. In particular, for nonlinear polarization terms with nonlinearity orders up to $m = 13$, the third harmonic remains the dominant signal. This means that for sufficiently large nonlinear susceptibilities and fields, low-order mixing signals are eventually dominated by the high-order nonlinear polarization terms. This conclusion is essential for this work and motivates that low-order mixing signals enable the characterization of the high-order nonlinear response of the medium subject to strong fields.

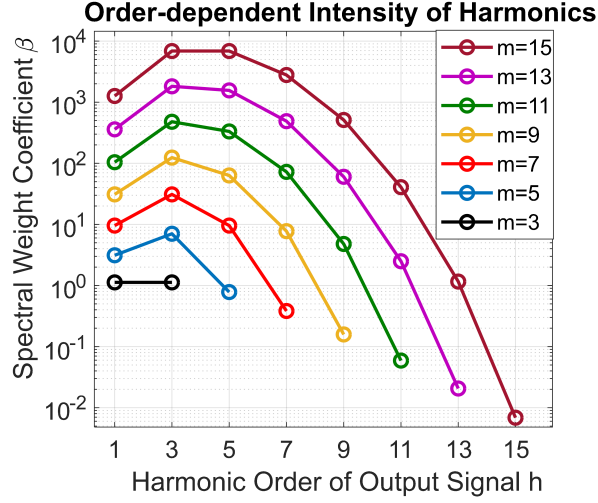


Figure 3.2.: Spectral weight coefficients β of harmonic intensity yield, eq. (3.7), for negligible phase mismatch (thin film or flat dispersion limit).

3.2.3. Role of transverse beam profile for spectral amplitudes

In the following, we show that this one-dimensional result for the spectral weight structure (Fig. 3.2) can be directly transferred to the paraxial scenario, present in the experiment. At first glance, the proportionality of the harmonic field to the local dipole velocity seems surprising, when examining the acceleration character of source terms in eq. (3.1), or comparing to the far field behavior of Hertzian dipole emitters (Appendix B.2), and has led to many opposing positions in the literature. Several authors use the dipole acceleration [100–103] due to finite size [104, 105] while also the dipole velocity [106] or the charge displacement of the dipole [34, 107, 108] is used to predict harmonic spectra. To resolve this issue, Baggesen and Madsen argue that in the one-dimensional scenario (previously discussed), the build-up of waves is proportional to the dipole velocity [109, 110]. In a comment on this paper [111], Perez-Hernandez and Plaja argue that the one-dimensional scenario is not valid, and the three-dimensional case, leading to the dipole acceleration, must be considered instead, a notion that is also adapted in other works [93]. In the following section, it is discussed that both arguments are relevant and that beam and detection geometry have to be considered.

In the relevant three-dimensional case, not the entire film is irradiated, but an incident Gaussian beam profile is assumed. The profile of the incident beam is indicated in Fig. 3.3 by red lines. The nonlinear polarization of order $m > 1$ shows a smaller transverse Gaussian amplitude profile (see gray color gradient). The emitted harmonic field is predicted by the thin film result, eq. (3.6), but only on length scales where the polarization gradient is negligible, that means on the surfaces of the film (shown in gray). This local harmonic field profile $\hat{\mathbf{E}}_h^{\text{film}}(r)$ at $z = 0$ (indicated in blue) is sufficient to see, that all harmonics are Gaussian beams and share the same reduced

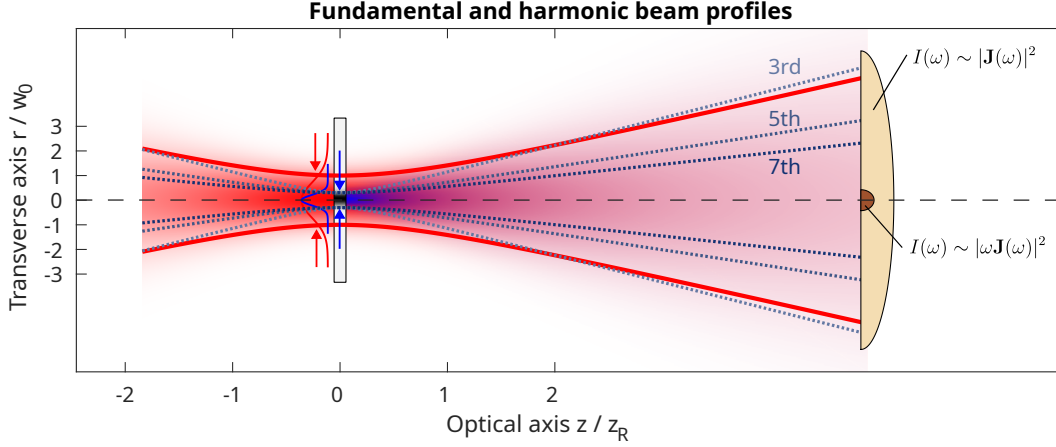


Figure 3.3.: Incident Gaussian beam (red) with waist w_0 (red arrows) drives high order non-linear polarization in a thin film (gray color gradient), defining the waist of several emitted harmonic orders (blue arrows and vertical profile) with distinct beam divergence (blue to violet dotted lines). The entire beam profiles captured by a detector (orange) in the far field corresponds to emission proportional to dipole velocity. Spectra consistent with dipole acceleration (see main text) are only observed on axis (smaller brown detector).

waist $w_0^{(m)} = \frac{w_0}{\sqrt{m}}$ (blue to violet emission cones²). From the frequency dependence of the Rayleigh length, however,

$$z_R = \frac{\pi w_0^2}{\lambda} = \frac{w_0^2}{2c} \omega, \quad (3.8)$$

it is found that the beam width in the far field $z \gg \lambda$,

$$w(z) = w_0 \sqrt{1 + \left(\frac{z}{z_R}\right)^2}, \quad (3.9)$$

becomes inversely proportional to the harmonic frequency $w_{\text{far}} \sim \frac{\sqrt{m}}{\omega_h}$. This finding that different harmonics show distinct divergence leads to two conclusions.

Emitted fields on axis show spectral fall-off as the dipole acceleration. First, on axis ($r = 0$) that is in the center of the detector (brown half-circle), the spectrum in this Gaussian beam scenario is indeed modified compared to the plane wave discussed before. Evaluating the analytic Gaussian beam yields that the on-axis far-field grows with harmonic frequency ω_h ,

$$\hat{\mathbf{E}}_{\text{far}} = \hat{\mathbf{E}}_h^{\text{film}} \frac{w_0^2}{2cz} \omega_h \sim \frac{1}{z} \frac{\partial \hat{\mathbf{J}}_h}{\partial t}, \quad (3.10)$$

²For a sub wavelength thick film emission in both directions is expected. For clarity, here only forward emission is shown, which dominates for finite targets due to phase matching. Reflected contributions are discussed in chapter 7.

for full calculation see Appendix eq. (B.11)–(B.17). Qualitatively, this can be viewed as an effect of the increasing collimation of harmonics (see dotted lines). Formally, the linear frequency enhancement of high spectral components has the same structure as a temporal derivative. Together with the thin film result, eq. (3.6), the origin of the on-axis spectrum can be linked to the amplitude (indicated by hats in eq. (3.10)) of the dipole acceleration, similar to the far-field result of the Hertzian dipole (Appendix B.2).

Spectral fall-off of integrated beam profile is consistent with dipole velocity. The second more important conclusion is that the beam divergence effect considered above needs to be compared to the size of the detector. As sketched in Fig. 3.3 harmonics (dotted) show less divergence than the driver (red solid line), as long as $\frac{\sqrt{m}}{h} < 1$. This condition is only for the third harmonic not fulfilled when assuming a representative ionization-induced nonlinearity of order $m = 11$ (as earlier found in Fig 2.5). In the present experiment, a collimation lens ($L2$ in Fig. 2.2) ensures that the entire beam is captured by the detector. For a corresponding calculation of the intensity spectrum, it is, therefore, necessary to integrate the squared far-field profile of the harmonic Gaussian beams,

$$\hat{\mathbf{E}}_{\text{far}}(r) = \hat{\mathbf{E}}_h^{\text{film}}(r=0) \frac{w_0}{w(z, \omega_h)} \cdot e^{-\left(\frac{r}{w(z, \omega_h)}\right)^2}, \quad (3.11)$$

over the entire transverse plane. In this step, all dependencies on the harmonic frequency cancel (c.f. Appendix (B.18)–(B.23)), showing that the detected yield is simply proportional to the squared nonlinear current,

$$I_{\text{out}}^{(m)}(h\omega_0) \sim \int_{-\infty}^{\infty} 2\pi r dr |\hat{\mathbf{E}}_{\text{far}}(r)|^2 = \pi w_0^2 \frac{|\hat{\mathbf{E}}_h|^2}{2} \sim |\hat{\mathbf{J}}_h|^2 = |\omega \hat{\mathbf{P}}_{\text{NL}}^{(m)}|^2. \quad (3.12)$$

From this section, we conclude that the spectral weight structure, measured on axis is slightly modified through increasing collimation of high harmonics. When the full beam profile is captured, however, the paraxial scenario establishes for spectral amplitude a one-to-one correspondence between harmonic field and negative dipole-velocity. In the next section, the analysis of the local response is generalized to multiple colors, that allows to mitigate two essential difficulties, firstly, that an intensity scan is less straight-forward as the active focal volume changes and secondly that there is very limited access to intra-pulse or sub-cycle dynamics.

3.3. Two-color wave-mixing

In the two-color scenario, further opportunities to characterize the source of harmonic generation emerge, as beam polarization and time delay become available for the ex-

traction of additional information. One important feature in the two-color scenario is that wave-mixing channels at new frequencies appear and that previously existing contributions are affected through additional permutations of positive and negative pump and probe frequency contributions, which have been observed for example in ultrahigh-order wave-mixing experiments [112]. Here we use a general plane wave description, that governs the well-known special case of polarization-dependent cross-phase modulation (XPM), that readily allows to develop a polarization-based metrology for the effective order of nonlinearity.

3.3.1. Parallel polarization scenario

We depart from the (parallel polarized) two-color plane wave scenario, where the superposition of four phase terms,

$$\mathbf{E} = \frac{\hat{\mathbf{E}}_{\text{pu}}}{2} \left(e^{i\omega_{\text{pu}}t} + e^{-i\omega_{\text{pu}}t} \right) + \frac{\hat{\mathbf{E}}_{\text{pr}}}{2} \left(e^{i\omega_{\text{pr}}t} + e^{-i\omega_{\text{pr}}t} \right), \quad (3.13)$$

yields the m^{th} order contribution to the nonlinear polarization

$$\mathbf{P}_{\text{NL}}^{(m)}(t) = \sum_{h_{\text{pu}}, h_{\text{pr}}} \frac{\hat{\mathbf{P}}_{h_{\text{pu}}, h_{\text{pr}}}^{(m)}}{2} D_{h_{\text{pu}}, h_{\text{pr}}}^{(m)} e^{i(h_{\text{pu}}\omega_{\text{pu}} + h_{\text{pr}}\omega_{\text{pr}})t} + c.c. \quad (3.14)$$

Now the degeneracy factor is described by the multinomial coefficient,

$$D_{h_{\text{pu}}, h_{\text{pr}}}^{(m)} = \binom{m}{N_{\text{pu}}^+, N_{\text{pu}}^-, N_{\text{pr}}^+, N_{\text{pr}}^-} = \frac{m!}{N_{\text{pu}}^+! N_{\text{pu}}^-! N_{\text{pr}}^+! N_{\text{pr}}^-!}, \quad (3.15)$$

where the N describe the number of superimposed pos. and neg. photon terms, $e^{\pm i\omega_{\text{pu/pr}}t}$. Since the harmonic order on the left-hand side, is given by the difference of positive and negative contributions $h = N^+ - N^-$, it is clear that in general multiple channels can form one particular frequency. To avoid unnecessary complication, examples for low amplitude probe beams are discussed in the following where frequencies of interest, $\omega_n^{\text{mix}} = 2n\omega_{\text{pu}} + \omega_{\text{pr}}$, contain only one probe photon. This simplifies the degeneracy in the parallel case to

$$D_n^{\parallel} = \binom{m}{\mu + n, \mu - n, 1} \quad \text{with} \quad \mu = \frac{m-1}{2}. \quad (3.16)$$

The simplest possible application of this formal result is cross-phase modulation, that is discussed as an example to illustrate the physical relevance of eq. (3.16). We employ the same line of argumentation, as for the motivation of the eff. nonlinearity in chapter 2.

3.3.2. Degeneracy in self-phase and cross-phase modulation

It is well known that Kerr-induced cross-phase modulation for parallel polarization is stronger than self-phase modulation [74]. This fact can be directly understood from the analysis of the degeneracy factors in table 3.1. The number of permutations of the self-phase modulation term $2E_{\text{pu}}^+E_{\text{pu}}^-$ in the single color case (first column), increases for the parallel cross-phase modulation case, corresponding to $E_{\text{pu}}^+E_{\text{pu}}^-E_{\text{pr}}^+$ (center column). For weak probe fields, contributions with more probe photons, such as $2E_{\text{pr}}^+E_{\text{pr}}^-$, become irrelevant and are not included. Next, we compare parallel and perpendicular cross-phase modulation scenarios that are key to understand the earlier introduced link between effective nonlinearity and intensity ratios.

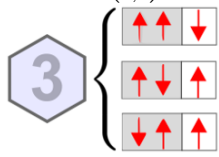
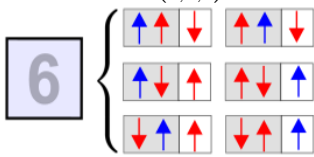
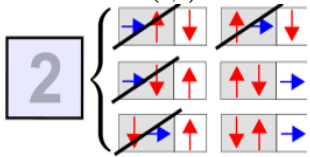
single color	two color	
	parallel pol.	perpendicular pol. \perp
$D_{\text{self}} = \binom{3}{2,1} = 3$ 	$D_{\text{cross}}^{\parallel} = \binom{3}{1,1,1} = 6$ 	$D_{\text{cross}}^{\perp} = \binom{2}{1,1} = 2$ 

Table 3.1.: Degeneracy of single color and two color scenario given by permutation number of positive (up) and negative frequency contributions (down) of pump (red) and probe photons (blue). Notation corresponds to the inset in Fig. 3.1 .

3.3.3. Intensity ratio: Parallel versus perpendicular scenario

The perpendicular polarization case (third column, table 3.1) shows different degeneracy due to the formal structure of the nonlinear coupling. For the considered inversion symmetric, isotropic medium, electric fields are multiplied by scalar products $\mathbf{P}_{\text{NL}}^{(m)} \sim |\mathbf{E} \cdot \mathbf{E}|^{\mu} \mathbf{E}$ (as discussed in eq. (3.2)), which is indicated by grayed boxes in the symbolic notation. Consequently, all scalar products with perpendicular polarization components must vanish, effectively restricting the probe photon to the last term and only the number of pump photon permutations (here two: up-down and down up, see red arrows in the third column) is relevant. This reduces the number of permutations by $\frac{1}{m}$ compared to the parallel case. Notably, this argument applies to all nonlinear mixing signals with one probe photon ω_n^{mix} ,

$$D_n^{\perp} = \binom{m-1}{\mu+n, \mu-n}. \quad (3.17)$$

Dividing eq. (3.16) by eq. (3.17) yields that the order of the mechanism equals the degeneracy ratio that is effectively accessible through the root of the intensity ratio,

$$m = \frac{D_n^{\parallel}}{D_n^{\perp}} = \sqrt{\frac{I^{\parallel}}{I^{\perp}}}. \quad (3.18)$$

A second important finding from the analysis of the parallel versus perpendicular scenario concerns the polarization direction of the harmonic.

3.3.4. Polarization direction of wave-mixing harmonics

In table 3.1, it is seen that the two-color wave-mixing signal is in the parallel and the perpendicular scenario polarized along the probe polarization direction (vectorial component shown in the white box). This theoretical prediction was confirmed in the experiment, for the perpendicular scenario, by inserting a polarizer into the beam (between the first lens (L1) and the beam splitter (BS), see Fig. 2.2). Scanning for different orientations the intensity of the harmonic signal, Fig. 3.4, it was verified that the probe (red) and $n = 1$ harmonic (violet) are both polarized in the same direction, while the pump (yellow) is perpendicular.

Mathematically, the results of the preceding sections can be summarized by writing nonlinear polarization contribution to the ω_n signal in both scenarios (parallel and perpendicular polarization) as,

$$\mathbf{P}_{\text{NL},n}^{(m),\parallel/\perp} = \varepsilon_0 \chi^{(m)} D_n^{\parallel/\perp} \left(\frac{\hat{E}_{\text{pu}}}{2} \right)^{m-1} \mathbf{E}_{\text{pr}}^+ e^{i2n\omega_{\text{pu}}} + c.c. \quad (3.19)$$

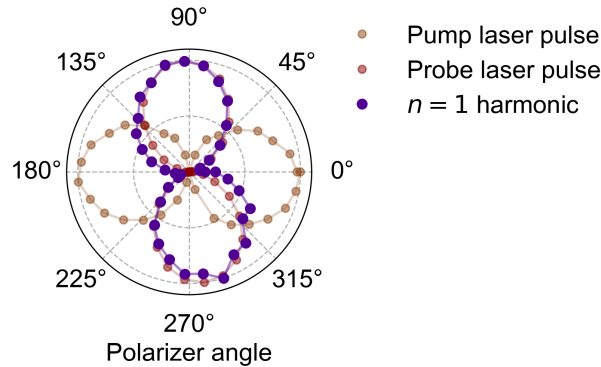


Figure 3.4.: Experimentally measured signal yield for the perpendicular scenario as function of polarizer angle. The polarization direction of harmonic wave-mixing signal is oriented along the probe polarization direction. Figure adapted from [JLK⁺22a].

For stronger probe beams the degeneracy analysis predicts for the perpendicular scenario, that the parity (even/odd number) of contained probe photons determines the polarization (parallel to pump/parallel to probe).

A similar behavior is seen when circular polarization for the pump is considered next. Switching from linear to circular pump polarization is in the literature proposed [69] as a cross-check to turn off ionization-induced harmonics. To critically review this notion, the next goal is to derive an expressions analogous to eq. (3.19) for circular pump polarization and to examine how the degeneracy and output polarization are affected.

3.3.5. Circularly polarized harmonics in two color case

Considering a circularly polarized pump field, with equal amplitude \hat{E}_{pu} as before,

$$\mathbf{E}_o(t) = \underbrace{\hat{E}_{\text{pu}}(\mathbf{e}_x + i\mathbf{e}_y) \frac{e^{i\omega_{\text{pu}}t}}{2}}_{\mathbf{E}_o^+} + \underbrace{\hat{E}_{\text{pu}}(\mathbf{e}_x - i\mathbf{e}_y) \frac{e^{-i\omega_{\text{pu}}t}}{2}}_{\mathbf{E}_o^-}, \quad (3.20)$$

it is found by simple algebraic calculation³ that no harmonics are generated under isotropic conditions in the single color case,

$$|\mathbf{E}_o \cdot \mathbf{E}_o|^\mu \mathbf{E}_o = \hat{E}_{\text{pu}}^{m-1} \mathbf{E}_o. \quad (3.22)$$

The RHS of eq. (3.22) only shows a circularly polarized nonlinear contribution generated at the fundamental frequency, while higher harmonics are absent. Interestingly, by adding a linearly polarized probe field, the $n = \pm 1$ mixing harmonic is revived. Mathematically, the circular pump photon is projected by the scalar product of the nonlinear interaction onto the linearly polarized probe, as seen in the second pair of brackets on the RHS of the harmonic polarization contribution,

$$\mathbf{P}_{\text{NL},n=1}^{(m),o,cf} = \varepsilon_0 \chi^{(m)} D_{n=1}^{\text{ol}} \left(\mathbf{E}_o^+ \mathbf{E}_o^- \right)^{\frac{m-3}{2}} \left(\mathbf{E}_o^+ \mathbf{E}_{\text{pr}}^+ \right) \mathbf{E}_o^+ + c.c. . \quad (3.23)$$

This distinct behavior also results in a structurally different degeneracy factor for a circularly polarized pump beam,

$$D_{n=1}^{\text{ol}} = (m-1) 2^{\frac{m-3}{2}}, \quad (3.24)$$

³Resubstituting the abbreviations defined in (3.20) and verifying that $\mathbf{E}_o^+ \mathbf{E}_o^+ = 0$, it is found that only the combination of forward and counter-rotating terms contribute in a scalar product,

$$|\mathbf{E}_o|^2 = \mathbf{E}_o^* \cdot \mathbf{E}_o = \mathbf{E}_o^- \mathbf{E}_o^+ + \mathbf{E}_o^+ \mathbf{E}_o^- + \mathbf{E}_o^+ \mathbf{E}_o^+ + \mathbf{E}_o^- \mathbf{E}_o^- = 2\mathbf{E}_o^- \mathbf{E}_o^+ = \hat{E}_{\text{pu}}^2. \quad (3.21)$$

which is derived in detail in Appendix B.4. In contrast to the linearly polarized cases, higher harmonics $n > 1$ are strongly suppressed, as each net pump photon that is not in the vectorial component must be paired up by a probe photon. For the next wave mixing signal, $n = 2$, already three probe photons are necessary,

$$\mathbf{P}_{NL,n=2}^{(m),\circ,cf} = \varepsilon_0 \chi^{(m)} D_{n=2}^{\circ} \left(\mathbf{E}_o^+ \mathbf{E}_o^- \right)^{\frac{m-7}{2}} \left(\mathbf{E}_o^+ \mathbf{E}_{pr}^+ \right)^2 \left(\mathbf{E}_o^- \mathbf{E}_{pr}^- \right) \mathbf{E}_o^+ + c.c. , \quad (3.25)$$

requiring already a nonlinear process of order $m \geq 7$. Due to the strong suppression, we restrict the following analysis to the first wave-mixing harmonic. The superscript 'cf' indicates that the amplitude of the pump field is kept constant, compared to the linear scenarios. The alternative case, common in experiments, that the intensity is kept constant, reduces the pump field by a factor of $1/\sqrt{2}$ and is denoted with superscript 'ci' in the following.

3.3.6. Intensity ratios between different polarization scenarios

Different intensity ratios are calculated from squared local polarization eq. (3.25) and eq. (3.19), where the perpendicular case is chosen as a reference. To determine the intensity of the circular cases, both polarization directions of emitted harmonics are taken into account,

$$\frac{I_{n=1}^{\parallel}}{I_{n=1}^{\perp}} = m^2 , \quad (3.26)$$

$$\frac{I_{n=1}^{\circ,cf}}{I_{n=1}^{\perp}} = 2^{2m-5} \left[\frac{\left(\frac{m-1}{2} + 1 \right)! \left(\frac{m-1}{2} - 1 \right)!}{(m-2)!} \right]^2 , \quad (3.27)$$

$$\frac{I_{n=1}^{\circ,ci}}{I_{n=1}^{\perp}} = 2^{m-4} \left[\frac{\left(\frac{m-1}{2} + 1 \right)! \left(\frac{m-1}{2} - 1 \right)!}{(m-2)!} \right]^2 . \quad (3.28)$$

These intensity ratios are shown in Fig. 3.5 as function of nonlinear order (solid lines) and agree very well with the reference data (dots), computed from numerically calculated spectra. This verifies the link between the theoretical degeneracy analysis and observable ratios.

In terms of the metrology developed here, it is found that the parallel versus perpendicular ratio provides the most direct access to the nonlinear order due to the simple m^2 scaling (dashed black line). Strikingly, it is seen that switching to circular polarization at constant field (cf), see red line, the nonlinear response at $n = 1$ is even *increased* for mechanisms beyond $m > 3$. Only when keeping the intensity constant (yellow line), a strong reduction of the harmonic at high nonlinearities is seen.

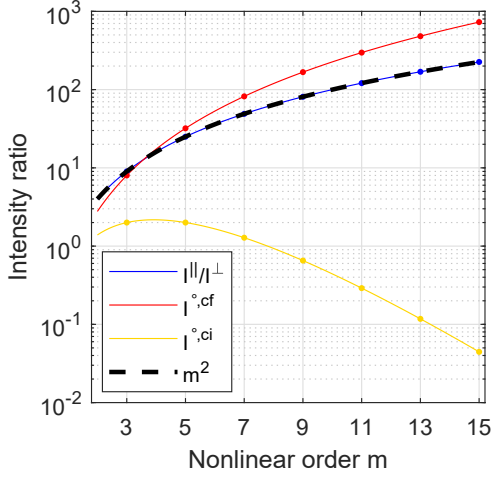


Figure 3.5.: Intensity ratio as function of nonlinear order. The intensity of the $\omega_{n=1}^{\text{mix}}$ harmonic is shown in the parallel (blue), and circular scenario at constant field (cf, red) and circular scenario at constant intensity (ci, yellow) relative to the intensity in perpendicular configuration.

3.4. Scaling analysis of injection and Brunel response

Next, we connect the previous formal analysis of intensity ratios with the ionization-induced nonlinearity (sect. 2.4). To obtain the characteristic scaling dependence of ionization-induced harmonics on the driving field, the no-depletion limit is considered, where the relative population of the conduction band $\rho < 1$ remains well below unity such that

$$\frac{\partial \rho}{\partial t} = (1 - \rho)\Gamma(|\mathbf{E}|), \quad (3.29)$$

with Γ being the atomic ionization rate, simplifies to,

$$\rho(t) = \int_{t_0}^t dt' \Gamma(|\mathbf{E}(t')|). \quad (3.30)$$

The lower integration limit t_0 is just an arbitrary initial time prior to the strong field interaction. Inserting this into the injection current eq. (2.14) and into the Brunel dipole acceleration, i.e. the first term of eq. (2.11) yields,

$$\frac{\partial \mathbf{J}_{\text{SFI}}}{\partial t} = n_0 E_g \frac{\partial}{\partial t} \left(\Gamma(|\mathbf{E}|) \frac{\mathbf{E}}{|E^2|} \right), \quad (3.31)$$

$$\frac{\partial \mathbf{J}_{\text{Br}}}{\partial t} = \frac{q^2 n_0}{m_0} \mathbf{E}(t) \int_{t_0}^t dt' \Gamma(|\mathbf{E}(t')|). \quad (3.32)$$

Both equations are used to analyze the amplitude scaling behavior of ionization harmonics⁴.

⁴Note that eq. (3.32) strictly applies only to harmonic frequencies. At the fundamental frequency, it is instrumental to further decompose the RHS into Brunel and free drift contributions that are distinct by their phase as discussed later in sect. 3.6.

3.4.1. Power-law ansatz for ionization rate

A recent measurement of the field dependence of optically driven carrier injection in SiO₂, published in [3], showed a power-law scaling dependence on the pulse amplitude [88]. To characterize the nonlinearity due to field-induced tunneling in our scenario, we consider the commonly used ADK rate [90], that is plotted in Fig. 3.6 (red line) for a bandgap of $E_g \equiv 7.7$ eV. Already for small variations of field strength, this rate changes by orders of magnitude. Hence, tunneling occurs predominantly at the crest of a laser cycle. Expanding the rate with a power-law ansatz,

$$\Gamma(|\mathbf{E}|) = \hat{\Gamma} \left(\frac{|\mathbf{E}|}{\hat{E}} \right)^s, \quad (3.33)$$

around the peak amplitude of the local electric field $\hat{E} \equiv \max(|\mathbf{E}|)$, with peak rate $\hat{\Gamma} \equiv \Gamma_{\text{ADK}}(\hat{E})$ and fixed tunneling exponent s , retains the characteristic scaling well, in the relevant time interval of one laser cycle. The tunneling exponent in eq. (3.33) characterizes the nonlinearity of the tunneling rate. It is well approximated by the slope of the rate in double logarithmic representation,

$$s \approx \left. \frac{\partial \ln \Gamma_{\text{ADK}}}{\partial (\ln E)} \right|_{E=\hat{E}} = \frac{\hat{E}}{\hat{\Gamma}} \left. \frac{\partial \Gamma_{\text{ADK}}}{\partial E} \right|_{E=\hat{E}}, \quad (3.34)$$

as indicated in the main panel by tangent lines at two representative points for expansion (for high-intensity pulse yellow and intermediate-intensity pulse gray).

The magnitude and field-dependence of the exponent s can be further rationalized by inspecting a simpler, one-dimensional reference model where instead of the tilted Coulomb potential (red hatched in inset **a**) a triangular barrier (green area) is assumed, with $V(x) = U_0 - eEx$ of height U_0 in the interval $0 < x < x_1 \equiv \frac{U_0 - \mathcal{E}_0}{eE}$ and with \mathcal{E}_0 being the energy of the penetrating electron wavepacket. According to lowest order WKB-expansion, the tunneling rate can be estimated from the amplitude ratio of the wavefunction on the outside and the inside of the barrier,

$$\Gamma_{\text{WKB}} \sim \frac{|\psi(x_1)|^2}{|\psi(0)|^2} = e^{\frac{2i}{\hbar} \int_0^{x_1} dx \sqrt{2m(\mathcal{E}_0 - V(x))}} \quad (3.35)$$

$$= e^{-\frac{4\sqrt{2m}}{3\hbar} \frac{(U_0 - \mathcal{E}_0)^{3/2}}{qE}}. \quad (3.36)$$

Substituting this expression for the tunneling rate in eq. (3.34) and identifying $U_0 - \mathcal{E}_0 = E_g$ with the bandgap, shows explicitly an inverse dependence of the tunneling exponent on driving amplitude,

$$s_{\text{WKB}}(\hat{E}, E_g) = \frac{4\sqrt{2m}}{3\hbar e} \frac{E_g^2}{\hat{E}^3}. \quad (3.37)$$

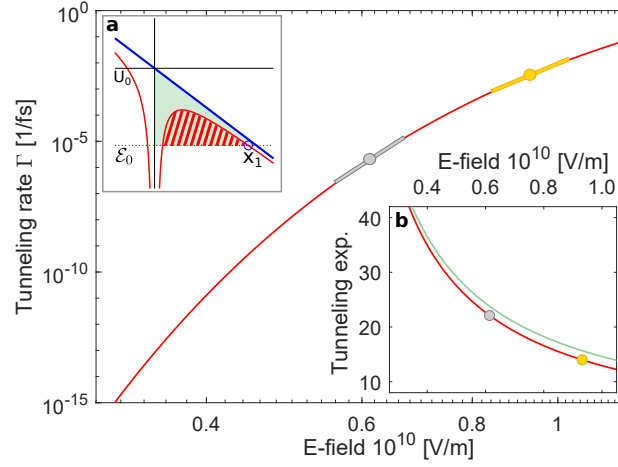


Figure 3.6.: ADK tunneling rate (red) with power-law expansion (tangents at circles) around representative field maxima of a 5 TW/cm² (gray) and a 12 TW/cm² pulse (yellow). Significant deviations from expansion are only seen when the tunneling rate is orders of magnitude below the peak rate. Inset **a** shows the barrier of the tilted Coulomb potential (red hatched), together with a simplified triangular model barrier (green area). In inset **b**, good agreement between ADK tunneling exponent s (red curve) and WKB exponent s_{WKB} (green curve) as function of peak field is found.

Comparing this result (green in inset **b**) with s from the ADK rate (red), good agreement is found, indicating that a decrease in the tunneling exponent, can be understood by the inverse scaling $s_{\text{WKB}} \sim \frac{1}{E}$ obtained in eq. (3.37). Furthermore, this equation provides the quantitative prediction for the nonlinear order of the tunneling process to be far beyond $s > 10$ for relevant field strengths. In the following, we use the tunneling exponent to characterize the ionization-induced nonlinearity of the different mechanisms.

3.4.2. Distinct nonlinear orders of Brunel and injection mechanism

We continue to examine the ionization-induced nonlinearities by inserting the power-law eq. (3.33) into the expression for Brunel and injection current eq. (3.31) and (3.32).

$$\frac{\partial \mathbf{J}_{\text{Br}}}{\partial t} = \frac{q^2 n_0}{m_e} \frac{\hat{\Gamma}}{\hat{E}^s} \left(\int_{t_0}^t dt' |\mathbf{E}(t') \cdot \mathbf{E}(t')|^{s/2} \right) \mathbf{E}(t). \quad (3.38)$$

$$\frac{\partial \mathbf{J}_{\text{inj}}}{\partial t} = n_0 E_g \frac{\hat{\Gamma}}{\hat{E}^s} \frac{\partial}{\partial t} \left(|\mathbf{E}(t) \cdot \mathbf{E}(t)|^{s/2-1} \mathbf{E}(t) \right), \quad (3.39)$$

Apart from differential and integral operators, both equations show on the RHS a structure that is similar to the m^{th} -order nonlinear polarization $\mathbf{P}_{\text{NL}}^{(m)} = \varepsilon_0 \chi^{(m)} |\mathbf{E} \cdot \mathbf{E}|^\mu \mathbf{E}$, discussed in the beginning of this chapter. The identification of the exponent of the modulus results in a distinct order of nonlinearity for each mechanism,

$$m_{\text{Br}} = s + 1, \quad (3.40)$$

$$m_{\text{inj}} = s - 1. \quad (3.41)$$

At first glance, this result, found with the power-law ansatz, is surprising as both mechanisms are generated by the same tunneling process.

3.4.3. Intensity ratios of Brunel and injection harmonics

A second feature that distinguishes the two mechanisms from each other is found by examining the intensity ratios. For this purpose, we explicitly state the $n = 1$ contributions for parallel, perpendicular, and circular polarization. Applying the combinatorial analysis as illustrated before in section 3.3, we find for injection,

$$\frac{\partial J_{\text{inj},n=1}^{\parallel}}{\partial t} = \frac{n_0 E_g \hat{\Gamma}}{\hat{E}^s} \frac{(s-1)!}{\left(\frac{s}{2}\right)! \left(\frac{s}{2}-2\right)!} (2\omega_{\text{pu}} + \omega_{\text{pr}}) i \frac{E_{\text{pu}}^{s-2} E_{\text{pr}}}{2^{s-2}} \frac{e^{i\omega_{n=1}^{\text{mix}} t}}{2} + c.c. \quad (3.42)$$

$$\frac{\partial J_{\text{inj},n=1}^{\perp}}{\partial t} = \frac{n_0 E_g \hat{\Gamma}}{\hat{E}^s} \frac{(s-2)!}{\left(\frac{s}{2}\right)! \left(\frac{s}{2}-2\right)!} (2\omega_{\text{pu}} + \omega_{\text{pr}}) i \frac{E_{\text{pu}}^{s-2} E_{\text{pr}}}{2^{s-2}} \frac{e^{i\omega_{n=1}^{\text{mix}} t}}{2} + c.c. \quad (3.43)$$

$$\frac{\partial J_{\text{inj},n=1}^{\circ}}{\partial t} = \frac{n_0 E_g \hat{\Gamma}}{\hat{E}^s} (s-2) 2^{s-4} (2\omega_{\text{pu}} + \omega_{\text{pr}}) i \frac{E_{\text{pu}}^{s-2} E_{\text{pr}}}{2^{s-2}} \frac{e^{i\omega_{n=1}^{\text{mix}} t}}{2} + c.c. \quad (3.44)$$

such that the intensity ratios read,

$$\frac{I_{\text{inj},n=1}^{\parallel}}{I_{\text{inj},n=1}^{\perp}} = (s-1)^2, \quad (3.45)$$

$$\frac{I_{\text{inj},n=1}^{\text{circ,cf}}}{I_{\text{inj},n=1}^{\perp}} = 2^{2s-7} \left[\frac{\left(\frac{s}{2}\right)! \left(\frac{s}{2}-2\right)!}{(s-3)!} \right]^2, \quad (3.46)$$

$$\frac{I_{\text{inj},n=1}^{\text{circ,ci}}}{I_{\text{inj},n=1}^{\perp}} = 2^{s-5} \left[\frac{\left(\frac{s}{2}\right)! \left(\frac{s}{2}-2\right)!}{(s-3)!} \right]^2. \quad (3.47)$$

Substituting in nonlinear order $m_{\text{inj}} = s - 1$ (c.f. eq. (3.41)), shows that injection harmonics follow the same intensity ratios as the m^{th} order nonlinear response, eq. (3.26)-(3.28). In particular, this means that the intensity ratio parallel versus perpendicular is related to the nonlinear order and that the signal grows for circular pump pulses at constant field, as discussed in sect. 3.3.6.

Notably, examining the Brunel mechanism in this way, we find different intensity ratios because the integral in expression for the Brunel current eq. (3.38) only acts on the scalar product, leading to frequency-dependent weights of the degeneracy factors D_{Br} ,

$$\frac{\partial J_{\text{Br}}}{\partial t} = \frac{q^2 n_0 \hat{\Gamma}}{m_e \hat{E}^s} \frac{D_{\text{Br}}}{i \omega_n^{\text{mix}}} \frac{E_{\text{pu}}^s E_{\text{pr}}}{2^s} \frac{e^{i \omega_n^{\text{mix}} t}}{2} + c.c., \quad (3.48)$$

with the following polarization dependence,

$$D_{\text{Br},n=1}^{\parallel} = \frac{\frac{\omega_{n=1}^{\text{mix}}}{2\omega_{\text{pu}}} s!}{\left(\frac{s}{2} + 1\right)! \left(\frac{s}{2} - 1\right)!} + \frac{\frac{\omega_{n=1}^{\text{mix}}}{3\omega_{\text{pu}} + \omega_{\text{pr}}} s!}{\left(\frac{s}{2} + 1\right)! \left(\frac{s}{2} - 2\right)!} + \frac{\frac{\omega_{n=1}^{\text{mix}}}{\omega_{\text{pu}} + \omega_{\text{pr}}} s!}{\left(\frac{s}{2}\right)! \left(\frac{s}{2} - 1\right)!}, \quad (3.49)$$

$$D_{\text{Br},n=1}^{\perp} = \frac{\frac{\omega_{n=1}^{\text{mix}}}{2\omega_{\text{pr}}} s!}{\left(\frac{s}{2} + 1\right)! \left(\frac{s}{2} - 1\right)!}, \quad (3.50)$$

$$D_{\text{Br},n=1}^{\circ} = (s 2^{s-2}) \frac{\omega_{n=1}^{\text{mix}}}{\omega_1 + \omega_2}. \quad (3.51)$$

The resulting intensity ratios also show this frequency dependence

$$\frac{I_{\text{Br},n=1}^{\parallel}}{I_{\text{Br},n=1}^{\perp}} = \left[1 + \frac{2\left(\frac{s}{2} - 1\right)}{3 + \frac{\omega_{\text{pr}}}{\omega_{\text{pu}}}} + \frac{2\left(\frac{s}{2} + 1\right)}{1 + \frac{\omega_{\text{pr}}}{\omega_{\text{pu}}}} \right]^2, \quad (3.52)$$

$$\frac{I_{\text{Br},n=1}^{\text{circ,cf}}}{I_{\text{Br},n=1}^{\perp}} = 2^{2s-3} \left[\frac{\left(\frac{s}{2} + 1\right)! \left(\frac{s}{2} - 1\right)!}{(s-1)!} \frac{2}{1 + \frac{\omega_{\text{pr}}}{\omega_{\text{pu}}}} \right]^2, \quad (3.53)$$

$$\frac{I_{\text{Br},n=1}^{\text{circ,ci}}}{I_{\text{Br},n=1}^{\perp}} = 2^{s-3} \left[\frac{\left(\frac{s}{2} + 1\right)! \left(\frac{s}{2} - 1\right)!}{(s-1)!} \frac{2}{1 + \frac{\omega_{\text{pr}}}{\omega_{\text{pu}}}} \right]^2, \quad (3.54)$$

which is a second distinct feature of the Brunel mechanism. This detailed analysis resulting in eq. (3.52) explains why the simulation without injection (orange dashed line in Fig 2.7 a) converges, for high intensities $I > 15 \text{ TW/cm}^2$, towards less than half of the effective nonlinear values compared to the simulation that includes injection. This simulation result was first unexpected, as it was shown in the previous section 3.4.2 that the Brunel mechanism shows a larger nonlinear order than injection. The formal finding that the relation between nonlinearity and intensity ratio is different for the Brunel mechanism is summarized in the following inequality,

$$m_{\text{Br}} > m_{\text{inj}} = \sqrt{\frac{I_{\text{inj},n=1}^{\parallel}}{I_{\text{inj},n=1}^{\perp}}} > \sqrt{\frac{I_{\text{Br},n=1}^{\parallel}}{I_{\text{Br},n=1}^{\perp}}}. \quad (3.55)$$

Although this deviating behavior seems to complicate the interpretation of measured intensity ratios, we show in the following that this issue is in fact mitigated by the dominant contribution of injection harmonics.

3.4.4. Dominant contribution of the ionization response

Comparing the intensity of injection and Brunel harmonics, it turns out that the injection mechanism is dominant for a wide range of laser and material parameters. In fact, the medium will be irreversibly damaged, for most solid materials, before the tunneling-induced Brunel response becomes dominant. To show this, we compute the intensity ratio between injection eq. (3.42) and Brunel harmonics eq. (3.48),

$$\frac{I_{\text{Inj}}}{I_{\text{Br}}} = \left[\frac{D_{\text{Inj}}}{D_{\text{Br}}} \frac{4 m_e \omega_n^{\text{mix}2} E_g}{q^2 E_1^2} \right]^2 = \left[\left(2n + \frac{\omega_{\text{pr}}}{\omega_{\text{pu}}} \right)^2 \frac{D_{\text{Inj}} E_g}{D_{\text{Br}} U_p} \right]^2, \quad (3.56)$$

where we identify in the central term the ratio between bandgap and the ponderomotive energy $U_p = \frac{q^2 E_1^2}{4m_e^2 \omega_{\text{pu}}^2}$ of a conduction band electron. For the parallel case, this intensity ratio, eq. (3.56), is shown in Fig. 3.7 a for a broad range of (vacuum) wavelength and intensities around the damage threshold of SiO₂. Here, the pump-probe frequency ratio $\frac{\omega_{\text{pr}}}{\omega_{\text{pu}}} = 2.6$ is fixed, ensuring that the harmonic signal of interest is not spectrally overlapped by other wave-mixing contributions. It is seen that the intensity of injection harmonics exceeds Brunel harmonics by more than one order of magnitude for a wide range of parameters (green area). Parameters present in our experiment are marked by a cross. Only in domains where the ponderomotive potential is sufficiently high, the Brunel mechanism shows a stronger contribution (red area).

In panel b, the intensity ratio is shown vs. bandgap and probe wavelength for fixed λ_{pu} , i.e. fixed ponderomotive potential, providing the relevance of the injection mechanism for a broad range of wide bandgap materials. We note that the degeneracy ratio $\frac{D_{\text{Inj}}}{D_{\text{Br}}}$ (RHS of eq. (3.56)) is fairly constant and plays a minor role in determining the dominant emission mechanism, as seen in panel c. Here variation in degener-

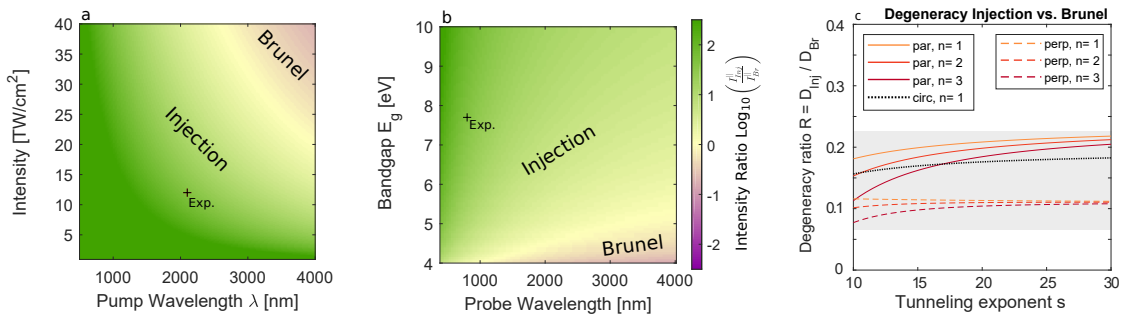


Figure 3.7.: **a** Intensity ratio of injection vs. Brunel response for parallel configuration and $E_g = 7.7\text{eV}$, $\frac{\omega_{\text{pr}}}{\omega_{\text{pu}}} = 2.6$. **b** The dependence of the intensity ratio is examined for fixed $\lambda_{\text{pump}} = 2100\text{ nm}$ and $I = 12\text{ TW/cm}^2$. The parameter set of the experiment is indicated. **c** Approximately constant degeneracy ratio, between injection and Brunel harmonics for the parameter range of interest.

acy ratio $\frac{D_{\text{Inj}}}{D_{\text{Br}}}$ with respect to polarization configuration (solid / dashed), wave-mixing order (orange to red), and tunneling exponent (horizontal axis) are found in a narrow band (gray), that is much smaller than the variation over multiple orders of magnitude in panel **a** and **b**. We conclude from this analysis that the intensity ratio between injection and Brunel harmonics is roughly described by the following proportionality,

$$\frac{I_{\text{Inj}}}{I_{\text{Br}}} \sim \left[\left(\frac{\omega_n^{\text{mix}}}{\omega_{\text{pu}}} \right)^2 \frac{E_g}{U_p} \right]^2. \quad (3.57)$$

The first term on the left shows, that the relative contribution of injection grows with mixing order n . This argument is further substantiated, by a generalization of the formal calculation eq. (3.45) - (3.51) in appendix B.5, showing that the intensity ratio grows, at least for low orders $n < \frac{s}{2}$. This result firstly justifies to neglect the Brunel contribution for low mixing orders in the non-destructive laser regime. Secondly, it provides that the similarity of the injection ratio $I_{\text{Inj}}^{\parallel}/I_{\text{Inj}}^{\perp} = (s-1)^2$ to the ratio of the perturbative response $I^{\parallel}/I^{\perp} = m^2$ also holds for any mixing order n . Hence, we propose to use the intensity ratio of low orders to classify the nonlinear mechanism. In the next section, the effect of high nonlinearities on the temporal structure of emitted harmonics is discussed.

3.5. Temporal signatures

Harmonics generated from a nonlinear interaction generally show a shorter pulse duration than the driving pulse that leads to broader spectral signatures. This holds as well for the two-color case, where in addition also the delay dependence of the signal is governed by the nonlinear order of the wave-mixing process. In this section, it is discussed how the nonlinear order is linked to both durations, and how these observables can be used to characterize the generating process.

Both properties, temporal pulse width $\tau_{\text{out}}^{(m)}$ and delay width $\tau_{\text{delay}}^{(m)}$ of the wave mixing signal, can be calculated analytically for Gaussian driving pulses, simply by multiplying respective field contributions. As before we discuss the results for the observed wave mixing signals ω_n^{mix} that contain one probe photon,

$$\tau_{\text{out}}^{(m)} = \frac{\frac{\tau_{\text{pu}}}{\sqrt{m-1}} \tau_{\text{pr}}}{\sqrt{\frac{\tau_{\text{pu}}^2}{m-1} + \tau_{\text{pr}}^2}} = \frac{\tau_{\text{pu}} \tau_{\text{pr}}}{\sqrt{(m-1)\tau_{\text{pr}}^2 + \tau_{\text{pu}}^2}}, \quad (3.58)$$

$$\tau_{\text{delay}}^{(m)} = \sqrt{\frac{\tau_{\text{pu}}^2}{m-1} + \tau_{\text{pr}}^2}, \quad (3.59)$$

while the general calculation is presented in appendix B.6. Here τ_{pu} and τ_{pr} are the pulse widths of pump and probe, respectively, defined by the full-width half-maximum (FWHM) of the intensity envelope on the temporal axis.

In Fig. 3.8 **a** the harmonic pulse duration, eq. (3.58), is plotted using the substitution $\tilde{\tau}_{\text{pu}} = \frac{\tau_{\text{pu}}}{\sqrt{m-1}}$. This representation indicates a low sensitivity to the nonlinear order for short probe pulses, that is seen as follows. For the probe pulse duration in our scenario of 45 fs (dashed line), the pulse width of harmonics $\tau_{\text{out}}^{(m)}$ (color coded) barely changes as a function $\tilde{\tau}_{\text{pu}}$. This impedes the extraction of $\tilde{\tau}_{\text{pu}}$ and the corresponding nonlinear order, that is shown for the pump pulse duration of 140 fs on the upper horizontal axis. A much improved sensitivity is seen for the delay dependence.

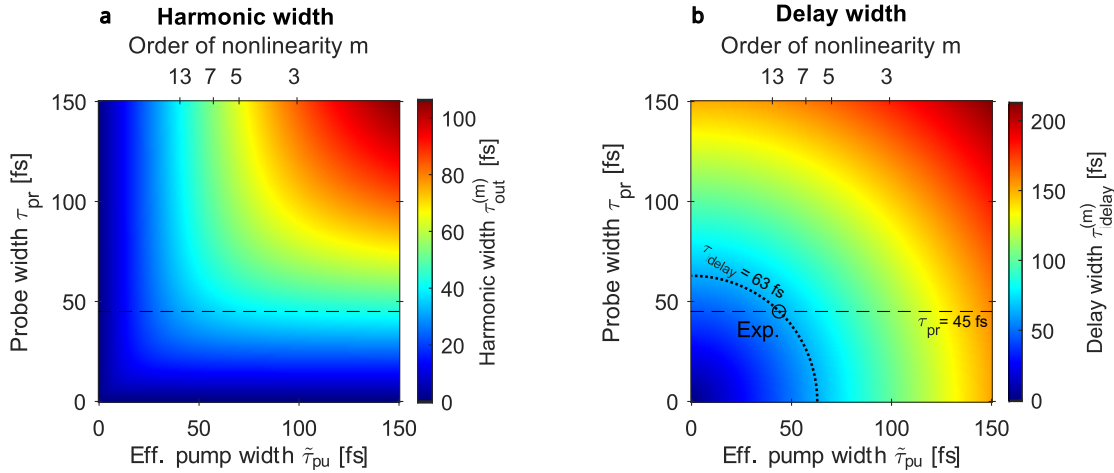


Figure 3.8.: Harmonic pulse duration $t_{\text{out}}^{(m)}$ in panel **a** and delay width $\tau_{\text{delay}}^{(m)}$ in panel **b** are shown as function of effective length of driving pulses (see main text) and order of nonlinearity m . The width of the probe pulse used in the experiment ($\tau_{\text{pr}} = 45$ fs) is marked by a dashed line. The delay width extracted from Fig. 2.3 **b** is shown by the dotted contour.

The delay width, shown in panel **b**, is more sensitive to the nonlinear order for short probe pulses, as seen by stronger variations in color along the dashed line. Using the experimentally delay width, earlier determined in Fig. 2.3 **b**, (here shown by dotted contour) the order of nonlinearity is read off (circled intersection). It is found that the detected harmonics are only consistent with a highly nonlinear process far beyond Kerr-type wave-mixing $m > 3$. This analysis underpins the interpretation of the experimental delay scan Fig. 2.3, which was found as one indicator that excludes the Kerr-type response and that suggests one common generation mechanism for all observed wave mixing harmonics $n = 1..4$ at high intensities.

In conclusion, the characterization of the dominant nonlinear mechanism based on the delay dependence can be understood to be complementary to the previously discussed characterization in terms of the effective nonlinearity. Corresponding intensity ratios I_{\parallel}/I_{\perp} allow for comparable easy quantitative characterization. However, the measured order is only an effective value, that accounts for one or more coexisting mechanisms that generate harmonics with different amplitudes. The delay width, on the other hand, allows to disentangle contributions from similarly contributing mechanisms, even at fixed intensity, if their nonlinear order is sufficiently distinct (for example Kerr-type and injection harmonics in the transition region of the

eff. nonlinearity, see Fig. 2.5 at $I \approx 10 \text{ TW/cm}^2$). We come back to this point when examining simulated delay spectra in chapter 4. For the remainder of this chapter, we focus the discussion on the phase of emitted harmonics which we identify as the fourth property for characterizing nonlinear mechanisms.

3.6. Characteristic phases of local response mechanisms

So far different mechanism-specific properties, such as intensity scaling with driving field, effective nonlinearity, and temporal widths have been discussed. Furthermore, our local semiclassical model provides the relative phase between the different nonlinear contributions and the driving field as discussed now.

For intensities well below the damage threshold, electrons in bound states are well described by the Lorentz-model i.e. a superposition of driven oscillators. The resonance frequencies in this case are usually above the Bandgap of the medium and far above the excitation frequency of an incoming infrared laser field. The polarization of bound electrons is therefore in phase with the driving field. Its time derivative, that is the current of bound electrons, J_{bound} , is a quarter period ahead of the driving field, see panel **a** in Fig. 3.9. Interestingly, once excited into the conduction band, both the injection and the Brunel mechanism generate contributions to the current of opposite phase, both distinct from bound and free electrons.

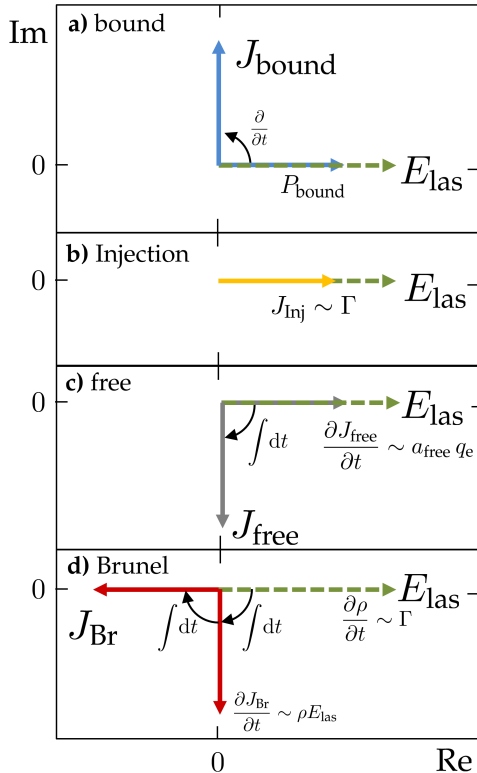


Figure 3.9.: Phase of mechanism-specific currents are represented by complex phasors of **a** bound electron current (blue), **b** Injection current (yellow), **c** free electron current (gray), **d** Brunel current (red). Bound polarization P_{bound} , tunneling rate Γ and charge acceleration of free electrons $a_{\text{free}} q_e$ are in phase with the driving laser field E_{las} (green dashed).

During injection, electron wave packets do not change their propagation direction anymore when the field is strongest, but tunnel a finite distance through the potential barrier and therefore further increase the charge displacement. Since the tunnel ionization rate follows nearly instantaneously the field in the long wavelength limit, it can also be interpreted as a modulation of the Ohm conductivity where the injection current (yellow) oscillates in phase with the incoming field, c.f. panel **b**. This distinguishes the injection current from the ballistic transport of free electrons \mathbf{J}_{free} (gray) see panel **c**, which is used to describe the Brunel mechanism.

For the Brunel mechanism, it is assumed that electrons propagate after excitation similar to free electrons, unperturbed in the conduction band. Hence, the charge acceleration $\mathbf{a}_{\text{free}}q_e$ is in phase with the driving field. Furthermore, it is taken into account that the conduction band population shows a step-wise increase, that follows from the time integration of the tunnel-ionization rate. This additional integration step (second integral in panel **d**) ensures that the phase of Brunel harmonics is distinct from all other specific phases **a-c** mentioned above. In summary, this semiclassical description explains the phase relation between individual current contributions at the fundamental frequency. To show that this analysis also applies to higher harmonics, the phase in sum-frequency mixing is examined.

3.6.1. Phase of harmonic currents

The phase of wave-mixing currents from a single nonlinear interaction (direct harmonics) shows two contributions,

$$\phi_n(t) = \underbrace{2n(\omega_{\text{pu}}t + \phi_{\text{pu}}) + (\omega_{\text{pr}}t + \phi_{\text{pr}})}_{\phi_n^{\text{mix}}(t)} + \phi^{\text{mech}}. \quad (3.60)$$

The first terms on the right-hand side are directly analog to sum-frequency generation $\omega_n^{\text{mix}} = 2n\omega_{\text{pu}} + \omega_{\text{pr}}$ and are found by calculating powers of $\mathbf{E}_{\text{pu}}^+ = \frac{\hat{\mathbf{E}}_{\text{pu}}}{2}e^{i(\omega_{\text{pu}}t + \phi_{\text{pu}})}$ and \mathbf{E}_{pr}^+ . The previously discussed, mechanism-specific constant phase shift from Fig. 3.9, here denoted by ϕ^{mech} , is just one additive term in the end. For the instantaneous response considered here, it is independent of the harmonic order, because the phase factors from time domain differentiation (i) and integration ($-i$) act on the total nonlinear current, including all harmonic contributions. In conclusion, the pointer diagram for higher harmonic currents shows identical relative phases as shown in Fig. 3.9 and just rotates with higher frequency.

3.6.2. Phase of harmonic fields in thin film scenario

To determine the phase of emitted odd harmonic fields we employ the plane wave result, $\mathbf{E} \sim -\mathbf{J}$, c.f. eq. (3.6), leading to the pointer diagram shown in Fig. 3.10.

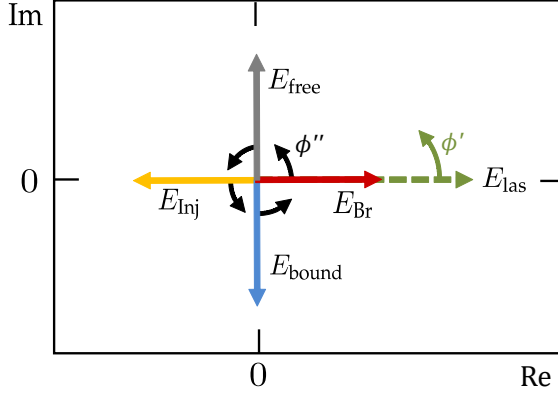


Figure 3.10.: Phase relation of emitted fields, from different mechanisms considering ballistic, collisionless motion in thin film (phase-matched) scenario. The dependence of the phase angles ϕ' , ϕ'' is discussed in the main text.

Due to the half period local phase shift between current and field $\phi_{\text{loc}} = \pi$, it is found that the injection field (yellow) is opposite to the phase of the driving field reference (green dashed), leading to destructive interference at the fundamental frequency ($\phi' = \phi'' = \omega_0 t$), which is expected from the discussion of energy conservation (sect. 2.4.4). Also, the quarter-period delayed phase of fields from the nonlinear bound polarization (blue arrow) is expected. It is simply analogous to the phase lag due to linear polarization that leads to a reduction of phase velocity in media.

So far, the phase relation between incident and emitted fields was discussed in Fig. 3.10 at the fundamental frequency. To extend the analysis to any incommensurate wave-mixing frequency, we use the concept of the carrier-envelope phase (CEP). The CEP of all harmonics follows directly from eq. (3.60),

$$\phi_n^{\text{CE}} = \phi_n^{\text{mix}}(t_p) + \phi^{\text{mech}} + \phi^{\text{loc}}, \quad (3.61)$$

where t_p denotes the peak time of harmonics that depends for finite pump-probe delay on the nonlinear order (Appendix B.6). Therefore, Fig. 3.10 reflects also the CEPs, if all harmonic field contributions are rotated by $\phi'' = \phi_n^{\text{mix}}(t_p)$ (see black arrows). Next, we extend the result for the CEP of harmonics from the plane wave to the Gaussian focussing scenario.

3.6.3. Effect of Gouy phase in Gaussian beam scenario

Upon propagation from the waist of a Gaussian focus (c.f. Fig. 3.3), fundamental and harmonic fields acquire a Gouy phase that converges towards $\pi/2$ for the $e^{+i\omega t}$ component in the far-field [113]. This Gouy phase directly affects the CEP [114] as the pulse envelope remains unchanged. Summarizing the discussed effects into one equation, the on-axis CEP in an idealized collinear thin film scenario is given by,

$$\phi_{n,\text{far}}^{\text{CE}} = \phi_n^{\text{mix}}(t_p) + \phi^{\text{mech}} + \phi^{\text{loc}} + \phi^{\text{Gouy}}(z) \quad \text{with,} \quad \phi^{\text{Gouy}}(z) = \tan^{-1} \left(\frac{z}{z_R} \right). \quad (3.62)$$

Notably, the last two terms, consisting of local phase and Gouy phase, complete the one-to-one correspondence of amplitude and phase between negative local dipole acceleration and on-axis far-field (small brown detector Fig. 3.3), resembling the Hertzian dipole behaviour (Appendix B.2).

3.7. Conclusion

In this chapter, the nonlinear medium response was first discussed based on a generic reference mechanism to physically interpret the effective order of nonlinearity. From this analysis, spectral weights of the electromagnetic far-field were extracted, showing that the high-order medium response dominates low-order harmonics for sufficiently strong driving. In particular, the steep, continuous fall-off of spectral weights with harmonic frequency was found to distinguish ionization-induced high-order nonlinear response from common HHG, generated by intraband anharmonicities and interband recombination. Furthermore, it was found that already a single high nonlinear response-order (here given by the tunneling exponent) can emit several low-order harmonics, that show the same intensity scaling and a uniform temporal structure. Based on this general analysis, four complementary signatures, specific to the driving mechanism, were identified. First, the effective nonlinearity, accessible via yield ratios in different polarization configurations, allows to distinguish the injection from the Brunel and Kerr-type response at high intensities. Second, the scaling with driving intensity was found to be strongest for the Brunel response and only slightly lower for the injection current. Third, the delay dependence, that separates high and low nonlinear contributions as narrow and broad signals along the delay axis. And forth, the emitted phase, that is specific to each source, as all analyzed mechanisms emit harmonics at a different phase. So far the formal analysis, based on the tunnel ionization rate, provided that the injection contribution dominates at harmonic frequencies. While impact ionization can not further contribute to the injection current, the following chapter addresses whether collisional ionization can lead for the present parameters to additional Brunel signatures in low-order wave mixing spectra.

4. Collisional Effects in the Extreme Nonlinear Response

In the preceding chapters, the nonlinear optical response from tunneling-induced plasma formation has been considered. In this chapter, we investigate whether collisions show an observable effect on ionization-induced harmonics. While it is widely accepted that collisional ionization contributes significantly to plasma formation at high intensities, the relative strength and its temporal modulation compared to the tunnel ionization rate is still debated [115]. Recently, Boltzmann-type collision approaches [116] and rate equation models for the laser-induced breakdown [23] have been proposed to address this question through the calculation of plasma density contributions. Here we start from an elastic collision rate to address the effect of collisions on the phase of nonlinear currents that were discussed above in a local, collision-less description (sect. 3.6). Next, the role of inelastic collisions is examined by employing a simple man's approach, that is in the course of the chapter further substantiated by a more detailed, kinetic simulation. In particular, the sub-cycle modulation of impact ionization is of particular interest, that can lead, similar to tunnel ionization, to a step-wise plasma density build-up. Therefore, our analysis aims at disentangling tunneling-induced from collision-induced Brunel contributions. Next, the amplitudes of both Brunel contributions are compared to injection and Kerr-type harmonics. It is investigated under which conditions impact-induced Brunel harmonics can compete with the injection contribution and become relevant to low-order mixing signals. We address this question by employing a kinetic model based on a rate equation description sampling the electron velocity distribution.

4.1. Phase shift of quiver motion and Brunel harmonics

The local description of Brunel emission [62] was originally proposed for plasma formation in gases, where the comparably large mean-free path of electrons allows for a ballistic quiver motion. The acceleration of electrons is there in phase with the driving field. At solid densities, the mean-free path is significantly reduced, such that the collision rate becomes comparable to the optical driving frequency. Hence, collisions can have a strong impact on the quiver phase of conduction band electrons. Since the Brunel mechanism, i.e. density modulation via tunneling is unaffected, it is expected that the collision-induced shift of the quiver phase is directly imprinted onto Brunel harmonics. To examine the collisional phase shift as function of elastic collision rate, we depart from the Drude model.

4.1.1. Drude model – Scenario of constant elastic damping

Within the Drude model, the electron motion is described by the classical equation of motion, where the location of a test electron x is given by,

$$\ddot{x} + \gamma\dot{x} = \frac{qE}{m}. \quad (4.1)$$

The damping term in the equation of motion $\frac{F_{\text{fric}}}{m} = -\gamma v$ is interpreted as the effect of collision events, where the drift contribution of the velocity is annihilated by scattering into a random direction. Elastic collisions turn directed into randomly nondirected motion. Formally, the Drude model corresponds to a driven and damped harmonic oscillator with vanishing resonance frequency. Here the simplifying assumption is made that the collision rate is fairly independent of the drift velocity. This results in a phase relation between the steady state solution of dipole excursion and driving field as shown in Fig. 4.1 (blue solid line) which is well-known [117] and summarized in Appendix C.1. For small collision rates, free electrons oscillate a half period out of phase, denoted as the ballistic limit. With increasing damping, the phase lag decreases towards $-\pi/2$, corresponding to the DC limit of the external driving field, where the conductivity obeys Ohm's law.

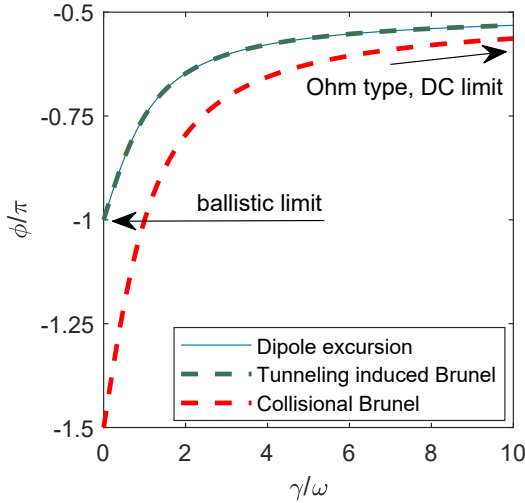


Figure 4.1.: Phase of tunneling (green) and collisional Brunel current (red). Phase of the excursion of conduction band electrons at driving frequency (blue), according to Drude model with constant damping rate γ . For calculation see Appendix C.1.

Next, we link this notion to the phase of Brunel harmonics. We use that the tunneling induced Brunel current is quarter period delayed wrt. the free current (previously pointed out in Fig. 3.9 c and d). This relative phase between drift and tunneling-induced Brunel current holds for any finite collision rate. Therefore, $J_{\text{Br}}^{\text{tun}}$ shows the same phase dependence as the free excursion (green dashed line in Fig. 4.1). Formally, this result can be written as,

$$\phi_{J_{\text{Br}}^{\text{tun}}}(\gamma) = \phi_{\Gamma} + \phi_{\rho} + \phi_v(\gamma) \quad (4.2)$$

where the phase difference between field and tunneling rate is set to $\phi_{\Gamma} = 0$ and the phase of the ionization degree due to time integration is $\phi_{\rho} = -\pi/2$ (corresponding

to the Fourier factor $\frac{1}{i\omega}$). Lastly, the phase of the Drude drift velocity $\phi_v(\gamma)$ introduces a dependence on the elastic collision rate. In the following, the effect of inelastic collisions on the phase provided by eq. (4.2) is examined.

4.2. Tunneling-induced vs. collisional Brunel harmonics

So far only the tunneling rate was considered as driving nonlinearity that leads through the sub-cycle modulation of the plasma density ρ_{sub} , according to eq. (2.9), to the emergence of Brunel harmonics,

$$\frac{\partial \mathbf{J}_{\text{Br}}}{\partial t} = qn_0\rho_{\text{sub}}\langle \ddot{\mathbf{x}} \rangle. \quad (4.3)$$

A similar, twice-per-cycle modulation of the plasma build-up can also be generated by impact ionization. For sufficiently cold plasmas and high quiver velocities, the electron kinetic energy can exceed the gap energy of the medium twice per laser cycle and trigger ionization. Due to the distinct nonlinearity, introduced by the threshold character of the rate, these collisional Brunel harmonics are expected to show specific phase and spectral weight structure, that is investigated next.

4.2.1. Phase of collisional Brunel harmonics in a simple man's approach

We examine the phase of impact-induced Brunel harmonics, by employing once more the simplified picture based on the Drude model. To use this model three assumptions are made. First, different Brunel contributions are separated such that tunnel ionization can be disregarded. Second, the elastic collision rate is fairly constant and larger than the impact rate, i.e. it can be well described by the γ -parameter of the Drude model. This argument will be further supplemented when discussing specific cross-sections in the following section. Third, it is assumed that only at high drift velocity a small fraction of electrons undergoes impact ionization.

From these assumptions, it follows that the drift is essentially the same as before, but now it defines also the phase of the impact ionization rate $\phi_v(\gamma) = \phi_{\gamma_{\text{imp}}}$. Replacing the ionization term, $\phi_{\Gamma} \rightarrow \phi_{\gamma_{\text{imp}}} = \phi_v(\gamma)$ in eq. (4.2) yields,

$$\phi_{\text{J}_{\text{Br}}}^{\text{imp}} = \phi_{\rho} + 2\phi_v(\gamma), \quad (4.4)$$

shown by a red dashed line in Fig. 4.1. It is found that at low damping rates, collisional contributions are further delayed by a quarter period with respect to tunneling contributions, however, for increased damping both converge quickly against the same limit of $-\pi/2$.

In conclusion, the Drude model provided a distinct signature of tunneling and impact-induced Brunel harmonics at low collision rates. The analysis poses furthermore the question whether impact ionization under our conditions is sufficiently strongly modulated such that collisional Brunel harmonics can compete with the amplitude of injection harmonics. Addressing this question also requires to take thermalization and the depletion of high-velocity states into account. Hence, we consider next a more detailed numerical model that resolves the full velocity distribution of electrons and therefore automatically accounts for inverse bremsstrahlung heating and impact-induced cooling of the plasma.

4.3. Kinetic model for capturing collisional effects

Goal of the following section is to examine the contribution of collisions to the harmonic response spectrum. We first inspect the properties of a more realistic ansatz for the collision rates, to motivate a suitable kinetic model for the electron dynamics.

4.3.1. Collision rates

The ansatz of constant damping parameters, discussed so far, is justified to obtain amplitude and phase information in time domain, that is dominated by the response at the fundamental frequency. This approach, however, does not contain higher frequency contributions, that are expected for a spectral analysis due to the velocity dependence of scattering rates. Therefore, a cross-section-based description of the form,

$$\gamma = n_0 |v| \sigma(|v|) \quad (4.5)$$

is considered that shows already even order frequency components ($2\omega, 4\omega, \dots$) due to the absolute modulus of the velocity in the second factor on the RHS. Furthermore, for elastic collisions the cross-section $\sigma(|v|)$ varies strongly at small velocities,

$$\sigma_{\text{el}}(|v|) = \frac{f_{\sigma_0} \sigma_0}{1 + \left(\frac{v}{v_0}\right)^2}, \quad (4.6)$$

as seen in Fig. 4.2 (blue curve), where suitable parameters for SiO_2 are used, i.e. $\sigma_0 = 30.738 \text{ \AA}^2$ and $v_0 = 2.1877 \frac{\text{m}}{\mu\text{s}}$ [118]. An even stronger modulation effect is expected for inelastic collisions due to a threshold behavior that rejects electrons with kinetic energy less than the bandgap $E < E_g$ that cannot trigger impact ionization (see red arrow). Here the Lotz cross-section is commonly used to describe inelastic

collisions [119],

$$\sigma_{\text{inel}} = \sigma_{\text{Lotz}} = a_L s_L \frac{\ln(E/E_g)}{E E_g}, \quad (4.7)$$

with parameters $a_L = 450 \text{ (eV\AA)}^2$ and $s_L = 2.1$ taken from [118]. The strong dependence on kinetic energy of both rates motivates to further examine the velocity distribution of electrons when excited by ultra-short pulses. In particular, the model introduced next allows to clarify the impact of collisional heating and the clipping of the high energy tail through the inelastic rate on harmonic emission. Since at high intensity, modifications to the Maxwell-Boltzmann distribution are expected, the full 3D velocity distribution is accounted for in a local model.

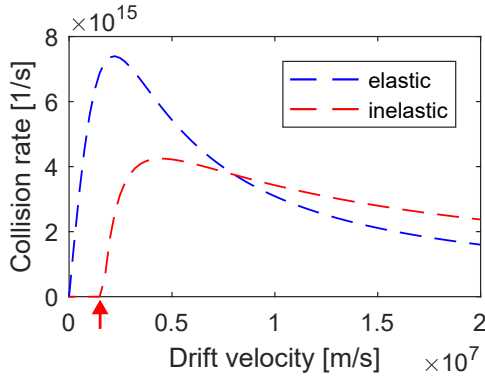


Figure 4.2.: Elastic (blue) and inelastic collision rate (red) per electron as function of electron velocity. At the threshold velocity (red arrow) the kinetic energy of one electron equals the band gap.

4.3.2. Calculation of the velocity distribution

Due to a large number of particles in the plasma, the local electron dynamics in the system is described by a kinetic model. In general, the electron distribution $f(\mathbf{x}, \mathbf{v}, t)$ in the classical six-dimensional phase-space is time-dependent and governed by Boltzmann's eq.

$$\left(\frac{\partial}{\partial t} + \mathbf{v} \cdot \nabla_{\mathbf{x}} + \frac{\mathbf{F}}{m} \cdot \nabla_{\mathbf{v}} \right) f = \left. \frac{\partial f}{\partial t} \right|_{\text{coll}} + \left. \frac{\partial f}{\partial t} \right|_{\text{ioni}} \quad (4.8)$$

where several approaches to incorporate the effect of the collision integral on the right-hand side exist [98, 120–122]. To expose the effect of collisions and ionization on the spectral response, we keep our model simple by considering only a local distribution $f(\mathbf{v}, t)$, removing any spatial dependence.

The local distribution is sampled on a numerical grid, where a few simplifying assumptions are made. First, assuming linearly polarized fields in the nonrelativistic limit $\mathbf{F} \approx q\mathbf{E}$ along one direction, the velocity distribution becomes cylindrical symmetric. For this effectively two-dimensional distribution, $f(v_{\perp}, v_{\parallel})$, external driving by the field and collisions are implemented as follows. To avoid numerical diffusion,

i.e. deformation of the distribution by field acceleration, an adaptive time step is employed that shifts electrons along the v_{\parallel} component parallel to the field by ± 1 or zero velocity bins. Next, elastic and inelastic decay cascade rates are solved to determine the relative amount of electrons that collided one or more times during one time step. These collision electrons are redistributed according to a three-dimensional isotropic distribution. While the absolute velocity of elastically scattered electrons is fixed, the kinetic energy of electrons triggering impact ionization is reduced according to the gap energy lost in the ionization event. For simplicity, newly born electrons from impact and tunnel ionization are initialized with zero velocity. It was verified that equal splitting of residual kinetic energy onto impinging and liberated electrons from an inelastic collision does not significantly affect the dynamics. From this velocity distribution, the mean drift current is analyzed in the following. Here, electrons originating from tunnel or collisional ionization were propagated in two different distributions, $f_{\text{tun}}(v_{\perp}, v_{\parallel})$ and $f_{\text{coll}}(v_{\perp}, v_{\parallel})$, to disentangle the corresponding contributions to Brunel harmonics.

4.4. Effect of impact ionization on nonlinear response

Goal is to understand the temporal and spectral structure of the collisional response, in particular, to clarify how collisions contribute to the ionization-induced harmonic spectrum. To study the collisional effect on different wave-mixing orders, we consider the same two-color scenario as before, with a strong pump pulse and weak probe field. From the electron velocity distribution, the nonlinear response current is analyzed with a Gabor transform¹ that provides time-dependent spectral analysis of each component of the current. For better comparison, the contributions to the nonlinear current from different mechanisms are overlapped in Fig. 4.3. This representation is selected to expose the dominating mechanisms in the response and reveal characteristic emission times.

The overall structure of the Gabor spectrum is governed by high-order harmonics and side band signals due to sum and difference frequency mixing around $t = 0$ where pump and probe pulse are peaked. This time-frequency-map shows more signals in the side band structure than the experimental spectrum (discussed in section 2.2) for two reasons. First, this local model is insensitive to the wavevector direction and therefore corresponds to collinear wave mixing where positive and negative probe photons contribute equally. Second, the harmonic yield is shown over several orders of magnitude, such that contributions with more than one probe photon become discernible.

The strongest contribution to the harmonic spectrum is provided by the injection mechanism (yellow signatures), that dominates the side bands from third harmonic (HH3) on. The point-symmetric, parabolic shape with respect to frequency

¹The Gabor transform used here is given in the Appendix, eq. (C.10).

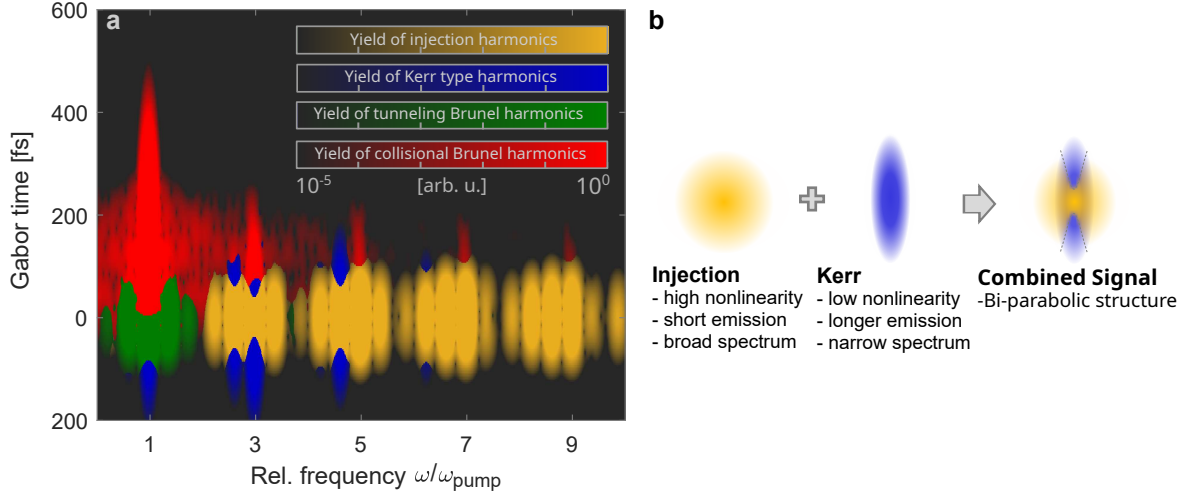


Figure 4.3.: The Gabor spectrum of injection (yellow), Kerr (blue), tunneling Brunel (green) and collisional Brunel harmonics (red), with window width $\tau_{\text{FWHM}}^{\text{Gabor}} = 50$ fs, calculated from the velocity distribution of tunneling and impact electrons at $I_{\text{pu}} = 10.5$ TW/cm², is shown in **a**. All other parameters are set as discussed in sect. 2.1. The qualitative origin of the bi-parabolic structures in the spectrum is illustrated in the schematic superposition of injection and Kerr-type contributions with exaggerated spectral-to-temporal width ratios for better visibility in **b**.

and time axis (clearly visible around HH9) is attributed to the Gaussian shape of the pump and probe pulse. At lower harmonic orders, in particular at the $n = 1$ signal ($\omega/\omega_{\text{pu}} = 4.7$), symmetric Kerr contributions are seen as blue tips in the rising and in the trailing edge. This signature is a result of the superposition of injection and Kerr contributions (see panel **b**). Kerr harmonics share the same parabolic shape, but are less spectrally broadened and generate a harmonic response of longer duration, due to the significantly lower order of nonlinearity, as discussed in section 3.5. Since the peak amplitude of Kerr harmonics at $t = 0$ is already below that of injection, Kerr can only compete in the edges. Additional simulations confirmed that these regions of dominant Kerr contribution (blue tips) shrink with increasing intensity. Here $\chi^{(3)}$ Kerr signals are only visible at the selected frequencies, due to the low order of nonlinearity. For these direct harmonics, that emerge in a single nonlinear interaction, only three photons are combined. Combinations with more photons, expected for cascaded 3rd order Kerr interaction require a finite propagation distance and are therefore not resolved by the local model. This explains that the $n = 1$ wavemixing harmonic shows Kerr contributions on the edges, while the $n = 2$ injection harmonic at $\omega/\omega_{\text{pu}} \approx 6.7$ is essentially background free. Further, it is seen that Kerr signals with two probe photons, i.e. $2\omega_{\text{pr}} \pm \omega_{\text{pu}}$ at the relative frequency $\omega/\omega_{\text{pu}} \approx 4.4, 6.4$ are significantly suppressed and barely visible.

The third symmetric response is the tunneling induced Brunel contribution that is only dominant at the fundamental frequency and respective side bands (green). At higher frequencies, tunneling-induced Brunel harmonics are dominated by the

injection response in accordance with the discussion in the previous chapter. The collision-induced Brunel response (red) shows a pronounced temporal asymmetry with a broad spectral and noisy contribution between $t = 0, \dots, 200$ fs that reaches from the third harmonic down to the DC component which is attributed to the thermal contribution of impact ionization. Stronger, more defined collisional signatures are seen in the trailing edge at the fundamental and odd harmonic frequencies. The largest peak at the fundamental emerges mainly from the free electron drift current. The effect of cold avalanching, where impact ionization is driven by the ponderomotive quiver-motion of electrons, is seen best at the third harmonic. Higher harmonics are attributed to the nonlinear dependence of the collision rate on the driving field. While contributions up to HH9 are discernible, no clear collisional wave mixing contributions are observed. One possible interpretation for this observation is, that the amplitude of the probe beam in this scenario is too weak compared to collisional damping to contribute sufficiently to the quiver motion.

In conclusion, the time resolved analysis of the ionization induced response, calculated from the electron velocity distribution, provided that collision induced Brunel harmonics contribute significantly in the trailing edge of the driving pulse. This contribution can be distinguished by the asymmetric time structure and is also seen with smaller contributions at odd harmonics of the strong pump pulse. No significant collisional contributions are found at the wave mixing frequencies of interest, that contain one photon from the much weaker probe pulse. While these wave mixing harmonics are mostly dominated by the tunneling injection current, temporally confined contributions from the third order Kerr response are found for the $n = 1$ signal. In the following, we use that the $n = 1$ signal is not screened by collisional contributions to reconstruct the tunneling-induced plasma build-up from the detected signal.

5. Reconstruction of the Strong-Field-Driven Plasma Dynamics

In this chapter, the reconstruction of the strong-field-induced plasma generation is discussed. Substantial parts of these results were published in [JLK⁺22a, MBJL⁺19]. Even though the main mechanism of strong-field tunnel ionization and impact ionization is known, it is so far experimentally challenging to distinguish respective contributions, leading to conflicting conclusions about their importance [123] and [121, 124]. The particular challenge is that both contributions lead to intrapulse excitation [120]. Available indirect measurements allowed so far to estimate the prevalence of each mechanism [67, 125]. In particular, transient absorption and reflectivity measurements were employed to obtain the cycle-averaged plasma build-up [126–130]. While the sub-cycle dynamics of carriers in solids became accessible through attosecond transient absorption and polarization spectroscopy [1, 131–133] these time-domain methods do not allow to isolate the contribution of SFI to the ionization yield. On the other hand, the existence of a specific optical SFI signature was reported in the literature [62, 68, 69, 92], associated with the 2ω -modulation of the plasma density [64, 134]. In the following, we utilize the detected below-bandgap injection response to reconstruct the sub-cycle tunnel ionization dynamics using time domain ptychography [135, 136].

Basis for the reconstruction of the field-driven ionization, is that the injection contribution of the nonlinear current

$$\mathbf{J}_{\text{inj}} = n_0 \dot{\rho}_{\text{tun}} E_g \frac{\mathbf{E}}{|E^2|}, \quad (5.1)$$

earlier introduced in eq. (2.11), becomes dominant at high intensities. From this equation, the reconstruction of the effective tunnel ionization rate $\dot{\rho}_{\text{tun}}$, based on the observable far-field intensity spectrum, is now developed. The first key element to access the temporal dynamics of the process is to employ the delay-dependent two-color wave-mixing analysis. As before, a weak probe pulse ensures that only signal contributions linear in the probe field are considered,

$$\mathbf{J}_{\text{inj}} = \sigma_{\text{eff}} \mathbf{E}_{\text{pr}}, \quad (5.2)$$

which allows the identification of an effective conductivity

$$\sigma_{\text{eff}}(t) = \frac{n_0 \dot{\rho}_{\text{tun}} E_g}{|E_{\text{pu}}|^2} \sim \frac{\dot{\rho}_{\text{tun}}(t)}{I_{\text{pu}}(t)}. \quad (5.3)$$

In the last step, the right-hand side has been simplified, by replacing the oscillatory squared pump field in the denominator by the cycle averaged, slowly evolving intensity envelope which is justified due to highly nonlinear dependence of $\dot{\rho}_{\text{tun}}(t)$. The

argument is that tunnel ionization only occurs when the field becomes maximal so that the denominator can be replaced by the slowly evolving amplitude.

Next, the left-hand side of eq. (5.2) is determined from the relation between injection current and measured delay-dependent intensity spectrum. In general, this link is not trivial. Here we come back to the harmonic emission scenario where the entire transverse profile is detected (as discussed in sect. 3.2.3). In this case, the intensity is, according to eq. (3.12), proportional to the square of the injection current $I(\omega) \sim |\mathbf{J}_{\text{inj}}(\omega)|^2$. Together with eq. (5.2), the measured intensity spectrum in the two color case is given by,

$$I_{\text{exp}}(\omega, \tau_j) \sim |\mathcal{F}[\sigma_{\text{eff}}(t) E_{\text{pr}}(t - \tau_j)]|^2, \quad (5.4)$$

where the operator $\mathcal{F} = \int_{-\infty}^{\infty} dt e^{-i\omega t}$ abbreviates the Fourier transform. In the next section, the reconstruction of $\sigma_{\text{eff}}(t)$ based on the measured intensity spectrum is discussed.

5.1. Phase retrieval algorithm and convergence

Due to the formal structure of eq. (5.4) that is reminiscent of a phase retrieval problem, the discussion of our reconstruction method is oriented along ptychographic engines that are typically used to reconstruct a local 2D field and a transmission mask from detected far fields. Here we adapt the method to two color pump-probe wave-mixing, similar to FROG and XFROG methods [137–139]. Goal of the following presentation is to provide a short pseudo-code that illustrates the key ideas of the algorithm.

Ptychographic iterative engines (PIE) were originally developed [140, 141] to retrieve from a set of measured diffraction images $I_j(\mathbf{q})$ the real-space distribution of incident field $E(\mathbf{r})$ and the transmittance $T(\mathbf{r} - \mathbf{r}_j)$,

$$I_j(\mathbf{q}) \sim |\mathcal{F}[E(\mathbf{r}) T(\mathbf{r} - \mathbf{r}_j)]|^2. \quad (5.5)$$

The index j labels small translations of the sample transverse to the field propagation. This mathematical convolution structure gave rise to the name of the method, that is derived from greek *ptyché*—fold and *gráphein*—writing. For time domain ptychography [135, 136] the spatial coordinates are replaced by time, establishing the correspondence between eq. (5.4) and (5.5).

To account for the fact that in the experiment no negative frequency mixing components are detected, only the positive frequency contributions i.e. complex functions are considered for the initially unknown conductivity and probe field. This mathematical constraint removes all negative mixing contributions, such as $2n\omega_{\text{pu}} - \omega_{\text{pr}}$, that

are missing due to the noncollinear setup of the experiment (c.f. sect. 2.2),

$$I_{\text{exp}}(\omega, \tau_j) \sim \underbrace{|\mathcal{F}[\sigma_{\text{eff}}^+(t) E_{\text{pr}}^+(t - \tau_j)]|^2}_{S(t, \tau_j)}. \quad (5.6)$$

Here positive frequency components are indicated by a plus in the superscript (as previously introduced in eq. (3.3)), however, in the following the formal superscript and the subscript "eff" are omitted for brevity.

Next, an update equation for σ is derived by minimizing the error in time domain between a guess for the source function $S(t, \tau_j)$ on the RHS and initially unknown true solutions $\check{\sigma}(t_i), \check{E}_{\text{pr}}$,

$$R_S = \sum_i \sum_j |S_{ij} - \check{\sigma}_i \check{E}_{ij}^{\text{pr}}|^2, \quad (5.7)$$

where the time is discretized and arguments are abbreviated by indices $S(t_i, \tau_j) \rightarrow S_{ij}$. The extremal condition is fulfilled if the gradient wrt. to all elements of the eff. conductivity, addressed by index ℓ , vanishes,

$$\frac{\partial R_S}{\partial \check{\sigma}_\ell} = \frac{\partial}{\partial \check{\sigma}_\ell} \sum_i \sum_j [S_{ij} - \check{\sigma}_i \check{E}_{ij}^{\text{pr}}] [S_{ij} - \check{\sigma}_i \check{E}_{ij}^{\text{pr}}]^* \quad (5.8)$$

$$= \sum_j \check{E}_{\ell j}^{\text{pr}} [S_{\ell j} - \check{\sigma}_\ell \check{E}_{\ell j}^{\text{pr}}]^* = 0. \quad (5.9)$$

Solving for σ and carrying out this expression for all times $t_\ell \rightarrow t$ yields,

$$\check{\sigma}(t) = \frac{\sum_j \check{E}_{\text{pr}}^*(t - \tau_j) S(t, \tau_j)}{\sum_j |\check{E}_{\text{pr}}(t - \tau_j)|^2}. \quad (5.10)$$

This result, obviously requires that the probe field in the sample is known. However, Maiden and Rodenburg developed an extended version of the algorithm, known as ePIE [142], where both quantities can be reconstructed on equal footing.

The idea of ePIE is to depart from a guess function for both quantities, that are solved iteratively by adapting the update eq. (5.10). The set of updates to iterate from step n to $n + 1$,

$$\sigma^{n+1}(t) = \sigma^n(t) + \beta_1 \frac{[E_{\text{pr}}^n(t - \tau_j)]^* \Delta S_j^n(t)}{\max(|E_{\text{pr}}^n(t)|^2)}, \quad (5.11)$$

$$E_{\text{pr}}^{n+1}(t - \tau_j) = E_{\text{pr}}^n(t - \tau_j) + \beta_2 \frac{[\sigma^n(t)]^* \Delta S_j^n(t)}{\max(|\sigma^n(t)|^2)}, \quad (5.12)$$

shows a few numerical tweaks, that are discussed in the following. In both equations the feedback parameter β controls, relative to the maximum square of the fixed variable, the robustness, and speed of convergence. For each update of $\sigma(t)$ and $E_{\text{pr}}(t)$

one random delay index $j(n)$ is selected. Good convergence is found by picking each delay once before addressing a particular j a second time, which is in practice realized by two nested iteration loops. The required source wave difference $\Delta S_j^n(t)$ is determined from a second constraint based on the available input data in frequency domain. The guess for the source wave at iteration n ,

$$S_j^n(t) = \sigma^n(t) E_{\text{pr}}^n(t - \tau_j), \quad (5.13)$$

is corrected, by replacing its spectral amplitudes with the measured intensity distribution

$$S_{j,\text{corr}}^n(t) = \mathcal{F}^{-1} \left[\sqrt{I_{\text{exp}}(\omega, \tau_j)} \frac{\mathcal{F}[S_j^n(t)]}{|\mathcal{F}[S_j^n(t)]|} \right], \quad (5.14)$$

according to eq. (5.6). The difference in the source function is then given by

$$\Delta S_j^n(t) = S_{j,\text{corr}}^n(t) - S_j^n(t). \quad (5.15)$$

Finally, between two iterations, the probe field $E_{\text{pr}}(t)$ is stored on a discretized grid. To apply and remove different delay shifts τ_j , the Fourier shift theorem,

$$E_{\text{pr}}(t - \tau_m) = \mathcal{F}^{-1} \left[\mathcal{F}[E_{\text{pr}}(t)] e^{-i\omega\tau_m} \right], \quad (5.16)$$

is employed prior to and after the iteration update of both variables as shown in the Pseudo-code of the algorithm, table 5.1.

loop iteration $n=1:N$		
loop delay $m=1:M$		
shift probe by delay τ_m	$E_{\text{pr}}(t - \tau_m)$	$= \mathcal{F}^{-1}[\mathcal{F}[E_{\text{pr}}(t)]e^{-i\omega\tau_m}]$.
get time domain sig.	$S(t, \tau_m)$	$= \sigma_{\text{inj}}^{\text{sub}}(t) E_{\text{pr}}(t - \tau_m)$
get freq. domain sig.	$S(\omega, \tau_m)$	$= \mathcal{F}(S(t, \tau_m))$
apply intensity constraint	$S_{\text{new}}(\omega, \tau_m)$	$= \sqrt{I_{\text{exp}}(\omega, \tau_m)} e^{i\angle S(\omega, \tau_m)}$
transform to time domain	$S_{\text{new}}(t, \tau_m)$	$= \mathcal{F}^{-1}[S_{\text{new}}(\omega, \tau_m)]$
get signal difference	$\Delta S(t, \tau_m)$	$= S_{\text{new}}(t, \tau_m) - S(t, \tau_m)$
update first pulse	$\sigma_{\text{inj,new}}^{\text{sub}}(t)$	$= \sigma_{\text{inj}}^{\text{sub}}(t) + \beta_1 \frac{\Delta S(t, \tau_m) E_{\text{pr}}(t - \tau_m)^*}{\max E_{\text{pr}}(t - \tau_m) ^2}$
update second pulse	$E_{\text{pr,new}}(t - \tau_m)$	$= E_{\text{pr}}(t - \tau_m) + \beta_2 \frac{\Delta S(t, \tau_m) \sigma_{\text{inj,new}}^{\text{sub}}(t)^*}{\max \sigma_{\text{inj,new}}^{\text{sub}}(t) ^2}$
shift pulse two back	$E_{\text{pr,new}}(t)$	$= \mathcal{F}^{-1}[\mathcal{F}[E_{\text{pr,new}}(t - \tau_m)]e^{i\omega\tau_m}]$.
end delay loop		
get error estimate	R	$= \frac{\sum_{\ell} \sum_n (S(\omega_{\ell}, \tau_n) ^2 - I_{\text{exp}}(\omega_{\ell}, \tau_n))}{\max_{\omega_{\ell}, \tau_n} I_{\text{exp}}(\omega_{\ell}, \tau_n) }$
end iteration loop		

Table 5.1.: Pseudo code of time domain ptychography retrieval algorithm.

After convergence is reached, the plasma dynamics is calculated from the effective conductivity by employing eq. (5.3). In the following section optimal conditions for reconstruction are examined.

5.2. Optimal conditions for reconstruction

In this section, the role of the polarization configuration and the pump intensity is considered to determine optimal conditions for reconstruction. Two lines of arguments are to be discussed. First, the interpretation of the parallel scenario. And second the effect of other nonlinear mechanisms.

5.2.1. Role of the polarization configuration

One basic assumption of the ePIE algorithm is that, according to eq. (5.6), one of the quantities of interest is delay independent. Interestingly, for the highly nonlinear injection response, this is only the case for the perpendicular configuration, when the probe photon must enter in the vectorial component of the injection current $\mathbf{J}_{\text{inj}}^{\perp} = \sigma_{\text{eff}} \mathbf{E}_{\text{pr}}$. In this case, only pump photons can contribute to the ionization rate (possible even number of probe photons are disregarded due to low probe intensity). Therefore the ionization trace $\rho_{\perp}(t) \approx \rho_0(t)$ stays effectively as in the pump-only scenario, indicated in the following by a subscript zero.

In the parallel configuration, on the other hand, the probe photon contributes much stronger to tunnel ionization leading to significant beating in step height of the trace. In fact, a direct result of the probe-modulated ionization rate is the stronger harmonic response in the parallel scenario. Hence, both unknowns of the reconstruction, i.e. eff. conductivity and driving field, become delay-dependent. Even though this seems to violate the basic assumption of ePIE, it is now discussed why the algorithm is still applicable.

Key argument is, that the injection response at considered low-order mixing signals is identical for both polarization configurations up to a constant factor $I^{\parallel}(\omega, \tau) = m^2 I^{\perp}(\omega, \tau)$. This means, data from the parallel measurement can be interpreted as if measured from the perpendicular scenario, where the ionization trace agrees well with the pump-only scenario. In conclusion, switching to parallel polarization changes ionization, however, the ePIE continues to retrieve the density of the pump-only scenario $\rho_0(t)$.

5.2.2. Role of competing nonlinear mechanisms

Depending on laser parameters also other mechanisms such as Kerr- or Brunel response [62, 92] can contribute to the wave-mixing signal. Their contribution is detrimental to the reconstruction. Especially the contribution of Kerr increases with absolute delay due to the lower nonlinear order as it has been seen already in sect. 4.4. Due to the higher contrast with respect to Kerr, it is expected that the reconstruction error is smaller in the parallel scenario. Next, we apply the algorithm to simulated two-color spectra. We define the error based on the difference between reconstructed $\rho_{\text{rec}}(t)$ and simulated reference ionization $\rho_{0,\text{sim}}(t)$ of the pump-only scenario,

$$R_{\rho(t)} = \sqrt{\frac{1}{T} \int_0^T [\rho_{\text{rec}}(t) - \rho_{0,\text{sim}}(t)]^2 dt}. \quad (5.17)$$

Examining the reconstruction error as function of intensity in Fig. 5.1 (same pulse parameters as before, see caption) shows for both polarization configurations three qualitatively different intervals.

The error is highest for low intensities where the emitted signal is dominated by the Kerr response that is systematically longer than the ionization response. As a result, the reconstructed ionization trace (thin blue in inset c) shows significantly wider

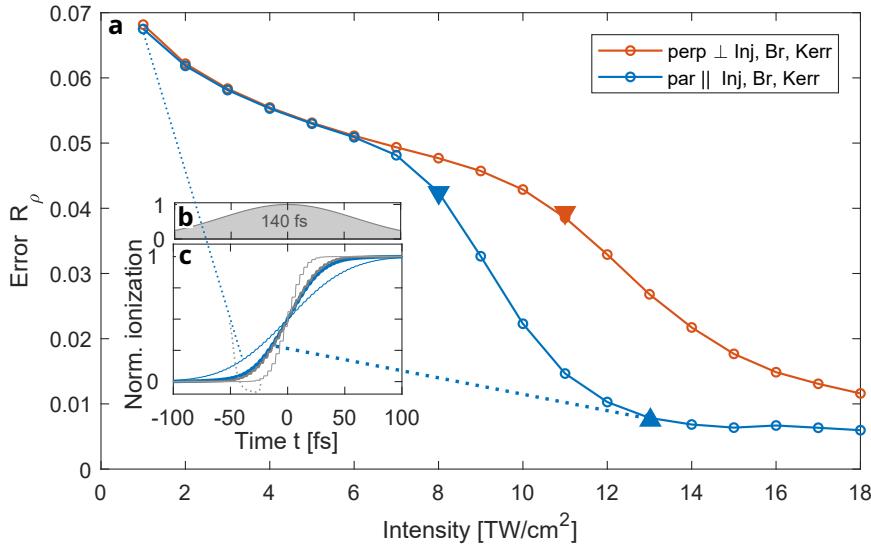


Figure 5.1.: Reconstruction error of plasma density as function of pump intensity for numerical test scenario **a**. Injection, Brunel and Kerr contributions to the nonlinear current are considered in parallel (blue) and perpendicular polarization configuration (orange) for a $\tau_{\text{pu}} = 140$ fs pulse (inset **b**), $\lambda_{\text{pu}} = 2100$ nm. Optimal conditions are reached for $I \geq 13$ TW/cm². At this intensity simulated $\rho_{0,\text{sim}}(t)$ (thick blue) and reconstructed ionization $\rho_{\text{rec}}(t)$ (thick gray) overlap (inset **c**). At lowest intensity, large deviations between simulated and reconstructed time trace (c.f. thin blue and thin gray in **c**) are attributed to the Kerr contribution (see main text).

wings compared to $\rho_{0,\text{sim}}(t)$ (thin gray line). With increasing pump intensity this error decreases, as seen in **a**. Initially, a slow decrease is observed. This is attributed to an increase of the tunneling period due to the reduction of the nonlinearity of the tunneling rate (see Fig. 3.6 **b** and Fig. 3.8 **a**). As the intensity increases, the tunneling period extends towards the duration of the Kerr response that is still longer and dominant.

Once the injection current exceeds the Kerr-type response, the reconstruction error decreases much faster. First, injection exceeds Kerr only at the center of the pulse i.e. for delays $\tau \approx 0$ such that the center of the ionization trace is well reconstructed. Due to higher injection yield, this happens in the parallel case (blue) at lower intensities than in the perpendicular case (orange), as seen by the position of the shoulders (downward triangles). Increasing the intensity further, leads to suppression of the relative Kerr contribution and improves the reconstruction also in the tails of the ionization trace.

Optimal conditions for reconstruction are reached for parallel polarization above $I_{\text{pu}} \geq 13 \text{ TW/cm}^2$ (blue upward triangle). Here injection becomes dominant for the relevant delay range. Even though the cycle average of the reconstructed ionization trace converges correctly, the reconstruction error is seen to saturate for higher intensities due to the unknown sub-cycle phase and sharpness of the ionization steps.

In conclusion, the relative ionization trace can be reconstructed from the delay-dependent intensity spectrum of the total nonlinear wave mixing response that contains also other nonlinear contributions such as Kerr and Brunel harmonics, for sufficiently high pump intensity. In the next step, the algorithm is applied to experimentally measured delay spectra, obtained close to the damage threshold at peak intensity of $I = 13 \text{ TW/cm}^2$.

5.3. Reconstruction from experimental spectra

To link the detected nonlinear response spectrum to the strong-field-induced plasma formation we first focus only on the strongest wave mixing harmonic, i.e. the $n = 1$ signal that is in the perpendicular scenario directly related to the $2\omega_{\text{pu}}$ -component of the tunneling rate. Using only this signal, the cycle-averaged component of the ionization rate can be still inferred as shown now.

The starting point is the effective strong field ionization rate $\Gamma = \frac{\partial \rho}{\partial t}$ that is physically governed by the laser-driven tunnel ionization rate and modified by several effects such as depletion of the valence band and the local field due to plasma reflection. Central argument of the following discussion is, that the effective strong field ionization rate is an instantaneous nonlinear function that depends on the modulus

of the electric field $\Gamma(|E(t)|)$. Hence, it can be written as even-order harmonic series,

$$\Gamma(t) = \sum_{h=0,2,4,\dots} \underbrace{\frac{\hat{\Gamma}(t)}{2} D_h e^{ih\omega_{\text{pu}}t}}_{\Gamma_h^+} + c.c. \quad (5.18)$$

with so far undetermined harmonic weights D_h in full analogy of the general nonlinear polarization (earlier discussed in eq. (3.5)). Important here is that all contributions are characterized by the same envelope function $\hat{\Gamma}(t) = \Gamma(\hat{E}(t))$. Therefore the time evolution of the cycle averaged component Γ_{ca} , i.e. the term with index zero,

$$\Gamma(t) = \underbrace{\hat{\Gamma}(t) D_0}_{\Gamma_{\text{ca}}} + \underbrace{\left[\sum_{h=2,4,6,\dots} \frac{\hat{\Gamma}(t)}{2} D_h e^{ih\omega_{\text{pu}}t} + c.c. \right]}_{\Gamma_{\text{sub}}} \quad (5.19)$$

can be determined from the square bracket, up to a constant factor. The missing ratio between cycle averaged (ca) and sub-cycle (sub) contribution is obtained from the fact that the ionization rate is strictly non-negative and vanishes when the field is zero. Hence Γ_{ca} must be equal to the envelope of the sub-cycle rate Γ_{sub} . In the following it is used that higher frequency components in the spectrum quickly fall off (c.f. discussion of spectral weights sect. 3.3) which allows to approximate the amplitude of the leading term $\Gamma_{\text{ca}} \approx 2|\Gamma_{h=2}^+|$ by the sub-cycle rate. Employing the proportionality to the conductivity $\Gamma_{h=2}^+ \sim \sigma_{h=2}^+(t) I_{\text{pu}}(t)$ (c.f. eq. (5.3)) yields,

$$\rho_{\text{sub}} \sim \int dt \operatorname{Re}(\Gamma_{h=2}^+) \quad \text{with} \quad \Gamma_{h=2}^+ \sim \sigma_{h=2}^+(t) I_{\text{pu}}(t), \quad (5.20)$$

$$\rho_{\text{ca}} \sim \int dt |\Gamma_{h=2}^+|, \quad (5.21)$$

where $\sigma_{h=2}^+(t)$ is reconstructed from the experimental time-frequency map of the isolated $n = 1$ signal,

$$I_{n=1}(\omega, \tau_j) \sim \left| \int dt \sigma_{h=2}^+(t) E_{\text{pr}}^+(t - \tau_j) e^{-i\omega t} \right|^2. \quad (5.22)$$

In Fig. 5.2 the delay-resolved experimental spectrum of the $n = 1$ wave-mixing signal, recorded at 13 TW/cm^2 , is depicted in panel **a**. The delay spectrum retrieved after 10^3 iterations of the ptychographic algorithm in panel **b** shows agreement, indicating that convergence is reached. The sub-cycle conductivity $\sigma_{\text{inj}}^{\text{sub}} \sim 2\operatorname{Re}(\sigma_{h=2}^+)$ determined by the ePIE algorithm is shown in panel **c**. The resulting sub-cycle component of the SFI rate $\dot{\rho}^{\text{sub}}$ is displayed together with the cycle-averaged, low-frequency contribution in panel **d**. Adding up the fast and the slow component leads to the total SFI rate plotted in panel **e**. Integrating the rate over time yields the strong-field plasma build-up ρ_{SFI} that is displayed together with results obtained by numerical simulations under identical conditions in panel **f**. The gray band indicates the tem-

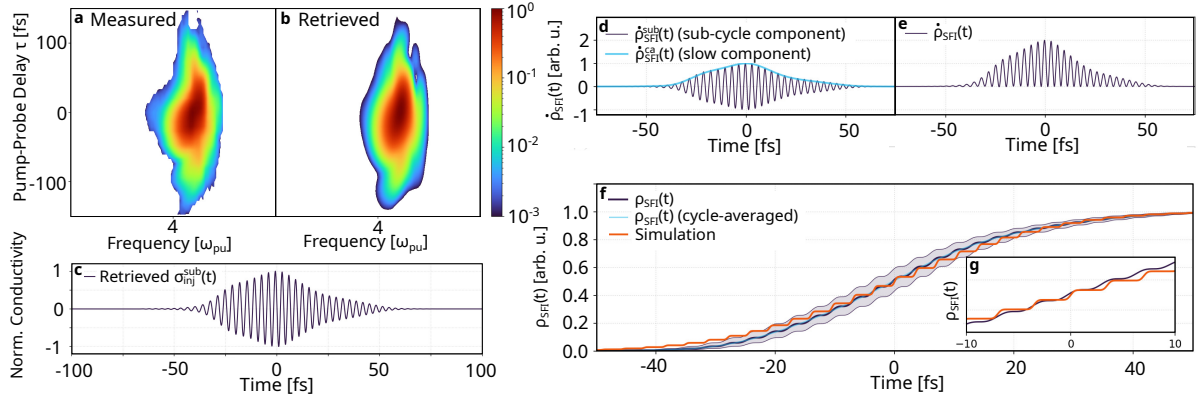


Figure 5.2.: Retrieval of tunnel ionization traces from $n = 1$ injection signal at 13 TW/cm^2 . The measured and retrieved signal of the delay spectrum after 1000 iterations is compared in panel **a** and **b**. Time traces of the effective sub-cycle conductivity **c**, the time derivatives of the tunnel ionization degree **d**, **e**, and the comparison with the simulation **f**, **g** show good convergence of the method. Figure adapted from [JLK⁺22a].

poral uncertainty by one cycle, as the retrieval algorithm is insensitive to the global phase i.e. the carrier-envelope phase of $\sigma_{n=1}^+$. Good agreement with the numerically simulated step-wise plasma density build-up is found around $t = 0$ (see inset **g**).

In conclusion, the SFI contribution to the plasma build-up was reconstructed from an experimentally measured time-resolved low-order wave mixing signal by means of a numerical reconstruction algorithm. This analysis shows one possible application of injection harmonics. Whereas the cycle-averaged build-up is accessible through the temporal signature of an arbitrary wave-mixing order, the sub-cycle plasma dynamics was reconstructed from the $n = 1$ wave-mixing harmonic. It was shown that this $2\omega_{\text{pu}} + \omega_{\text{pr}}$ signal suffices to characterize both, the cycle-averaged and the $2\omega_{\text{pu}}$ modulated increase of the plasma density. This provides direct evidence for the number, location, and relative height of ionization steps within the strong driving pulse, while the timing of ionization bursts is linked to the phase between driving pulse and emitted harmonics. Lastly, the relative contribution between strong field and impact ionization is accessible by comparison between the reconstructed and total plasma evolution that is further discussed based on the spatially resolved simulation in the next chapter.

6. FDTD Ionization-Radiation Model

Goal of this chapter is the analysis of the field-induced plasma build-up including pulse propagation effects. To this end a self-consistent simulation has been developed that is based on a time-domain description of field propagation and includes the nonlinear contributions from bound electrons and the emerging plasma. The presented simulation takes into account forward and backpropagating waves, i.e. radiation in transmission and reflection direction for the fundamental as well as for the generated harmonic orders. The foundation of this model and starting point of the discussion are Maxwell's equations [143]. Their numerical solution by means of the finite-difference time-domain (FDTD) method [80, 82] is briefly discussed. Next, we explain the calculation of the free plasma current through a rate ansatz for drift- and temperature-dependent collision rates [23, 118] and the nonlinear polarization of bound electrons through a dispersive nonlinear Lorentz model [144, 145]. After this introduction to our numerical tool, spatially resolved plasma formation is investigated where we focus on plasma hotspots arising from so-called Lippman interference [146] in standing waves from backward reflection. Thereby, we address in particular the self-reconfiguration [16, 89, 147] of observed laser-induced plasma patterns.

6.1. Electromagnetic field propagation via FDTD

The classical electromagnetic field is governed by Maxwell's equations. Here, the differential formulation of the curl equations for the macroscopic fields,

$$\nabla \times \mathbf{E} = -\frac{\partial \mathbf{B}}{\partial t}, \quad (6.1)$$

$$\nabla \times \mathbf{H} = \left(\mathbf{J}_f + \frac{\partial \mathbf{D}}{\partial t} \right), \quad (6.2)$$

is particularly useful to determine the propagating electric field \mathbf{E} and magnetic field \mathbf{B} , where intra-molecular to inner atomic field contributions are excluded. In this formulation the current density of free electrons \mathbf{J}_f enters explicitly, while the medium response of bound electrons is included via auxiliary material fields, i.e. the displacement field \mathbf{D} and the magnetic field strength \mathbf{H} , given by the constitutive relations

$$\mathbf{D}(\mathbf{r}, t) = \varepsilon_0 \mathbf{E}(\mathbf{r}, t) + \mathbf{P}(\mathbf{r}, t), \quad (6.3)$$

$$\mathbf{H}(\mathbf{r}, t) = \frac{1}{\mu_0} \mathbf{B}(\mathbf{r}, t) - \mathbf{M}(\mathbf{r}, t). \quad (6.4)$$

These relations are determined by the electric polarization density \mathbf{P} , in the following denoted as "polarization" and the magnetization that vanishes for non-magnetic media, $\mathbf{M} = \mathbf{0}$, considered here. This set of equations (6.1)–(6.4) is now solved numerically.

In the simplest scenario of one-dimensional propagation along the Cartesian z -coordinate, of a linearly x -polarized electric field, Faraday's law eq. (6.1) simplifies to a scalar update equation for the magnetic field component,

$$B_y|_z^{t+\frac{1}{2}} = B_y|_z^{t-\frac{1}{2}} - \Delta t \left(\frac{E_x|_{z+\frac{1}{2}}^t - E_x|_{z-\frac{1}{2}}^t}{\Delta z} \right) \quad (6.5)$$

where temporal and spatial derivatives are replaced by centered finite difference stencils. These numerical derivatives require, that both fields are evaluated on two temporally and spatially staggered grids. Here t and z behind the vertical bar denote unitless discretized temporal and spatial indices, separated by Δt and Δz , respectively. The corresponding electric field update follows analogously from Ampere's law eq. (6.2) after inserting the constitutive material equations (6.3)–(6.4),

$$E_x|_{z+\frac{1}{2}}^{t+1} = E_x|_{z+\frac{1}{2}}^t - \frac{1}{\varepsilon_0} \left[\frac{c_0^2 \Delta t}{\Delta z} \left(B_y|_{z+1}^{t+\frac{1}{2}} - B_y|_z^{t+\frac{1}{2}} \right) + \Delta t J_x^{t+\frac{1}{2}} + \left(P_x^{t+1} - P_x^t \right) \right]. \quad (6.6)$$

Expressions for the y -polarized electromagnetic field are calculated accordingly. The right-hand side indicates, that the medium response is included via the bound nonlinear polarization evaluated at the same time as the electric field, and via the nonlinear drift determined at the time of the magnetic field. Both quantities are evaluated at the spatial grid point of the electric field. To simplify the notation in the following, the time index on medium quantities is written without vertical bar, i.e. in the super-script of the current $\mathbf{J}^{t+\frac{1}{2}}$ and polarization \mathbf{P}^t vector. Starting point for the calculation of the free current density is the relative ionization degree ρ^t . Next, the full update cycle to iterate the time index is presented in an overview diagram, before update equations needed for the calculation of the nonlinear current and the nonlinear polarization from Lorentz oscillator model are introduced.

6.2. Self-consistent polarization, ionization and plasma response

The algorithm of the ionization radiation model advances all fields and medium quantities self consistently in iterative cycles. The overall structure of one temporal iteration, depicted in Fig 6.1 consists, according to the staggered \mathbf{E} and \mathbf{B} -fields, of updates at full and half-integer index, shown by the blue and red background, respectively. In principle, this iterative, cyclic algorithm can be started at any point. To ensure consistency of indices, we choose to formally start with given electric field

\mathbf{E}^t at time index t (upper right corner). All other quantities are given at time indices before either at $t - \frac{1}{2}$ or $t - 1$.

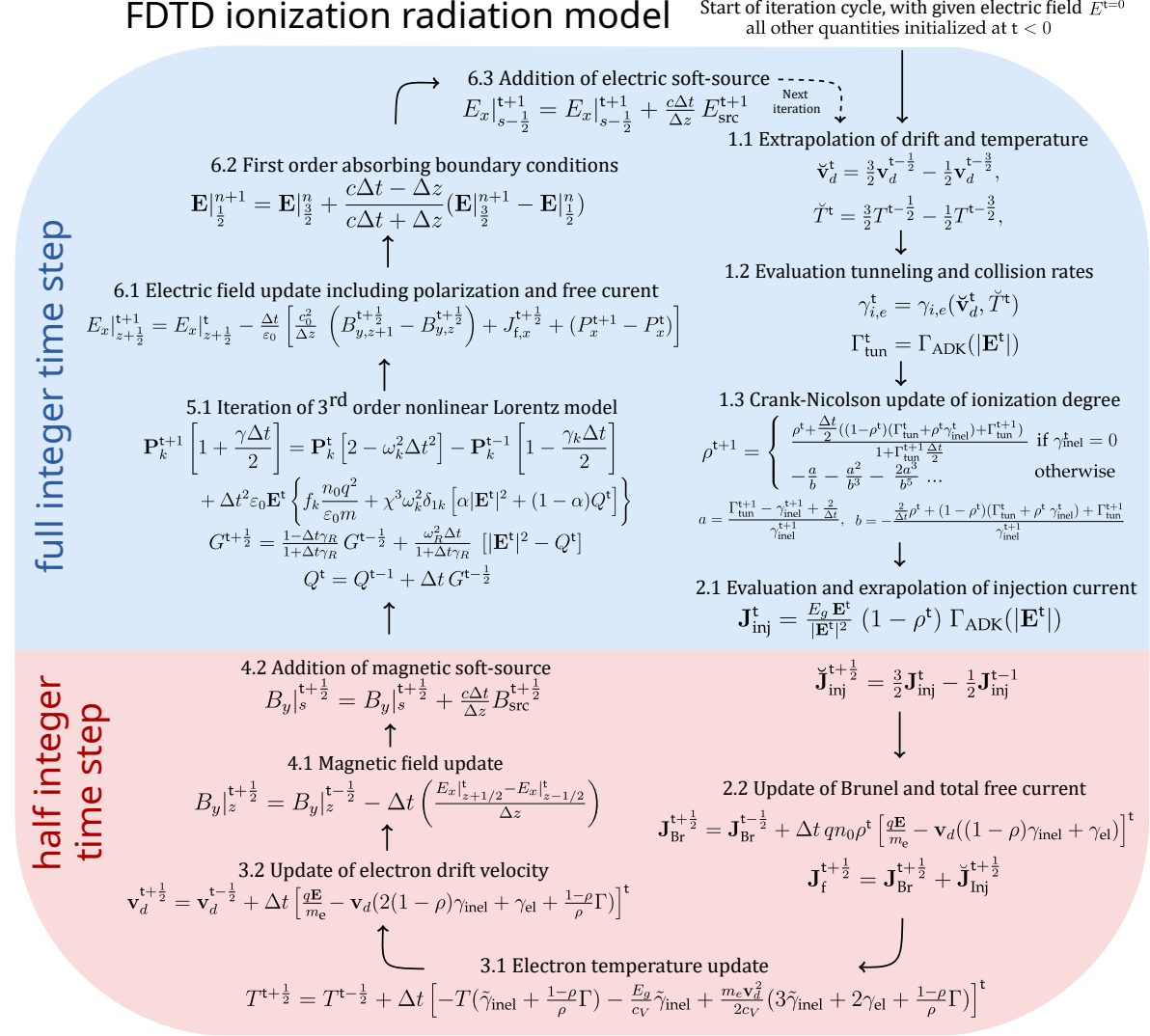


Figure 6.1.: Update equations of the FDTD ionization radiation model for a full time iteration. The equations are iterated clockwise, with grid updates at integer time index t shown on blue, and half-integer time index $t + \frac{1}{2}$ on red background. The time index of quantities in square brackets is indicated at the closing bracket. Linear extrapolated quantities are indicated by a half-circle accent.

First, to determine field-driven ionization, extrapolated values for electron drift and temperature are used to calculate collision rates, while the tunneling rate can be directly determined from the given field (step 1.1–1.2). These rates are used to update the ionization degree (step 1.3). Since this update is pivotal for the nonlinear response of interest, we will provide further details in the next section. Based on the ionization degree the injection and Brunel current are readily available (step 2.1–2.2). Afterwards, a more detailed discussion of the electron ensemble is provided to

derive update equations for temperature and drift velocity, seen at the lower end of the update cycle (step 3.1–3.2). Magnetic field updates conclude the calculation at the half-integer time index (step 4.1–4.2). At full-integer time index, the polarization of bound electrons is determined by a nonlinear Lorentz model (step 5.1), that is discussed in a separate section. Based on bound polarization and free current, the electric field is updated on the entire grid (step 6.1). Finally, boundary conditions and soft sources for the computational domain (step 6.2 and 6.3) that constitute the end of one cycle, are discussed.

6.2.1. Ionization degree

The relative ionization degree is driven by the ADK tunneling rate $\Gamma_{\text{tun}}(|\mathbf{E}|)$ [90] and the inelastic collision rate per electron γ_{inel} , where the currently available conduction band electron density is included by the prefactor ρ ,

$$\frac{\partial \rho}{\partial t} = (1 - \rho) [\Gamma_{\text{tun}}(|\mathbf{E}|) + \rho \gamma_{\text{inel}}(|\mathbf{v}_d|, T)]. \quad (6.7)$$

The saturation term $(1 - \rho)$ in front of the square bracket, accounts for valence band depletion. Since we are particularly interested in high-frequency contributions of the ionization degree, numerical time integration of this nonlinear differential equation is carried out using the Crank-Nicolson algorithm, that evaluates all quantities at full timestep t . This particularly stable solver is applicable because the root of the implicit equation can be analytically determined,

$$\rho^{t+1} = \begin{cases} \frac{\rho^t + \frac{\Delta t}{2} ((1 - \rho^t)(\Gamma_{\text{tun}}^t + \rho^t \gamma_{\text{inel}}^t) + \Gamma_{\text{tun}}^{t+1})}{1 + \Gamma_{\text{tun}}^{t+1} \frac{\Delta t}{2}} & \text{for: } \gamma_{\text{inel}}^{t+1} = 0, \\ -\frac{a}{b} - \frac{a^2}{b^3} - \frac{2a^3}{b^5} \dots & \text{for: } \gamma_{\text{inel}}^{t+1} > 0, \end{cases} \quad (6.8)$$

with quadratic coefficients

$$a = \frac{\Gamma_{\text{tun}}^{t+1} - \gamma_{\text{inel}}^{t+1} + \frac{2}{\Delta t}}{\gamma_{\text{inel}}^{t+1}}, \quad (6.9)$$

$$b = -\frac{\frac{2}{\Delta t} \rho^t + (1 - \rho^t)(\Gamma_{\text{tun}}^t + \rho^t \gamma_{\text{inel}}^t) + \Gamma_{\text{tun}}^{t+1}}{\gamma_{\text{inel}}^{t+1}}. \quad (6.10)$$

With this update equation for the ionization degree, the nonlinear current can be readily calculated.

6.2.2. Nonlinear currents

The different contributions of the nonlinear current, i.e. injection and Brunel currents are propagated independently to allow for separate analysis. With available field and

ionization degree, the injection current at the full time step,

$$\mathbf{J}_{\text{inj}}^t = \frac{E_g \mathbf{E}^t}{|\mathbf{E}^t|^2} (1 - \rho^t) \Gamma_{\text{ADK}}(|\mathbf{E}^t|), \quad (6.11)$$

follows from the earlier derived expression (2.14)–(2.15). To extrapolate to the next half time step, required by the E-field update eq. (6.6), the Adams-Bashforth linear extrapolation is used,

$$\check{\mathbf{J}}_{\text{inj}}^{t+1/2} = \frac{3}{2} \mathbf{J}_{\text{inj}}^t - \frac{1}{2} \mathbf{J}_{\text{inj}}^{t-1}. \quad (6.12)$$

The update of the combined Brunel and drift current,

$$\mathbf{J}_{\text{Br}}^{t+\frac{1}{2}} = \mathbf{J}_{\text{Br}}^{t-\frac{1}{2}} + qn_0\rho^t \left[\frac{q\mathbf{E}}{m_e} - \mathbf{v}_d((1-\rho)\gamma_i + \gamma_e) \right]^t, \quad (6.13)$$

follows from the finite difference discretization of eqs. (2.9)–(2.10). The time index at the closing square bracket denotes that all enclosed quantities are evaluated at time step t . Next, the calculation of required elastic and inelastic collision rates is discussed.

6.2.3. Temperature and drift-dependent elastic and inelastic collision rates

Collision rates are calculated with high spatial resolution, i.e. at every grid point of the electromagnetic field. To keep the numerical effort under control, the velocity-dependent single electron collision rates $\gamma_1(|\mathbf{v}|)$, (earlier discussed in section 4.3.1) are parameterized by the electron temperature and average drift. This is done by assuming a Maxwell-Boltzmann distribution in every time step,

$$F(\mathbf{v}; \mathbf{v}_d, T) = \sqrt{\left(\frac{m_e}{2\pi k_B T}\right)^3} e^{-\frac{m_e(\mathbf{v}-\mathbf{v}_d)^2}{2k_B T}}, \quad (6.14)$$

that is uniformly shifted by the average drift \mathbf{v}_d in velocity space. Drift and temperature dependent average collision rates are then given by,

$$\gamma(|\mathbf{v}_d|, T) = \int d^3\mathbf{v} \gamma_1(|\mathbf{v}|) F(\mathbf{v}; |\mathbf{v}_d|, T). \quad (6.15)$$

The costly numerical evaluation of the integral is carried out for elastic and inelastic collision rates prior to the simulation using spherical coordinates,

$$\gamma(|\mathbf{v}_d|, T) = 2\pi \int dv_T \int \sin\theta d\theta v_T^2 F(v_T, 0, T) \gamma_1\left(\sqrt{(|\mathbf{v}_d| + v_T \cos^2\theta)^2 + v_T \sin^2\theta}\right), \quad (6.16)$$

where a sufficiently large parameter interval is stored in a look-up table that is displayed in Fig. 6.2. This approach captures the smearing of threshold behavior of the

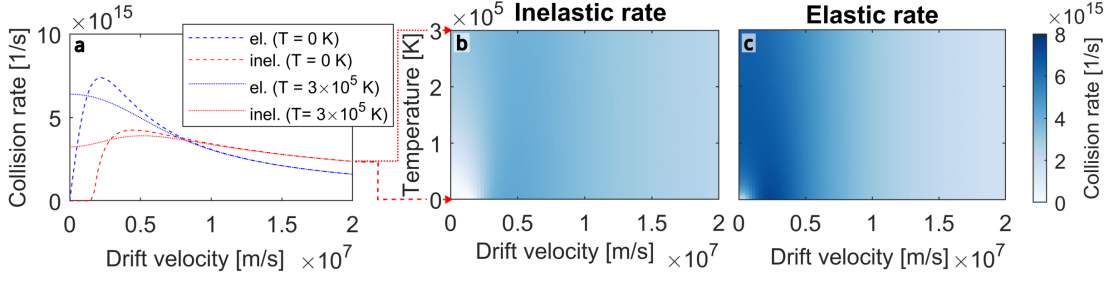


Figure 6.2.: Collision rates parameterized by drift velocity and temperature. Panel **a** shows line-outs along the Drift velocity axis of the inelastic γ_{inel} **b** and elastic γ_{el} **c** collision rate.

inelastic collision rate, as seen as follows. At low temperatures, the inelastic collision rate vanishes below the critical drift velocity (panel **a** red dashed line). The latter corresponds to the critical kinetic energy needed to surpass the band energy (intersection of red dashed line with horizontal axis). This threshold is quickly smeared out as function of temperature, as seen in panel **b**. At very high temperatures of $T > 3 \times 10^5 \text{ K}$, the impact ionization rate becomes fairly independent of the drift velocity (see dotted red line in **a**). The elastic collision rate in panel **c** shows a similar qualitative behavior.

6.2.4. Valance band depletion

To take the charge state of the medium into account, collision rates are multiplied with the ratio of available neutral atoms,

$$\tilde{\gamma}_{\text{inel}} = (1 - \rho) \gamma_{\text{inel}}^{(\text{neut})}(\mathbf{v}_d, T), \quad (6.17)$$

$$\tilde{\gamma}_{\text{el}} = (1 - \rho) \gamma_{\text{el}}^{(\text{neut})}(\mathbf{v}_d, T) + \rho \gamma_{\text{el}}^{(\text{ions})}(\mathbf{v}_d, T). \quad (6.18)$$

The tildes on the LHS, indicate the inclusion of depletion effects from here on. These are only relevant for inelastic collisions as we assume that elastic cross sections of atoms and ions are approximately the same $\gamma_{\text{el}} \approx \gamma_{\text{el}}^{(\text{neut})}(\mathbf{v}_d, T) \approx \gamma_{\text{el}}^{(\text{ions})}(\mathbf{v}_d, T)$.

6.2.5. Temperature and drift update

Energy and drift velocity updates are calculated by considering energy of continuum (and conduction band) electrons,

$$E_{\text{tot}} = \frac{1}{2} m \sum_i v_i^2 = \frac{1}{2} m N \langle v^2 \rangle, \quad (6.19)$$

that is decomposed into the kinetic energy of the center of mass (com) and thermal energy,

$$E_{\text{tot}} = E_{\text{kin}}^{\text{com}} + E_{\text{therm}}, \quad (6.20)$$

$$E_{\text{kin}}^{\text{com}} = \frac{1}{2}mN \langle \mathbf{v} \rangle^2, \quad (6.21)$$

$$E_{\text{therm}} = \frac{1}{2}mN \left(\langle \mathbf{v}^2 \rangle - \langle \mathbf{v} \rangle^2 \right) = C_V T. \quad (6.22)$$

Assuming that the velocity is normally distributed, the thermal energy becomes independent of the drift and remains fixed if the same external force is applied to all particles. Therefore, the thermal energy of the electron gas is linked to temperature by the heat capacity.

Depending on the relevant temperature range two models for the heat capacity are relevant. At high temperatures the non-degenerate (classical) electron gas is considered. According to the equipartition theorem of classical statistical mechanics, energy is equally distributed over all accessible degrees of freedom, f_{dof} . This average energy per degree of freedom determines the thermodynamic temperature,

$$\langle E_{\text{dof}} \rangle = \frac{\langle E_{\text{particle}} \rangle}{f_{\text{dof}}} = \frac{1}{2}k_B T. \quad (6.23)$$

The resulting heat capacity of an N electron gas,

$$C_V^{\text{cl.}} = \frac{f_{\text{dof}}}{2} N k_B, \quad (6.24)$$

overestimates the heat capacity of metals at room temperature by about 2 orders of magnitude, due to Pauli blocking of electrons below the Fermi energy [148] if all electrons are considered. For low temperatures and high density, i.e. for temperatures below the Fermi temperature $T < T_F = \frac{E_f}{k_B}$ with

$$E_F = \frac{\hbar^2}{2m_0} \left(\frac{3\pi^2 N}{V} \right)^{2/3} \quad (6.25)$$

where the mean particle distance is smaller than the thermal wavelength $d \leq \sqrt{\frac{2\pi\hbar^2}{mk_B T}}$, a quantum mechanical estimate for the heat capacity of the degenerate electron gas is known as,

$$C_V^{\text{deg.}} = c_V^{\text{deg.}} N = \frac{\pi^2}{2} N \frac{k_B^2 T}{E_f}. \quad (6.26)$$

Since only the free electron subsystem is considered in the following, the classical heat capacity, eq. (6.24), is used where N/V corresponds to the ionization degree ρ .

The time derivative of the temperature is given, according to eqs. (6.20)–(6.22), by derivatives of the total and center-of-mass kinetic energy caused by collisions and

ionization,

$$\frac{\partial T}{\partial t} = \frac{1}{c_V} \left(\frac{\partial \langle E \rangle}{\partial t} - \frac{\partial \langle E_{\text{kin}}^{\text{com}} \rangle}{\partial t} \right)_{\text{coll. ioni.}} = \frac{1}{c_V} \left(\frac{\partial \langle E \rangle}{\partial t} - m_e \langle \mathbf{v} \rangle \frac{\partial \langle \mathbf{v} \rangle}{\partial t} \right)_{\text{coll. ioni.}}. \quad (6.27)$$

The angled brackets indicate ensemble averages. Hence, all quantities on the RHS, including c_V , are understood as intrinsic quantities per particle. In the following, it is used that changes in $\langle E \rangle$ and $\langle \mathbf{v} \rangle$ during the infinitesimal time interval dt can be determined by examining partitions of the electron ensemble [149]. These partitions consist, as shown in table 6.1, of unperturbed electrons, existing electrons that undergo elastic as well as inelastic collisions and electrons promoted to the conduction band by electron impact and tunnel ionization.

electron partition a	avg. energy $\langle E_a \rangle(t + dt)$	avg. vel. $\langle \mathbf{v}_a \rangle(t + dt)$	$\frac{\partial \rho_a}{\partial t}$
unperturbed	$\langle E \rangle(t)$	$\langle \mathbf{v} \rangle(t)$	$-(\gamma_e + \tilde{\gamma}_i)\rho$
el. coll.	$\langle E \rangle(t)$	0	$\gamma_e \rho$
inel. coll.	$\langle E \rangle(t) - E_g$	0	$\tilde{\gamma}_i \rho$
born by coll.	0	0	$\tilde{\gamma}_i \rho$
born by tunneling	0	0	$(1 - \rho) \Gamma_t$

Table 6.1.: Changes in mean energy per electron and drift velocity due to collisions and ionization for each of the five electron partitions $a \in \{\text{unperturbed, elastically colliding impinging electrons, inelastically colliding impinging electrons, electrons born by collisions, electrons born by tunneling}\}$.

The last column of the table accounts for the abundance changes of each partition. The effective inelastic collision rate $\tilde{\gamma}_i = (1 - \rho)\gamma_i^{\text{neut}}$ is given by the rate of the neutral system, scaled by the available electron population in the highest valance band. Although only inelastic collisions and tunnel ionization contribute to the ionization degree $\rho = \rho_{\text{el}} + \rho_{\text{inel}}$, an abundance change per time interval can also be defined for elastic collisions $\frac{\partial \rho_{\text{el}}}{\partial t} = \gamma_e \rho$ such that a calculation of the ensemble derivatives, as discussed for the calculation of the injection current in eq. (2.6), becomes directly applicable. Thus, weighted energy average according to column 2 and 4 of table 6.1 yield the difference quotient for the desired time derivative,

$$\left. \frac{\partial \langle E \rangle}{\partial t} \right|_{\text{coll. ioni.}} = \lim_{\Delta t, \Delta \rho \rightarrow 0} \frac{\langle E \rangle(\rho - \Delta \rho_i - \Delta \rho_e) + \langle E \rangle \Delta \rho_e + (\langle E \rangle - E_g) \Delta \rho_i - \langle E \rangle}{\rho + \Delta \rho_i + \Delta \rho_t} \frac{1}{\Delta t} \quad (6.28)$$

$$= \lim_{\Delta t, \Delta \rho \rightarrow 0} -\frac{1}{\Delta t} \frac{E_g \Delta \rho_i + \langle E \rangle (\Delta \rho_i + \Delta \rho_t)}{\rho + \Delta \rho_i + \Delta \rho_t} \quad (6.29)$$

$$= -\frac{1}{\rho} \left(E_g \frac{\partial \rho_i}{\partial t} + \langle E \rangle \left(\frac{\partial \rho_i}{\partial t} + \frac{\partial \rho_t}{\partial t} \right) \right). \quad (6.30)$$

From eq. (6.30) it is found that the mean energy is reduced due to the ionization potential (given by the band-gap, first term) and also by dilution of the ensemble with electrons at rest (inner bracket, second term). The change in average drift velocity is calculated analogously from column 3 and 4,

$$\left. \frac{\partial \langle \mathbf{v} \rangle}{\partial t} \right|_{\text{coll. ioni.}} = \lim_{\Delta t, \Delta \rho \rightarrow 0} \frac{1}{\Delta t} \left(\frac{\langle \mathbf{v} \rangle (\rho - \Delta \rho_i - \Delta \rho_e)}{\rho + \Delta \rho_i + \Delta \rho_t} - \langle \mathbf{v} \rangle \right) \quad (6.31)$$

$$= \lim_{\Delta t, \Delta \rho \rightarrow 0} \frac{\langle \mathbf{v} \rangle}{\rho} \frac{-\Delta \rho_i - \Delta \rho_e - \Delta \rho_i - \Delta \rho_t}{\Delta t} \quad (6.32)$$

$$= -\frac{\langle \mathbf{v} \rangle}{\rho} \left(2 \frac{\partial \rho_i}{\partial t} + \frac{\partial \rho_e}{\partial t} + \frac{\partial \rho_t}{\partial t} \right). \quad (6.33)$$

The impact rate in the last term shows a factor of two, as both impinging and newly born electrons are assumed to have no drift contribution in the velocity after interaction. Inserting the resulting center-of-mass kinetic energy per particle,

$$\left. \frac{\partial \langle E_{\text{kin}}^{\text{com}} \rangle}{\partial t} \right|_{\text{coll. ioni.}} = m_e \langle \mathbf{v} \rangle \left. \frac{\partial \langle \mathbf{v} \rangle}{\partial t} \right|_{\text{coll. ioni.}} = -\frac{\langle E_{\text{kin}}^{\text{com}} \rangle}{\rho} \left(4 \frac{\partial \rho_i}{\partial t} + 2 \frac{\partial \rho_e}{\partial t} + 2 \frac{\partial \rho_t}{\partial t} \right) \quad (6.34)$$

and the average total energy eq. (6.30) into the expression for temperature derivative eq. (6.27) yields,

$$\frac{\partial T}{\partial t} = -\frac{T}{\rho} \left(\frac{\partial \rho_i}{\partial t} + \frac{\partial \rho_t}{\partial t} \right) - \frac{E_g}{c_V \rho} \frac{\partial \rho_i}{\partial t} + \frac{\langle E_{\text{kin}}^{\text{com}} \rangle}{c_V \rho} \left(3 \frac{\partial \rho_i}{\partial t} + 2 \frac{\partial \rho_e}{\partial t} + \frac{\partial \rho_t}{\partial t} \right) \quad (6.35)$$

$$= -T \left(\tilde{\gamma}_i + \frac{1-\rho}{\rho} \Gamma \right) - \frac{E_g}{c_V} \tilde{\gamma}_i + \frac{m_e \langle \mathbf{v} \rangle^2}{2c_V} (3\tilde{\gamma}_i + 2\gamma_e + \frac{1-\rho}{\rho} \Gamma). \quad (6.36)$$

From this expression, it is found that impact ionization and tunneling lead to cooling, proportional to existing temperature at equal weights (see first bracket of eq. (6.35)) whereas inverse bremsstrahlung heating from existing drift shows distinct prefactors for inelastic, elastic collisions, and tunneling (third term). The finite-difference temperature update, needed for the FDTD scheme, is determined by discretizing the LHS using half-integer time indices $t \pm \frac{1}{2}$ and evaluating the RHS of eq. (6.36) at integer time index t . This requires that T , γ_i , γ_e , and $\langle \mathbf{v} \rangle$ are extrapolated by half a time step.

$$T^{t+\frac{1}{2}} = T^{t-\frac{1}{2}} + \Delta t \left[-T \left(\tilde{\gamma}_{\text{inel}} + \frac{1-\rho}{\rho} \Gamma \right) - \frac{E_g}{c_V} \tilde{\gamma}_{\text{inel}} + \frac{m_e \langle \mathbf{v} \rangle^2}{2c_V} (3\tilde{\gamma}_{\text{inel}} + 2\gamma_{\text{el}} + \frac{1-\rho}{\rho} \Gamma) \right]^t \quad (6.37)$$

Employing the same discretization, the finite difference update for the average drift $\mathbf{v}_d = \langle \mathbf{v} \rangle$ is obtained from the electric field in addition to the ionization-induced loss of average drift, given by (6.33),

$$\mathbf{v}_d^{t+\frac{1}{2}} = \mathbf{v}_d^{t-\frac{1}{2}} + \Delta t \left[\frac{q\mathbf{E}}{m} - \mathbf{v}_d (2(1-\rho)\gamma_i + \gamma_e + \frac{1-\rho}{\rho} \Gamma) \right]^t. \quad (6.38)$$

Comparing the loss term of the average drift velocity, eq. (6.38) to that of the Brunel drift current eq. (6.13) two differences are seen. Firstly, it is noticed that the average

drift velocity includes a factor of 2 for inelastic collisions. This is due to the randomization of the velocity direction of the incoming electron and the newly born electron. The latter is born at rest and does initially not contribute to the current. Secondly, the same argument applies to electrons excited by tunneling, seen in the last term of eq. (6.38), that do also not contribute to the current.

6.2.6. Bound electron response: Dispersive nonlinear Lorentz model

The polarization response is calculated from a nonlinear Lorentz model [144]. In each cell, a set of damped and driven harmonic oscillators with oscillator strength f_k is solved,

$$\mathbf{P} = n_0 q \sum_k f_k \mathbf{x}_k \quad \text{with:} \quad \frac{\partial^2 \mathbf{x}_k}{\partial t^2} + \gamma_k \frac{\partial \mathbf{x}_k}{\partial t} + \omega_k^2 \mathbf{x}_k = \frac{q}{m} \mathbf{E}(t), \quad (6.39)$$

where damping and resonance parameters given in table 6.2 are used to model the linear response of SiO₂ and gold. In the case of the dielectric, the Lorentz model

SiO ₂			Au		
f_k	$\hbar\omega_k$ [eV]	γ_k [s]	f_k	$\hbar\omega_k$ [eV]	γ_k [1/fs]
7.54	18.1	0	2.04	0	0.08
1.53	10.7	0	0.06	0.41	0.37
5×10^{-4}	0.12	0	0.03	0.83	0.52
			0.19	2.96	1.32
			1.62	4.30	3.79
			11.80	13.32	3.37

Table 6.2.: Oscillator strength, resonance energy, and effective collision rate of the Lorentz-oscillator model, eq. (6.39), for fused silica (SiO₂) [144] and gold (Au) [150].

accounts exclusively for the bound electron response, since we have already incorporated the plasma contribution with a temperature and drift depended model in the previous sects. 6.2.1–6.2.5. For the metal coating, here gold, the plasma contribution is included via the first oscillator with vanishing resonance frequency (top row of right table), which is therefore sometimes denoted as Drude-Lorentz model, typically used for the response of several metals [150] or even for the plasma and self-trapped excitonic (STE) response in SiO₂ [128]. Identifying the polarization in the equation of motion eq. (6.39),

$$\frac{\partial^2 \mathbf{P}_k}{\partial t^2} + \gamma_k \frac{\partial \mathbf{P}_k}{\partial t} + \omega_k^2 \mathbf{P}_k = f_k \frac{n_0 q^2}{\varepsilon_0 m} \varepsilon_0 \mathbf{E}(t), \quad (6.40)$$

and employing finite differences for the first and second time derivative according to the full integer index of the driving field \mathbf{E}^t , yields for the linear part of the polariza-

tion,

$$\mathbf{P}_k^{t+1} \left(1 + \frac{\gamma_k \Delta t}{2} \right) = \mathbf{P}_k^t [2 - \omega_k^2 \Delta t^2] - \mathbf{P}_k^{t-1} \left[1 - \frac{\gamma_k \Delta t}{2} \right] + f_k \frac{n_0 q^2 \Delta t^2}{m} \mathbf{E}^t. \quad (6.41)$$

For the nonlinear bound polarization of SiO₂, an instantaneous third-order contribution and a delayed component due to stimulated molecular Raman scattering [74],

$$\mathbf{P}^{(3)}(t) = \varepsilon_0 \chi^{(3)} \alpha |\mathbf{E}|^2 \mathbf{E} + \varepsilon_0 \chi^{(3)} (1 - \alpha) Q \mathbf{E}, \quad (6.42)$$

is added with weight $\alpha = 0.7$ [144] to the first Lorentz-oscillator. The delayed vibrational coordinate Q can be also described by a harmonic oscillator,

$$\frac{\partial^2 Q}{\partial t^2} + 2\gamma_R \frac{\partial Q}{\partial t} + \omega_R^2 Q = \omega_R^2 |\mathbf{E}|^2 \quad (6.43)$$

with Raman resonance $\omega_R = 57.7$ meV, that is small compared to the optical transitions, and long-lived Raman damping constant $\gamma_R = 31.25$ ps⁻¹. Eq. (6.43) is written as a set of two first-order differential equations, using the substitution $G = dQ/dt$, and is discretized,

$$G^{t+\frac{1}{2}} = \frac{1 - \gamma_R \Delta t}{1 + \gamma_R \Delta t} G^{t-\frac{1}{2}} + \frac{\omega_R^2 \Delta t}{1 + \gamma_R \Delta t} (|\mathbf{E}^t|^2 - Q^t), \quad (6.44)$$

$$Q^{t+1} = Q^t + \Delta t G^{t+\frac{1}{2}}. \quad (6.45)$$

These equations conclude the update of the dispersive nonlinear Lorentz model summarized in Fig. 6.1.

Next, the energy that is reversibly and irreversibly transferred to the polarization degree is briefly discussed, that will be used as benchmark quantity in the results section of this chapter. The Lorentz oscillators store kinetic and potential energy density according to

$$u_{\text{kin}} = \frac{mn_0}{2} \sum_k f_k \left| \frac{\partial \mathbf{x}_k}{\partial t} \right|^2 = \frac{m}{2n_0 q^2} \sum_k \frac{1}{f_k} \left| \frac{\partial \mathbf{P}_k}{\partial t} \right|^2, \quad (6.46)$$

$$u_{\text{pot}} = \frac{mn_0}{2} \sum_k f_k |\omega_k \mathbf{x}_k|^2 = \frac{m}{2n_0 q^2} \sum_k \frac{|\omega_k \mathbf{P}_k|^2}{f_k}. \quad (6.47)$$

Most of the potential energy of the oscillators is usually included in the field energy density given by $u_{\text{EM}} = \frac{1}{2}[\mathbf{E}\mathbf{D} + \mathbf{B}\mathbf{H}]$. A much smaller contribution, $\tilde{u}_{\text{pot}} = u_{\text{pot}} - \frac{1}{2}\mathbf{E}\mathbf{P}$ and the kinetic part u_{kin} are not included in u_{EM} . Both \tilde{u}_{pot} and u_{kin} have the same amplitude.

The irreversible energy transfer, due to finite damping of the electronic response in gold is obtained by integrating the loss power $P_{\text{loss}} = \mathbf{F}_{\text{fr}} \frac{\partial \mathbf{x}}{\partial t}$ over time. Inserting the friction force from eq. (6.39) and multiplying with the number density yields the

dissipated energy density,

$$u_{\text{loss}} = \int dt mn_0 \sum_k f_k \gamma_k \left| \frac{\partial \mathbf{x}_k}{\partial t} \right|^2 = \int dt \frac{m}{n_0 q^2} \sum_k \frac{\gamma_k}{f_k} \left| \frac{\partial \mathbf{P}_k}{\partial t} \right|^2. \quad (6.48)$$

In the final section of the model description, boundaries and sources for the electromagnetic grid are discussed.

6.2.7. Unidirectional source – Total-field scattered-field boundary

A soft source for the electric and magnetic field is used to couple a right propagating laser pulse into the simulation grid, also known as total-field scattered-field (TFSF) boundary [82]. With this approach, the energy that is coupled onto the grid equals the energy of the source pulse, as long as there is no other right traveling wave present at the location of the source. This condition is ensured by combining the soft source together with an absorbing boundary condition. At the half integer position index $z_{\text{src}} - \frac{1}{2}$, the source wave of the electric field, defined by $E_{\text{src}}(t)$, is added to the already updated field,

$$E'_x|_{z_{\text{src}} - \frac{1}{2}}^{t+1} = E_x|_{z_{\text{src}} - \frac{1}{2}}^{t+1} + \frac{c\Delta t}{\Delta z} E_{\text{src}}((t+1)\Delta t). \quad (6.49)$$

A $\frac{\Delta z}{2}$ -step to the right, the magnetic field is updated at z_{src} ,

$$B'_y|_{z_{\text{src}}}^{t+\frac{1}{2}} = B_y|_{z_{\text{src}}}^{t+\frac{1}{2}} + \frac{\Delta t}{\Delta z} E_{\text{src}}((t+1)\Delta t + \frac{\Delta t}{4} + \frac{\Delta z}{4c}). \quad (6.50)$$

The time argument of the magnetic source is shifted by two terms that account for the spatio-temporal staggering of magnetic and electric grid.

6.2.8. Absorbing boundary condition

For one-dimensional grids, so-called perfect absorbing boundary conditions,

$$\mathbf{E}|_{\frac{1}{2}}^{t+1} = \mathbf{E}|_{\frac{3}{2}}^{t-N+1}, \quad (6.51)$$

are usually employed, that require to adjust the time step $\Delta t = \frac{\Delta z}{Nc}$ such that N temporal steps are needed to propagate the wave one spatial step. In this study, it was more practical to adjust time and spatial step independently. Hence, both ends of the numerical grid are terminated by first-order boundary conditions [82],

$$\mathbf{E}|_{\frac{1}{2}}^{t+1} = \mathbf{E}|_{\frac{3}{2}}^t + \frac{c\Delta t - \Delta z}{c\Delta t + \Delta z} (\mathbf{E}|_{\frac{3}{2}}^{t+1} - \mathbf{E}|_{\frac{1}{2}}^t). \quad (6.52)$$

Other suitable choices are Mur-boundary [151] or perfectly matched layers [152, 153]. In the remainder of this chapter, results exhibiting the distribution of energy and the plasma dynamics are presented that allow to address the effect of the spatially confined plasma build up on nonlinear optical properties.

6.3. Energy deposition via ionization

To assess the quality of the discussed model and to reveal the relevant time scales of the excitation dynamics in the irradiated medium, the energy balance of the simulation is considered first. A thin SiO₂ target, irradiated by a close-to-threshold intense laser pulse (see Fig. 6.3) is simulated for three different pulse lengths (parameters see caption). The rear side of the target is gold coated, to enhance the effect of reflected fields, which is discussed in detail in the next section. Panel a–c shows a benchmark for the energy conservation. The temporally integrated intensity emitted by the laser source is shown by the envelope (thick black line). Energy coupled from the electromagnetic field to different electronic degrees of freedom and eventually to the surrounding boundary conditions is represented by colored areas. The fact, that all areas together match the outer envelope, confirms energy conservation and numerical convergence of the simulation method. The time step of $\Delta t = 10^{-17}$ s and $\Delta z = 10^{-9}$ m are chosen to fulfill the Courant-criterion¹ and simultaneously to resolve high temporal oscillations in the field due to high harmonics beyond order $h > 20$ as well as high spatial oscillations of the plasma density. Next, the displayed time evolution of the energy balance is further analyzed to start the discussion of the plasma formation.

For the shortest driving pulse (20 fs), most of the pulse energy is transmitted through the front interface and coupled to the electromagnetic field in the medium (blue area). Upon rear side reflection ($t \approx 50$ fs) a considerable fraction of pulse energy ($> 10\%$) is absorbed by the tunneling injection current (green area). Field-induced tunneling is quickly followed by strong impact ionization, seen by fast increase of the pink area. Less than a quarter of the total energy remains in the thermal motion of electrons (red). Approximately the same amount of energy leaves the sample through the front interface (khaki). Comparison with the 80 fs pulse shows firstly the reduced relative contribution of tunneling injection to absorption. Secondly, impact ionization already sets in once the pulse center reaches the front interface ($t = 0$). This trend continues for the largest considered pulse duration of 140 fs, where a long-lasting

¹Stability of the numerical grid is ensured if the Courant-Friedrichs-Lewy number, that describes the propagation length of the field per time step relative to the maximum spacing of grid points, is less than unity,

$$C = \frac{c \Delta t}{\sqrt{\Delta x^2 + \Delta y^2 + \Delta z^2}} < 1. \quad (6.53)$$

For simulations in less than 3 dimensions, the sum is restricted to present grid spacings.

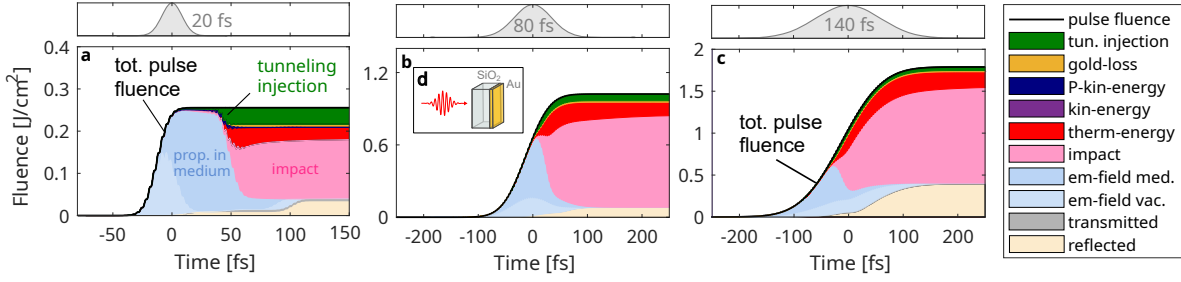


Figure 6.3.: Energy balance of tunneling-induced plasma formation in a thin $10\ \mu\text{m}$ SiO_2 slab with a $20\ \text{nm}$ thin gold coating for pump pulse durations of $20\ \text{fs}$ **a**, $80\ \text{fs}$ **b** and $140\ \text{fs}$ **c** at peak intensity of $I = 12\ \text{TW}/\text{cm}^2$. The normalized intensity envelope is shown on top of each panel, that corresponds to the pulse fluence (thick black envelope) in **a–c**. One-dimensional simulation setup sketched in **d**.

impact ionization avalanche (pink) is triggered once the rising edge of the pulse enters the medium ($t < 0$). From this result we conclude, that the injection current is particularly relevant for the energy balance of short pulses, while energy absorption of longer pulses is stronger affected by impact ionization. Finally, a negligible relative contribution of energy transfer to the quiver motion of electrons (purple and dark blue) and heating of the reflective coating (gold) is found for all three scenarios. Next, to understand the feedback of the emerging plasma and to localize the interaction, the spatio-temporal structure of tunneling and impact ionization is examined.

6.3.1. Impact of standing waves on the spatio-temporal plasma build-up

In the previous sections, the full one-dimensional numerical model for solving self-consistently the dispersive field propagation and the local plasma formation and plasma response has been described. As a first application of this model, the role of transient standing wave fields for the plasma generation will be investigated. To this end the ionization of an extended SiO_2 slab ($d_{\text{SiO}_2} \gg \lambda$) is studied. To emphasize reflection-induced standing wave effects, the target is back-coated with a thin, highly reflective gold film ($d_{\text{Au}} \ll \lambda$). As before, we consider a field intensity that is near the damage threshold to drive substantial ionization.

Figure 6.4 compares the detailed spatio-temporal evolution of the propagating laser field and the sub-cycle ionization dynamics along the optical axis for three representative pulse durations. The displayed examples have been selected to highlight the relevant dynamical stages of the ionization process and different regimes for structured plasma formation.

The top row illustrates the case for a short pulse (**a**). In this case, the pulse is short enough to propagate inside the target for a certain distance without any interference with reflected parts of the pulse (see panel **b**). In this first phase, continuous traces in

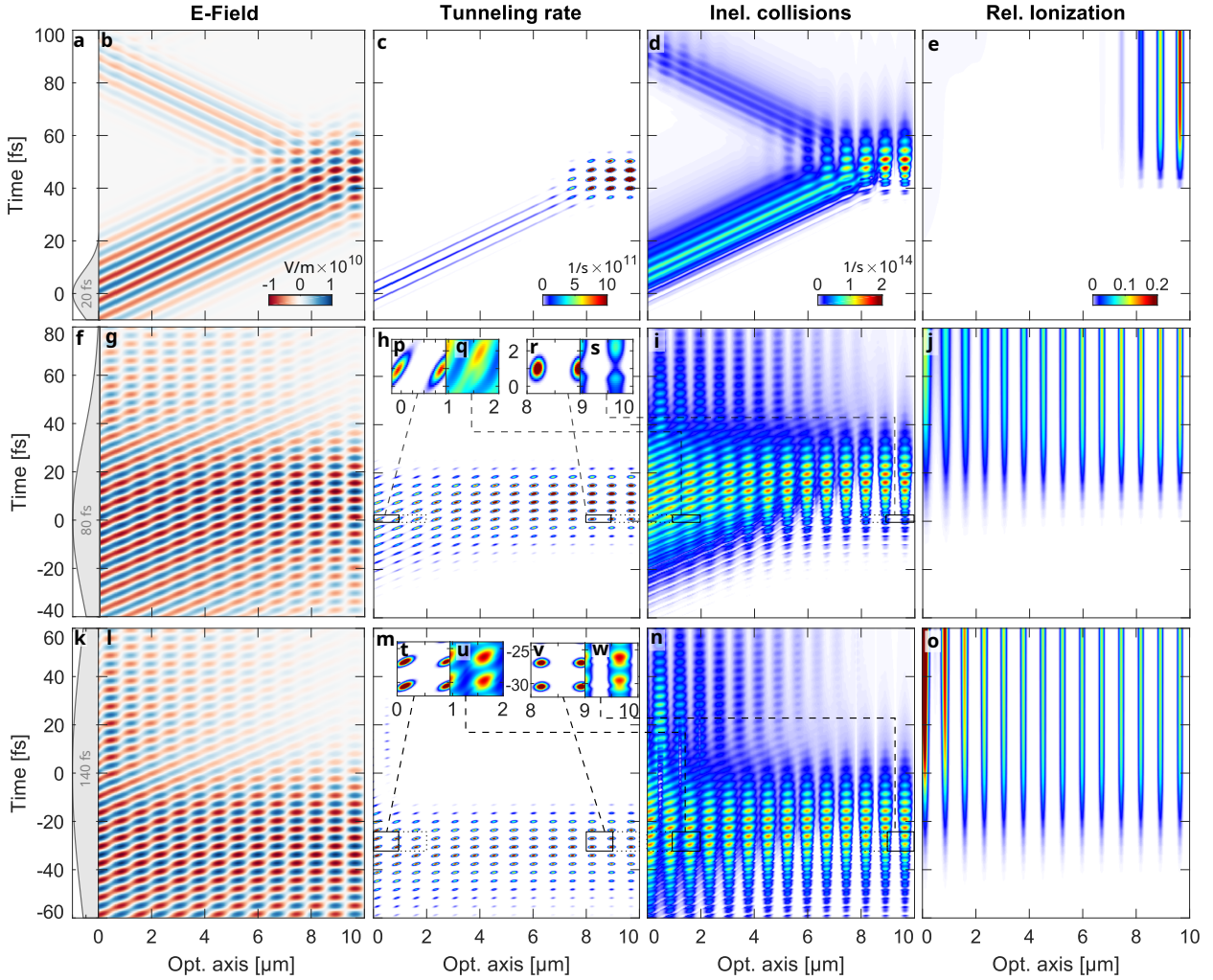


Figure 6.4.: Tunneling induced plasma formation in a 10 μm SiO_2 slab with a 20 nm thin gold coating. From left to right it is shown the normalized incident laser intensity, total electric field, tunneling rate, inelastic collision rate, and total relative ionization for pulse widths of 20 fs (a–e), 80 fs (f–j) and 140 fs (k–o), at $12 \text{ TW}/\text{cm}^2$. Insets indicate temporal shifts of the tunneling rate **p**, **r** wrt. inelastic collision rate **q**, **s** in the magnified region marked in **h** and **i** for 80 fs. Similarly, the second set of insets **t–w** applies to **m** and **n**.

the tunnel ionization probability (panel c) are predicted and remain sharply locked to the most intense half cycles of the pulse (up to $t \approx 35$ fs). The resulting free carriers generated in the respective region of the target undergo both, ponderomotive motion and collisional heating, resulting in a mixture of cold and hot avalanching. The presence of cold avalanching is signified by the sub-cycle modulation of the impact ionization rate (panel d) while a cycle-averaged baseline is attributed to the thermal (hot) avalanching. This aspect will be discussed in more detail later.

The next important dynamical stage begins with the arrival of the leading pulse edge at the coated back surface around $t = 40$ fs. The interference with the reflected pulse induces a strongly enhanced and spatially structured standing wave field (c.f.

panel **b**), that is predicted to leave a clear spatial and sub-cycle temporal fingerprint in the tunnel ionization rate (**c**). The resulting spatial modulation of free carriers remains visible in the subsequent collisional ionization dynamics (**d**). After the reflection of the pulse, a much weaker ionization trace (now again with a continuous shape) is generated by the backpropagating pulse (see, e.g. in panel **d**) that, however, is insignificant for the total final ionization level for this short pulse case.

As a result of the interaction, the total ionization is dominated by the regular lattice of ionization sheets near the back side of the target (**e**). Due to the highly non-linear tunnel ionization, the spatial hot spot structure of the standing wave field is transferred with high contrast to the spatial population profile of the free carriers (**e**). The short pulse duration for this example is associated with a standing wave field that induces three pronounced ionization layers at the back, with the highest plasma density in the layer just below the reflecting interface.

With increasing pulse duration (see middle row), the extension of the ionization grating grows (see panel **j**) and eventually reaches up to the front surface for the considered model scenario. For the selected pulse parameters, the reflection of the leading pulse edge results in an extended standing wave field that persists in the time window $t = -20..20$ fs (panel **g**). Note that only in the rear part the field is dominated by the standing wave component, which is associated with nearly equal amplitude of the incoming and reflected fields. In the remainder of the target, the incoming field remains substantially stronger, as seen by the tilt of the spatio-temporal hot spots (panel **g** and **h**). Nevertheless, the hot spot character of the field is pronounced enough to generate a high-contrast plasma sheet lattice in the whole target with comparable population in the plasma density peaks (panels **i** and **j**).

The time evolution of the impact ionization displays two interesting features. First, in the front region of the target, a superposition of the continuous and strongly modulated ionization is seen. Second, in the falling edge of the pulse, a spatial shift of the layer structure within the ionization rate is found (c.f. $t > 40$ fs in panel **i**). This shift in the impact ionization rate can be attributed again to standing wave effects at the emerging plasma sheets. When reaching sufficient plasma density, the plasma layers act as mirrors that induce a reflection. Each reflection produces a new standing wave field with a field node at the conductive plasma sheets and a field hot spot at a distance of a quarter wavelength. Hence, the transiently generated plasma mirror grating results in a shift of the hot spots to location where the primary standing wave field showed nodes. This hot spot migration explains the shifted feature observed in the ionization rate profile, but so far does not fundamentally change or destroy the plasma layer structure (panel **j**). As a consequence, however, it is seen that the emergence of the plasma mirror shields the rear side of the sample such that further ionization is mainly found in the front region once plasma reflection becomes significant (panel **j**). Both features, i.e. the tilted structures in the ionization rate at the front as well as the hot spot migration due to transient plasma mirror formation are also found at further increased pulse duration (lower row). Here, the ionization in the front region becomes so strong, that a plasma mirror emerges already near the pulse

peak ($t \approx 0$). The strong plasma mirror grating leads to even more pronounced migrated hot spots that appear as well in the ionization rate (panel **l** and **n**). Eventually, the first few plasma mirror sheets limit the penetration of the pulse into the target substantially such that a plasma grating with highest ionization degree near the front surface is produced for the long pulse case (panel **o**).

So far, the analysis of the three representative scenarios has shown that the duration of the driving pulse plays an important role in the ionization dynamics and the standing-wave induced plasma profile. While short and moderately long pulses generate plasma layers at the back and in the interior of the target, longer pulses trigger the formation of a plasma mirror grating with increasingly localized ionization near the front interface and significantly increased reflectivity.

As the next step, the detailed evolution of ionization and its relation to standing wave features is analyzed in selected spatial regions. As was already pointed out above, the standing wave field in the rear region displays an almost spatially fixed hot spot profile that oscillates only in time (Fig 6.4 **b**, **g**, **l**). In contrast, the standing wave features in the front region show a remaining spatial movement of the hot spots that was attributed to the stronger forward propagating wave component in this area (panels **g**, **l**). The detailed impact of these different hot spot profiles on ionization is illustrated in the zoomed plots of the tunnel and impact ionization rates (insets **t** - **w** in Fig. 6.4). In general, the more roundish (rear) and tilted (front) hot spots are directly translated to the tunnel ionization rate, reflecting its direct dependence on the instantaneous electric field (**p**, **r** and **t**, **v**). The impact ionization rate also displays the respective hot spot features, but with reduced contrast and a systematically delayed response (panels **q**, **s**, **u**, **w**) when compared to the features in the tunnel ionization rate. This is attributed to the required buildup time of kinetic and thermal energy after ionization prior to new collisional ionization events. The delay in the observed features in the impact ionization rate is somewhat below a quarter field period. The latter would be the expected delay for the peak kinetic energy for fully ballistic (ponderomotive) motion. The observed reduced delay is attributed to a collision-induced phase shift (see also discussion in section 4.1).

The detailed temporal structure and sub-cycle modulation of the impact ionization rate for short and long pulses deserves additional attention. Corresponding time traces of the tunneling and impact ionization rates are displayed in Fig. 6.5 for selected spatial regions as marked in panels **a** and **d**, by red and cyan rectangles. Compared to the sharply modulated tunneling rate, that is quenched twice per optical cycle (panel **c**), the sub-cycle modulation of the inelastic collision rate is less pronounced and fades over time (panel **b**). In addition, a smooth, cycle-independent contribution emerges in the impact ionization (violet dashed line). Qualitatively, these two contributions are attributed to the cold and hot avalanching. While the former is confined to the high intensity region of the pulse, the latter displays a longer decay phase that extends over the trailing edge of the pulse. This cycle-independent contribution of the rate is attributed to the high temperature part of the electron distribution. Comparing the modulation amplitude (gray arrow) to the thermal contribution (violet arrow)

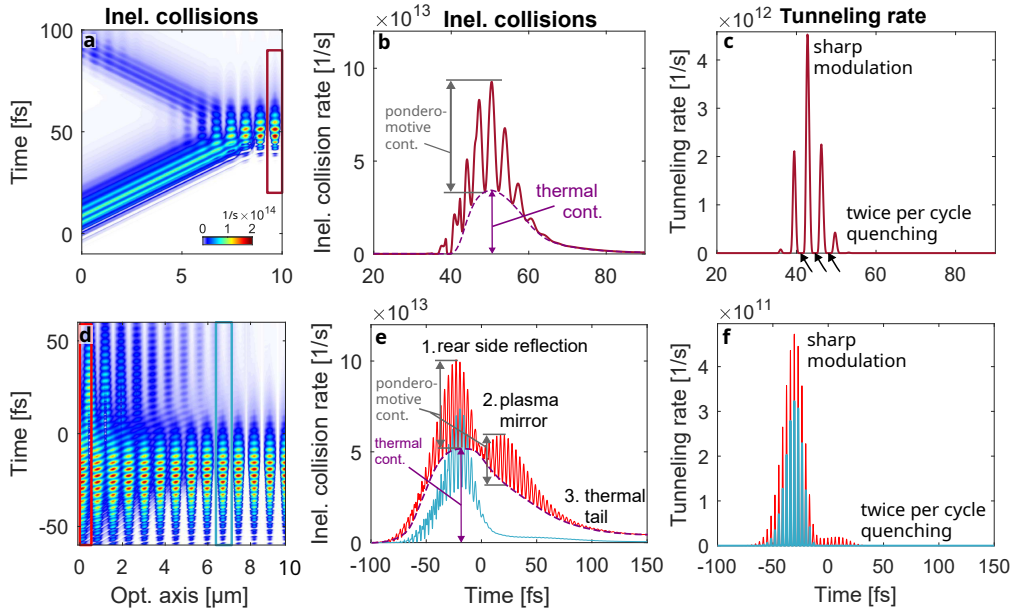


Figure 6.5.: Temporal line-outs of inelastic collision rate, marked in **a** and **d**, are shown in **b** and **e**, respectively. Contributions to cold avalanching, amplified by rear side reflection and plasma mirror (gray arrows), and hot avalanching (violet) from thermal contribution are indicated. Tunneling rates from the same region are shown in **c** and **f** for comparison.

allows to estimate the rate ratio of both impact ionization processes. In panel **b**, the strong thermal contribution grows quickly in the weakly modulated rising edge and exhibits a much longer decay time in the end.

Line-outs for the long-pulse scenario seen in panel **d** and **e** confirm this general trend. Furthermore, the inelastic rate shows in this case at the front (red line in panel **e**) three distinct features. First, the highest peak in the ionization rate is caused by the standing wave from rear side reflection. The second peak, forming a shoulder, is clearly attributed to the standing wave, induced by the plasma mirror. This signature is missing when inspecting the inelastic rate a few micrometer down the optical axis (cyan line in panel **d** and **e**). However, the third signature, the long-lasting, weakly modulated thermal tail is observable at both positions (cyan and red line, panel **e**).

The relatively strong thermal contribution in all cases can be partially attributed to the simplicity of the model. Here an equilibrated Maxwell-Boltzmann distribution was assumed in each time step, only parameterized by temperature and drift velocity. It is expected that a fully resolved velocity distribution shows a faster depopulation of high velocity states. Hence, the thermal contribution, predicted by this computationally much cheaper model, can be understood as an upper estimate.

In conclusion, the analysis of the plasma formation revealed four distinct dynamical phases, consisting of (i) free propagation, (ii) rear-side standing wave formation, (iii) emergence of a reflective plasma grating, and (iv) the generation of a secondary

standing wave resulting in front side-ionization and hot-spot migration. The relative contribution of these phases to the plasma dynamics was found to depend on the pulse width. While the plasma formation was initiated by tunnel ionization, the impact ionization contributed most electrons in all cases. The time dependence of the inelastic ionization rate revealed that hot avalanching is accompanied by ponderomotive (cold) contributions of comparable magnitude in the falling edge of pure forward propagation and in the stationary standing waves. In the following section, the impact of discussed processes on experimentally accessible observables such as absorption, reflection, and transmission is investigated.

6.4. Effect of plasma formation on reflection, transmission, and absorption

Time-resolved plasma diagnostics is typically realized in experiments by measuring the pump-probe-delay dependence of reflection R , transmission T , and absorption A [87, 128, 154] where weak probe intensity ensures that the plasma formation depends exclusively on the reproducible pump pulse. In the following, simulated delay scans for $I = 12 \text{ TW/cm}^2$ on a pristine SiO_2 target are used to relate characteristic signatures in the delay dependence of the three observables to the temporal features of tunneling and impact ionization rate. Starting the discussion for fixed pulse parameters (see section 2.1), the strong correlations: (i) transmission—tunneling, (ii) absorption—bulk-impact ionization, and (iii) reflection—front-surface-ionization are discussed. In a second step, the effect of beam profiles and focal averaging is examined.

6.4.1. Delay dependence

In Fig. 6.6 the probe transmission is found to signal well the onset of the plasma formation as seen by comparison of the solid blue line (panel a) to the rising flank of the bulk averaged tunnel ionization rate, Γ_{bulk} (thick green line in panel b). The inflection point of T_{probe} is found at the maximum Γ_{bulk} . In the lower panel, both bulk-averaged tunneling and impact rate (thick red) are shown on normalized scale together with front surface rates (darker thin lines). Only ionization at the front surface ($0 < z < 0.5 \mu\text{m}$) exhibits extended dynamics in the falling edge of the driving pulse, in accordance with the discussion in the previous section. The fact that Γ_{front} is peaked at the falling flank is a result of the plasma reflection that enhances the field. Around the same time, at $t \approx 40 \text{ fs}$, the averaged bulk inelastic collision rate γ_{bulk} shows a maximum, that can be correlated with the peak in the absorption (dotted blue). The interpretation that the absorption peak signals the maximum inelastic collisions is in particular underpinned by the energy balance (Fig. 6.3), confirming that most energy is absorbed by impact ionization.

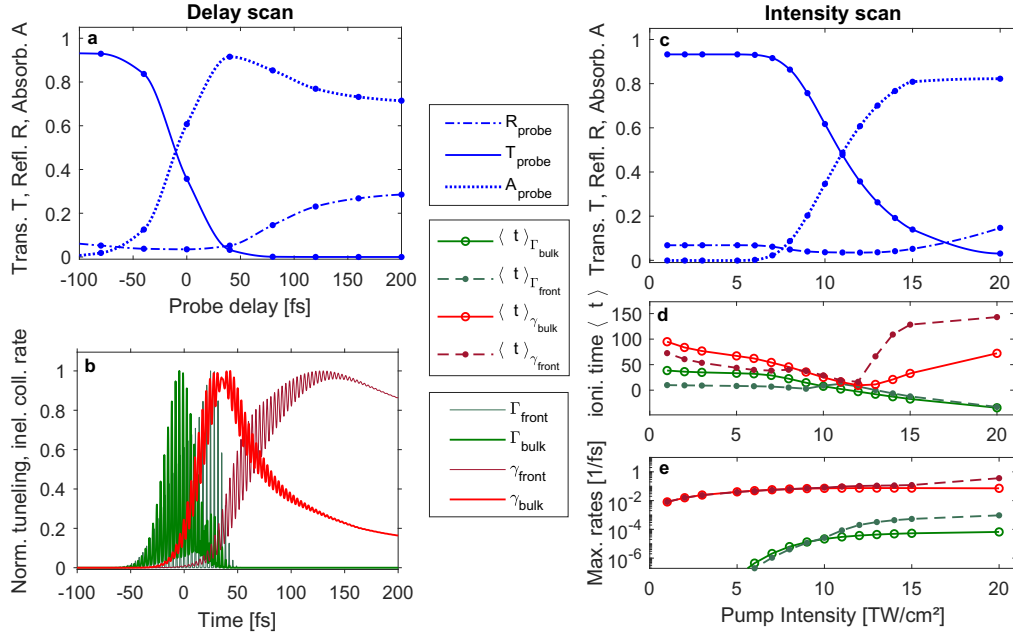


Figure 6.6.: Transmittance T , reflectance R , and absorption A of the probe, as function of probe delay **a** and pump intensity **c** are shown next to time series of normalized ionization rates at the front and in the bulk (see legend) **b**. From ionization time traces, mean ionization times, and maximum ionization rates are extracted and displayed in **d**, **e**, respectively. Beam parameters from section 2.1 are used for an uncoated 10 μm SiO_2 sample, panel **a** and **b** recorded at $I = 12 \text{ TW}/\text{cm}^2$.

The third observable, the inflection point of the probe reflection (dot-dashed in panel **a**), is further delayed by about ≈ 70 fs wrt. the drop in transmittance and is only seen once the front side ionization is further increased by inelastic collisions (thin dark red). Over a period of more than 150 fs the plasma density is still increased even though the pump intensity dropped by more than one half. The impact ionization avalanche, characterized by weaker temporal modulation, continues to run for a longer time, in particular at the front surface. The resulting late increase in front side reflectivity also explains the drop in absorption seen for $\tau \approx 100$ fs (blue dotted). From Fig. 6.6 **a** and **b** the interpretation of the observables in terms of ionization rates has been motivated for one parameter set. In the following, it is shown that this correspondence holds also at other pump intensities.

6.4.2. Intensity dependence

The first central finding is, that changing the intensity leads mainly to temporal shifts in the peak position of the rates. These shifts can explain that the intensity dependence of observables R , T and A in panel **c** is similar to the delay dependence examined before in panel **a**. To discuss how intensity affects the dynamics, the first

temporal moments of tunneling and impact ionization rates,

$$\langle t \rangle_{\Gamma} = \frac{\int dz \int t \Gamma(z, t) dt}{\int dz \int dt \Gamma(z, t)}, \quad (6.54)$$

are examined in panel **d**. Increasing the intensity, shifts bulk tunneling monotonously to earlier times. Depending on intensity this has two different reasons. At high intensities, for $I \geq I_{\text{crit}} = 12 \text{ TW/cm}^2$ this is caused by quenching, as seen by peak positions on rising flank indicated i.e. $\langle t \rangle_{\Gamma_{\text{bulk}}} < 0$ in panel **d**. For $I < I_{\text{crit}}$, on the other hand, no quenching is observed. Here the negative gradient $\frac{\partial \langle t \rangle_{\Gamma_{\text{bulk}}}}{\partial I}$ is attributed to the longer time that is required to form the spatially smaller standing wave at the rear interface. This finding for lower intensity interval is consistent with instantaneous tunneling at the surface, seen as constant peak time at the maximum of the impinging driving pulse (see green dashed line, panel **d**). In both intensity intervals also impact ionization shows distinct behavior.

At low intensities impact ionization shifts together with the tunneling rate. The delay is decreased as tunneling supplies a higher electron density for cold avalanching, which quickly decays with the trailing edge of the laser pulse. A swift change towards much more extended hot-avalanching is seen, beyond the critical intensity $I > I_{\text{crit}}$. In particular, the front surface impact ionization extends to later times as more energy is supplied by the driving pulse.

In conclusion, the detailed analysis shows at early time and low-intensity similar behavior in all three observable due to the dilute plasma. This correspondence remains as the intensity growth leads to a shift in ionization to earlier times, and simultaneous increase in maximum rates. Finally, the late increase of reflectivity signals for the delay- and the intensity scan a continued growth of front side ionization. This exemplary analysis shows, how the 1D simulation is used to relate experimentally accessible fluences from delay and intensity scans to the ionization dynamics. These calculated results correspond to ideal experimental conditions where the waist of the probe beam is sufficiently small, to irradiate a homogeneous transverse plasma density. In the setup discussed earlier, however, the waist of both beams is of similar order of magnitude. Therefore, the impact of the radial intensity profile on focal averaging is investigated next.

6.4.3. Focal averaging

In the weak focusing limit, paraxial beam propagation allows to estimate the transverse intensity profile by integrating the intensity-dependent observable. In the present experiment, the loss in transmission $L = 1 - T$ was detected, for Gaussian pump and probe beams with waists of $w_0^{\text{pu}} = 33 \mu\text{m}$ and $w_0^{\text{pr}} = 75 \mu\text{m}$. Using these parameters, contributions for each intensity are weighted by the occupied area of the

beam mode. The focal averaged relative loss in probe transmission than reads,

$$\langle L_{\text{pr}} \rangle_{\text{foc}}(I) = \frac{\int r L_{\text{pr}}(I_{\text{pu}}(r)) I_{\text{pr}}(r) dr}{\int r I_{\text{pr}}(r) dr}, \quad (6.55)$$

where I corresponds to the maximum on-axis pump intensity. According to Fig. 6.7 the focal averaged loss in probe transmission (dashed blue) is significantly reduced compared to a flat beam profile (solid blue).

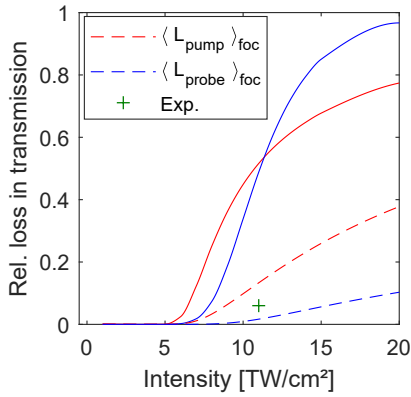


Figure 6.7.: Loss of transmission of pump (red) and probe pulse (blue), for flat-profile (solid) and focal averaged Gaussian profile (dashed).

This result is in good agreement with a recent experiment that reports a relative loss in transmission by the plasma of 5–6% at 11 TW/cm² [87], indicated by the green cross. The loss in pump transmission (red) is less affected by focal averaging due to the smaller beam waist. To further reduce averaging effects and to detect the steep increase seen in the solid lines, a reduced waist ratio $w_0^{\text{pr}}/w_0^{\text{pu}}$ well below unity seems instrumental in future measurements.

6.5. Conclusion

In this chapter, the Lorentz model was extended by a temperature and drift dependent plasma model for self-consistent pulse propagation within the FDTD method. Examining the energy balance of the simulation, the dominant role of collisions in the absorption of long pulses was contrasted by the increasing relative significance of the injection current for the absorption of few-cycle pulses. Furthermore, our simulation allowed for the detailed analysis of the spatio-temporal structure of emerging plasma. In particular, the feedback of the emerging plasma mirror was examined that leads to a spatial shift of impact ionization hot spots by a quarter wavelength opposite to the propagation direction. Furthermore, from the time dependence of the inelastic ionization rate it was found that hot avalanching and cold impact ionization contribute with comparable magnitude during pure forward propagation and in stationary standing wave regions. Finally, good agreement with experimental plasma diagnostics was confirmed, when comparing focal averaged calculations of the transmittance with delay-dependent measurements.

7. Harmonics from Nonlinear Reflection

The structure of below-band-gap harmonic spectra from bulk generally depends on the medium dispersion and therefore on phase-matching conditions [74]. In particular, cross-phase modulation, generated by any nonlinear mechanism, can disturb the spectral weight structure discussed in sect. 3.2.2 in transmission direction. Therefore, we investigate harmonics in the reflection direction which offer two strong advantages. First, harmonics propagate after front-side reflection in vacuum and therefore essentially dispersion free towards the detector. Second, reflected harmonics are locally fixed to the interfaces as phase matching prohibits large bulk contributions. Furthermore, it is shown in the following that the carrier-envelope phase is sensitive whether harmonics stem from the interface with bulk properties or from a thin layer of modified (e.g. stronger) nonlinear response. These arguments provide that comparing reflected and transmitted below-bandgap harmonics allows to systematically turn on and off the influence of propagation effects. One disadvantage of the reflection scenario is that harmonics reflected from the front interface show a comparably low amplitude, in particular for under-critical plasma densities. Nevertheless, in two recent works, harmonics in reflection direction were successfully detected. In the first case, Vampa et al. [155] compared the angle dependence of several low harmonic orders to the generalized Fresnel coefficient for nonlinear scenarios predicted by Bloembergen and Pershan [156]. In the second work by Hui et al. [157], reflected radiation was used to determine the attosecond reflectivity and extract the time-resolved density of excited carriers at the interface. The authors report a remarkably high agreement between a local model and extracted quantities. From both works, it can be concluded that reflected fields from the front interface are well explained by the local models, which we further explore next.

7.1. Amplitude and phase for nonlinear reflection

So far the amplitude scaling of harmonics, relevant for the correct reconstruction ansatz, was discussed for transmitted fields in sect. 3.2, where a dependence on detection geometry was found. Here we discuss how the emission geometry also determines the amplitude and phase of emitted harmonics. As before we consider a one-dimensional plane wave description, that can be directly related to the harmonic yield from Gaussian beam profiles (see sect. 3.2.3). Fig. 7.1 a–c summarizes the effective relation between local response and spectral amplitude and phase.

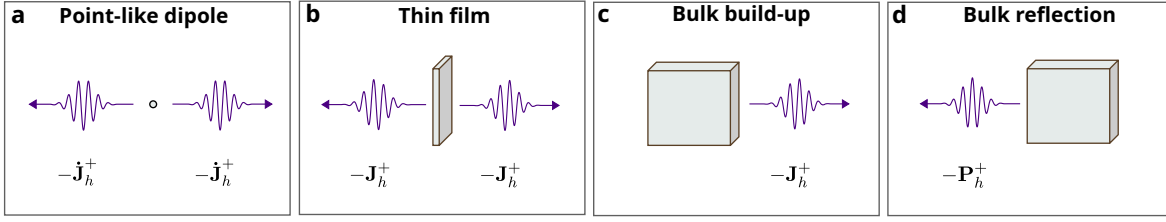


Figure 7.1.: Far-field phase and amplitude of harmonics generated in different emission geometries. Point-like sources **a** show dipole-acceleration type emission $-\dot{\mathbf{J}}_h^+$, thin film and phase matched bulk dipole-velocity like $-\mathbf{J}_h^+$ and bulk reflection show dipole-like $-\mathbf{P}_h^+$ emission.

For a point-like emitter (panel **a**), the far-field is proportional to the negative dipole acceleration (c.f. Appendix B.2). Increasing the transverse size of the emitter to a thin foil (panel **b**), the far field becomes proportional to the negative dipole velocity (earlier discussed in eq. (3.6) and Appendix B.1), effectively removing a temporal derivative from the far field dependence. Hence, the spectral weight acquires an inverse frequency factor and is delayed in phase by a quarter period. Considering as emission geometry a bulk medium with negligible phase mismatch (panel **c**), the forward harmonic signal is coherently amplified, such that the far-field dependence remains proportional to the retarded negative dipole velocity. In the following of this chapter, we focus on the reflection scenario (panel **d**) where harmonics are generated from a thin surface region of bulk medium, exhibiting effectively dipole-type emission, and therefore a distinct spectral fingerprint than the thin film reflection.

In this context, the term "effectively" is used to indicate that the amplitude and phase of harmonics, match those of the negative dipole density. It is important to recognize that this discussion does not concern the physical origin of the radiated fields. Radiated fields are generated by accelerated charges—a charge in constant, non-relativistic motion does not emit radiation.

The full relation between reflected harmonic field and local, time-dependent polarization is derived from the nonlinear wave eq. and the continuity equations at the interface (Appendix D) and reads,

$$\mathbf{E}_{\text{harm}}^{\text{ref}}(t) = \frac{-1}{\underbrace{2\varepsilon_0 n_{\text{ior}}(1 + n_{\text{ior}})}_{f_{\text{PNL}}^{\text{ref}}}} \mathbf{P}_{\text{NL}}(t_r) \quad (7.1)$$

where $\mathbf{P}_{\text{NL}}(t_r)$ contains the bound polarization plus the time-integrated free current, evaluated at the retarded time. The linear index of refraction is denoted by n_{ior} . All coefficients are summarized into the nonlinear reflection factor and $f_{\text{PNL}}^{\text{ref}}$.

7.1.1. Benchmark of reflected injection and Brunel harmonics

Next, we utilize the nonlinear reflection eq. (7.1) to determine separate analytic expressions for ionization-induced injection and Brunel spectra, based on the tunneling expansion. This prediction is used for a benchmark comparison with our self-consistent simulation introduced in chapter 6 to verify on the one hand the formal description and to validate on the other hand that low-order harmonics are correctly propagated on the numerical grid.

First, the polarization in the reflection relation, eq. (7.1), is replaced by the time integral of the injection current

$$\mathbf{E}_{\text{inj}}^{\text{ref}} = f_{P_{\text{NL}}}^{\text{ref}} \int dt \mathbf{J}_{\text{inj}} \quad \text{with,} \quad (7.2)$$

$$\mathbf{J}_{\text{inj}} = n_0 \frac{E_g \mathbf{E}}{|\mathbf{E}|^2} (1 - \rho(t)) \Gamma(|\mathbf{E}|) \approx \frac{n_0 E_g \hat{\Gamma}}{\hat{E}^s} |\mathbf{E}|^{s-2} \mathbf{E}. \quad (7.3)$$

Here the injection current from eq. (2.14) has been inserted. To calculate the spectrum, we transform the Gaussian pulse to the frequency domain, where the time integral in eq. (7.2) turns into the inverse frequency factor $\frac{1}{i\omega}$. Furthermore, we utilize that the $|\mathbf{E}|^{s-2} \mathbf{E}$ term can be written as harmonic series, where the tunneling exponent s is extracted as before from the ADK rate eq. (3.34),

$$E_{\text{Inj}}^{\text{ref}}(\omega) = f_{P_{\text{NL}}}^{\text{ref}} \frac{\sqrt{\pi}}{a_{\text{Inj}}} \frac{\hat{J}_{\text{Inj}}}{2} \sum_{\text{odd } h} \frac{D_h^{(s-1)}}{i\omega} e^{-\left(\frac{\omega - \omega_h}{2a_{\text{Inj}}}\right)^2}, \quad \text{with,} \quad \begin{aligned} \hat{J}_{\text{Inj}} &= 2 \frac{n_0 E_g \hat{\Gamma}}{2^{s-1} \hat{E}}, \\ a_{\text{Inj}} &= \sqrt{s-1} \frac{\sqrt{2 \ln 2}}{t_{\text{FWHM}}^{\text{Inj}}}. \end{aligned} \quad (7.4)$$

The degeneracy weights $D_h^{(m)}$ and current amplitude \hat{J}_{Inj} follow, analogous to the polarization series eq. (3.5). The spectral width parameter a_{Inj} is determined from the harmonic pulse duration, eq. (3.58).

In Fig. 7.2 a, the analytic reflected injection spectrum, i.e. the absolute value of eq. (7.4), (yellow dashed) agrees well with the fast-Fourier-transformed reflected fields from the ionization-radiation FDTD simulation (green), recorded a few micrometers in front of the medium. For this benchmark, all other nonlinear effects besides the injection response are switched off. Spectra in this figure are not normalized and agree on absolute scale. This agreement confirms on the one hand the validity of the derived harmonic series including approximations made for the tunneling expansion. On the other hand, agreement up to the $h \leq 13$ injection harmonic shows that fields are correctly propagated by the algorithm. Furthermore, the calculation confirms, that amplitude scaling of reflected injection harmonics is characterized by $|E_{\text{Inj},h}(\omega)| \sim \frac{1}{\omega} D_{\text{Inj},h}$.

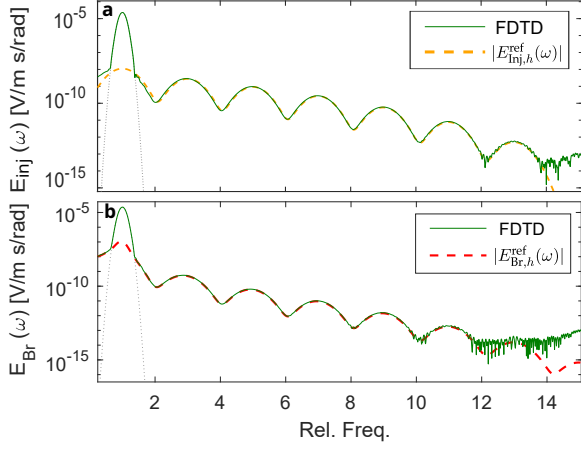


Figure 7.2.: Single color reflection benchmark. Calculated spectra of injection (yellow) and Brunel harmonics (red) in reflection direction show excellent agreement with the simulation of isolated nonlinear response using the ionization radiation model introduced in chapter 6 (green). The spectra confirm the characteristic amplitude fall-off $|E_{\text{Inj},h}^{\text{ref}}(\omega)| \sim \frac{1}{\omega} D_{\text{Inj},h}$ and $|E_{\text{Br},h}^{\text{ref}}(\omega)| \sim \frac{1}{\omega^2} D_{\text{Br},h}$.

Similar good agreement is found when comparing the isolated Brunel response from the simulation (green) in panel **b** with the modulus of the formal solution,

$$E_{\text{Br}}^{\text{ref}}(\omega) = f_{\text{P}_{\text{NL}}}^{\text{ref}} \frac{\sqrt{\pi}}{a_{\text{Br}}} \frac{\hat{J}_{\text{Br}}}{2} \sum_{\text{odd } h} \frac{D_{\text{Br},h}}{(i\omega)^2} e^{-\left(\frac{\omega-\omega_h}{2a_{\text{Br}}}\right)^2} \quad \text{with,} \quad \hat{J}_{\text{Br}} = 2 \frac{q^2 n_0 \hat{\Gamma} \hat{E}}{2^{s+1} m_e i \omega_0} \quad (7.5)$$

$$a_{\text{Br}} = \sqrt{s+1} \frac{\sqrt{2 \ln 2}}{t_{\text{FWHM}}^{\text{Ints}}},$$

shown by the red dashed line. The expression for the degeneracy weight of the Brunel mechanism is slightly more involved than for the injection current as shown in appendix D.2. In this case, the numerical result validates the spectrum up to $h \leq 11$. Comparing the width of harmonics in both spectra, it is seen that Brunel harmonics are more spectrally broadened, which is a result of the increased nonlinearity $m_{\text{Br}} = m_{\text{inj}} + 2$ (see sect. 3.4.2). Moreover, the characteristic amplitude fall-off $|E_{\text{Br},h}^{\text{ref}}(\omega)| \sim \frac{1}{\omega^2} D_{\text{Br},h}$ is confirmed.

7.1.2. Signatures of the nonlinear reflection mechanism

An overview for the distinct amplitude fall-offs in the different scenarios is provided in table 7.1. Here the relevant emission geometries are given in the center and right column and the different emission mechanisms are listed row-wise. For clarity, the general relation between emitted field and local charge dynamics for the thin film, from eq. (3.6) as well as for bulk reflection from eq. (7.1) is given in the first row.

For the Kerr-type emission also the multiple interaction with the third-order nonlinearity is accounted for, which can also lead to a response beyond the third harmonic. Here the integer ℓ denotes the number of repeated, so-called cascaded, interactions with the third-order nonlinearity. As the cascaded response is exponentially suppressed with harmonic order, it is here only considered for the low-order Kerr-type mechanism, while for the high-order ionization-induced nonlinearity the direct response (single interaction) turns out to be dominant. We come back to this par-

		Amplitude scaling $E(\omega)$	
		Thin film (Ch. 3) Phase matched medium	Bulk reflection
field—charge-carrier relation	$ E(\omega) $	$\sim J(\omega) $	$ E^{\text{ref}}(\omega) \sim P(\omega) $
Kerr-type	$ E_{\text{Kerr},h}(\omega) $	$\sim \omega D_h^{(m),\ell} z^\ell$	$ E_{\text{Kerr},h}^{\text{ref}}(\omega) \sim D_h^{(m),\ell}$
Injection	$ E_{\text{Inj},h}(\omega) $	$\sim D_{\text{Inj},h} z$	$ E_{\text{Inj},h}^{\text{ref}}(\omega) \sim \frac{1}{\omega} D_{\text{Inj},h}$
Brunel	$ E_{\text{Br},h}(\omega) $	$\sim \frac{1}{\omega} D_{\text{Br},h} z$	$ E_{\text{Br},h}^{\text{ref}}(\omega) \sim \frac{1}{\omega^2} D_{\text{Br},h}$

Table 7.1.: Harmonic amplitude scaling $E_h(\omega)$ for ℓ -times cascaded Kerr, direct injection and direct Brunel harmonics from thin film, phase-matched bulk along propagation distance z , and the bulk-reflected scenario. In the case of Kerr-type harmonics, ℓ denotes the number of nonlinear interactions.

		Harmonic phase $\Phi_{\text{mech}}^{\text{scen}}$	
		Thin film (Ch. 3) Phase matched bulk	Bulk reflection
field—charge-carrier relation		$-J_h^+(0, t_r)e^{-i\omega_h t}$	$-P_h^+(0, t_r)e^{-i\omega_h t}$
Kerr-type		$(-i)^\ell$	$(-1)^\ell$
Injection		-1	$+i$
Brunel		$+1$	$-i$

Table 7.2.: Mechanism-specific harmonic phases of the complex positive frequency component E_h^+ for different emission geometries. In this notation, a positive phase factor $\Phi_{\text{mech}}^{\text{scen}} > 0$ corresponds to a shift of field crests to earlier times.

ticular point when comparing transmitted and reflected harmonics for a two-color scenario, where the relevant nonlinearities act concurrently.

To complement the comparison of similarly strong mechanisms, also the characteristic phases are extracted from eqs. (7.1)-(7.5) and summarized in table 7.2 below. It is seen that bulk reflection is a quarter period delayed with respect to thin film emission and in particular with respect to thin film reflection (c.f. center to right column). These characteristic phases can be used to identify the mechanism and to determine the spatial origin of harmonic emission. For instance, the phase of cascaded Kerr-type harmonics is for the bulk reflection scenario always distinct from injection or Brunel harmonics. This distinguishes bulk reflection from the thin film result, where two interactions with the third-order nonlinearity ($\ell = 2$, typically found in the spectrum at the 5th harmonic or the $n = 2$ wave-mixing signal) result in the same phase factor as the injection response (see center column of table 7.2).

7.1.3. Longitudinal length-scale of reflection response

Next, as a representative example for the spatial resolution gained by the distinct harmonic phase between thin film and phase-matched bulk reflection (center vs. right column), we examine the length scale for the transition of the harmonic phase in the simplest scenario i.e. the direct $\chi^{(3)}$ response at the bulk interface. In forward direction, the Kerr-type third harmonic is a quarter period delayed (center column, $\ell = 1$ in table 7.2) wrt. the driving reference. In reflection direction, however, it is half a period out of phase. This transition of the phase is examined using our simulation as function of propagation distance in Fig. 7.3.

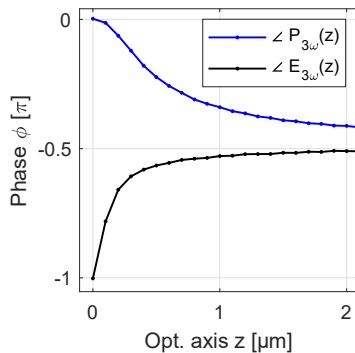


Figure 7.3.: Phase of harmonic polarization and field as function of propagation depth at the front interface. Initially in phase with the driving field, the third harmonic polarization (blue) quickly accumulates a phase delay of a quarter period. The third harmonic field (black) is initially half a period out of phase and converges toward the same quarter-period phase delay.

At low intensity where the Kerr contribution is dominant, the phase of the third harmonic field (black line), shows as function of propagation depth two limiting cases that are consistent with the above discussion. It is found that the phase of $\angle E_{3\omega}(z) = -\pi$ at the front interface $z = 0$, converges rapidly, i.e. within sub wavelength distance ($\lambda = 2100$ nm) to the phase delay expected for bulk. The phase of the third harmonic polarization (blue line) shows convergence behavior on similar length scale. Zero phase delay of the polarization at the interface ($z = 0$) indicates its instantaneous dependence on the fundamental field. The convergence to a quarter-period phase delay is attributed to the contribution of the linear polarization driven by the third harmonic field.

This finding leads to the important conclusion that the thickness of the nonlinear medium determines the phase of reflected harmonics, which is particularly useful if the nonlinear response from the surface is stronger [158]. Once the mechanism of nonlinear response is determined, for example by the previously discussed spectral fingerprint of the amplitude scaling, the phase can be used to determine if the radiation originated from the interface and if so from which thickness.

7.2. Linking reflected harmonics and local current

In the previous section the tight relation between local response and nonlinearly reflected fields was established, that explains amplitude and phase properties of the

harmonic radiation response. Next we show that these reflected harmonics are robust against propagation effects and remain sensitive to the local dynamics even at high intensities where plasma formation already affects the transmitted field. We apply the formal concepts to our wave-mixing scenario and examine the harmonic scaling from a macroscopic SiO₂ slab in Fig. 7.4 a, that is obtained from calculated spectra in forward **b** and reflected direction **c**, using our 1D self-consistent simulation. The setup is sketched in inset **e** with incident, right-propagating driving pulse (red) and reflected left-propagating harmonic (purple).

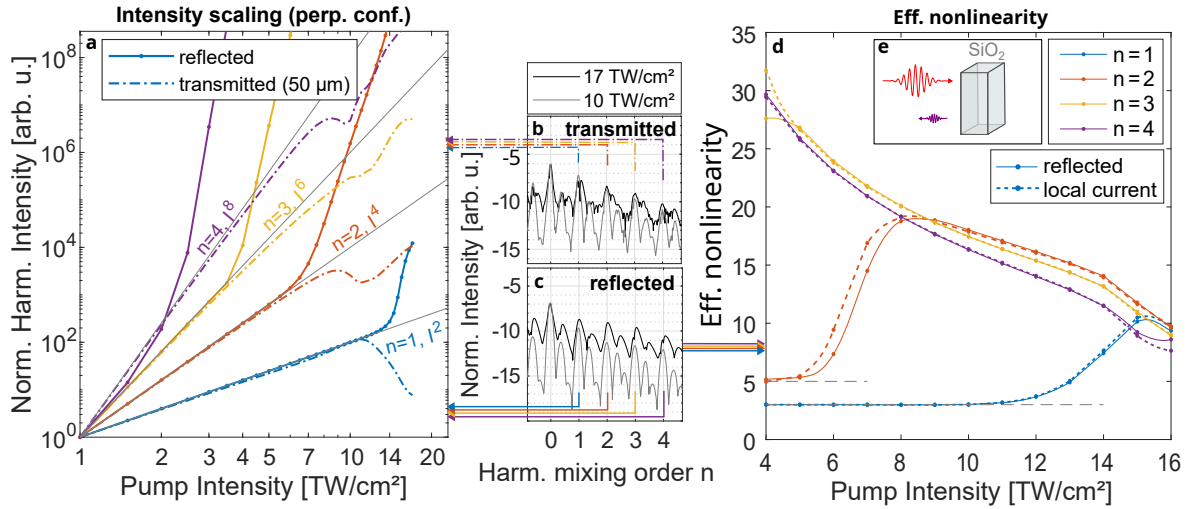


Figure 7.4.: Scaling of wave-mixing harmonics in reflection direction, normalized to lowest intensity **a** in reflection direction (solid) and transmission direction (dot-dashed). This scaling is obtained from calculated spectra in perpendicular pump-probe configuration, recorded behind **b** and in front of a 50 μm SiO₂ sample **c**, shown for two representative pump intensities 10 TW/cm² (gray) and 17 TW/cm² (black). To extract only the harmonic field reflected from the front side, a temporal filter is applied. Panel **d** shows the eff. nonlinearity of reflected harmonics (solid) and the corresponding local current at the front surface of the target (dotted). For pulse parameters, see Sect. 2.1.

To reveal the intensity scaling of the $n = 1..4$ low-order wave-mixing signal at $\omega_{\text{sig}}^{\text{mix}} = 2n\omega_{\text{pu}} + \omega_{\text{pr}}$ wrt. the pump intensity, the yield of each harmonic in panel **a**, is normalized to the lowest data point. The strongest signal (i.e. $n = 1$) shows in transmission (dashed blue) and in reflection direction (solid blue) perturbative scaling of the yield $Y_{n=1} \sim I^2$ (c.f. gray reference line). The perturbative scaling of higher wave-mixing harmonics exhibits, as expected, the characteristic I^{2n} dependence (see orange, yellow and purple curves on top of gray reference line), that stems here from the interaction of $2n$ pump photons and one probe photon in the cascaded $\chi^{(3)}$ process. This shows that the thin surface layer, where reflected harmonics are generated, suffices to generate cascaded nonlinear response. In the following we focus on the lift-off from the perturbative, Kerr-type, scaling that signifies the plasma response.

We start by examining the transmitted harmonic signal detected behind the target (dot-dashed line, panel **a**). The drop at about 12 TW/cm^2 (all dot-dashed curves) indicates that in this perpendicular configuration, the saturation effect due to the plasma mirror sets in, before ionization harmonics surpass the Kerr contribution. This interpretation is supported by the structure of the harmonic spectrum in **b**. At high intensities, the transmitted spectrum is heavily distorted (c.f. black line) compared to spectra obtained below the threshold (gray). Further, transmitted harmonics show stronger attenuation for low orders ($n < 3$), which is consistent with the frequency dependence of the critical plasma density $n_{\text{crit}} = \varepsilon_0 m \omega^2 / e^2$.

The intensity scaling of reflected harmonics (solid lines in panel **a**), however, show eventually a steep lift-off of comparable slope for all wave mixing orders. It is seen that this swift increase occurs for higher n already at lower intensities. We attribute this to the steeper amplitude decay of the cascaded Kerr harmonics compared to the spectral weights of the injection response. This apparently reduced signal background with increasing wave mixing order can be interpreted as improved sensitivity to the injection signal. Furthermore, the fact that the lift-off of the $n = 1$ signal is only seen when transmitted fields are already quenched, is one indicator, that ionization harmonics in reflection direction are robust against the emerging high plasma density. This finding is consistent with the clearer spectral structure of reflected harmonics at high intensities, (compare black lines in panel **b** and **c**). In order to show that the harmonic signal can be directly linked to the local response, the effective nonlinearity (i.e. the intensity ratio parallel versus perpendicular, introduced in sect. 2.3), is analyzed next.

In Fig. 7.4 **d** the eff. nonlinearity of reflected harmonics (solid lines) is now shown on linear intensity axis. The $n = 1$ harmonic (solid blue) follows the behavior already seen in the experiment (c.f. sect. 2.3). In accordance with the previous discussion, high wave-mixing harmonics show an earlier increase in the effective nonlinearity. The $n = 2$ mixing harmonic (orange line) departs from a nonlinearity of 5 due to cascading at small intensities, the position of the lift-off agrees with that seen in panel **a**. For $n = 2, 3, 4$ the expected decline in nonlinearity that indicates the decreasing slope of the tunneling rate (c.f. discussion of fig. 3.6) is observed. The good agreement with the corresponding amplitude ratio of the local source current (dotted), that was recorded in the simulation on the front surface of the medium, confirms the direct relation between interface harmonics and local response.

To summarize, the comparison of transmitted and reflected harmonics using our fully self-consistent FDTD-ionization-radiation model, revealed two advantages of the reflection scenario. First, the absence of phase matching and absorption for reflected harmonics allowed to observe the undisturbed spectral weights, resulting in an effective nonlinearity that agrees with the local current at the surface at several wave-mixing orders. Second, reflected harmonics are found to be robust against high plasma densities. Both advantages are in particular instrumental to study the relative phase between ionization-induced harmonics. Hence, the reflection scenario constitutes an ideal platform to identify nonlinear mechanisms at the interface based on ef-

fective order and carrier-envelop phase of emitted harmonics. In particular, reflected fields are promising to the study injection mechanism beyond the semi-classical prediction. To provide an outlook, we qualitatively examine the excitation dynamics based on a quantum dynamical calculation next.

7.3. Real space perspective on tunneling injection in periodic potential

Our semi-classical model (introduced in sect. 2.4.2) predicted short pulses of current through the effective potential barrier, with temporal width much shorter than one half-cycle of the laser field (c.f. eq. (3.39)). However, the full electron trajectory in space can not be described in this simplified model as it is classically forbidden. Instead the full quantum calculation of the current becomes necessary. Goal in the following is to identify the injection current also in the full quantum dynamics and to determine the role of the periodic potential for the dynamics of liberated tunnel electrons.

7.3.1. SiO₂ model for quantum mechanical tunneling dynamics

As a model system for SiO₂ we consider a finite, one dimensional chain, where the external laser field is focused tightly onto the center. To facilitate the analysis in real-space and to follow the trajectory of the tunneling electron wave-packet, we consider a focus far beyond the diffraction limit that drives ionization only in the center well of the lattice. For the finite periodic part of the lattice, a cosine-shaped pseudo-potential is adopted, where parameters are adjusted, to capture the relevant properties of the SiO₂ band structure, with lower edge of the conduction band at $E_C = -1.3$ eV below the vacuum level [159] and a band gap of $E_g = 7.7$ eV corresponding to the sample used in the earlier experiment¹, resulting in a upper valance band edge at $E_V = -9.0$ eV.

The potential, the band structure, and field free eigenstates, computed from imaginary time propagation [161], are shown in Fig. 7.5. The first two states from each band are shown in panel **a** and inset **b-d**, indicating the characteristic shape of $|\psi|^2(x)$ of tightly bound valence states (blue), conduction states (light red) and continuum states (dark red). Each valence band contains $N = 21$ states, one for each well of the potential shown below in panel **e**. The same energy scale is used in panel **f** that shows the free-dispersion parabola (dark red) and the band structure of the finite periodic potential. All bands in the full Brillouin zone are computed by solving the TISE eigenvalue problem in k -space (Appendix D.3). This independent calculation is used

¹Possible reasons for varying gap-values for amorphous SiO₂ were earlier reported in [160].

to benchmark our eigenstates. For their comparison the Fourier transformed absolute square of the eigenstates can be examined [162]. They are plotted in panel **g-i** on logarithmic color-scale at their corresponding eigenenergies. Excellent agreement with the TISE results (dashed overlays in first Brillouin zone) confirm convergence of ground states by imaginary-time propagation [161].

Next, the $2N$ states from the two completely filled valance bands are used as initial conditions to simulate the laser-driven tunneling dynamics by solving the TDSE

$$i\hbar \frac{\partial \psi}{\partial t} = \left[-\frac{\hbar^2}{2m_e} \nabla^2 + V_0(x) + V_{\text{las}}(x, t) \right] \psi(x, t) \quad (7.6)$$

numerically. Physically, it is expected that already at small field strength, the valance band electron density, initially centered around potential minima (inset **c, d**), is displaced. This displacement, however, can due to Pauli-blocking only be realized by instantaneous (virtual) population of higher lying conduction states (red lines, panel **f**) that are immediately depopulated once the electron density returns to the equilibrium position. For persistent (real) population due to tunneling from the upper edge of the valance band into the lower edge of the conduction band, subsequent acceleration of

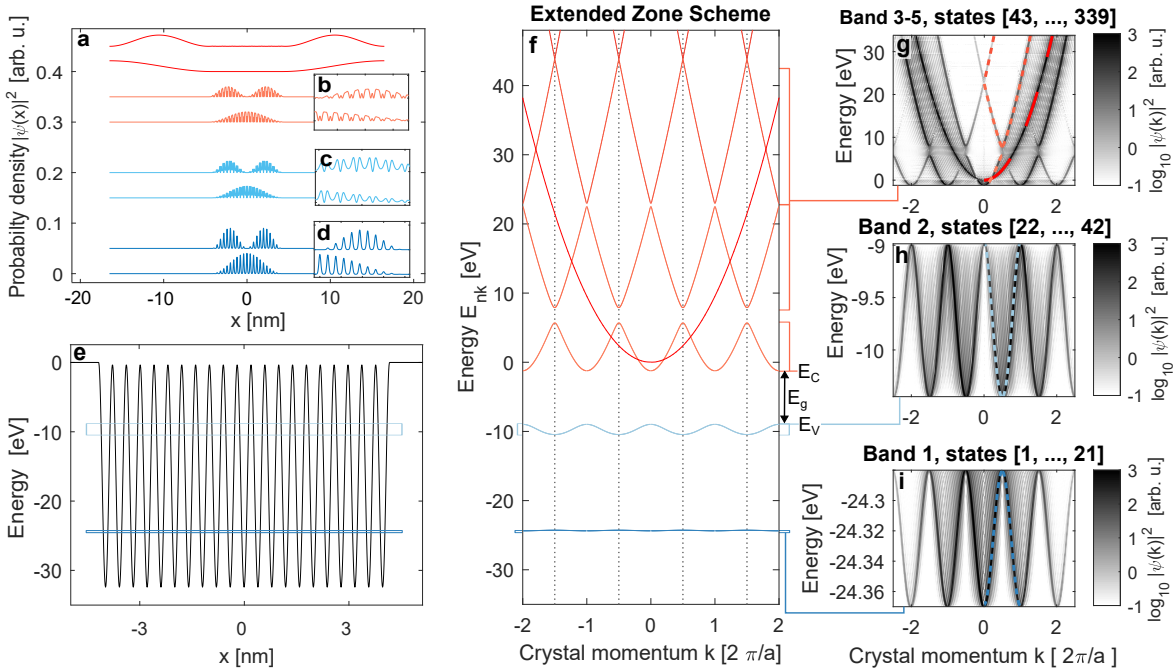


Figure 7.5.: Bandstructure, eff. potential, and energy eigenstates of our SiO_2 model system used for numerical solution of the TDSE. Panel **a** shows the lowest two energy eigenstates $|\psi(x)|^2$ of the two valance bands (blue), the lowest conduction band (pink), and free continuum states (dark red), shifted for visibility and magnified in inset **b-d**. The eff. real space potential V_0 , constructed from a cosine with $N = 21$ wells is shown in **e** (black), next to the corresponding band structure $E_n(k)$ in **f** that is compared (dashed lines in panel **g-i**) with Fourier transformed energy eigenstates $|\psi(k)|^2$ (color coded), see main text.

conduction electrons along the crystal momentum axis according to the acceleration theorem in dipole approximation,

$$k(t) = k_0 + \frac{q_e}{\hbar} \int_{-\infty}^t E(x(t'), t') dt', \quad \text{with} \quad v_n(k) = \frac{1}{\hbar} \frac{\partial E_n(k)}{\partial k} \quad (7.7)$$

being the group velocity of the wave packet, is expected. The higher curvature of the conduction band $E_n(k)$, compared to the free dispersion parabola (panel **f**), indicates a reduced effective mass of electrons in accordance with ab initio calculations of the real system [159].

7.3.2. Quantum mechanical strong-field ionization current

In the following the total current from all electrons that initially fully occupy both valance bands (VB), is examined for three representative intensities. In Fig. 7.6 **a** the spatial profile of the total current density is shown as function of space and time. Electrons are injected into the conduction band (CB) seen as diagonal stripes pointing outwards, that become more pronounced with increasing intensity (see titles). Currents due to virtual population are localized at the focal region $x \approx 0$ and seen best at lowest intensity (alternating colored spots in **a**). The effective lattice plus laser potential at the crest of the field is shown for the corresponding intensity of 16 TW/cm² in inset **b** by a black line (gray lines for 25, 50 TW/cm², respectively).

To examine different contributions to the current, the excitation dynamics of electrons from the upper VB is further analyzed using the window operator method, in the panels below. Panel **c** shows the energy-resolved population of electrons over time. Here virtual excitation that is in phase with the cw-laser field, is seen as blue peaks in the conduction and lower valance band. In the lowest band at least the same amount of probability density is transferred to higher states (not shown), as orthogonality of all states is preserved by the Hermitian interaction Hamiltonian. Hence, the Pauli exclusion principle remains automatically fulfilled by the TDSE. From the excitation dynamics in **c**, the energy windows corresponding to the VB and CB are selected to isolate respective electron dynamics.

The corresponding electron density in the CB is shown in panel **d**, where the outgoing trajectories show a clear modulation by the potential (inset **e**), which can be attributed to a hopping from one potential well to the next. These straight hopping trajectories in the field-free region indicate an approximately constant group velocity of the electron wave packet. At the interface only a small fraction of electrons with high kinetic energy is transmitted into the vacuum, as most electrons remain at the lower edge of the VB and therefore below the free dispersion curve (c.f. Fig. 7.5 **f**).

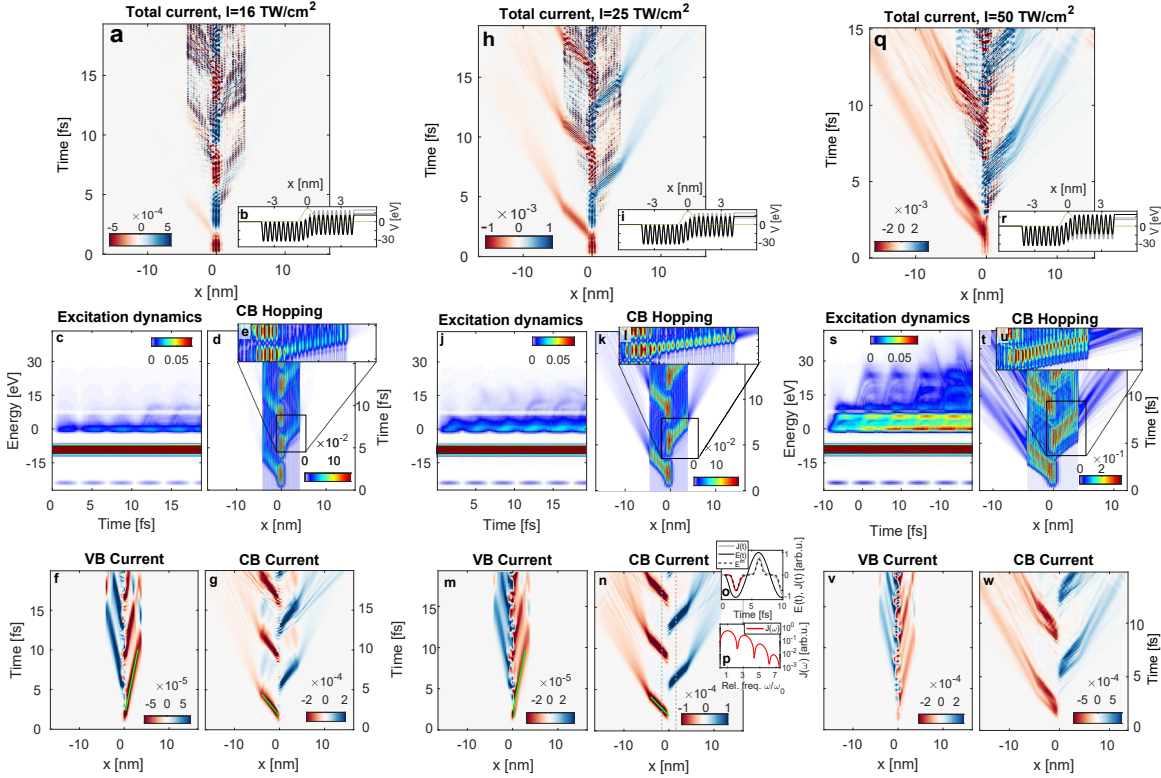


Figure 7.6.: The strong-field-induced, quantum mechanical particle current, $J_{\text{el}}(x) = \frac{\hbar}{m_e} \text{Im} \{ \psi^* \nabla \psi \}$, is shown as function of space and time in panel **a** (color coded in arb. u.), together with the eff. potential (black inset **b**) at the crest of the tightly focused field (spatial envelope green). The energy and time resolved occupation dynamics of electrons from the upper valance band in **c**, is used to extract the real-space probability of conduction band population in **d**, where hopping trajectories are magnified in inset **e**. Intraband currents from the upper VB and the lowest CB are shown in **f**, **g** and compared with trajectories from eq. (7.7) (green). Panel **h-w** display corresponding results for higher intensities (see titles). Cuts of the CB current along dashed lines in **n** are shown in inset **o** vs. time and in inset **p** vs. frequency.

Interestingly, the intraband particle-current,

$$\mathbf{J}_{\text{CB}}^{\text{intra}} = \frac{\hbar}{m_e} \sum_{\kappa=1}^N \sum_{n \in \text{CB}} \text{Im} \{ \phi_{n\kappa}^* \nabla \phi_{n\kappa} \}, \quad (7.8)$$

calculated by summing the flux over all windowed wave functions $\phi_{n\kappa}$ with energy index of the window operator n and initial eigenstate index κ exhibits a different behavior, see Fig. 7.6 **g**. This conduction band contribution of the intraband current does neither show virtual excitation nor the clear hopping modulation from before. Instead, a uniform particle flux is seen, that is partially reflected at the interface, leading to a sign flip (changed color) and back-propagation towards the center of the lattice. In the VB (panel **f**), similar straight trajectories are seen but with reversed colors. Although the first trajectory points to the right, red color indicates an electron flux to the left. It is deduced that this representation of the VB particle current reveals the

trajectory of holes, which is consistent with absent flux into free-space. This real space analysis thus represents a concrete example for the hole dynamics according to the physical "empty seat" picture. Pictorially speaking, valence electrons move from one side into the hole so that the hole moves in the opposite direction. This explains the initial *opposite* real space acceleration of electrons and holes. The smaller hole velocity (higher slope in **f** and **g**) is attributed to the higher effective hole mass around the top of the VB. For this extreme focusing case, this leads to holes being spatio-temporally overlapped only with conduction electrons from later laser cycles.

The interpretation of the quantum mechanical current given so far is supported by the good agreement with semiclassical trajectories (see green lines), using the integration of the acceleration theorem eq. (7.7) by means of the velocity Verlet method (Appendix D.4). This calculation shows at the same time that in reciprocal space unoccupied states² move according to the "bubble within a stream" picture. The electrons and the vacant states are accelerated immediately after the tunneling according to eq. (7.7) in the *same* direction along the k-axis, so that the vacancy resembles a bubble which is carried along by a flowing fluid (valence electrons). Because of the highly confined focus in our scenario, the conduction electron can leave the focal region faster due to the lower effective mass, while the crystal momentum of the hole is further modified. Finally, the superposition of electron and hole trajectories (**g** and **f**) can explain the interference spots seen in the total current in panel **a** from the second emitted electron burst on. This notion is further supported, by inspecting the same scenario at higher intensities.

With increasing intensity, the total current density grows, as seen from the second and third column of panels, i.e. **h-p** and **q-w**. In particular in **h** and **q** electrons now show increased transmission and reduced internal reflection at the medium interface, as they are accelerated to higher energies, c.f. **j**, **s**. For the highest shown intensity, electrons are accumulated at the lower and upper edge of the first conduction band (red maxima in panel **s**) that leads to the separation of the wave packet as seen in inset **u** and panel **w**. Comparison of the latter with the total current **q**, shows good agreement of the electron trajectories. However, the total current density shows additional features. From the second field cycle on, i.e. for $t > 10$ fs, spotted current densities are seen on the opposite side of the focus (red dots, panel **q**). Due to the matching sign, we attribute these to the hole dynamics (panel **v**) where interference spots can be attributed to interband effects, including recombination of electrons with holes which will be further examined in the following sect. 7.3.3.

The main finding from this TDSE simulation is, that the intraband current of the lowest conduction band shows for intensities $I \lesssim 25$ TW/cm², a single wave packet, that is injected during a short time interval at the crests of the field-cycle and propagates afterwards essentially undisturbed through the crystal lattice. It is the time

²An unoccupied valence state is characterized by the absence of mass and charge. It is distinguished from a hole quasi-particle, often simply denoted as "hole", that carries a net positive charge $+e$ and is used to describe the collective effect of all remaining valence band electrons [163]. As we propagated all electrons explicitly, we did not employ the hole particle concept in calculations.

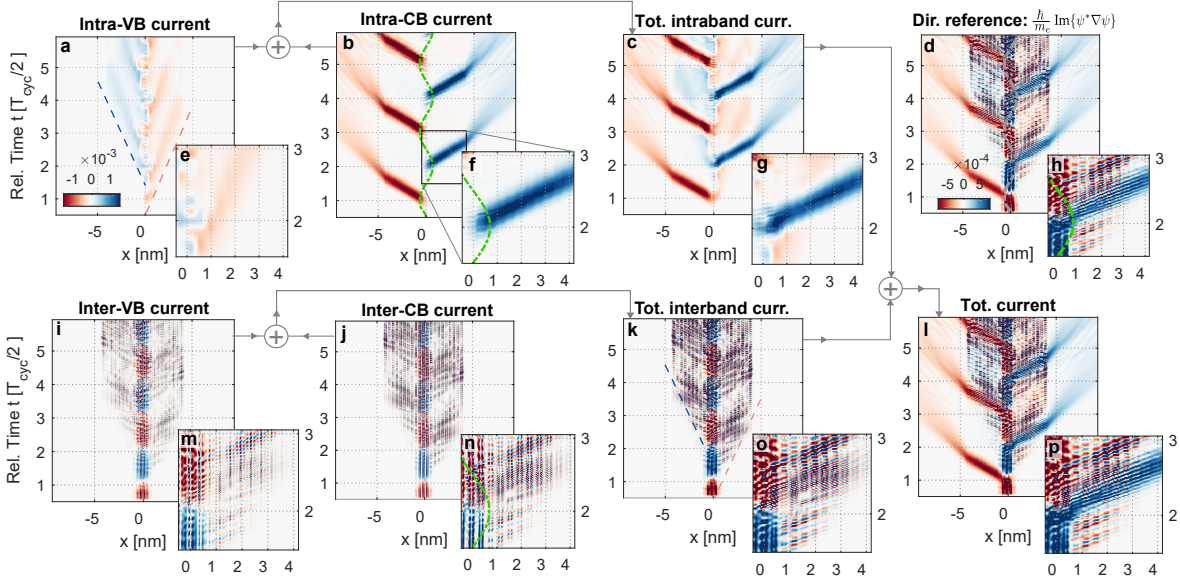


Figure 7.7.: Spatio-temporal structure of intra-, **a-c**, and interband contributions, **i-k**, of the field-induced particle current (same color scale) in SiO_2 , with rescaled ext. force, $q_e \mathbf{E}$ in **b**, are obtained for $I = 25 \text{ TW/cm}^2$ from the window operator method. The sum of these contributions, seen in **l**, agrees well with the particle current directly obtained from the wavefunctions **d**. The same section is magnified in each image for detailed analysis (main text).

structure of this current that can give rise to LOHG, as discussed earlier in sect. 2.4. To confirm this also in this quantum simulation, representative cuts of the current at fixed location (panel **n**, gray dashed lines), are extracted, see inset **o**. The current injected into the conduction band (red line) shows the expected nonlinear dependence on the driving field (black line). Here good agreement with E^m where the order of nonlinearity $m = 11$ is evident (dashed line). The Fourier transform (inset **p**) clearly reveals the low-order harmonic spectrum of the current. We note, that the corresponding total dipole acceleration, that is the microscopic source of any emitted radiation, is localized at the starting point of the wave packet trajectory, i.e. at the tunneling exits in the laser focus (here $x \approx 0$).

7.3.3. Decomposition and analysis of the field-induced current

So far we identified the strong-field injection current from the temporal structure of the intraband current in the conduction band. Next, we compare the relative contributions and the spatial structure of intra- and interband currents to expose the underlying physical mechanisms.

To this end, we focus more closely on the $I = 25 \text{ TW/cm}^2$ scenario, where the intraband particle currents (previously seen in Fig. 7.6 **m, n**) are now shown on the same color scale in Fig. 7.7 **a, b** to emphasize the relative importance. For temporal

reference, the x-component of the external driving force, qE , is shown in **b** by a green line as function of time (vertical axis in units of half laser periods for all panels). The current from the first two panels is superimposed in **c** that shows already the main features from the total current extracted directly from the wave functions (panel **d**). To better compare the temporal structure insets **e-h** magnify the same time interval as marked in **b**. It is seen that tunneling injection contributions are emitted close to the crest of the field (inset **f**). From inset **h** it is found that additional, fine modulated features appear prior and after the main electron trace, which can be attributed to the interband current seen in **i, j**, respectively. Both VB and CB interband contributions,

$$\mathbf{J}_{\text{CB}}^{\text{inter}} = \frac{\hbar}{m_e} \sum_{\kappa=1}^N \sum_{n \in \text{CB}} \sum_{n' \notin n} \text{Im}\{\phi_{n'\kappa}^* \nabla \phi_{n\kappa}\}, \quad (7.9)$$

show a strong spatial modulation, that forms upon superposition fine striped diagonal traces of alternating positive and negative flux (panel **k** and inset **o**). It is confirmed that adding inter- and intraband contributions, calculated from the window operator, (panel **c, k**) to the total flux (**l**) closely resembles the directly computed quantum mechanical current (panel **d**).

From this decomposition it is concluded that intra- and interband contributions show several complementary physical features. The intra CB current corresponds closely to the predicted semi-classical electron trajectories, where the tunneling picture can explain the nonlinear dependence on the instantaneous field that is imprinted on the temporal envelope of the current trace (inset **f**). Real interband polarization (fine striped trajectories) on the other hand, are far less temporally confined, and are therefore consistent with the multi-photon picture. The weak initial modulation, seen in **k** (half period above dashed lines), lag by about a quarter period behind previously discussed traces and seems to wash out into more evenly distributed spots from the fourth half-cycle on. Outside the focusing region interband contributions are spatio-temporally correlated with the abundance of holes, seen best from the leading edges marked by dashed lines in panel **a** and **k**, being consistent with electron-hole recombination. Furthermore, in **l, p** it is seen that the fine temporal modulation of the interband current oscillates more rapidly where it is overlapped by the injected intraband current. Hence, we find that multiple physical effects are possibly needed to describe the more delicate structure of the interband contribution.

In conclusion, the full quantum mechanical calculation supports the use of the semiclassical model of injection current plus drift to account for the ionization-induced nonlinear intra-conductionband response. Comparing the tunneling current obtained from our quantum-mechanical pseudo-potential calculation with experimental measurements of the nonlinear reflection response, will perspectively allow to identify the limitations and possible refinements to better capture the underlying physics of LOHG and therefore improve the local model for nonlinear pulse propagation.

8. Conclusions and Outlook

The central goal of this thesis was to explore the significance of strong-field ionization and plasma formation on the nonlinear optical response of dielectric solids. Here, the role of ionization-induced nonlinearities for low-order harmonic emission and nonlinear pulse propagation was addressed through analytical calculations, self-consistent numerical field propagation, local semi-classical and quantum mechanical models, and the comparison with experimental measurements of our partners. The key results of this dissertation comprise the identification of the injection current as the dominant mechanism for ionization induced low order harmonic emission, the demonstration of non-perturbative wave mixing as a robust diagnostic tool to monitor ultrafast plasma formation, and the reconstruction of sub-cycle plasma formation with tailored laser pulses in scenarios of sub-wavelength laser material modification.

The main conclusion from the first part of this study is based on our semi-classical ionization-radiation model that shows that the injection current provides a major contribution to the low-order harmonic spectrum in crystalline and amorphous SiO_2 as typical representatives for wide band-gap dielectric materials. From the semi-classical description of tunnel ionization we determined the effective order of non-linearity as a characteristic observable. Its major advantage is its accessibility via the mere comparison of intensities in parallel and cross-polarized two-color driving without the requirement of intensity scans. The good agreement between experimental measurements and the prediction of the local model reflects the robustness of this metrology with respect to propagation effects and ultimately allowed us to use injection signals for the reconstruction of the sub-cycle tunneling dynamics.

An important prerequisite for reconstructing the tunneling dynamics was to clarify the role of electron impact ionization and elastic collisions with the lattice for ionization-induced harmonic wave mixing. Solving the Boltzmann equation for a local electron velocity distribution subject to the intense two-color laser field showed that collision-induced harmonic contributions appear only at low-order odd harmonics, with a distinct asymmetric temporal signature in the trailing edge of the radiation response. The analysis of the temporal structure of the harmonic wave-mixing has further demonstrated that Kerr components are the dominant contribution to the nonlinear response only in the pulse edges. Applying our reconstruction algorithm systematically to simulated data showed at which intensity level the Kerr term become negligible and thus need not be included in the reconstruction process. This has further facilitated the accurate reconstruction of the SFI contribution to the plasma from experimentally measured time-resolved low-order wave mixing signals, reinforcing the validity of our approach. Therefore, we see application potential of this method for online diagnosis of laser micromachining.

As the next logical step, we investigated the effects of nonlinear pulse propagation, including electron scattering from the bulk lattice and impact ionization on the

plasma formation. To address the high sensitivity of the system to the electric field in the optical breakdown regime, a self-consistent electromagnetic field simulation based on a dispersive nonlinear Lorentz model for the finite-difference-time-domain (FDTD) method was implemented. It was further extended by coupled rate equations for the collision and ionization dynamics which inherently includes any reflected field contributions from interfaces or the plasma itself. Examining the energy balance of the simulation, the dominant role of collisions in the absorption of long pulses was contrasted by the increasing relative significance of the injection current for the absorption of few-cycle pulses. Furthermore, our simulation allowed for the detailed analysis of the spatio-temporal structure of the emerging plasma. In particular, the feedback of the emerging plasma mirror was examined and shown to lead to a spatial shift of field and plasma hot spots as well as in the impact ionization rate by a quarter wavelength opposite to the propagation direction. These results demonstrate new opportunities to control plasma formation with shaped laser fields in order to from sub-wavelength structures and gratings.

Lastly, to further refine our understanding of the plasma-induced radiation, we proposed harmonic emission from the front interface as a scenario to experimentally exclude propagation effects from the local ionization response. This approach circumvents the usual challenge that the ionization response itself leads to nonlinear pulse propagation, which is even imprinted on weak probe fields via nonlinear wave-mixing. Following this idea, we compared the transmitted and reflected harmonic fields by means of our self-consistent simulation and extracted distinct amplitude and phase characteristics of the interface response that are specific to the thickness of the reflecting nonlinear layer. The absence of propagation effects in the reflection scenario will in particular help to better separate the injection response from harmonics generated by conduction band anharmonicities or electron-hole recombination, for example, to determine conditions where these mechanisms become important.

Perspectively, we see two relevant directions to further improve the description of the nonlinear medium response. One route, broadly considered in the literature, is to incorporate the quantum-mechanical nature of the local response, e.g. [88, 164] and [KLPF20]. So far, the quantum mechanical analysis within this research field was mainly concentrated on harmonic generation at high orders where, for example, details of ultrafast electron dynamics could be related to material-specific intra- and interband effects. In this work, however, we focused the analysis of our TDSE simulation on low harmonic orders and identified the injection contribution as one part of the intra-conduction-band current that is generally important for the absorption of short driving pulses. This suggests that a more detailed understanding of the non-classical behavior of electrons and holes may provide routes to refine the description of the local nonlinear response by effective models. The second route, concerning the effect of propagation and distribution of the driving field on low-order harmonic emission, is much less considered in the literature. Here, our FDTD simulation, extended by local models for the fully-reversible medium response, collisions and ionization, provided an efficient means for the self-consistent treatment of the

complex field-induced plasma formation. Conducting full three-dimensional simulations with this tool will prospectively allow to capture the focusing of the incident field and the evolution of the plasma geometry at interfaces and in the bulk volume. To ultimately combine both directions requires experimentally accessible benchmark scenarios for advanced simulation models. Here, the simultaneous analysis of transmitted and reflected fields from the interfaces where the nonlinear radiation response can be studied with and without propagation effects at fixed irradiation conditions, presents a promising scenario.

A. Identification of Tunneling-Induced Low-Order Harmonics

A.1. Difference quotient for ensemble derivative

Formally, the product rule for an ensemble derivative follows from the difference quotient, where the definition of the arithmetic mean, $\langle x \rangle = \frac{1}{N} \sum_{i=1}^N x_i$ is used,

$$\frac{d}{dt} N \langle x \rangle = \lim_{\Delta t \rightarrow 0} \frac{N(t + \Delta t) \langle x \rangle(t + \Delta t) - N(t) \langle x \rangle(t)}{\Delta t} \quad (\text{A.1})$$

$$= \lim_{\Delta t \rightarrow 0} \frac{\sum_{\text{ex. } i} x_i(t + \Delta t) + \sum_{\text{new } i} x_i(t + \Delta t) - \sum_{\text{ex. } i} x_i(t)}{\Delta t} \quad (\text{A.2})$$

$$= \lim_{\Delta t \rightarrow 0} \frac{\sum_{\text{ex. } i} x_i(t + \Delta t) - \sum_{\text{ex. } i} x_i(t)}{\Delta t} + \frac{\sum_{\text{new } i} x_i(t + \Delta t)}{\Delta t} \quad (\text{A.3})$$

$$= \lim_{\Delta t \rightarrow 0} \sum_{\text{ex. } i} \frac{\Delta x_i}{\Delta t} + \frac{\Delta N \langle x_0 \rangle_{\text{new}}}{\Delta t} \quad (\text{A.4})$$

$$= N \left\langle \frac{\partial x}{\partial t} \right\rangle_{\text{ex.}} + \frac{\partial N}{\partial t} \langle x_0 \rangle_{\text{new}}. \quad (\text{A.5})$$

As in the main text, the sum is decomposed into elements existing (ex.) at time t and ensemble elements generated in the interval $[t, t + \Delta t]$ (new). The formal result (A.5) is used in eq. (2.6).

B. Local Strong-Field Medium Response

B.1. Fields emitted from currents in a thin sheet

We start from the inhomogenous wave equation, here written with a source current for the complex positive frequency part (defined in eq. (3.3)),

$$\frac{\partial^2}{\partial z^2} \mathbf{E}^+(z, t) - \frac{n^2}{c^2} \frac{\partial^2}{\partial t^2} \mathbf{E}^+(z, t) = \frac{1}{c^2 \epsilon_0} \frac{\partial}{\partial t} \mathbf{J}^+(z, t), \quad (\text{B.1})$$

that is restricted to a thin sheet, with thickness d_z less than the driving wavelength, and pointing along one Cartesian axis,

$$\mathbf{J}^+(z, t) = \begin{cases} \mathbf{e}_x \frac{\hat{J}}{2} e^{i\omega t} & \text{if } 0 < z < d_z < \lambda = \frac{c\omega}{2\pi}, \\ 0 & \text{otherwise.} \end{cases} \quad (\text{B.2})$$

Outside of the foil, waves propagate away from the surface. Due to symmetry, the differential equation is fulfilled by the following plane waves,

$$E_x^+(z, t) = \begin{cases} A_R e^{i\omega(t - \frac{n_{\text{ior}} z}{c})} & \text{for } z \geq d_z, \\ A_L e^{i\omega(t + \frac{n_{\text{ior}} z}{c})} & \text{for } z \leq 0. \end{cases} \quad (\text{B.3})$$

To determine the complex amplitude coefficients A_L and A_R , describing the wave left and right of the foil, the differential equation is solved in the medium by integrating the inhomogeneous wave equation along the optical axis

$$\left. \frac{\partial E_x^+}{\partial z} \right|_{z=d_z} - \left. \frac{\partial E_x^+}{\partial z} \right|_{z=0} - \frac{n_{\text{ior}}^2}{c^2} \frac{\partial^2}{\partial t^2} \int_0^{d_z} E_x^+(z, t) dz = \int_0^{d_z} dz \frac{1}{c^2 \epsilon_0} \frac{\partial}{\partial t} J_x^+(z, t). \quad (\text{B.4})$$

Here the integral on the left is much smaller than the integral on the right, which is seen as follows. We approximate the field under the integral by its maximum $E_x(z) \leq \max(E_x(z))$. Further, we assume a finite electrical current I in the foil, such that the homogeneous current density is given by $J_x = \frac{I}{d_z L_y}$, with L_y being the macroscopic size of the foil,

$$\left. \frac{\partial E_x^+}{\partial z} \right|_{z=d_z} - \left. \frac{\partial E_x^+}{\partial z} \right|_{z=0} - d_z \max_z \left(\frac{n_{\text{ior}}^2}{c^2} \frac{\partial^2}{\partial t^2} E_x^+(z, t) \right) = \frac{1}{c^2 \epsilon_0} \frac{\partial}{\partial t} \frac{I^+}{L_z}. \quad (\text{B.5})$$

While the right-hand side is fully given by macroscopic quantities, the third term on the left can be made arbitrarily small by decreasing the thickness. Into the remaining

first and second term of eq. (B.4) we inset the ansatz for the field (B.3) and obtain,

$$-\frac{i\omega n}{c}(A_R + A_L)e^{i\omega(t - \frac{n_{\text{ior}}z}{c})} = \frac{d_z}{c^2\varepsilon_0} \frac{\partial}{\partial t} J_x^+(z, t). \quad (\text{B.6})$$

Setting $z = 0$ and recognizing the symmetry of the system, coefficients on the left and on the right are found to be equal, $A_R = A_L$, which allows to determine the complex field,

$$E_x^+(z, t) = A_R e^{i\omega(t - \frac{|z|}{c})} = -\frac{d_z}{2n_{\text{ior}}c\varepsilon_0} \frac{\hat{j}}{2} e^{i\omega(t - \frac{|z|}{c})}. \quad (\text{B.7})$$

Here, the current needs to be evaluated at the retarded time $t_r = t - \frac{|z|}{c}$. To determine the real-valued field, the complex conjugate is added,

$$E_x(z, t) = E_x^+ + (E_x^+)^* = -\frac{d_z}{2n_{\text{ior}}} \sqrt{\frac{\mu_0}{\varepsilon_0}} J_x(t_r). \quad (\text{B.8})$$

The square root term is known as the vacuum impedance. From this result, it is concluded that for sufficiently thin media, the harmonics' amplitude and phase are given by the negative current density in both directions, as further examined in eq. (3.6) in the main text and also used in the discussion of Fig. 7.1.

B.2. Amplitude and phase of the Hertzian dipole

It is well known that the radiation emitted by each frequency component of a dipole $\mathbf{p}^+(t) = \mathbf{p}_0 e^{i\omega t}$, is given by the Hertzian dipole field [143],

$$\mathbf{E}^+(\mathbf{r}, t) = \frac{e^{i(\omega t - \frac{\omega}{c}r)}}{4\pi\varepsilon_0\varepsilon_r} \left[(3\mathbf{e}_r(\mathbf{e}_r \cdot \mathbf{p}_0) - \mathbf{p}_0) \left(\frac{1}{r^3} + \frac{i\omega}{c} \frac{1}{r^2} \right) - (\mathbf{e}_r \times \mathbf{p}_0) \times \mathbf{e}_r \left(\frac{i\omega}{c} \right)^2 \frac{1}{r} \right] \quad (\text{B.9})$$

with near-, intermediate- and far-field contributions on the RHS, scaling with $\frac{1}{r^3}$, $\frac{1}{r^2}$ and $\frac{1}{r}$, respectively. It is clear that without acceleration of charge, no fields are emitted at all. However, only the far-field contribution shows with the $(i\omega)^2$ term a one-to-one correspondence of spectral amplitude fall-off and phase with the local, negative dipole acceleration. The intermediate field corresponds with $(i\omega)$ to the dipole velocity and the near-field to the dipole itself. This characteristic property of the Hertzian dipole is used as a reference for the discussion in sect. 3.2.3 and sect. 3.6.3.

B.3. Harmonic emission in Gaussian beam scenario

The spectral weight structure of harmonics emitted from a Gaussian beam is investigated. It is shown that the dipole-velocity-like scaling holds as long as the full beam profile is captured by the detector. This fact might be at first glance surprising as the source of emission, can be thought of as a superposition of Hertzian dipoles with known ω^2 dependence in the far field. We find that the geometric effect discussed in the following is essential to understand how the far field term of the Hertzian dipole that scales as ω^2 is reduced to ω . We depart from the amplitude E_0 of one harmonic that is given at the beam waist by the thin film result (B.7),

$$E_0 = E_h^+ = \frac{dz}{2n_{\text{ior}}c\epsilon_0} \frac{\hat{J}_h}{2} e^{i\omega(t-\frac{|z|}{c})}, \quad (\text{B.10})$$

$$= \frac{dz}{2n_{\text{ior}}c\epsilon_0} \frac{i\omega\hat{P}_h}{2} e^{i\omega(t-\frac{|z|}{c})}. \quad (\text{B.11})$$

Axial field amplitude The first goal is to relate the field amplitude on the optical axis to the amplitude of the local polarization, \hat{P} , using Gaussian beams,

$$E(r, z, \omega) = E_0(\omega) \frac{w_0}{w(z, \omega)} \cdot e^{-\left(\frac{r}{w(z)}\right)^2} \cdot e^{-ik\frac{r^2}{2R(z)}} \cdot e^{-i(kz-\zeta(z))}. \quad (\text{B.12})$$

The beam width radius,

$$w(z, \omega) = w_0 \sqrt{1 + \left(\frac{z}{z_R}\right)^2}, \quad (\text{B.13})$$

with Rayleigh length,

$$z_R(\omega) = \frac{\pi \cdot w_0^2}{\lambda} = \frac{w_0^2 \omega}{2c}, \quad (\text{B.14})$$

is close to the origin, i.e. for small z , independent of frequency

$$w(z) \approx w_0. \quad (\text{B.15})$$

Inserting eqs. (B.15), (B.11) into (B.12) it is found that in the near field, the amplitude on the beam axis scales as the dipole velocity, i.e. $E(0, z < z_R) \sim \omega\hat{P}_h$.

The situation is different in the far field, $z \gg z_R$, where the beam-width radius is inversely proportional to the Rayleigh length,

$$w(z) \approx w_0 \frac{z}{z_R} = \frac{2zc}{w_0\omega}. \quad (\text{B.16})$$

Inserting this expression into eq. (B.12), the on-axis amplitude ($r = 0$) reads,

$$|E(0, z \gg z_R, \omega)| = |E_{\text{far}}(0, z, \omega)| = E_0 \frac{w_0}{w(z)} \approx E_0 \frac{z_R}{z} = E_0 \frac{w_0^2 \omega}{2cz}. \quad (\text{B.17})$$

This equation provides the distinct, dipole-acceleration-like scaling of the on-axis far-field, $E(0, z \gg z_R) \sim \omega^2 \hat{P}_h$. Physically this is because high frequencies are more collimated due to a higher Rayleigh length, as discussed in the main text at eq. (3.10) and shown in Fig. 3.3.

Transverse integrated field amplitude Next, the Gaussian beam eq. (B.12) and the far-field width radius eq. (B.16) are used to understand why the integrated far-field yield (intensity integrated over detector area) scales like the dipole velocity. In our scenario a collimation lense in front of the detector (L2 in Fig. 2.2) ensures that the full radial beam profile is captured. This simplifies the integration limits in the transverse direction, that are set to $\pm\infty$ for mathematical convenience. Applying the Gaussian integral,

$$\int_{-\infty}^{\infty} dx \int_{-\infty}^{\infty} dy e^{-\frac{x^2+y^2}{w(z)^2}} = \pi w(z)^2, \quad (\text{B.18})$$

to the beam amplitude profile,

$$|E(r, z \gg z_R, \omega)| = E_0(\omega) \frac{w_0}{w(z, \omega)} \cdot e^{-\left(\frac{r}{w(z)}\right)^2}, \quad (\text{B.19})$$

yields the integrated field amplitude,

$$\int_{-\infty}^{\infty} dx \int_{-\infty}^{\infty} dy |E(r, z)| = E_0 \pi w_0 w(z). \quad (\text{B.20})$$

The far-field at the detector follows by inserting eq. (B.16) for $w(z)$,

$$\int_{-\infty}^{\infty} dx \int_{-\infty}^{\infty} dy |E(r, z \gg z_R)| = E_0 \pi \frac{2cz}{\omega} \quad (\text{B.21})$$

Here the ω in the denominator cancels the ω -factor from the thin film result when substituting the eq. (B.11) for E_0 . This shows that the integrated field amplitude scales with the dipole (excursion length). Furthermore, it is seen that the integrated field amplitude grows with distance. This is expected as the detected power must be independent of the detector distance as shown in the next step where we determine the corresponding relation harmonic yield and local current.

Scaling of detected harmonic yield Employing the Gaussian integral to the squared field connects the detected harmonic yield $Y(\omega)$,

$$Y(\omega) \sim \int_{-\infty}^{\infty} dx \int_{-\infty}^{\infty} dy |E(r, z \gg z_R)|^2 = \pi w_0^2 \frac{|E_0(\omega)|^2}{2}, \quad (\text{B.22})$$

with the amplitude at the beam waist $|E_0(\omega)|$. Because the field at the waist is proportional to the current $E_0 \sim J$ the detected yield scales as

$$Y \sim E_0^2 \sim J^2. \quad (\text{B.23})$$

It is concluded from eq. (B.22) that beam propagation does not change the spectrum of the integrated yield. Therefore, the measured harmonic spectrum is identical to the spectrum at the beam waist where the signal is generated. This result is used to determine the proportionality factor between the intensity in the 1D plane wave scenario and in the (transverse integrated) Gaussian beam scenario, as discussed in eq. (3.12) of the main text.

B.4. Calculation of circular pump polarization direction

Degeneracy of $n = 1$ signal in circular-linear configuration

From the constraints discussed in eq. (3.21), it follows that one positive circular pump photon must be in the vectorial component (last box where no scalar product is taken). Another positive pump photon is paired with the probe. Remaining positive pump photons must be matched with a negative pump in the remaining scalar products. In total there are $N_{\text{sc}} = \frac{m-1}{2}$ scalar products.

$$D_{n=1}^{\circ|} = \binom{N_{\text{sc}}}{1} \mathcal{P}[\mathbf{E}_o^+ \mathbf{E}_{\text{pr}}^+] \left(\mathcal{P}[\mathbf{E}_o^+ \mathbf{E}_o^-] \right)^{N_{\text{sc}}-1} \quad (\text{B.24})$$

The permutation \mathcal{P} of two distinct fields yields in each case a factor of 2. The binomial coefficient in the front accounts for the fact that the first scalar product permutes with all others. Resubstituting the number of scalar products yields

$$D_{n=1}^{\circ|} = N_{\text{sc}} 2^{N_{\text{sc}}} = (m-1) 2^{\frac{m-3}{2}}, \quad (\text{B.25})$$

which is the result used in eq. (3.24). The m -th order polarization for the $n = 1$ signal then reads,

$$\mathbf{P}_{\text{NL}, n=1}^{(m), \text{circ}, \text{cf}} = \varepsilon_0 \chi^{(m)} D_{n=1}^{\circ|} \left(\mathbf{E}_o^+ \mathbf{E}_o^- \right)^{N_{\text{sc}}-1} \left(\mathbf{E}_o^+ \mathbf{E}_{\text{pr}}^+ \right) \mathbf{E}_o^+ + c.c. . \quad (\text{B.26})$$

Inserting positive and negative frequency contributions $\mathbf{E}_{\text{pr}}^+ = \frac{\hat{\mathbf{E}}_{\text{pr}}}{2} e^{i\omega_{\text{pr}}t}$, c.f. eq. (3.13), simplifies the expression,

$$\mathbf{P}_{\text{NL},n=1}^{(m),\text{circ,cf}} = \varepsilon_0 \chi^{(m)} D_{n=1}^{\text{ol}} \left(\frac{\hat{E}_{\text{pu}}^2}{2} \right)^{N_{\text{sc}}-1} \frac{\hat{E}_{\text{pu}} \hat{E}_{\text{pr}}}{4} \mathbf{E}_{\text{o}}^+ e^{i(\omega_{\text{pu}}+\omega_{\text{pr}})t} + c.c. \quad (\text{B.27})$$

$$= \varepsilon_0 \chi^{(m)} \frac{m-1}{4} \hat{E}_{\text{pu}}^{m-1} \hat{E}_{\text{pr}} \frac{\mathbf{e}_x + i\mathbf{e}_y}{2} e^{i(2\omega_{\text{pu}}+\omega_{\text{pr}})t} + c.c. \quad (\text{B.28})$$

This relation is used to calculate intensity ratios (3.27) – (3.28).

B.4.1. Intensity ratio: Circular versus Perpendicular

To calculate intensity ratios, the perpendicular polarization configuration,

$$\mathbf{P}_{\text{NL},n=1}^{(m),\perp} = \varepsilon_0 \chi^{(m)} D_{n=1}^{\perp} \left(\frac{\hat{E}_{\text{pu}}}{2} \right)^{m-1} \mathbf{E}_{\text{pr}}^+ e^{i2\omega_{\text{pu}}t} + c.c. \quad (\text{B.29})$$

is chosen as a reference. The numerator of the intensity ratio at constant field amplitude (cf) follows by taking both polarization directions of the circular polarization, eq. (B.28), into account,

$$\frac{I_{n=1}^{\text{circ,cf}}}{I_{n=1}^{\perp}} = \frac{|\mathbf{P}_{\text{NL},n=1}^{(m),\text{circ,cf}}|^2}{|\mathbf{P}_{\text{NL},n=1}^{(m),\perp}|^2} = \frac{2 \left(\frac{m-1}{4} \right)^2}{\left(\frac{(m-1)!}{\left(\frac{m-1}{2} + 1 \right)! \left(\frac{m-1}{2} - 1 \right)!} \right)^2} = 2^{2m-5} \left[\frac{\left(\frac{m-1}{2} + 1 \right)! \left(\frac{m-1}{2} - 1 \right)!}{(m-2)!} \right]^2. \quad (\text{B.30})$$

For the scenario of constant pump intensity (ci) when switching from linear to circular polarization, the RHS of eq. (B.28) has to be multiplied by the factor $1/\sqrt{2}^{m-1}$. The intensity ratio then reads,

$$\frac{I_{n=1}^{\text{circ,ci}}}{I_{n=1}^{\perp}} = 2^{m-4} \left[\frac{\left(\frac{m-1}{2} + 1 \right)! \left(\frac{m-1}{2} - 1 \right)!}{(m-2)!} \right]^2. \quad (\text{B.31})$$

Comparison with the numerical calculation shows excellent agreement (main text Fig. 3.5), verifying the degeneracy analysis. The results in eqs. (B.30) and (B.31) are discussed in section 3.3.6.

B.5. Generalization of intensity ratios for $n > 1$ mixing signals

We depart from the full formal expressions, used to prepare Fig. 3.7,

$$\frac{I_{\text{Inj},n=1}^{\parallel}}{I_{\text{Br},n=1}^{\parallel}} = \left[\frac{\frac{2}{s} \left(2 + \frac{\omega_{\text{pr}}}{\omega_{\text{pu}}}\right)}{\frac{1}{\left(\frac{s}{2}+1\right)\left(\frac{s}{2}-1\right)} + \frac{2}{\left(3+\frac{\omega_{\text{pr}}}{\omega_{\text{pu}}}\right)\left(\frac{s}{2}+1\right)} + \frac{2}{\left(1+\frac{\omega_{\text{pr}}}{\omega_{\text{pu}}}\right)\left(\frac{s}{2}-1\right)}} \frac{E_g}{U_p} \right]^2, \quad (\text{B.32})$$

$$\frac{I_{\text{Inj},n=1}^{\perp}}{I_{\text{Br},n=1}^{\perp}} = \left[\left(2 + \frac{\omega_{\text{pr}}}{\omega_{\text{pu}}}\right) \left(\frac{1}{2} + \frac{2}{s} - \frac{3}{2s-2}\right) \frac{E_g}{U_p} \right]^2, \quad (\text{B.33})$$

$$\frac{I_{\text{Inj},n=1}^{\circ}}{I_{\text{Br},n=1}^{\circ}} = \left[\frac{1 - \frac{2}{s}}{4} \left(\frac{\omega_{\text{pr}}^2}{\omega_{\text{pu}}^2} + \frac{3\omega_{\text{pr}}}{\omega_{\text{pu}}} + 2\right) \frac{E_g}{U_p} \right]^2. \quad (\text{B.34})$$

where degeneracy factors from the previous section have been inserted. According to the false color plot, this set of equations, (B.32)-(B.34), provides that injection is the dominant contribution for lowest order ($n = 1$) wave mixing. Next, we show that for higher orders n , the ratio even increases, which ultimately allows us to drastically simplify the interpretation of the measured intensity ratio.

Generalization of intensity ratio to $n > 1$ For higher signal orders $n > 1$ the number of absorbed pump photons with $e^{+i\omega_{\text{pu}}t}$ increases, whereas the number of $e^{-i\omega_{\text{pu}}t}$ terms decreases. Combinatorial analysis shows that the denominator of the degeneracy factor is modified,

$$\frac{\partial J_{\text{inj},n}^{\perp}}{\partial t} = \frac{n_0 E_g \hat{\Gamma}}{\hat{E}^s} \frac{(s-2)!}{\left(\frac{s}{2}-1+n\right)!\left(\frac{s}{2}-1-n\right)!} i\omega_{\text{sig},1} \frac{E_{\text{pu}}^{s-2} E_{\text{pr}}}{2^{s-2}} \frac{e^{i\omega_{\text{sig},1}t}}{2} + c.c. \quad (\text{B.35})$$

$$\frac{\partial J_{\text{Br},n}^{\perp}}{\partial t} = \frac{q^2 n_0 \hat{\Gamma}}{m_e \hat{E}^s} \frac{\frac{\omega_{\text{sig},1}}{2\omega_1} s!}{\left(\frac{s}{2}+n\right)!\left(\frac{s}{2}-n\right)!} \frac{1}{i\omega_{\text{sig},1}} \frac{E_{\text{pu}}^s E_{\text{pr}}}{2^s} \frac{e^{i\omega_{\text{sig},1}t}}{2} + c.c. \quad (\text{B.36})$$

such that the generalized intensity ratio illustrates, that the relative contribution of injection grows roughly quadratically with harmonic order n

$$\frac{I_{\text{Inj},n}^{\perp}}{I_{\text{Br},n}^{\perp}} = \left[\left(n + \frac{\omega_2}{\omega_1}\right) \left(1 + \frac{1}{s} - \frac{4n-1}{s(s-1)}\right) \frac{E_g}{U_p} \right]^2. \quad (\text{B.37})$$

Note, that the negative term in the second bracket is $\frac{4n-1}{s(s-1)} \ll 1$ negligible for low-order harmonics. Also for the parallel configuration we find a dominant contribution for injection for low order signals $n < \frac{s}{2}$,

$$D_{\text{Inj},n}^{\parallel} = \frac{(s-1)!}{\left(\frac{s}{2} + n - 1\right)! \left(\frac{s}{2} - n - 1\right)!}, \quad (\text{B.38})$$

$$D_{\text{Br},n}^{\parallel} = \frac{\frac{\omega_{\text{sig},1}}{2n\omega_1} s!}{\left(\frac{s}{2} + n\right)! \left(\frac{s}{2} - n\right)!} + \frac{\frac{\omega_{\text{sig},1}}{(2n+1)\omega_1 + \omega_2} s!}{\left(\frac{s}{2} + n\right)! \left(\frac{s}{2} - n - 1\right)!} + \frac{\frac{\omega_{\text{sig},1}}{(2n-1)\omega_1 + \omega_2} s!}{\left(\frac{s}{2} + n - 1\right)! \left(\frac{s}{2} - n\right)!}, \quad (\text{B.39})$$

$$\frac{I_{\text{Inj},n}^{\parallel}}{I_{\text{Br},n}^{\parallel}} = \left[\frac{\frac{2}{s} \left(2n + \frac{\omega_2}{\omega_1}\right)}{\frac{1}{n\left(\frac{s}{2} + n\right)\left(\frac{s}{2} - n\right)} + \frac{2}{(2n+1 + \frac{\omega_2}{\omega_1})\left(\frac{s}{2} + n\right)} + \frac{2}{(2n-1 + \frac{\omega_2}{\omega_1})\left(\frac{s}{2} - n\right)}} \frac{E_g}{U_p} \right]^2. \quad (\text{B.40})$$

For circular pump polarization, such an analysis is not relevant, because wave-mixing with a single probe photon simply vanishes for $n > 1$. These arguments are used in the discussion of Fig. 3.7.

B.6. Temporal width and delay dependence of wave-mixing signals

The shape of the output signals in a delay-dependent pump-probe spectrum is understood in terms of the temporal field envelope of both incident pulses. The duration of the output signal as well as its width on the delay axis are determined next.

Multiplication of two Gaussians Two Gaussian pulses are considered with intensity full-width-half-maximum envelope τ_1 and τ_2 separated by the delay τ . For an output wave-mixing signal that is generated by $N_1 = N_1^+ + N_1^-$ photons from the first, and by $N_2 = N_2^+ + N_2^-$ photons from the second pulse, the output envelope reads,

$$\hat{E}_{\text{out}}(t) \sim \left(\hat{E}_1(t)\right)^{N_1} \left(\hat{E}_2(t)\right)^{N_2} \sim \left(e^{-2\ln(2)\frac{t^2}{\tau_1^2}}\right)^{N_1} \left(e^{-2\ln(2)\frac{(t-\tau)^2}{\tau_2^2}}\right)^{N_2}. \quad (\text{B.41})$$

To determine the temporal width of the output signal, it is sufficient to compute its time constant and neglect all prefactors. Introducing the suitable substitution $a = \frac{\sqrt{2N_1 \ln(2)}}{\tau_1}$, $b = \frac{\sqrt{2N_2 \ln(2)}}{\tau_2}$, we find,

$$\hat{E}_{\text{out}}(t) \sim e^{-(at)^2} e^{-(b(t-\tau))^2} = \exp\{-a^2 t^2 - b^2 t^2 + 2b^2 \tau t - b^2 \tau^2\}, \quad (\text{B.42})$$

$$= \exp\left\{-\underbrace{(a^2 + b^2)}_{c^2} \left(t^2 - 2 \underbrace{\frac{b^2 \tau}{c^2}}_{\tilde{\tau}} t + \tilde{\tau}^2 - \tilde{\tau}^2 + \frac{b^2 \tau^2}{c^2}\right)\right\}, \quad (\text{B.43})$$

$$= \underbrace{e^{-(c(t-\tilde{\tau}))^2}}_{G(t,\tilde{\tau})} \underbrace{e^{-c^2(\tau\tilde{\tau}-\tilde{\tau}^2)}}_{A_{\text{out}}(\tau)}. \quad (\text{B.44})$$

Eq. (B.44) shows, firstly, that the output field has again a Gaussian time envelope $G(t, \tilde{\tau})$ peaked at $\tilde{t} = \frac{b^2}{c^2} \tau = \frac{\tau_1^2}{\tau_1^2 + \tau_2^2} \tau$ and secondly, a delay-dependent term for the harmonic amplitude $A_{\text{out}}(\tau)$.

Identifying the width of the harmonic pulse The time constant of the output field $c^2 = a^2 + b^2$ is determined by re-substituting the temporal width of the input field and the number of photons each field contributes,

$$\tau_{\text{out}} = \sqrt{\frac{2 \ln(2)}{c^2}} = \frac{1}{\sqrt{\frac{N_1}{(\tau_1)^2} + \frac{N_2}{(\tau_2)^2}}}. \quad (\text{B.45})$$

Thus the duration of the signal does not depend on delay. However, the amplitude of output signal A_{out} , given by the second part of Eq. (B.44), shows a dependence on τ . This amplitude has also a Gaussian shape, but now in the delay domain, and can be measured in a delay scan. The width of the signal on the delay axis is determined by similarly from eq. (B.44) and (B.43),

$$A_{\text{out}}(\tau) = e^{-c^2(\tau\tilde{\tau}-\tilde{\tau}^2)} = e^{-(b^2 - \frac{b^4}{a^2+b^2})\tau^2} = \exp\left\{-\underbrace{\left(\frac{a^2b^2}{a^2+b^2}\right)}_{d^2}\tau^2\right\} = e^{-(d\tau)^2}. \quad (\text{B.46})$$

In the last term on the RHS the time constant $d = \frac{\sqrt{2 \ln(2)}}{\tau_{\text{delay}}}$ is identified. Here τ_{delay} denotes width on the delay axis, whereas τ is the delay between the two pulses, c.f. eq. (B.41).

Identification of the delay dependence The delay width also follows from re-substitution

$$\tau_{\text{delay}} = \frac{\sqrt{2 \ln(2)}}{d} = \sqrt{2 \ln(2) \frac{a^2 + b^2}{(ab)^2}} = \sqrt{\frac{(\tau_1)^2}{N_1} + \frac{(\tau_2)^2}{N_2}}. \quad (\text{B.47})$$

Relation to effective order Note that all four widths are connected by the following relation that may allow for a consistency check,

$$d^2 = \frac{a^2b^2}{c^2} \quad \Rightarrow \quad \frac{\tau_1 \tau_2}{\tau_{\text{out}} \tau_{\text{delay}}} = \sqrt{N_1 N_2}. \quad (\text{B.48})$$

If it is ensured that there is only one probe photon ($N_2 = 1$), the width on the delay axis Eq. (B.47) as well as the temporal duration of the output Eq. (B.45) are directly

connected to the effective order ($m = N_1 + N_2$),

$$\tau_{\text{delay}}^{(m)} = \sqrt{\frac{(\tau_1)^2}{m-1} + (\tau_2)^2}, \quad (\text{B.49})$$

$$\tau_{\text{out}}^{(m)} = \frac{\tau_1 \tau_2}{\sqrt{(m-1)(\tau_2)^2 + (\tau_1)^2}}. \quad (\text{B.50})$$

This result, eq. (B.49) -(B.50), is further examined in section 3.5 of the main text.

C. Collisional Effects in the Extreme Nonlinear Response

C.1. Phase of quiver motion according to Drude model

The well-known phase relation of the Drude model system [117] is summarized starting from, the equation of motion, eq. (4.1),

$$\dot{v} + \gamma v = \frac{qE}{m}, \quad (\text{C.1})$$

with collision rate $\gamma = \frac{1}{\tau}$ and collision time τ corresponds to a driven harmonic oscillator with vanishing resonance frequency,

$$\ddot{x} + \gamma \dot{x} + \omega_0^2 x = \frac{\hat{E}}{m} e^{i\omega t}. \quad (\text{C.2})$$

A harmonic ansatz $x = \hat{x} e^{i\omega t}$ yields the widely known dipole excursion

$$x(t) = \frac{q\hat{E}/m}{\omega_0^2 - \omega^2 + i\gamma\omega} e^{i\omega t}, \quad (\text{C.3})$$

$$= \frac{q\hat{E}/m}{(\omega_0^2 - \omega^2)^2 + (\gamma\omega)^2} (\omega_0^2 - \omega^2 - i\gamma\omega) e^{i\omega t} = \hat{x} e^{i(\omega t + \phi)}, \quad (\text{C.4})$$

$$\hat{x}(\omega) = \frac{q\hat{E}/m}{\sqrt{(\omega_0^2 - \omega^2)^2 + (\gamma\omega)^2}}, \quad (\text{C.5})$$

and the dipole phase

$$\tan \phi = \frac{-\gamma\omega}{\omega_0^2 - \omega^2}, \quad (\text{C.6})$$

$$\phi = \text{atan2}(-\gamma\omega, \omega_0^2 - \omega^2). \quad (\text{C.7})$$

The dipole phase is always non-positive $-\pi \leq \phi \leq 0$ indicating that the dipole lags behind the driver depending on driving frequency and damping coefficient. For the vanishing resonance case, $\omega_0 = 0$, relevant to the Drude model, the phase lag grows with damping,

$$\phi = \text{atan2}(-\gamma, -\omega). \quad (\text{C.8})$$

The function atan2 is the arcus tangent that takes the signs of both catheti in the argument into account. This dipole phase is shown as a solid blue line in Fig. 4.1. For the discussion of the Brunel response the phase of the dipole velocity, that runs a

quarter period ahead,

$$\phi_v = \text{atan2}(-\gamma, -\omega) + \frac{\pi}{2}, \quad (\text{C.9})$$

is used in eq. (4.2) and eq. (4.4).

C.2. Gabor transform

The Gabor transform [165] is a short-time Fourier transform,

$$G(\omega, \tau) = \int dt f(t) e^{-i\omega t} e^{-4 \ln(2) \left(\frac{t-\tau}{\tau_{\text{FWHM}}^{\text{Gabor}}} \right)^2}, \quad (\text{C.10})$$

where time resolution is obtained from the Gaussian window function of width $\tau_{\text{FWHM}}^{\text{Gabor}}$, seen in the last term. The Gabor transform is employed for the time-resolved spectral analysis shown in Fig. 4.3.

D. Harmonics from Nonlinear Reflection

We start the derivation of the reflected harmonic with the nonlinear wave equation (3.1), repeated here for convenience,

$$\nabla \times (\nabla \times \mathbf{E}) + \frac{1}{c^2} \frac{\partial^2 \mathbf{E}}{\partial t^2} = -\frac{1}{\varepsilon_0 c^2} \left[\frac{\partial^2 \mathbf{P}_L}{\partial t^2} + \frac{\partial^2 \mathbf{P}_{NL}}{\partial t^2} \right]. \quad (\text{D.1})$$

This equation is simplified by writing the linear polarization contribution as reduced phase velocity $c_{\text{med}} = \frac{c}{n_{\text{ior}}} = \mu_0 \varepsilon_0 \varepsilon_r(\omega_h)$ where the dielectric function is evaluated at the harmonic frequency ω_h of interest,

$$\nabla \times (\nabla \times \mathbf{E}_h) + \mu_0 \varepsilon_0 \varepsilon_r(\omega_h) \frac{\partial^2 \mathbf{E}_h}{\partial t^2} = -\mu_0 \frac{\partial^2 \mathbf{P}_{NL,h}}{\partial t^2}. \quad (\text{D.2})$$

The solution of this differential equation is given by the superposition of a homogeneous and an inhomogeneous solution, as given in [156] and detailed below.

Homogeneous solution The trivial solution to the homogeneous equation, where the source term on the right of eq. (D.2) is set to zero, is given by plane wave,

$$\mathbf{E}_{h,\text{hom}}^T = \mathbf{e}^T \hat{E}_h^T \expi(\mathbf{k}_h^T \mathbf{r} - \omega_h t). \quad (\text{D.3})$$

Here the label T indicates that the homogeneous wave has been written down for the transmitted wave. The same equation holds for the reflected wave (*R*), with wavevector k_h^R instead of medium wavevector k_h^T . The inhomogeneous solution, that co-propagates with the driving field \mathbf{E} through the medium has formally a similar structure but modified amplitude, polarization, and wave vector.

Inhomogeneous solution Assuming a general m^{th} order nonlinear polarization source,

$$\mathbf{P}_{NL,h}^{(m)}(\mathbf{r}, t) = \hat{P}_{NL,h} \mathbf{e}_P \expi(\mathbf{k}_P \mathbf{r} - \omega_h t), \quad (\text{D.4})$$

with wave vector \mathbf{k}_P , polarization vector \mathbf{e}_P , and a polarization amplitude for example given by $\hat{P}_{NL} = \varepsilon_0 \chi^{(m)} \hat{E}_1^m$, one particular solution for the transmitted harmonic field that fulfills eq. (D.1) is given by,

$$\mathbf{E}_{h,\text{inh}}^T = -\frac{\hat{P}_{NL} \left(\frac{\omega_h}{c}\right)^2}{(k_h^T)^2 - (k_P)^2} \left[\mathbf{e}_P - \frac{\mathbf{k}_P(\mathbf{k}_P \mathbf{e}_P)}{(k_P)^2} \right] \expi(\mathbf{k}_P \mathbf{r} - \omega_h t), \quad (\text{D.5})$$

as verified in the following.

Verification of the inhomogeneous solution First, the double curl of the wave equation is simplified and acted on the inhomogeneous solution. Expressing rot rot by grad div minus Laplace operator,

$$\nabla \times (\nabla \times \mathbf{E}) = \nabla(\nabla \cdot \mathbf{E}) - \Delta \mathbf{E}, \quad (\text{D.6})$$

one finds for the separate terms,

$$\nabla(\nabla \cdot \mathbf{E}_{h,\text{inh}}^T) = -\mathbf{k}_P(\mathbf{k}_P \cdot \mathbf{E}_{h,\text{inh}}^T), \quad (\text{D.7})$$

$$\Delta \mathbf{E}_{h,\text{inh}}^T = -|k_P|^2 \mathbf{E}_{h,\text{inh}}^T, \quad (\text{D.8})$$

$$\frac{\partial^2 \mathbf{E}_{h,\text{inh}}^T}{\partial t^2} = -\omega_h^2 \mathbf{E}_{h,\text{inh}}^T, \quad (\text{D.9})$$

$$\frac{\partial^2 \mathbf{P}_{\text{NL},h}}{\partial t^2} = -\omega_h^2 \mathbf{P}_{\text{NL},h}. \quad (\text{D.10})$$

Before inserting the above terms into the wave equation (D.2), the common factor on both sides of the equation,

$$\frac{\hat{P}_{\text{NL},h}}{\varepsilon_0} \left(\frac{\omega_h}{c} \right)^2 \exp(i(\mathbf{k}_P \mathbf{r} - \omega_h t)), \quad (\text{D.11})$$

seen on the RHS and in the electric field eq. (D.5), is divided out. After inserting the remaining terms into the wave equation, the denominator $(k_h^T)^2 - (k_P)^2$ is put on the RHS of the equation, leading to

$$\mathbf{k}_P \left(\mathbf{k}_P \left[\mathbf{e}_p - \frac{\mathbf{k}_P(\mathbf{k}_P \cdot \mathbf{e}_p)}{(k_h^T)^2} \right] \right) - (k_P)^2 \left[\mathbf{e}_p - \frac{\mathbf{k}_P(\mathbf{k}_P \cdot \mathbf{e}_p)}{(k_h^T)^2} \right] \quad (\text{D.12})$$

$$+ \underbrace{\frac{\varepsilon(\omega_h)}{c^2} (\omega_h)^2}_{(k_h^T)^2} \left[\mathbf{e}_p - \frac{\mathbf{k}_P(\mathbf{k}_P \cdot \mathbf{e}_p)}{(k_h^T)^2} \right] = \mathbf{e}_p \left[(k_h^T)^2 - (k_P)^2 \right].$$

$$(\text{D.13})$$

To show that this equation is indeed fulfilled, brackets are solved and terms are kept in place. It is verified that all terms are of unit wavenumber squared. Finally, terms are labeled to aid comparison,

$$\underbrace{\mathbf{k}_P(\mathbf{k}_P \cdot \mathbf{e}_p)}_{T_1} - \underbrace{\mathbf{k}_P \frac{(\mathbf{k}_P)^2(\mathbf{k}_P \cdot \mathbf{e}_p)}{(k_h^T)^2}}_{T_2} - \underbrace{(k_P)^2 \mathbf{e}_p}_{T_3} + \underbrace{\mathbf{k}_P \frac{(\mathbf{k}_P)^2(\mathbf{k}_P \cdot \mathbf{e}_p)}{(k_h^T)^2}}_{-T_2} + \underbrace{(k_h^T)^2 \mathbf{e}_p}_{T_4} - \underbrace{\mathbf{k}_P(\mathbf{k}_P \cdot \mathbf{e}_p)}_{-T_1} = \underbrace{\mathbf{e}_p (k_h^T)^2}_{T_4} - \underbrace{\mathbf{e}_p (k_P)^2}_{T_3}. \quad (\text{D.14})$$

It is seen that term one to term four (labeled as T_1, \dots, T_4) cancel on both sides, verifying the inhomogeneous solution eq. (D.5).

D.1. Reflected harmonics

Interface conditions To determine the amplitude of the reflected and the transmitted wave, the interface conditions [143] that follow from Maxwell's equations using Stokes law,

$$\nabla \times \mathbf{E} = -\frac{\partial \mathbf{B}}{\partial t} \quad \rightarrow \quad \oint_{\partial A} \mathbf{E} \, d\ell = -\int_A \frac{\partial \mathbf{B}}{\partial t} \, dA. \quad (\text{D.15})$$

are applied. Shrinking the distance between the boundary and the interface to zero, the integral on the right vanishes. On the LHS, the tangential components from both sides of the interface remain, proving their equality $E_1^{\text{tan}} = E_2^{\text{tan}}$. This can be written as a cross-product with the interface normal,

$$\mathbf{n} \times (\mathbf{E}_1 - \mathbf{E}_2) = 0, \quad (\text{D.16})$$

$$\mathbf{n} \times (\mathbf{H}_1 - \mathbf{H}_2) = 0. \quad (\text{D.17})$$

The continuity of the tangential components of the H -field, eq. (D.17), follows analogously from Ampere's law. The continuity of normal components, on the other hand, is derived from the divergence equations, where integration over a cylindrical volume and application of Gauss theorem yields,

$$\nabla \cdot \mathbf{D} = \rho \quad \rightarrow \quad \oint_V \mathbf{D} \, d\mathbf{A} = \int \rho \, dV. \quad (\text{D.18})$$

Shrinking the radius to zero yields the continuity of the displacement that is normal to the interface $D_1^{\text{perp}} = D_2^{\text{perp}}$. This can be written as a scalar product with the interface normal,

$$\mathbf{n} \cdot (\mathbf{D}_1 - \mathbf{D}_2) = 0, \quad (\text{D.19})$$

$$\mathbf{n} \cdot (\mathbf{B}_1 - \mathbf{B}_2) = 0. \quad (\text{D.20})$$

Next, we consider the simplest case, that transmitted and reflected harmonics only have non-vanishing polarization components that are tangential to the interface. This configuration is also called s-polarization (s \rightarrow German senkrecht) which is perpendicular to the plane spanned by the incident and surface normal.

Continuity of tangential components Consequently, also the polarization of the medium has only a tangential vector component. We exploit the continuity of tangential field components (D.16), that provides the reflected wave (medium 1), given by the free-space solution, $E_1 = E_{\text{hom}}^R$ is equal to the transmitted wave (medium 2), that is given by the superposition of homogeneous and inhomogeneous solution, $E_2 = E_{\text{hom}}^T + E_{\text{inh}}^T$. Dropping common prefactors and exploiting that in the inhomoge-

neous solution the \mathbf{k}_P contribution is perpendicular to the polarization, yields,

$$\hat{E}_h^R = \hat{E}_h^T - \frac{\hat{P}_{\text{NL},h} \left(\frac{\omega_h}{c}\right)^2}{(k_h^T)^2 - (k_P)^2}, \quad (\text{D.21})$$

using $ck = \omega$ and $n^2 = \varepsilon_r$, yields,

$$\hat{E}_h^R = \hat{E}_h^T - \frac{\hat{P}_{\text{NL},h}}{\varepsilon_r(\omega_h) - \varepsilon_r(\omega_1)}. \quad (\text{D.22})$$

Eq. (D.22) still contains two unknowns the reflected \hat{E}_h^R and transmitted harmonic amplitude \hat{E}_h^T . They are related next by the second continuity equation.

Exploiting the continuity of the magnetizing field To eliminate the transmitted field from eq. D.22, the continuity of the magnetizing field \mathbf{H} is considered next,

$$\mathbf{n} \times (\mathbf{H}_1 - \mathbf{H}_2) = 0. \quad (\text{D.23})$$

The amplitude of the magnetizing field is related to the electric field via the medium speed of light in the following way,

$$\mathbf{H} = \mu_0 \mu_r \mathbf{B}, \quad (\text{D.24})$$

$$\mathbf{B} = \frac{1}{\omega_1} \mathbf{k} \times \mathbf{E}. \quad (\text{D.25})$$

Here, $\mu_r = 1$ which holds for most materials in optics. Hence we find $\mathbf{H} \sim \mathbf{k} \times \mathbf{E}$ and insert into eq. (D.23),

$$\mathbf{n} \times (\mathbf{k}_1 \times \mathbf{E}_1 - \mathbf{k}_2 \times \mathbf{E}_2) = 0, \quad (\text{D.26})$$

we notice that the magnitude of the wave vector is usually different on both sides (1 and 2) of the interface. Carrying out the double cross product, we exploit that the electric field is tangential, i.e. perpendicular to the surface normal,

$$\left(\mathbf{k}_1 \underbrace{(\mathbf{nE}_1)}_0 - \mathbf{E}_1(\mathbf{nk}_1) \right) - \left(\mathbf{k}_2 \underbrace{(\mathbf{nE}_2)}_0 - \mathbf{E}_2(\mathbf{nk}_2) \right) = 0. \quad (\text{D.27})$$

The scalar product yields the cosine of the angle of incidence. The magnitude of the wave vector is proportional to the index of refraction i.e. the square root of the relative permittivity, $|k| = \frac{n_{\text{ior}}\omega}{c} = \sqrt{\varepsilon_r} \frac{n_{\text{ior}}\omega}{c}$. If the projection of the wavevectors on the surface normal points in the same direction,

$$\sqrt{\varepsilon_{r,1}} E_1 \cos \theta_1 = \sqrt{\varepsilon_{r,2}} E_2 \cos \theta_2, \quad (\text{D.28})$$

otherwise, a minus sign needs to be introduced on the LHS,

$$-\sqrt{\varepsilon_{r,1}} E_1 \cos \theta_1 = \sqrt{\varepsilon_{r,2}} E_2 \cos \theta_2 . \quad (\text{D.29})$$

Inserting the vacuum and the medium fields, i.e. $E_1 = E_{\text{hom}}^R$ and $E_2 = E_{\text{hom}}^T + E_{\text{inh}}^T$ yields,

$$\boxed{-\hat{E}^R \cos \theta^R = \sqrt{\varepsilon_r(\omega_h)} \cos \theta^T \hat{E}^T - \sqrt{\varepsilon_r(\omega_1)} \cos \theta^S \frac{P_{\text{NL},h}/\varepsilon_0}{\varepsilon_r(\omega_h) - \varepsilon_r(\omega_1)}} . \quad (\text{D.30})$$

Here, the source wave sees a different refractive index, than the transmitted harmonic. For this reason, the angle of propagation of the transmitted harmonic θ^T and the source wave θ^S can be different in general.

Amplitude of reflected wave To determine the amplitude of the reflected wave, the amplitude of the transmitted wave in eq. (D.30) is eliminated by inserting the intermediate result eq. (D.22),

$$-\hat{E}^R \cos \theta^R = \sqrt{\varepsilon_r(\omega_h)} \cos \theta^T \left[\hat{E}^R + \frac{P_{\text{NL},h}/\varepsilon_0}{\varepsilon_r(\omega_h) - \varepsilon_r(\omega_1)} \right] - \sqrt{\varepsilon_r(\omega_1)} \cos \theta^S \frac{P_{\text{NL},h}/\varepsilon_0}{\varepsilon_r(\omega_h) - \varepsilon_r(\omega_1)} . \quad (\text{D.31})$$

Factoring out the reflected field and terms proportional to the nonlinear polarization,

$$-\hat{E}^R \left[\cos \theta^R + \sqrt{\varepsilon_r(\omega_h)} \cos \theta^T \right] = \left[\sqrt{\varepsilon_r(\omega_h)} \cos \theta^T - \sqrt{\varepsilon_r(\omega_1)} \cos \theta^S \right] \frac{P_{\text{NL},h}/\varepsilon_0}{\varepsilon_r(\omega_h) - \varepsilon_r(\omega_1)} , \quad (\text{D.32})$$

yields the reflected amplitude,

$$\hat{E}^R = \frac{\sqrt{\varepsilon_r(\omega_h)} \cos \theta^T - \sqrt{\varepsilon_r(\omega_1)} \cos \theta^S}{\cos \theta^R + \sqrt{\varepsilon_r(\omega_h)} \cos \theta^T} \frac{-P_{\text{NL},h}/\varepsilon_0}{\varepsilon_r(\omega_h) - \varepsilon_r(\omega_1)} . \quad (\text{D.33})$$

Case of normal incidence In the case of normal incidence, all cosine terms become unity, such that the reflected amplitude simplifies according to the third binomial formula to,

$$\hat{E}^R = \frac{\sqrt{\varepsilon_r(\omega_h)} - \sqrt{\varepsilon_r(\omega_1)}}{1 + \sqrt{\varepsilon_r(\omega_h)}} \frac{-P_{\text{NL},h}/\varepsilon_0}{\varepsilon_r(\omega_h) - \varepsilon_r(\omega_1)} \quad (\text{D.34})$$

$$= \frac{-P_{\text{NL},h}/\varepsilon_0}{[1 + \sqrt{\varepsilon_r(\omega_h)}][\sqrt{\varepsilon_r(\omega_h)} + \sqrt{\varepsilon_r(\omega_1)}]} . \quad (\text{D.35})$$

This relation is further simplified for a flat dispersion, i.e. $\sqrt{\varepsilon_r(\omega_1)} = \sqrt{\varepsilon_r(\omega_2)} = n_{\text{ior}}$,

$$\hat{E}^R = \frac{-P_{\text{NL},h}/\varepsilon_0}{2n_{\text{ior}}(1+n_{\text{ior}})}, \quad (\text{D.36})$$

which used in eq. (7.1).

D.2. Degeneracy of Brunel emission

In this section, the degeneracy weights of Brunel harmonics are calculated, which consist, in the single color case, of two components. To see this, we chose as a starting point the Brunel dipole acceleration in the no-depletion limit of the plane wave scenario, see eq. (3.38), that is repeated here for convenience

$$\frac{\partial \mathbf{J}_{\text{Br}}}{\partial t} = \frac{q^2 n_0}{m_e} \frac{\hat{\Gamma}}{\hat{E}^s} \mathbf{E}(t) \int_{t_0}^t dt' |\mathbf{E}(t')|^s. \quad (\text{D.37})$$

Here the function under the integral can be represented by an even order harmonic series, similar to the derivation of the m^{th} order nonlinear polarization in eq. (3.5).

$$\frac{\partial \mathbf{J}_{\text{Br}}}{\partial t} = \frac{q^2 n_0}{m_e} \frac{\hat{\Gamma}}{2^s} \mathbf{E} \int_{t_0}^t \sum_{h=0,2,4,\dots}^s D_h^{(s)} e^{ih\omega_0 t} + c.c. \quad , \quad D_h^{(s)} = \binom{s}{\frac{s+h}{2}}. \quad (\text{D.38})$$

The time integral turns into an inverse frequency weight of each term up to the $h = 0$ term. This DC contribution to the integral I_{DC} is only relevant for the response at the fundamental frequency and is disregarded in the following.

$$\frac{\partial \mathbf{J}_{\text{Br}}}{\partial t} = \frac{q^2 n_0}{m_e} \frac{\hat{\Gamma}}{2^s} (\mathbf{E}^+ + \mathbf{E}^-) \left[\sum_{h=2,4,6,\dots}^s \frac{D_h^{(s)}}{i\omega_0} e^{ih\omega_0 t} + I_{\text{DC}} \right] + c.c. \quad (\text{D.39})$$

Finally, writing the field factor in front of the sum as a superposition of positive and negative frequency contribution, shows that the frequencies in the series are once shifted up and once shifted down. Combining the different paths leading to the same harmonic yields,

$$\frac{\partial \mathbf{J}_{\text{Br}}}{\partial t} = \mathbf{e}_x \sum_{h=1,3,5,\dots}^m D_{\text{Br},h} \frac{\hat{J}_{\text{Br}}}{2} e^{ih\omega_0 t} + c.c., \quad (\text{D.40})$$

with degeneracy weight,

$$D_{\text{Br},h} = \frac{D_h^-}{h-1} + \frac{D_h^+}{h+1} \quad \text{with,} \quad D_h^\pm = \binom{s}{\frac{s \pm 1 + h}{2}} \quad \text{for} \quad h > 1, \quad (\text{D.41})$$

and amplitude of the dipole acceleration,

$$\hat{J}_{\text{Br}} = 2 \frac{q^2 n_0 \hat{\Gamma} \hat{E}}{2^{s+1} m_e i \omega_0}. \quad (\text{D.42})$$

In summary, the two possible channels contributing to one harmonic are weighted differently as seen in eq. (D.41). These separated channels are due to the integral acting only on one part of the E-field dependence in the initial eq. (D.37), while one field term remains outside the integral. Hence, the formal structure of the Brunel response makes the degeneracy factor less simple compared to that of the injection mechanism.

D.3. Computing the band structure in Fourier representation

For a precise calculation of the band structure imaginary time-step propagation in coordinate space can be time-consuming, as the convergence against the different states can be challenging for several reasons.

Here we also use an alternative method, namely by expanding the wavefunction in a Fourier series and solving Fourier coefficients self consistently for different bands n through a single matrix inversion [148]. Starting point of this approach is an expansion of an arbitrary superposition state $\psi(x)$ and lattice periodic potential $V(x)$ in Fourier coefficients,

$$\psi(x) = \sum_k C_k e^{ikr}, \quad (\text{D.43})$$

$$V(x) = \sum_G V_G e^{iGx}, \quad \text{with: } G \in \frac{2\pi}{a} \{0, \pm 1, \pm 2, \dots\}. \quad (\text{D.44})$$

So far there are no restrictions on k as we allow ψ to take any form. However, the potential $V(x) = V(x+a)$ is assumed to be lattice periodic. Hence, it is expanded into Fourier terms at reciprocal lattice points G . Inserting eq. (D.43), (D.44) into the

The k dependence of the band matrix \bar{V}_k is contained in the diagonal elements $\tilde{V}_N = V_0 + \frac{(k-G_N)^2}{2}$. In principle, this matrix is of infinite dimension. However, it turns out that only ten rows are needed to converge the eigenenergies of the lowest band $E_{1,k}$. For additional bands, additional pairs has to be appended at the top and the bottom of this matrix equation. Considering 19 rows of the form of eq. (D.51) is sufficient to converge $E_{1,k}, \dots, E_{10,k}$ inside the first Brillouin zone. Numerically, this can be done with Coleski or QR decomposition that is built into the `eig()` function of Matlab. The corresponding Bloch wave is given by the eigenvectors $C_{n,k}$ as,

$$\psi_{n,k}(x) = \sum_G C_{n,k-G} e^{i(k-G)x} . \quad (\text{D.52})$$

In the main text, in sect. 7.3.1 this very fast, auxiliary method is used to compare the band structure with relaxed eigenstates obtained from Numerov boosted Crank-Nicolson imaginary time propagation that utilizes the Sherman-Morrison-Woodbury formula for the periodic boundary conditions [166].

D.4. Velocity-Verlet integration of electron and hole trajectories

To compute semi-classical electron trajectories, we discretize the acceleration theorem (7.7) according to the velocity-Verlet integration scheme around the integer time index t ,

$$\dot{k}^t = \frac{q}{\hbar} E_x(x^t, t) \quad (\text{D.53})$$

$$a^t = \frac{1}{\hbar} \left. \frac{\partial^2 E_n}{\partial k^2} \right|_{k^t} \dot{k}^t \quad (\text{D.54})$$

$$x^{t+1} = x^t + v^t \Delta t + \frac{1}{2} a^t \Delta t^2 \quad (\text{D.55})$$

$$k^{t+1} = k^t + \frac{q}{\hbar} \frac{E_x(x^t, t) + E_x(x^{t+1}, t + \Delta t)}{2} \Delta t \quad (\text{D.56})$$

$$v^{t+1} = \frac{1}{\hbar} \left. \frac{\partial E_n}{\partial k} \right|_{k^t} \quad (\text{D.57})$$

with $q = -e$ being the charge of the electron, E_n the k -dependent eigenenergy and E_x the x-component of the linearly polarized electric field.

We use that states obey same dynamics in the single-active electron picture regardless whether they are occupied or unoccupied, which is a direct consequence of the linearity of the one-electron TDSE. Hence, vacancies follow the same equation of motion as electrons above. In accordance with this argument, the same physical result

for $x(t)$ is found for positively charged hole particles $q = +e$, that carry by convention $E_h(k) = -E_e(k)$ the negative electron energy [148].

The semiclassical trajectories for holes in the valence band and electrons in the conduction band, determined from numerical integration of the equations (D.53)–(D.57), are shown by green lines in Fig. 7.6.

Bibliography

- [1] A. Sommer, E. Bothschafter, S. Sato, C. Jakubeit, T. Latka, O. Razskazovskaya, H. Fattahi, M. Jobst, W. Schweinberger, V. S. Shirvanyan, Vand Yakovlev, R. Kienberger, K. Yabana, N. Karpowicz, M. Schultze and F. Krausz, *Attosecond nonlinear polarization and light–matter energy transfer in solids*, [Nature](#) **534**, 86–90 (2016).
- [2] A. M. Sommer, *Ultrafast strong field dynamics in dielectrics*, PhD thesis, [Ludwig-Maximilians-Universität München](#) (2016).
- [3] A. Schiffrin, T. Paasch-Colberg, N. Karpowicz, V. Apalkov, D. Gerster, S. Mühlbrandt, M. Korbman, J. Reichert, M. Schultze, S. Holzner et al., *Optical-field-induced current in dielectrics*, [Nature](#) **493**, 70 (2013).
- [4] M. Garg, M. Zhan, T. T. Luu, H. Lakhotia, T. Klostermann, A. Guggenmos and E. Goulielmakis, *Multi-petahertz electronic metrology*, [Nature](#) **538**, 359–363 (2016).
- [5] M. T. Hassan, T. T. Luu, A. Moulet, O. Raskazovskaya, P. Zhokhov, M. Garg, N. Karpowicz, A. Zheltikov, V. Pervak, F. Krausz and E. Goulielmakis, *Optical attosecond pulses and tracking the nonlinear response of bound electrons*, [Nature](#) **530**, 66–70 (2016).
- [6] L. Englert, M. Wollenhaupt, L. Haag, C. Sarpe-Tudoran, B. Rethfeld and T. Baumert, *Material processing of dielectrics with temporally asymmetric shaped femtosecond laser pulses on the nanometer scale*, [Appl. Phys. A](#) **92**, 749–753 (2008).
- [7] B. Rethfeld, D. S. Ivanov, M. E. Garcia and S. I. Anisimov, *Modelling ultrafast laser ablation*, [Journal of Physics D: Applied Physics](#) **50**, 193001 (2017).
- [8] L. Sudrie, A. Couairon, M. Franco, B. Lamouroux, B. Prade, S. Tzortzakis and A. Mysyrowicz, *Femtosecond laser-induced damage and filamentary propagation in fused silica*, [Physical Review Letters](#) **89**, 186601 (2002).

- [9] M. Malinauskas, A. Zukauskas, S. Hasegawa, Y. Hayasaki, V. Mizeikis, R. Buividas and S. Juodkazis, *Ultrafast laser processing of materials: from science to industry*, *Light: Science & Applications* **5**, e16133–e16133 (2016).
- [10] D. Blömer, A. Szameit, F. Dreisow, T. Schreiber, S. Nolte and A. Tünnermann, *Nonlinear refractive index of fs-laser-written waveguides in fused silica*, *Optics express* **14**, 2151–2157 (2006).
- [11] D. Du, X. Liu, G. Korn, J. Squier and G. Mourou, *Laser-induced breakdown by impact ionization in SiO₂ with pulse widths from 7 ns to 150 fs*, *Applied physics letters* **64**, 3071–3073 (1994).
- [12] R. R. Gattass and E. Mazur, *Femtosecond laser micromachining in transparent materials*, *Nature photonics* **2**, 219–225 (2008).
- [13] Y. Jia, S. Wang and F. Chen, *Femtosecond laser direct writing of flexibly configured waveguide geometries in optical crystals: fabrication and application*, *Opto-Electronic Advances* **3**, 190042–1 (2020).
- [14] T. Brabec and H. Kapteyn, *Strong field laser physics*, Springer (2008), ISBN: 978-0-387-34755-4.
- [15] S. Nisar, L. Li and M. Sheikh, *Laser glass cutting techniques - A review*, *Journal of Laser Applications* **25**, 042010 (2013).
- [16] R. Taylor, C. Hnatovsky and E. Simova, *Applications of femtosecond laser induced self-organized planar nanocracks inside fused silica glass*, *Laser & Photonics Reviews* **2**, 26–46 (2008).
- [17] M. Olbrich, E. Punzel, R. Roesch, R. Oettking, B. Muhsin, H. Hoppe and A. Horn, *Case study on the ultrafast laser ablation of thin aluminum films: dependence on laser parameters and film thickness*, *Applied Physics A* **122**, 1–8 (2016).
- [18] A. Couairon, L. Sudrie, M. Franco, B. Prade and A. Mysyrowicz, *Filamentation and damage in fused silica induced by tightly focused femtosecond laser pulses*, *Physical Review B* **71**, 125435 (2005).
- [19] M. Lenzner, J. Krüger, S. Sartania, Z. Cheng, C. Spielmann, G. Mourou, W. Kautek and F. Krausz, *Femtosecond optical breakdown in dielectrics*, *Physical Review Letters* **80**, 4076 (1998).

- [20] M. Mero, J. Liu, W. Rudolph, D. Ristau and K. Starke, *Scaling laws of femtosecond laser pulse induced breakdown in oxide films*, *Physical Review B* **71**, 115109 (2005).
- [21] B. Schütte, M. Arbeiter, A. Mermillod-Blondin, M. J. Vrakking, A. Rouzée and T. Fennel, *Ionization avalanching in clusters ignited by extreme-ultraviolet driven seed electrons*, *Phys. Rev. Lett.* **116**, 033001 (2016).
- [22] P. Zhokhov and A. Zheltikov, *Optical breakdown of solids by few-cycle laser pulses*, *Scientific reports* **8**, 1–10 (2018).
- [23] J.-L. Déziel, L. J. Dubé and C. Varin, *Dynamical rate equation model for femtosecond laser-induced breakdown in dielectrics*, *Physical Review B* **104**, 045201 (2021).
- [24] Q. Liu, L. Seiffert, F. Süßmann, S. Zherebtsov, J. Passig, A. Kessel, S. A. Trushin, N. G. Kling, I. Ben-Itzhak, V. Mondes, C. Graf, E. Rühl, L. Veisz, S. Karsch, J. Rodríguez-Fernández, M. I. Stockman, J. Tiggesbäumker, K.-H. Meiwes-Broer, T. Fennel and M. F. Kling, *Ionization-induced subcycle metallization of nanoparticles in few-cycle pulses*, *ACS Photonics* **7**, 3207–3215 (2020).
- [25] M. Kitzler and S. Gräfe, *Ultrafast Dynamics Driven by Intense Light Pulses*, *Springer Series on Atomic, Optical, and Plasma Physics* **86**, (2016).
- [26] L. Keldysh, *Behavior of non-metallic crystals in strong electric fields*, *Soviet Journal of Experimental and Theoretical Physics* **6**, 763 (1958).
- [27] C. B. Schaffer, A. Brodeur and E. Mazur, *Laser-induced breakdown and damage in bulk transparent materials induced by tightly focused femtosecond laser pulses*, *Meas. Sci. Technol.* **12**, 1784 (2001).
- [28] P. Agostini, F. Fabre and G. Mamfray, *G. Petite and N K. Rahman*, *Phys. Rev Letters* **42**, 1127 (1975).
- [29] T.-M. Yan and D. Bauer, *Sub-barrier Coulomb effects on the interference pattern in tunneling-ionization photoelectron spectra*, *Physical Review A* **86**, 053403 (2012).
- [30] F. Lindner, M. G. Schätzel, H. Walther, A. Baltuska, E. Goulielmakis, F. Krausz, D. Milosević, D. Bauer, W. Becker and G. G. Paulus, *Attosecond double-slit experiment*, *Physical review letters* **95**, 040401 (2005).
- [31] P. B. Corkum and F. Krausz, *Attosecond science*, *Nature Physics* **3**, 381–387 (2007).

- [32] M. Wegener, *Extreme nonlinear optics: an introduction*, Springer Science & Business Media (2005), ISBN: 978-3-540-26688-4.
- [33] T. Brabec and F. Krausz, *Intense few-cycle laser fields: Frontiers of nonlinear optics*, *Reviews of Modern Physics* **72**, 545 (2000).
- [34] P. B. Corkum, *Plasma perspective on strong field multiphoton ionization*, *Phys. Rev. Lett.* **71**, 1994 (1993).
- [35] M. Lewenstein, P. Balcou, M. Y. Ivanov, A. L’huillier and P. B. Corkum, *Theory of high-harmonic generation by low-frequency laser fields*, *Physical Review A* **49**, 2117 (1994).
- [36] S. Ghimire and D. A. Reis, *High-harmonic generation from solids*, *Nature physics* **15**, 10–16 (2019).
- [37] S. Jiang, S. Gholam-Mirzaei, E. Crites, J. E. Beetar, M. Singh, R. Lu, M. Chini and C. Lin, *Crystal symmetry and polarization of high-order harmonics in ZnO*, *Journal of Physics B: Atomic, Molecular and Optical Physics* **52**, 225601 (2019).
- [38] E. Goulielmakis and T. Brabec, *High harmonic generation in condensed matter*, *Nature Photonics* **16**, 411–421 (2022).
- [39] S. Ghimire, A. D. DiChiara, E. Sistrunk, P. Agostini, L. F. DiMauro and D. A. Reis, *Observation of high-order harmonic generation in a bulk crystal*, *Nature physics* **7**, 138–141 (2011).
- [40] A. Lanin, E. Stepanov, A. Fedotov and A. Zheltikov, *Mapping the electron band structure by intraband high-harmonic generation in solids*, *Optica* **4**, 516–519 (2017).
- [41] G. Vampa, T. Hammond, N. Thiré, B. Schmidt, F. Légaré, C. McDonald, T. Brabec and P. Corkum, *Linking high harmonics from gases and solids*, *Nature* **522**, 462–464 (2015).
- [42] G. Vampa, *Role of Electron-Hole Recollisions in High Harmonic Generation from Bulk Crystals*, PhD thesis, University of Ottawa (2016).
- [43] M. Hohenleutner, F. Langer, O. Schubert, M. Knorr, U. Huttner, S. Koch, M. Kira and R. Huber, *Real-time observation of interfering crystal electrons in high-harmonic generation*, *Nature* **523**, 572–575 (2015).

- [44] O. Schubert, M. Hohenleutner, F. Langer, C. Urbanek, Band Lange, U. Huttner, D. Golde, T. Meier, M. Kira, S. W. Koch and R. Huber, *Sub-cycle control of terahertz high-harmonic generation by dynamical Bloch oscillations*, *Nature Photonics* **8**, 119–123 (2014).
- [45] T. T. Luu, M. Garg, S. Y. Kruchinin, A. Moulet, M. T. Hassan and E. Goulielmakis, *Extreme ultraviolet high-harmonic spectroscopy of solids*, *Nature* **521**, 498–502 (2015).
- [46] P. Mulser and D. Bauer, *High power laser-matter interaction*, Springer Science & Business Media (2010), ISBN: 978-3-540-46065-7.
- [47] G. Ndabashimiye, S. Ghimire, M. Wu, D. A. Browne, K. J. Schafer, M. B. Gaarde and D. A. Reis, *Solid-state harmonics beyond the atomic limit*, *Nature* **534**, 520–523 (2016).
- [48] G. Vampa, P. Corkum and T. Brabec, *Apparatus and method for tunable generation of coherent radiation*, US Patent, no. US20160149371 A1 (2016).
- [49] M. Garg, H.-Y. Kim and E. Goulielmakis, *Ultimate waveform reproducibility of extreme-ultraviolet pulses by high-harmonic generation in quartz*, *Nature Photonics* **12**, 291–296 (2018).
- [50] F. Krausz and M. I. Stockman, *Attosecond metrology: from electron capture to future signal processing*, *Nature Photonics* **8**, 205–213 (2014).
- [51] M. Siviş, M. Taucer, G. Vampa, K. Johnston, A. Staudte, A. Y. Naumov, D. Villeneuve, C. Ropers and P. Corkum, *Tailored semiconductors for high-harmonic optoelectronics*, *Science* **357**, 303–306 (2017).
- [52] Z. Wang, H. Park, Y. H. Lai, J. Xu, C. I. Baga, F. Yang, P. Agostini and L. F. DiMauro, *The roles of photo-carrier doping and driving wavelength in high harmonic generation from a semiconductor*, *Nature communications* **8**, 1–7 (2017).
- [53] Y. S. You, Y. Yin, Y. Wu, A. Chew, X. Ren, F. Zhuang, S. Gholam-Mirzaei, M. Chini, Z. Chang and S. Ghimire, *High-harmonic generation in amorphous solids*, *Nature communications* **8**, 1–5 (2017).
- [54] C. Yu, S. Jiang and R. Lu, *High order harmonic generation in solids: a review on recent numerical methods*, *Advances in Physics: X* **4**, 1562982 (2019).

- [55] L. Yue and M. B. Gaarde, *Introduction to theory of high-harmonic generation in solids: tutorial*, *JOSA B* **39**, 535–555 (2022).
- [56] G. Vampa, C. McDonald, G. Orlando, D. Klug, P. Corkum and T. Brabec, *Theoretical analysis of high-harmonic generation in solids*, *Physical review letters* **113**, 073901 (2014).
- [57] D. Golde, T. Meier and S. Koch, *High harmonics generated in semiconductor nanostructures by the coupled dynamics of optical inter-and intraband excitations*, *Physical Review B* **77**, 075330 (2008).
- [58] C. Yu, X. Zhang, S. Jiang, X. Cao, G. Yuan, T. Wu, L. Bai and R. Lu, *Dependence of high-order-harmonic generation on dipole moment in SiO₂ crystals*, *Physical Review A* **94**, 013846 (2016).
- [59] G. Wachter, *Simulation of condensed matter dynamics in strong femtosecond laser pulses*, PhD thesis, *Technische Universität Wien* (2014).
- [60] K. K. Hansen, D. Bauer and L. B. Madsen, *Finite-system effects on high-order harmonic generation: From atoms to solids*, *Physical Review A* **97**, 043424 (2018).
- [61] I. Floss, C. Lemell, G. Wachter, V. Smejkal, S. A. Sato, X.-M. Tong, K. Yabana and J. Burgdörfer, *Ab initio multiscale simulation of high-order harmonic generation in solids*, *Physical Review A* **97**, 011401 (2018).
- [62] F. Brunel, *Harmonic generation due to plasma effects in a gas undergoing multiphoton ionization in the high-intensity limit*, *JOSA B* **7**, 521–526 (1990).
- [63] D. Bauer, R. Salomaa and P. Mulser, *Generation of ultrashort light pulses by a rapidly ionizing thin foil*, *Physical Review E* **58**, 2436 (1998).
- [64] C. W. Siders, G. Rodriguez, J. L. Siders, F. G. Omenetto and A. J. Taylor, *Measurement of ultrafast ionization dynamics of gases by multipulse interferometric frequency-resolved optical gating*, *Physical Review Letters* **87**, 263002 (2001).
- [65] M. Uiberacker, T. Uphues, M. Schultze, A. J. Verhoef, V. Yakovlev, M. F. Kling, J. Rauschenberger, N. M. Kabachnik, H. Schröder, M. Lezius, K. L. Kompa, H.-G. Muller, M. J. J. Vrakking, S. Hendel, U. Kleineberg, U. Heinzmann, M. Drescher and F. Krausz, *Attosecond real-time observation of electron tunnelling in atoms*, *Nature* **446**, 627–632 (2007).

- [66] A. L. Cavalieri, N. Müller, T. Uphues, V. S. Yakovlev, A. Baltuska, B. Horvath, B. Schmidt, L. Blümel, R. Holzwarth, S. Hendel, M. Drescher, U. Kleineberg, P. M. Echenique, R. Kienberger, F. Krausz and U. Heinzmann, *Attosecond spectroscopy in condensed matter*, *Nature* **449**, 1029–1032 (2007).
- [67] M. Gertsvolf, M. Spanner, D. Rayner and P. Corkum, *Demonstration of attosecond ionization dynamics inside transparent solids*, *Journal of Physics B: Atomic, Molecular and Optical Physics* **43**, 131002 (2010).
- [68] A. J. Verhoef, A. V. Mitrofanov, E. E. Serebryannikov, D. V. Kartashov, A. M. Zheltikov and A. Baltuska, *Optical detection of tunneling ionization*, *Physical review letters* **104**, 163904 (2010).
- [69] A. V. Mitrofanov, A. J. Verhoef, E. E. Serebryannikov, J. Lumeau, L. Glebov, A. M. Zheltikov and A. Baltuska, *Optical detection of attosecond ionization induced by a few-cycle laser field in a transparent dielectric material*, *Physical review letters* **106**, 147401 (2011).
- [70] M. Geissler, G. Tempea, A. Scrinzi, M. Schnürer, F. Krausz and T. Brabec, *Light propagation in field-ionizing media: extreme nonlinear optics*, *Physical review letters* **83**, 2930 (1999).
- [71] K. Yabana, T. Sugiyama, Y. Shinohara, T. Otobe and G. Bertsch, *Time-dependent density functional theory for strong electromagnetic fields in crystalline solids*, *Physical Review B* **85**, 045134 (2012).
- [72] S. Ghimire, A. D. DiChiara, E. Sistrunk, G. Ndabashimiye, U. B. Szafruga, A. Mohammad, P. Agostini, L. F. DiMauro and D. A. Reis, *Generation and propagation of high-order harmonics in crystals*, *Physical Review A* **85**, 043836 (2012).
- [73] G. Vampa, H. Liu, T. F. Heinz and D. A. Reis, *Disentangling interface and bulk contributions to high-harmonic emission from solids*, *Optica* **6**, 553–556 (2019).
- [74] R. W. Boyd, *Nonlinear optics*, Academic press (2002), ISBN: 978-0123694706.
- [75] M. Gertsvolf, *Controlled material modification of transparent dielectrics by femtosecond laser pulses*, PhD thesis, University of Ottawa (Canada) (2009).
- [76] G. L. Yudin and M. Y. Ivanov, *Nonadiabatic tunnel ionization: Looking inside a laser cycle*, *Physical Review A* **64**, 013409 (2001).

- [77] A. Couairon, E. Brambilla, T. Corti, D. Majus, O. d. J. Ramírez-Góngora and M. Kolesik, *Practitioner's guide to laser pulse propagation models and simulation*, *The European Physical Journal Special Topics* **199**, 5–76 (2011).
- [78] M. Kolesik, J. Moloney and M. Mlejnek, *Unidirectional optical pulse propagation equation*, *Physical review letters* **89**, 283902 (2002).
- [79] A. Husakou and J. Herrmann, *Supercontinuum generation of higher-order solitons by fission in photonic crystal fibers*, *Physical Review Letters* **87**, 203901 (2001).
- [80] A. Taflove, S. C. Hagness and M. Picket-May, *Computational electromagnetics: the finite-difference time-domain method*, *The Electrical Engineering Handbook* **3**, 629–670 (2005).
- [81] D. M. Sullivan, *Electromagnetic simulation using the FDTD method*, John Wiley & Sons (2013), ISBN: 9781118646700.
- [82] J. B. Schneider, *Understanding the finite-difference time-domain method*, School of electrical engineering and computer science, Washington State University **28**, (2021).
- [83] E. M. L. Bothschafter, *Femtosecond and Attosecond Electron Dynamics in Semiconductors and Dielectrics*, PhD thesis, Technische Universität München (2014).
- [84] T. Boolakee, C. Heide, A. Garzón-Ramírez, H. B. Weber, I. Franco and P. Hommelhoff, *Light-field control of real and virtual charge carriers*, *Nature* **605**, 251–255 (2022).
- [85] D. Jang, R. M. Schwartz, D. Woodbury, J. Griff-McMahon, A. H. Younis, H. M. Milchberg and K.-Y. Kim, *Efficient terahertz and Brunel harmonic generation from air plasma via mid-infrared coherent control*, *Optica* **6**, 1338–1341 (2019).
- [86] P. Jürgens, *Strong-field induced plasma formation in solid dielectrics*, PhD thesis, Freie Universität Berlin (2020).
- [87] P. Jürgens, M. Vrakking, A. Husakou, R. Stoian and A. Mermillod-Blondin, *Plasma formation and relaxation dynamics in fused silica driven by femtosecond short-wavelength infrared laser pulses*, *Applied Physics Letters* **115**, 191903 (2019).
- [88] S. Y. Kruchinin, M. Korbman and V. S. Yakovlev, *Theory of strong-field injection and control of photocurrent in dielectrics and wide band gap semiconductors*, *Physical Review B* **87**, 115201 (2013).

- [89] R. Buschlinger, S. Nolte and U. Peschel, *Self-organized pattern formation in laser-induced multiphoton ionization*, *Physical Review B* **89**, 184306 (2014).
- [90] M. Ammosov, N. Delone and V. Krainov, *Tunnel ionization of complex atoms and of atomic ions in an alternating electric field*, *Sov. Phys. - JETP* **64**, (1986).
- [91] I. Babushkin, Á. J. Galán, J. R. C. de Andrade, A. Husakou, F. Morales, M. Kretschmar, T. Nagy, V. Vaicaitis, L. Shi, D. Zuber, L. Bergé, S. Skupin, I. A. Nikoleeva, N. A. Panow, D. E. Shipilo, O. G. Kosareva, A. N. Pfeiffer, A. Demircan, M. J. Vrakking, U. Morgner and M. Ivanov, *All-optical attoclock for imaging tunnelling wavepackets*, *Nature Physics* **18**, 417–422 (2022).
- [92] I. Babushkin, C. Brée, C. M. Dietrich, A. Demircan, U. Morgner and A. Husakou, *Terahertz and higher-order Brunel harmonics: from tunnel to multiphoton ionization regime in tailored fields*, *Journal of Modern Optics* **64**, 1078–1087 (2017).
- [93] T. Balciunas, A. Verhoef, A. Mitrofanov, G. Fan, E. Serebryannikov, M. Ivanov, A. Zheltikov and A. Baltuška, *Optical and THz signatures of sub-cycle tunneling dynamics*, *Chemical Physics* **414**, 92–99 (2013).
- [94] K.-Y. Kim, J. H. Glowia, A. J. Taylor and G. Rodriguez, *Terahertz emission from ultrafast ionizing air in symmetry-broken laser fields*, *Optics Express* **15**, 4577–4584 (2007).
- [95] K.-Y. Kim, A. Taylor, J. Glowia and G. Rodriguez, *Coherent control of terahertz supercontinuum generation in ultrafast laser–gas interactions*, *Nature photonics* **2**, 605–609 (2008).
- [96] I. Babushkin, S. Skupin, A. Husakou, C. Köhler, E. Cabrera-Granado, L. Bergé and J. Herrmann, *Tailoring terahertz radiation by controlling tunnel photoionization events in gases*, *New Journal of Physics* **13**, 123029 (2011).
- [97] F. Campi, S. D. C. Roscam Abbing, Z.-Y. Zhang, M. van der Geest and P. M. Kraus, *Efficient extreme-ultraviolet multi-band high-order wave mixing in silica*, *SPIE Proceedings* **11886**, 117–124 (2021).
- [98] C. Liu, V. Tripathi and B. Eliasson, *High-power laser-plasma interaction*, *Cambridge University Press* (2019), ISBN: 9781108635844.

- [99] M. R. Snider WC, Uman MA, *Is a Propagating Infinite Plane Wave a "Radiation Field?"*, *International Journal of Magnetism and Electromagnetism*, (2021).
- [100] B. Sundaram and P. W. Milonni, *High-order harmonic generation: simplified model and relevance of single-atom theories to experiment*, *Physical Review A* **41**, 6571 (1990).
- [101] J. Eberly and M. Fedorov, *Spectrum of light scattered coherently or incoherently by a collection of atoms*, *Physical Review A* **45**, 4706 (1992).
- [102] D. Lappas, M. Fedorov and J. Eberly, *Spectrum of light scattered by a strongly driven atom*, *Physical Review A* **47**, 1327 (1993).
- [103] K. Burnett, V. Reed, J. Cooper and P. Knight, *Calculation of the background emitted during high-harmonic generation*, *Physical Review A* **45**, 3347 (1992).
- [104] C. Jürß and D. Bauer, *Topological edge-state contributions to high-order harmonic generation in finite flakes*, *Physical Review B* **106**, 054303 (2022).
- [105] L. Bielke, C. Jürß and D. Bauer, *Size and sampling effects in solid-state high-harmonic generation*, *arXiv preprint arXiv:2211.06244*, (2022).
- [106] D. Diestler, *Harmonic generation: quantum-electrodynamical theory of the harmonic photon-number spectrum*, *Physical Review A* **78**, 033814 (2008).
- [107] A. D. Bandrauk, S. Chelkowski, S. Kawai and H. Lu, *Effect of nuclear motion on molecular high-order harmonics and on generation of attosecond pulses in intense laser pulses*, *Physical review letters* **101**, 153901 (2008).
- [108] J. Zhao and Z. Zhao, *Probing H²⁺ vibrational motions with high-order harmonic generation*, *Physical Review A* **78**, 053414 (2008).
- [109] J. C. Baggesen and L. B. Madsen, *On the dipole, velocity and acceleration forms in high-order harmonic generation from a single atom or molecule*, *Journal of Physics B: Atomic, Molecular and Optical Physics* **44**, 115601 (2011).
- [110] J. C. Baggesen and L. B. Madsen, *Reply to 'Comment on "On the dipole, velocity and acceleration forms in high-order harmonic generation from a single atom or molecule"'*, *Journal of Physics B: Atomic, Molecular and Optical Physics* **45**, 028002 (2011).

- [111] J. Pérez-Hernández and L. Plaja, *Comment on 'On the dipole, velocity and acceleration forms in high-order harmonic generation from a single atom or molecule'*, *Journal of Physics B: Atomic, Molecular and Optical Physics* **45**, 028001 (2012).
- [112] J. Bertrand, H. J. Wörner, H.-C. Bandulet, É. Bisson, M. Spanner, J.-C. Kieffer, D. Villeneuve and P. B. Corkum, *Ultra-high-order wave mixing in noncollinear high harmonic generation*, *Physical review letters* **106**, 023001 (2011).
- [113] B. E. Saleh and M. C. Teich, *Fundamentals of photonics*, John Wiley & sons (1991), ISBN: 9780471213741.
- [114] F. Lindner, G. G. Paulus, H. Walther, A. Baltuska, E. Goulielmakis, M. Lezius and F. Krausz, *Gouy phase shift for few-cycle laser pulses*, *Physical review letters* **92**, 113001 (2004).
- [115] B. Rethfeld, *Unified model for the free-electron avalanche in laser-irradiated dielectrics*, *Physical review letters* **92**, 187401 (2004).
- [116] N. Brouwer and B. Rethfeld, *Transient electron excitation and nonthermal electron-phonon coupling in dielectrics irradiated by ultrashort laser pulses*, *Physical Review B* **95**, 245139 (2017).
- [117] W. Demtröder, *Experimentalphysik 1, Mechanik und Wärme*, Springer (1998), ISBN: 978-3-662-54847-9.
- [118] L. Seiffert, Q. Liu, S. Zherebtsov, A. Trabattoni, P. Rupp, M. Castrovilli, M. Galli, F. Süßmann, K. Wintersperger, J. Stierle, G. Sansone, L. Poletto, F. Frassetto, I. Halfpap, V. Mondes, C. Graf, E. Rühl, F. Krausz, M. Nisoli, T. Fennel, F. Calegari and M. F. Kling, *Attosecond chronoscopy of electron scattering in dielectric nanoparticles*, *Nature physics* **13**, 766–770 (2017).
- [119] W. Lotz, *Electron-impact ionization cross-sections for atoms up to $Z=108$* , *Zeitschrift für Physik A Hadrons and nuclei* **232**, 101–107 (1970).
- [120] A. Kaiser, B. Rethfeld, M. Vicanek and G. Simon, *Microscopic processes in dielectrics under irradiation by subpicosecond laser pulses*, *Physical Review B* **61**, 11437 (2000).
- [121] B. Stuart, M. Feit, A. Rubenchik, B. Shore and M. Perry, *Laser-induced damage in dielectrics with nanosecond to subpicosecond pulses*, *Physical review letters* **74**, 2248 (1995).

- [122] M. Sparks, D. Mills, R. Warren, T. Holstein, A. Maradudin, L. Sham, E. Loh Jr and D. King, *Theory of electron-avalanche breakdown in solids*, *Physical Review B* **24**, 3519 (1981).
- [123] M. Lebugle, N. Sanner, N. Varkentina, M. Sentis and O. Utéza, *Dynamics of femtosecond laser absorption of fused silica in the ablation regime*, *Journal of Applied Physics* **116**, 063105 (2014).
- [124] N. S. Shcheblanov, E. P. Silaeva and T. E. Itina, *Electronic excitation and relaxation processes in wide band gap dielectric materials in the transition region of the Keldysh parameter*, *Applied surface science* **258**, 9417–9420 (2012).
- [125] M. Jupe, L. Jensen, A. Melninkaitis, V. Sirutkaitis and D. Ristau, *Calculations and experimental demonstration of multi-photon absorption governing fs laser-induced damage in titania*, *Optics express* **17**, 12269–12278 (2009).
- [126] P. Audebert, P. Daguzan, A. Dos Santos, J. Gauthier, J. Geindre, S. Guizard, G. Hamoniaux, K. Krastev, P. Martin, G. Petite and A. Antonetti, *Space-time observation of an electron gas in Si O₂*, *Physical Review Letters* **73**, 1990 (1994).
- [127] P. Martin, S. Guizard, P. Daguzan, G. Petite, P. D'oliveira, P. Meynadier and M. Perdrix, *Subpicosecond study of carrier trapping dynamics in wide-band-gap crystals*, *Physical Review B* **55**, 5799 (1997).
- [128] M. García-Lechuga, L. Haahr-Lillevang, J. Siegel, P. Balling, S. Guizard and J. Solis, *Simultaneous time-space resolved reflectivity and interferometric measurements of dielectrics excited with femtosecond laser pulses*, *Physical Review B* **95**, 214114 (2017).
- [129] T. Winkler, L. Haahr-Lillevang, C. Sarpe, B. Zielinski, N. Götte, A. Senftleben, P. Balling and T. Baumert, *Laser amplification in excited dielectrics*, *Nature Physics* **14**, 74–79 (2018).
- [130] S. H. Møller, S. T. Andersen and P. Balling, *Transient optical properties of highly excited dielectric materials: Apparent birefringence and delayed reflectivity increase*, *Physical Review Research* **2**, 043010 (2020).
- [131] M. Schultze, E. M. Bothschafter, A. Sommer, S. Holzner, W. Schweinberger, M. Fiess, M. Hofstetter, R. Kienberger, V. Apalkov, M. I. S. Yakovlev, Vladislav S and F. Krausz, *Controlling dielectrics with the electric field of light*, *Nature* **493**, 75 (2013).

- [132] M. Schultze, K. Ramasesha, C. Pemmaraju, S. Sato, D. Whitmore, A. Gandman, J. S. Prell, L. Borja, D. Prendergast, K. Yabana, D. M. Neumark and S. R. Leone, *Attosecond band-gap dynamics in silicon*, *Science* **346**, 1348–1352 (2014).
- [133] F. Schlaepfer, M. Lucchini, S. A. Sato, M. Volkov, L. Kasmi, N. Hartmann, A. Rubio, L. Gallmann and U. Keller, *Attosecond optical-field-enhanced carrier injection into the GaAs conduction band*, *Nature Physics* **14**, 560–564 (2018).
- [134] E. Serebryannikov, A. Verhoef, A. Mitrofanov, A. Baltuska and A. Zheltikov, *Signatures of attosecond electron tunneling dynamics in the evolution of intense few-cycle light pulses*, *Physical Review A* **80**, 053809 (2009).
- [135] D. Spangenberg, P. Neethling, E. Rohwer, M. H. Brüggemann and T. Feurer, *Time-domain ptychography*, *Physical Review A* **91**, 021803 (2015).
- [136] T. Witting, D. Greening, D. Walke, P. Matia-Hernando, T. Barillot, J. Marangos and J. Tisch, *Time-domain ptychography of over-octave-spanning laser pulses in the single-cycle regime*, *Optics letters* **41**, 4218–4221 (2016).
- [137] R. Trebino and D. J. Kane, *Using phase retrieval to measure the intensity and phase of ultrashort pulses: frequency-resolved optical gating*, *JOSA A* **10**, 1101–1111 (1993).
- [138] R. Trebino, K. W. DeLong, D. N. Fittinghoff, J. N. Sweetser, M. A. Krumbügel, B. A. Richman and D. J. Kane, *Measuring ultrashort laser pulses in the time-frequency domain using frequency-resolved optical gating*, *Review of Scientific Instruments* **68**, 3277–3295 (1997).
- [139] S. Linden, H. Gießen and J. Kuhl, *XFROG—a new method for amplitude and phase characterization of weak ultrashort pulses*, *physica status solidi (b)* **206**, 119–124 (1998).
- [140] J. M. Rodenburg and H. M. Faulkner, *A phase retrieval algorithm for shifting illumination*, *Applied physics letters* **85**, 4795–4797 (2004).
- [141] P. Thibault, M. Dierolf, O. Bunk, A. Menzel and F. Pfeiffer, *Probe retrieval in ptychographic coherent diffractive imaging*, *Ultramicroscopy* **109**, 338–343 (2009).
- [142] A. M. Maiden and J. M. Rodenburg, *An improved ptychographical phase retrieval algorithm for diffractive imaging*, *Ultramicroscopy* **109**, 1256–1262 (2009).
- [143] J. D. Jackson, *Classical electrodynamics*, Wiley (1999), ISBN: 978-0-471-30932-1.

- [144] C. Varin, R. Emms, G. Bart, T. Fennel and T. Brabec, *Explicit formulation of second and third order optical nonlinearity in the FDTD framework*, *Computer Physics Communications* **222**, 70–83 (2018).
- [145] C. Varin, G. Bart, R. Emms and T. Brabec, *Saturable Lorentz model for fully explicit three-dimensional modeling of nonlinear optics*, *Optics express* **23**, 2686–2695 (2015).
- [146] P. K. Velpula, M. Bhuyan, F. Courvoisier, H. Zhang, J.-P. Colombier and R. Stoian, *Spatio-temporal dynamics in nondiffractive Bessel ultrafast laser nanoscale volume structuring*, *Laser & Photonics Reviews* **10**, 230–244 (2016).
- [147] J.-L. Déziel, L. J. Dubé, S. H. Messaddeq, Y. Messaddeq and C. Varin, *Femtosecond self-reconfiguration of laser-induced plasma patterns in dielectrics*, *Physical Review B* **97**, 205116 (2018).
- [148] R. Gross, A. Marx, D. Einzel and S. Geprägs, *Festkörperphysik*, de Gruyter (2018), ISBN: 9783110566130.
- [149] T. Bredtmann, M. Ivanov, C. Peltz, T. Fennel, P. Polinkin and A. Husakou, *A finite-difference model for intense light Interaction with dielectrics in the Ultrafast Ionization regime*, private communication , (2017).
- [150] A. D. Rakić, A. B. Djurisić, J. M. Elazar and M. L. Majewski, *Optical properties of metallic films for vertical-cavity optoelectronic devices*, *Applied optics* **37**, 5271–5283 (1998).
- [151] G. Mur, *Absorbing boundary conditions for the finite-difference approximation of the time-domain electromagnetic-field equations*, *IEEE transactions on Electromagnetic Compatibility* **23**, 377–382 (1981).
- [152] J.-P. Berenger, *A perfectly matched layer for the absorption of electromagnetic waves*, *Journal of computational physics* **114**, 185–200 (1994).
- [153] S. D. Gedney, *An anisotropic perfectly matched layer-absorbing medium for the truncation of FDTD lattices*, *IEEE Trans. Antennas Propag.* **44**, 1630–1639 (1996).
- [154] D. Puerto, J. Siegel, W. Gawelda, M. Galvan-Sosa, L. Ehrentraut, J. Bonse and J. Solis, *Dynamics of plasma formation, relaxation, and topography modification induced by femtosecond laser pulses in crystalline and amorphous dielectrics*, *JOSA B* **27**, 1065–1076 (2010).

- [155] G. Vampa, Y. You, H. Liu, S. Ghimire and D. Reis, *Observation of backward high-harmonic emission from solids*, *Optics express* **26**, 12210–12218 (2018).
- [156] N. Bloembergen and P. Pershan, *Light waves at the boundary of nonlinear media*, *Physical review* **128**, 606 (1962).
- [157] D. Hui, H. Alqattan, S. Yamada, V. Pervak, K. Yabana and M. T. Hassan, *Attosecond electron motion control in dielectric*, *Nature Photonics* **16**, 33–37 (2021).
- [158] J. Seres, E. Seres, C. Serrat and T. Schumm, *Non-perturbative generation of DUV/VUV harmonics from crystal surfaces at 108 MHz repetition rate*, *Optics express* **26**, 21900–21909 (2018).
- [159] S. Nekrashevich and V. Gritsenko, *Electronic structure of silicon dioxide (a review)*, *Physics of the Solid State* **56**, 207–222 (2014).
- [160] T. Koslowski, W. Kob and K. Vollmayr, *Numerical study of the electronic structure of amorphous silica*, *Physical Review B* **56**, 9469 (1997).
- [161] D. Bauer, H. Bauke, T. Brabec, T. Fennel, C. R. McDonald, D. B. Milosević, S. Pabst, C. Peltz, G. Pöplau, R. Santra and C. Varin, *Computational strong-field quantum dynamics. Intense light-matter interactions*, *De Gruyter* (2017), ISBN: 9783110417265.
- [162] K. K. Hansen, T. Deffge and D. Bauer, *High-order harmonic generation in solid slabs beyond the single-active-electron approximation*, *Physical Review A* **96**, 053418 (2017).
- [163] C. Kittel, *Introduction to solid state physics*, *John Wiley and Sons* (2021), ISBN: 978-0-471-41526-8.
- [164] T. Ikemachi, Y. Shinohara, T. Sato, J. Yumoto, M. Kuwata-Gonokami and K. L. Ishikawa, *Trajectory analysis of high-order-harmonic generation from periodic crystals*, *Physical Review A* **95**, 043416 (2017).
- [165] D. Gabor, *Theory of communication. Part 1: The analysis of information*, *Journal of the Institution of Electrical Engineers-Part III: Radio and Communication Engineering* **93**, 429–441 (1946).
- [166] T. Fennel and D. Bauer, *Many-particle theory & numerical methods*, *Lecture Notes*, Institute for Physics, University of Rostock, (2022).

Academic Curriculum Vitae

Personal Information

Name: Benjamin Liewehr
Date of birth: 07.04.1991, Itzehoe, Germany
Residence: Voßstraße 10, 18059 Rostock, Germany
Contact: Benjamin.Liewehr@outlook.de

Academic Education

Since 01.01.2017 PhD Student at Strong-Field Nano-Physics Group,
led by Prof. Dr. T. Fennel, Institute for Physics,
University of Rostock

01.08.14 – 31.07.16 Master of Science in Physics, Soft Matter Systems
Research Group, led by Prof. Dr. M. Bachmann,
Department of Physics and Astronomy,
Center for Simulational Physics, University of Georgia, USA

01.10.11 – 30.09.14 Bachelor of Science in Physics, Quantum Theory and
Many-Particles Group, led by Prof. Dr. D. Bauer,
Institute for Physics, University of Rostock

Teaching Experience

01.04.22 - 26.08.22 – Master Level Seminar:
14.04.21 - 09.08.21 Many Particle Theory and Numerical Methods (English)
20.04.20 - 25.09.20

12.10.21 – 31.01.22 – Master Level Seminar:
03.11.20 – 31.01.21 Atoms and Clusters (English)
14.10.19 – 31.01.20
15.10.18 – 31.01.19

- 07.01.19 – 30.09.19 – Supervision of Bachelor Thesis:
Ph. Zischke – Quantum-Mechanical Description of
Metal Clusters by means of the Jellium Model
- 01.04.19 – 12.07.19 – Bachelor’s Practical Lab Training:
04.04.18 – 13.07.18 Mechanics and Heat (German)
- 01.01.16 – 31.07.16 – Bachelor’s Practical Lab Training:
Electromagnetism and Optics (English)
- 15.08.14 – 31.12.15 – Bachelor’s Practical Lab Training:
Mechanics and Heat (English)
- 01.10.13 – 31.01.14 – Tutorial Class: for Experimental Physics (German)
- 24.09.13 – 05.10.13 – Tutorial Class: for Calculus (German)

Awards

- 2021 Teaching Award, Faculty of Mathematics and Natural Sciences (MNF),
University of Rostock
- 2019 PhD State-Scholarship Mecklenburg-Vorpommern, Germany
- 2016 Anderson-Pioletti Award for Outstanding Early Graduate Student,
Department for Physics & Astronomy, University of Georgia, USA
- 2014 Study Abroad Fellowship,
Studienstiftung des deutschen Volkes
- 2012 Scholarship for Physics Studies,
Studienstiftung des deutschen Volkes
- 2009 Scholarship for Computer Science Studies,
University of Kiel

List of Presentations

Talks

- 2022 Reconstruction of Tunnel Ionization Dynamics in Dielectrics from Injection Harmonics, DPG Spring Meeting 2022 (online), Erlangen, Germany
- 2021 Signatures and Scaling of Injection Harmonics in Solids, Optics and Applications 2021, Rostock, Germany
- 2018 Simulation of Brunel Harmonics from Laser-Driven Dielectric Solids, DPG-Spring-Meeting 2018, Erlangen, Germany
- 2017 High Harmonic Generation from thin Solid Targets, Graduate School of Physics Seminar 2017, Rostock, Germany
- 2016 Homopolymer Adsorption on Hexagonal Surfaces: A Replica-Exchange Monte Carlo Study, APS March Meeting 2016, Baltimore, MD, USA
- 2015 Homopolymer Adsorption on a Hexagonal Surface: A Replica-Exchange Monte Carlo Study, VIIIth Brazilian Meeting on Simulational Physics 2015, Mar de Canavieiras Hotel, Florianopolis, Brazil
- 2015 Thermodynamic and Structural Behavior of Polymers: How Computer Simulations Reveal New Insights, Colloquium: Mestrado em Física 2015, Instituto de Física, Universidade Federal de Mato Grosso, Cuiabá, Brazil

Posters

- 2022 Signatures and Scaling of Injection Harmonics in Solids,
LiMatI Summer School 2022, Rostock, Germany
- 2020 Origin of Strong-Field Induced Low-Order Harmonic Generation in Amorphous Solids, QUTIF Young Researcher Meeting 2020 (online), Oldenburg, Germany
- 2020 Effects of Tunnel Ionization on Non-Linear Response of Solids,
CMD 2020 GEFES (online), Madrid, Spain
- 2020 Collisional Effects in the Extreme Nonlinear Response of Dielectrics,
DPG Frühjahrstagung 2020 (conference canceled), Hannover, Germany
- 2019 Origin of Strong-Field Induced Low-Order Harmonic Generation in Amorphous Solids, Atto 2019, Szeged, Hungary
- 2019 Effective Nonlinearity of Ionization Harmonics in Amorphous Solids,
DPG Frühjahrstagung 2019, Rostock, Germany
- 2017 High Harmonic Generation from Thin SiO₂ Foils,
Clustertreffen 2017, Burg Stahleck, Bacharach, Germany
- 2016 Surface Pattern Effects upon Polymer Adsorption,
29th Annual CSP Workshop 2016, University of Georgia, Athens, GA, USA
- 2015 Effects of Bonded Interactions on the Structural Phase Properties of a Flexible Elastic Homopolymer, 28th Annual CSP Workshop 2015, University of Georgia, Athens, GA, USA

Statement of Authorship

according to §4 of the doctoral regulations of the Faculty of Mathematics and Natural Sciences of the University of Rostock

I make the following declaration:

1. The opportunity for the present doctoral project has not been commercially procured for me. In particular, I have not engaged any organization that seeks supervisors for a dissertation for a fee, or to take care of all or part of the duties incumbent upon me with regard to the examination.
2. I hereby declare in lieu of an oath that I have written this thesis on my own independently and without external help. For this purpose I have not used any aids or sources other than those indicated by me. Passages taken verbatim and in terms of content from the works are marked accordingly.

Rostock, 14. April 2023

Selbstständigkeitserklärung

gemäß §4 der Promotionsordnung der Mathematisch-Naturwissenschaftlichen Fakultät der Universität Rostock

Ich gebe folgende Erklärung ab:

1. Die Gelegenheit zum vorliegenden Promotionsvorhaben ist mir nicht kommerziell vermittelt worden. Insbesondere habe ich keine Organisation eingeschaltet, die gegen Entgelt Betreuerinnen/Betreuer für die Anfertigung von Dissertationen sucht oder die mir obliegenden Pflichten hinsichtlich der Prüfungsleistungen für mich ganz oder teilweise erledigt.
2. Ich versichere hiermit an Eides statt, dass ich die vorliegende Arbeit selbstständig angefertigt und ohne fremde Hilfe verfasst habe. Dazu habe ich keine außer den von mir angegebenen Hilfsmitteln und Quellen verwendet und die den benutzten Werken inhaltlich und wörtlich entnommenen Stellen habe ich als solche kenntlich gemacht.

Rostock, 14. April 2023

Acknowledgement – Danksagung

Diese Arbeit wäre nicht ohne die Zusammenarbeit zahlreicher Menschen möglich gewesen. An erster Stelle möchte ich mich bei dem Betreuer dieser Promotion, Prof. Dr. Thomas Fennel, bedanken, der mir die Bearbeitung dieses spannenden, hochaktuellen Forschungsthemas in der Arbeitsgruppe ermöglicht hat und mich stets in diesem Projekt unterstützt hat. Hierbei bin ich besonders dankbar für die zahlreichen Möglichkeiten bei spannenden Lehrveranstaltungen unterstützen zu können, zu Tagungen zu reisen und Ergebnisse vor Fachpublikum zu diskutieren. Insbesondere möchte ich auch die herzliche und aufgeschlossene Zusammenarbeit mit Dr. Alexandre Mermillod-Blondin und Dr. Peter Jürgens vom Max-Born Institut dankend hervorheben, die mir bereits in der Anfangsphase meiner Promotion bei einem Messaufenthalt direkte Laboreinblicke in das Experiment ermöglicht haben. Auch der regelmäßige Austausch mit meinem Bürokollegen und Mitdoktoranden Björn Kruse zu neuen Fragestellungen war stets eine wertvolle Bereicherung. Nicht weniger Danke ich dem ganzen Team der AG Starkfeld-Nanophysik, Dr. Christian Peltz, Dr. Lennart Seiffert, Jonas Apportin, Paul Tümmeler, Richard Altenkirch, Anne Herzig und Jana Mütze. Als besonders lehrreich behalte ich gern die intensiven Diskussionsrunden in der AG zur Vorbereitung von Vorträgen in Erinnerung. Letzlich möchte ich mich bei meiner Ehefrau, meinen Eltern und der Familie für die fortwährende Unterstützung bedanken.